

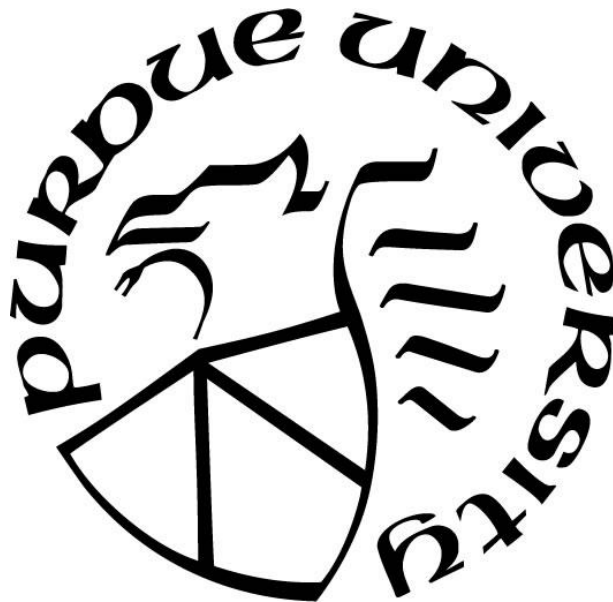
**INFLUENCE OF IRRADIATION AND LASER WELDING ON
DEFORMATION MECHANISMS IN AUSTENITIC STAINLESS STEELS**

by
Keyou Mao

A Dissertation

*Submitted to the Faculty of Purdue University
In Partial Fulfillment of the Requirements for the degree of*

Doctor of Philosophy



School of Materials Engineering

West Lafayette, Indiana

August 2019

**THE PURDUE UNIVERSITY GRADUATE SCHOOL
STATEMENT OF COMMITTEE APPROVAL**

Dr. Janelle P. Wharry, Chair

School of Nuclear Engineering

School of Materials Engineering

Dr. Xinghang Zhang, Co-Chair

School of Materials Engineering

Dr. Michael S. Titus

School of Materials Engineering

Dr. Maria Okuniewski

School of Materials Engineering

Approved by:

Dr. David F. Bahr

Head of the Graduate Program

Soli Deo Gloria. To the beloved.

ACKNOWLEDGMENTS

“For from him and through him and to him are all things. To him be glory forever. Amen”

-Roman 11:36.

The past three years of my doctoral study at Purdue was an advantageous journey to experience the truth, grace and love from Him above. If I had a chance to reselect the school, Purdue would still be my top choice. To continue my Ph.D. at Purdue was demonstrated as a wise choice and I am proud to be a Boilermaker. The heritage of Purdue will be maintained to impact my future. Hopefully I will bring this legacy to let the world feel the Purdue spirit.

My family has always been my base along this journey. I could not even think of any meaningful words to express my appreciation for the support I have been receiving from my parents and my other family members, Qinyong Mao, Hongyan Xiong, and my grandparents Huanliang Mao, Qiaodi Shi, Guoqi Xiong and Yulan Gong, and my aunt Qinjuan Mao, my cousin Xuyang Xiang, and Yi-Xuewen Zhu.

I am grateful to my advisor Dr. Janelle P. Wharry for her guidance and encouragement during my graduate studies at Purdue University. She is an extraordinary person and I regard her as my Shi-Fu and the best professor ever met. I wish to extend my thanks to Dr. Maria A. Okuniewski, Dr. Michael S. Titus, and Dr. Xinghang Zhang for their service on my dissertation committee as well as their valuable input to improve the work being presented.

This work is supported by the Idaho National Laboratory Directed Research & Development (LDRD) Program under Department of Energy (DOE) Idaho Operations Office Contract DE-AC07-051D14517. This work was also supported by the U.S. Department of Energy, Office of Nuclear Energy under DOE Idaho Operations Office Contract DE-AC07-051D14517 as part of a Nuclear Science User Facilities experiment. Portions of this work were also funded by the DOE Office of Nuclear Energy contract DE-NE0008525.

I would like to take this opportunity to thank my mentor, Dr. Cheng Sun, and staff members from the advanced characterization and PIE division of the Idaho National Laboratory and other peers who helped me with the small-scale mechanical testing, including Dr. Xiang Liu, Dr. Fei Teng, Dr. David Frazer, Ching-Heng Shiau, James Madden, Dr. Jan-Fong Jue, Dr. Emmanuel Perez, Dr. Jian Gan, Dr. Mitchell K. Meyer and Dr. Jeffery Giglio. Our collaborators, including Dr. Lin Shao and Mr. Aaron French at Texas A&M University, also helped us with the ion-beam irradiation. I would also like to thank Ms. Jatu Burns, Ms. Joanna Taylor, Dr. Yaqiao Wu, Dr. Megha Dubey and Mr. Bryan Forsmann from the Microscopy and Characterization Suite at the Center for Advanced Energy Studies (CAES) for their assistance with microscopy and sample preparation. People during my internship at Idaho National Laboratory I should also thank: Dr. Fabiola Cappia, Dr. Fidelma Oconnel, Dr. Yongfeng Zhag, Dr. Jianguo Yu, Ms. Charlyne Smith, Ms. Tanvi Ajantiwalay, Ms. Carol Bruinsma, Ms. Xiaoqin Wiklund, Ms. Grace Wiklund, Mr. Likuo Chi, Ms. Fujen Jue, Mr. Matthew McGukin, Mr. Ronald Carlson and Mrs. Angela Carlson. Moreover, I want to express my special thanks to Dr. Frank A. Garner for providing the valuable “hex block” samples and insightful suggestions as well as Paula D. Freyer, and Dr. Lucille A. Giannuzzi for the sample transfer and extremely useful technical discussion. Furthermore, I would like to extend my appreciation to my group members including Dr. Kayla Yano, Mr. Priyam Patki, Ms. Amrita Sen, Jerry Qu, Patrick Warren, George Warren, and Chidubem N Enebechi. They are awesome individuals and our home team is becoming stronger and stronger every day.

Even though I cannot share this wonderful moment and joy with her, I still feel thankful to my separated partner Aubree A. Burns, who had encouraged me and led me to become a better person. I wish her all the best. Life at Purdue would not have been complete without my friends Yuhao Wang, Shan Zhu, Zhe Ren, Li Cheng, Hao Wang, Krishina Chetty, Sen Xiang, Yang Zhao and Mark Brown as well as Dr. Jun Wang, my first research mentor. I wish to first thank my fellow classmates: Dr. Stylianos Chatzidakis, now at Oak Ridge National Laboratory, Dr. Avinash Vaidheeswaran, now at National Energy Technology Laboratory, and Dr. Bryan Sims, now at National Nuclear Security Administration, for their constructive criticism to help me improve during my time in graduate school. My sincerest apologies for forgetting to mention anyone who was instrumental in my success. I wish everyone the best in life, health, happiness, and prosperity. God bless you all.

TABLE OF CONTENTS

LIST OF TABLES	9
LIST OF FIGURES	10
ABSTRACT	19
1. INTRODUCTION	21
2. BACKGROUND	23
2.1 Significance of laser welding	23
2.1.1 Laser beam welding	23
2.1.2 Helium-induced cracking	24
2.1.3 Weldability of irradiated materials	26
2.2 Neutron irradiated AISI 304L stainless steel hex blocks	28
2.3 Microstructural characterization	29
2.3.1 Grain structures	30
2.3.2 Dislocations	30
2.3.3 Cavities	31
2.3.4 Precipitation	32
2.3.5 Radiation Induced Segregation	33
2.3.6 Role of He/dpa ratio	33
2.4 Micromechanical testing	34
2.4.1 Nanoindentation	35
2.4.1.1 Irradiation hardening	35
2.4.1.2 Grain orientation dependency	36
2.4.1.3 Indentation Size Effect	37
2.4.2 Micropillar compression	37
2.5 Deformation mechanisms	39
2.5.1 Dislocation glide	40
2.5.2 Deformation twinning	42
2.5.3 Deformation-induced martensitic transformation	43
2.5.4 Effect of irradiation	44
3. OBJECTIVE	81

4. EXPERIMENTAL.....	83
4.1 Hex-block materials	83
4.2 Laser welding and metallographic preparation.....	84
4.3 Electron Microscopy	87
4.3.1 Grain orientation	87
4.3.2 FIB lift outs.....	88
4.3.3 Microstructure characterization	89
4.4 Mechanical testing	90
4.4.1 Ex-situ Nanoindentation	90
4.4.2 <i>In-situ</i> micropillar compression.....	92
5. MICROSTRUCTURAL RESULTS.....	110
5.1 Irradiated microstructure.....	110
5.1.1 Dislocation Loops	110
5.1.2 Cavities	111
5.1.3 Precipitates.....	111
5.2 Post-welded microstructure	111
5.2.1 Loops	112
5.2.2 Cavities	112
5.2.3 Precipitates.....	112
5.3 Comparison of microstructural trends	113
5.3.1 Grain structure	113
5.3.2 Comparison of loops and cavities.....	113
5.3.3 Comparison of radiation-induced segregation.....	114
6. MECHANICAL TESTING RESULTS.....	131
6.1 Mechanical properties by nanoindentation	131
6.1.1 Hardness and elastic modulus.....	131
6.1.2 Post-nanoindentation microstructure	132
6.1.2.1 Archive versus irradiated AISI 304L SS	133
6.1.2.1.1 Bain transformation.....	134
6.1.2.2 Base metal versus HAZ	135
6.2 Mechanical properties by micropillar compression.....	136

6.2.1	Hardness and modulus	137
6.2.2	Post-compression microstructure.....	137
7.	DISCUSSION.....	162
7.1	Comparison of mechanical properties	162
7.1.1	Irradiation hardening	162
7.1.2	Laser welding softening.....	165
7.1.3	He/dpa effect.....	167
7.2	Deformation-induced martensitic transformation in high He and dose condition.....	168
7.2.1	Base metal.....	168
7.2.2	HAZ.....	169
7.3	Deformation twinning in low He and dose condition.....	170
7.4	Deformation transition criteria in austenitic stainless steels.....	173
7.4.1	Direct austenite-to-martensite phase transformation	174
7.4.2	Transition into hcp martensite	174
7.4.3	Transition into twinning	175
8.	CONCLUSTIONS AND FUTURE WORKS	187
	APPENDIX.....	189
	REFERENCES	209
	VITA.....	241
	PUBLICATIONS.....	242

LIST OF TABLES

Table 2.1 Schmid factors (SFs) for perfect and Shockley partial dislocations in fcc slip systems.	46
Table 2.2 Stacking fault energy (SFE) for fcc alloys (elemental composition in wt%).	47
Table 4.1 Hex coin triangles selected for removal of rectangular coupon for welding.....	93
Table 4.2 Summary of weld parameters used to prepare welds.	94
Table 5.1 Summary of microstructure features in the laser welds of all conditions.....	115
Table 6.1 Mechanical testing on all conditions.	140
Table 6.2 Hardness and modulus measurement by nanoindentation of the laser welds of irradiated AISI 304L SS of 23 dpa, 3 appm He.	141
Table 6.3 Summary of the fcc-bcc orientation relationship.....	142
Table 6.4 The Pitsch orientation relationships.....	143
Table 6.5 Schmid factors (SFs) for slip and twinning systems along the [101] loading direction.	144
Table 7.1 Quantitative analysis of the hardening contribution of the unirradiated and neutron irradiated AISI 304L SS (base metal) with 23 dpa and 3 appm He.	176
Table 7.2 Quantitative analysis of the softening contribution of the base metal and HAZ of the laser weld of irradiated AISI 304L SS with 23 dpa and 3 appm He.	177
Table 7.3 Nanoindentation hardness dependence on He and dpa level.....	178

LIST OF FIGURES

Figure 2.1 Schematic diagram of the laser weldment.....	48
Figure 2.2 Conventional gas tungsten arc weld on irradiated 304 SS containing 1.5 appm helium [44].	49
Figure 2.3 Schematic diagram showing the progression of He generation, He bubble formation, and grain boundary fracture.	50
Figure 2.4 Typical laser weld cross-section with dendritic grain structure and centerline [40]..	51
Figure 2.5 Comparison of weld cracking in He doped and irradiated 316 SS [43].	52
Figure 2.6 Reduction of cracking in laser welded 304 SS containing 50 appm He when heat input is reduced from (a) 20 kJ/cm to (b) 4 kJ/cm [5]. With a fixed heat input of 2 kJ/cm in 316L SS, GTAW produces microcracking (c), while (d) laser welding does not [6].	53
Figure 2.7 Effective laser weld heat input threshold of (a) 304SS and (b) 316SS (dashed line) as a function of He concentration. Below the threshold, welds do not produce He-induced cracks (green), but above the threshold, welds do produce He-induced cracks (red) [47].	54
Figure 2.8 Planar EBSD GROD maps for the deformed unirradiated specimens (SW') and a relationship between the maximum observed GROD value and strain level [53]. ...	55
Figure 2.9 Microstructure of unirradiated archive hex-block observed using electron microscopy, derived at a depth in the middle of the block, showing dislocation and slip structure characteristic of ~5% cold-work [54].	56
Figure 2.10 Bright-field TEM imaging of cavities from different specimens from hex-block 3D-28 dpa, 8 appm irradiated at 418°C and 3E-29 dpa, 8 appm irradiated at 420°C [54].	57
Figure 2.11 Backscattered electron (BSE) scanning microscopy imaging of cavities in hex-block of 28 dpa, 8 appm irradiated at 418°C shown in Figure 2.10 [64].	58
Figure 2.12 Comparison of void swelling of Fe ion irradiated 304L SS with neutron irradiated 304L SS with different grain sizes [66].	59
Figure 2.13 Ni and Si rich precipitates in (a) 0.4 dpa material and (b) 28 dpa material; (c) to (f): line profiles measured by placing a 10 nm diameter cylinder along the arrows indicated in (a) and (b) [61].	60
Figure 2.14 Fe ion irradiation-enhanced $M_{23}C_6$ precipitation in CG 304L SS [63].	61

Figure 2.15 APT data of concentration of elements through the grain boundary of 304 SS of 24 dpa [79].....	62
Figure 2.16 (a-b) Si ion irradiated 304 with pre-planted He indicates (a) loops increase as He increases and (b) cavity grows as dpa increases [81]. (c) He bubbles on a grain boundary [82].	63
Figure 2.17 (a) Array of nanoindents on an irradiated alloy [89]; (b) microcompression pillar [108]; (c) microcantilever on an irradiated alloy [87]; and (d) levels of difficulty in small-scale mechanical testing in the plane of experimental and data analysis [91]. 64	
Figure 2.18 Fe-20Cr-25Ni: color-coded standard stereographic triangles (SST) and distributions of elastic modulus and hardness of the indents close to {001}, {101}, and {111} grains [104].....	65
Figure 2.19 Irradiated 800H: hardness and modulus profiles as a function of depth and temperature of grains of (a-b) <111> and (c-d) <113> orientations [101].....	66
Figure 2.20 Nanoindentation data for hardness and modulus in two different grains and at grain boundary for an iron-based material [105].....	67
Figure 2.21 Relationship between damage and hardness profiles in ion irradiated SS316 using nanoindentation – experiments and modelling [98]......	68
Figure 2.22 SEM image of ion beam irradiated 304 SS (a-c) and (d) the engineering stress-strain curve with (e) TEM image of the post-compression irradiated sample [127].....	69
Figure 2.23 Experimentally quantifying critical stresses associated with basal slip and twinning in magnesium using micropillars [131].....	70
Figure 2.24 Schematic diagram of a perfect dislocation l into leading partial with Burgers vector b_1 and trailing partials with Burgers vector b_2 [145].....	71
Figure 2.25 Stacking faults of 316LN SS after 8% strain deformation from disk bending at 150 °C [232].....	72
Figure 2.26 Fault energy evolution in terms of the distance of partial <112> direction [166]....	73
Figure 2.27 Schematic diagram of twinning in an fcc lattice [233].....	74
Figure 2.28 Effect of grain orientation on twinning of Fe-Mn: (a) 0.05 and (b) 0.3 true strain [176].	75
Figure 2.29 Schematic diagram of martensitic transformation in an fcc lattice [233].	76
Figure 2.30 Schematic diagram of martensitic transformation in 304 SS [192].	77

Figure 2.31 Deformation mode changes from martensitic transformation to twinning with the increase of SFE by the concentration of Ni in an Fe-Cr-Ni [204].	78
Figure 2.32 Engineering stress versus strain curves of unirradiated and irradiated steels (a) solution annealed (SA) 304 at 19.4 dpa and (b) cold worked (CW) 316 at 19.7 dpa [100].	79
Figure 2.33 Deformation mode map of 316 SSs in terms of true stress and dose [222] domain.	80
Figure 4.1 Rectangular coupons were sectioned from 3 hex-block “triangles” to obtain 3 welding coupons. (a-g) Example showing selection of left triangle 5D2 (previously obtained from Coin 5D in 2012 of 1 dpa and 0.2 appm He) and sectioning of rectangular coupon from this triangle to obtain 1 of the 3 needed welding coupons. (h-j) Three hex-block triangles selected for welding studies.	95
Figure 4.2 Sketches showing how rectangular coupon was removed from 3 different hex-block triangle samples to obtain 3 welding coupons.	96
Figure 4.3 Example of in-cell process used to section rectangular coupon from hex-block triangle: photographs from inside the Westinghouse High Level Hot Cell showing milling of the surfaces on the rectangular plate removed from hex-block triangle 5D2 in preparation for subsequent welding.	97
Figure 4.4 Hot-cell pulsed laser welding equipment set-up.	98
Figure 4.5 Keyence digital microscope images showing the typical appearance of the WPS1 pulsed laser weld.	99
Figure 4.6 Sketch of cross-sectional weld sample geometries.	100
Figure 4.7 Photographs illustrating Step 1: cutting of thin cross-sectional slices through welds of interest.	101
Figure 4.8 Photographs of Step 2: further reduction of thin plate, include only the weld and a very limited amount of surrounding base material.	102
Figure 4.9 General appearance of further reduced weld cross sections with approximate dimensions of 3 mm × 2 mm × 1 mm (i.e., after Step 2 completed).	103
Figure 4.10 Light optical microscope images of selected weld samples obtained from weld coupon (post-etch images shown). Red arrows indicate laser weld-induced pores and red circles represent laser weld-induced cracks.	104
Figure 4.11 Images indicate locations for FIB lift-outs from laser welded specimen of 1 dpa, 0.2 appm He from 5D2 hex block.	105
Figure 4.12 Images document weld, HAZ, and weld + HAZ FIB lift-outs and grid positions from laser weldments shown in Fig. 4.11.	106

Figure 4.13 Images document different FIB lift-out locations in the base metal, weld, and HAZ from laser weldments shown in Fig. 4.11.	107
Figure 4.14 Schematic diagram of the mechanical testing and the follow-up post-deformed microstructural analysis on deformation mechanisms.	108
Figure 4.15 Hysitron PI-88 in-situ SEM mechanical testing system at Electron Microscopy Laboratory (EML) at Materials and Fuels Complex (MFC) in Idaho National Laboratory (INL). (a) PI-88 in operation and (b) holder.....	109
Figure 5.1 Comparison of microstructure before and after neutron irradiation. (a) Dislocations in the archive AISI 304L SS and (b) defect networks in irradiated AISI 304L SS at 23 dpa and 3 appm He under dark-field TEM mode with $g = 200$	116
Figure 5.2 Dislocation loops in the irradiated AISI 304L SS with 23 dpa and 3 appm He under the bright-field STEM mode. (a) Bright-field STEM imaging of dislocation loops on [001] zone axis (inset diffraction pattern). (b) Loop size distribution in (a) with overlaid Gaussian distribution.....	117
Figure 5.3 Rel-rod method of imaging Frank loops. (a-b) Frank loops with precipitate groups and single precipitates of neutron irradiated AISI 304L SS of 23 dpa and 3 appm He condition.....	118
Figure 5.4 Detailed microscopy and statistical analysis of irradiation induced-cavities on the irradiated AISI 304L SS of 23 dpa and 3 appm He. (a) HAADF STEM imaging of cavities. (b) Size distribution of cavities overlaid with a Gaussian distribution. (c-d) HRTEM (with inset FFTs) of a cavity enveloped by the dashed rectangle in (a) shows the incoherent interface between the cavity and the matrix under different focusing conditions: (c) overfocus and (d) underfocus.	119
Figure 5.5 Bright-field STEM images of loops in the HAZ on 113 zone axis with inset diffraction patterns. (a) 23 dpa, 3 appm He and (b) 28 dpa, 8 appm He.	120
Figure 5.6 Rel-rod images of interstitial Frank loops in the HAZ: (a) 23 dpa, 3 appm He and (b) 28 dpa, 8 appm He.....	121
Figure 5.7 HAADF of cavities in the HAZ: (a) 23 dpa, 3 appm He and (b) 28 dpa, 8 appm He.	122
Figure 5.8 Weak-beam dark-field image of precipitates in the HAZ of a 28 dpa, 8 appm He sample.....	123
Figure 5.9 Cr enriched precipitate in the HAZ of the 23 dpa, 3 appm He sample. EDS line scan across the boundary shows Cr enrichment in the precipitate compared with the matrix.....	124
Figure 5.10 Detailed analysis of the Cr enriched precipitate in the HAZ. (a) Laser weld-induced precipitates in the 1dpa, 0.2 appm He sample. (a) SAD of the matrix versus the	

- precipitate with inset of HRTEM image of the interface between the interface and the precipitate. (c) EDS line scan across the boundary shows Cr enrichment in the precipitate compared to the matrix. 125
- Figure 5.11 Laser weldment of a neutron irradiated AISI 304L SS of 23 dpa and 3 appm He. (a) SEM micrograph of the finished laser weld cross-section. Red arrows indicate weld-induced pores. Straight green box shows the interface of the weld boundary between the weld and the HAZ. Dotted blue oval represents the laser weld-induced cracking in the HAZ. (b) OIM maps of the weldment cross-section of the dashed red rectangular box in (a): transition from elongated dendritic grains in the weld region to the equiaxed grains in the base metal and the HAZ has a combination of both dendritic and equiaxed grain structure. 126
- Figure 5.12 Selected 23 dpa, 3 appm He laser welds-SEM imaging and crack analysis. 127
- Figure 5.13 Summary of microstructure of the laser welds of neutron irradiated AISI 304L SS at different dose levels (1, 23, 28 dpa) and He (0.2, 3, 8 appm) concentrations: grain structure with OIM mapping, HAZ cracking, images of the loops and cavities in the base metal and HAZ. 128
- Figure 5.14 Microstructural evolution in the base metal and HAZ versus the dose level He concentration. (a) Average cavity density and diameter and (b) average loop density and diameter. 129
- Figure 5.15 Radiation-induced segregation (RIS) at the grain boundary of the laser weld for Cr, Ni, Mn: (a) 1 dpa, 0.2 appm He in the base metal, (b) 1 dpa, 0.2 appm He in the HAZ, (c) 23 dpa, 3 appm He in the HAZ, and (d) 28 dpa, 8 appm He in the HAZ. 130
- Figure 6.1 Typical load-displacement curve of the nanoindentation. (a-d) snapshots of the Berkovich tip indenting the (111) grain of the base metal in the 1dpa, 0.2 appm He sample. (e-f) Indentation mapping with the grain structure under light optical microscope. (e) Indentation marks with TEM lift-out in the base metal of the 23 dpa, 3 appm He sample. (f) Indentation marks with TEM lift-out in the HAZ of the 23 dpa, 3 appm He sample. 145
- Figure 6.2 Nanoindentation measurements of (a) hardness and (b) modulus on {100}, {101} and {111} grains of the archive AISI 304L SS, base metal, and HAZ. OIM maps of area of the grains tested by the nanoindentation experiments. (c) Corresponding indenting area of the archive sample. (d) Corresponding indenting area of the irradiated base metal. 146
- Figure 6.3 (a) Hardness and (b) modulus along the indentation across the HAZ. 147
- Figure 6.4 Comparison of hardness and modulus data from all indentation experiments in the archive and irradiated base metal of AISI 304L SS of the 23 dpa and 3 appm He condition. (a) Hardness histogram. (b) Modulus histogram. 148

Figure 6.5 TEM micrographs of the post-indentation microstructure: (a) archive AISI 304L SS containing deformation twins, and (b) irradiated AISI 304L SS of the 23 dpa and 3 appm He containing martensite needles. (c) Comparison of load-displacement curves of the archive (black line) and irradiated (red line) AISI 304L SS on {110} grains with the Hertzian elastic solution (blue line). Dotted red circles indicate the initiation of pop-ins..... 149

Figure 6.6 Bright-field TEM micrographs of the post-indentation microstructure of: (a) archive AISI 304L SS at 111 zone axis and (b) neutron irradiated AISI 304L SS at 131 zone axis. Diffraction patterns of (c) archive matrix, red circles represent the minor diffraction spots of the twins and (d) major spots indicate the matrix (solid white box) and the minor spots indicate the α' martensite laths (dashed red box). 150

Figure 6.7 Comparison of post-indentation microstructure of neutron irradiated 304L SS under different load rates (a) ~ 200 nm (0.25 mN/s for 40s) with no phase transformation and (b) ~ 400 nm (0.5 mN/s for 40s) with martensitic phase transformation. 151

Figure 6.8 TEM micrographs of nanoindentation-induced α' martensite in irradiated AISI 304L SS; (a) bright-field TEM of martensite (red arrows) with cavities, (b) enlarged image of the martensite, (c) HRTEM of martensite and zoom-in image of the martensite tips, and (d) HRTEM of an incoherent void-martensite interface..... 152

Figure 6.9 Comparison of post-indentation microstructure of the base (a-c) and the HAZ (d-f) with a loading rate of 5 mN/s and an indentation depth of 1500 nm. (a) BFTEM micrograph of martensite laths in the base metal. (b) Corresponding diffraction pattern in (a). (c) HRTEM image of martensite laths across the cavity. (d) BFTEM micrograph of martensite laths in the HAZ metal. (e) Corresponding diffraction pattern in (d). (f) HRTEM images of formation of bcc- α' at the intersection region of two hcp- ϵ plates. Solid white box represents the reciprocal lattice of fcc- γ matrix. Dashed red box represents the reciprocal lattice of the bcc- α' martensite. Dotted yellow box represents the reciprocal lattice of the hcp- ϵ martensite..... 153

Figure 6.10 Formation of martensite laths at different indentation depths of 200 nm (a-b) and 400nm (d-e). (a) BFTEM micrograph of the dislocations near the surface under the indent in the base metal with a loading rate of 0.25 mN/s. (b) BFTEM micrograph of the dislocations near the surface under the indent in the HAZ with a loading rate of 0.25 mN/s. (c) FEM maps of the stress field under a 200 nm indent of the AISI 304L SS. (d) BFTEM micrograph of α' martensite laths at a depth of ~ 500 nm under the indent in the base metal with a loading rate of 0.5 mN/s (red arrows indicate the α' martensite laths). (e) BFTEM micrograph of the two hcp- ϵ martensite laths at a depth of ~ 500 nm under the indent in the HAZ with a loading rate of 0.5 mN/s. (f) FEM maps of the stress field under a 400 nm indent of the AISI 304L SS. Magenta box in (c) and (f) corresponds to the approximate depth in (a-b) and (d-e), respectively.. 154

Figure 6.11 Micropillar compression engineering stress-strain curves for tests performed on AISI 304L SS welds of 1 dpa and 0.2 appm He along {101} grains in (a) base metal and

(b) the HAZ. Effective modulus, Y_{eff} , determined as secant modulus during the compression tests of (c) base metal and (d) HAZ. 155

Figure 6.12 Additional stress-strain curves from pillar compression experiments of the laser welds of irradiated AISI 304L SS of 1 dpa, 0.2 appm He: (a) base metal {111} grains (b) base metal {221} grains with post-compression pillar images, (c) base metal {331} grains with post-compression pillar images, in which load drops correspond to slip events, and (d) the HAZ random grain orientations. 156

Figure 6.13 Snapshots of *in-situ* SEM micropillar compression tests of irradiated AISI 304 SS welds along {101} grains at room temperature: (a-d) base metal at strains of 0, 7%, 12% and 25%, and (g-i) the HAZ at strains of 0, 5%, 10% and 22%. TEM micrographs of compressed pillars of the (e-f) base metal showing the formation of ϵ martensite. (k-l) the HAZ showing the formation of deformation twins and 3D SOLIDWORKS® modeling of (m) activated slip planes S1 111 in the base and (n) twinning planes of T1 111 and T2 111 in the HAZ. 157

Figure 6.14 Nanotwins in the post-compression pillar of the (101) grain in the HAZ. 158

Figure 6.15 (a-b) Before/after snapshots of *in-situ* SEM micropillar compression tests of unirradiated archive AISI 304 SS welds along {101} grains at room temperature: (c) stress-strain curves of different pillars from {101} grains. (d) Dark-field TEM micrographs of compressed pillars showing the formation of twinings and (e) the corresponding selected diffraction pattern in (d). 159

Figure 6.16 Final SEM micropillar compression video still-frame from {101} grains in the base metal and the HAZ shown in greater detail in Fig. 6.13, showing: (a) $\gamma \rightarrow \epsilon$ martensitic transformation, and (b) twinning, with (c) the corresponding engineering stress-strain curves. 160

Figure 6.17 Thompson tetrahedron illustrates possible twin systems in an fcc crystal corresponding to Table 6.5. 161

Figure 7.1 Calculated irradiation hardening and laser weld softening leading to the change of the yield strength in the laser weldment of neutron irradiated AISI 304L SS of 23 dpa, 3 appm He irradiated at 415 °C. The horizontal axis at the origin is the yield strength of the archive AISI 304L SS of 905 MPa. Each contribution of change in yield strength includes dislocation lines, loops, precipitates, and cavities. The net total values of the calculated hardening in the base metal and softening in the HAZ by the proposed model are the white rectangular columns with error bars. The measured total values of the irradiation hardening of the base metal versus the laser weld-induced softening in the HAZ has been shown as the yellow rectangular columns with error bars. 179

Figure 7.2 Nanoindentation measurements of hardness in the base metal and HAZ with regard to the He concentration and dose levels. 180

- Figure 7.3 (a) Schematic diagram of stress-induced martensite nucleating through the cavities of direct $\gamma \rightarrow \alpha'$ transformation. (d) Smaller and less cavities retard the nucleation of α' martensite, enabling the dislocation slip for hcp- ϵ plates and further $\gamma \rightarrow \epsilon \rightarrow \alpha'$ transformation. 181
- Figure 7.4 (a) Two hcp plates shear and form bcc structure at the intersection. (b) Schematic diagram of the Bogers-Burgers-Olson-Cohen (BBOC) model [194,195]. 182
- Figure 7.5 (a) Critical twinning stress for fcc metals and alloys, with (b) higher magnification of critical twinning stress map, focusing on austenitic steels. The current work is enveloped by dashed black (base metal) and red (HAZ) rectangular boxes. Irradiation-induced cavities change the critical twinning stress and cause phase transformation. 183
- Figure 7.6 Dislocations and dendrites in the HAZ imaged using the bright-field STEM method. 184
- Figure 7.7 Deformation map of irradiated AISI 304L SS in the domain of cavity density and dose level and He concentration. 185
- Figure 7.8 Proposed deformation regime map compared with experimental data for irradiated AISI 304L SS. Horizontal green line is the average mean-free path of dislocations. Horizontal red line is the separation distance of partials at equilibrium state. 186
- Figure A 1 Schematic diagram of the lattice distortion of the deformation-induced martensitic transformation (a-b) fcc Fe in 110 projection. (c-d) hcp Fe in 1120 projection. (e-f) bcc Fe in 111 projection [233,315]. 189
- Figure A 2 Schematic representation of the austenite-to-martensite transformation through lattice deformation. 190
- Figure A 3 Irradiation-induced voids in the base metal of laser welds of AISI 304L SS of 1 dpa and 0.2 appm He: in the (a) overfocused, and (b) underfocused conditions. 191
- Figure A 4 Martensite-void interface in the irradiated AISI 304L SS of 23 dpa and 3 appm He, shown at different magnifications: (a) STEM image, and (b)-(d) BFTEM images of the voids with martensite laths penetrating through. 192
- Figure A 5 TEM micrographs of as-welded 304SS, neutron irradiated to 0.4 dpa, 1 appm He, 0.2-0.5% swelling, showing dislocation morphologies in (a) weld metal, (b) heat affected zone, and (c) base metal; (d) voids and (e) dislocation loops in weld metal indicated by arrows; and (f) Cr precipitates in HAZ. 193
- Figure A 6 SEM images of additional pillars (i.e., other than those shown in Fig. 6.13) of the $\{101\}$ grains from the HAZ before and after compression (a-b), (c-d), (e-f), and (g-h). 194

Figure A 7 Cavities of the 0.2 appm, 1dpa (a) base, (b) HAZ and 3appm, 20dpa (c) base and (d) HAZ neutron irradiated 304L SS.	195
Figure A 8 Bright-field STEM micrographs of loops of the 0.2 appm, 1dpa (a) base, (b) HAZ and 3appm, 20dpa (c) base and (d) HAZ neutron irradiated 304L SS.....	196
Figure A 9 Twins and Frank loops in the HAZ of laser welds of irradiated AISI 304L SS of 28 dpa and 8 appm He.....	197
Figure A 10 Dislocations in the HAZ of laser welds of irradiated AISI 304L SS of 28 dpa and 8 appm He.	198
Figure A 11 Histogram for hardness and modulus with predicted Gaussian distribution fitting of hardness and modulus of indents at {100}, {101}, {111} grains (a)-(c)distribution of hardness and (d)- (f) distribution of modulus for archived 304L SS, base metal of the laser weld and HAZ.....	199
Figure A 12 Nanoindentation-induced martensitic transformation (a) base and (b) alpha prime bct martensite, (c) HAZ and (d) alpha prime bct and epsilon hcp martensite.....	200
Figure A 13 <i>In-situ</i> nanoindentation on 0.2 appm, 1 dpa neutron irradiated AISI 304L SS.	201
Figure A 14 Finished micropillars at {112} grains using FIB milling technique.....	202
Figure A 15 0.2 appm, 1 dpa neutron irradiated 304L SS sample: slip bands and twinning after microcompression pillar test (a) single slip band at {112} grain and (b) multiple slip bands in 111 grain.....	203
Figure A 16 Crack analysis of the HAZ ([111] and [112] of $\Sigma 5$ boundary) in laser welds of AISI 304 L SS of 23 dpa and 3 appm He.....	204
Figure A 17 OIM mapping of the grains from base to HAZ in the laser welds of irradiated AISI 304L SS of 23 dpa and 3 appm He.....	205
Figure A 18 OIM mapping of the grains from base to HAZ in the laser welds of irradiated AISI 304L SS of 28 dpa and 8 appm He.....	206
Figure A 19 Crack analysis of the HAZ in the laser weldment on block 3 of 23 dpa and 3 appm He.	207
Figure A 20 Strain mapping of a void-martensite interface of the base metal of irradiated AISI 304L SS of 23 dpa and 3 appm He.....	208

ABSTRACT

Author: Mao, Keyou. PhD

Institution: Purdue University

Degree Received: August 2019

Title: Influence of Irradiation and Laser Welding on Deformation Mechanisms in Austenitic Stainless Steels.

Committee Chair: Janelle Wharry, Xinghang Zhang

This dissertation describes the recent advancements in micromechanical testing that inform how deformation mechanisms in austenitic stainless steels (SS) are affected by the presence of irradiation-induced defects. Austenitic SS is one of the most widely utilized structural alloys in nuclear energy systems, but the role of irradiation on its underlying mechanisms of mechanical deformation remains poorly understood. Now, recent advancement of microscale mechanical testing in a scanning electron microscope (SEM), coupled with site-specific transmission electron microscopy (TEM), enables us to precisely determine deformation mechanisms as a function of plastic strain and grain orientation.

We focus on AISI 304L SSs irradiated in EBR-II to $\sim 1\text{-}28$ displacements per atom (dpa) at ~ 415 °C and contains $\sim 0.2\text{-}8$ atomic parts per million (appm) He amounting to $\sim 0.2\text{-}2.8\%$ swelling. A portion of the specimen is laser welded in a hot cell; the laser weld heat affected zone (HAZ) is studied and considered to have undergone post-irradiation annealing (PIA). An archival, virgin specimen is also studied as a control. We conduct nanoindentation, then prepare TEM lamellae from the indent plastic zone. In the 3 appm He condition, TEM investigation reveals nucleation of deformation-induced α' martensite in the irradiated specimen, and metastable ε martensite in the PIA specimen. Meanwhile, the unirradiated control specimen exhibits evidence only of dislocation slip and twinning; this is unsurprising given that alternative deformation mechanisms such as twinning and martensitic transformation are typically observed only near cryogenic temperatures in austenitic SS. Surface area of irradiation-produced cavities contribute enough free energy to accommodate the martensitic transformation. The lower population of cavities in the PIA material enables metastable ε martensite formation, while the higher cavity number density in the irradiated material causes direct α' martensite formation. In the 0.2 appm He condition, SEM-based

micropillar compression tests confirm nanoindentation results. A deformation transition map with corresponding criteria has been proposed for tailoring the plasticity of irradiated steels. Irradiation damage could enable fundamental, mechanistic studies of deformation mechanisms that are typically only accessible at extremely low temperatures.

1. INTRODUCTION

To extend the life of commercial Light Water Reactors (LWRs) in the U.S. fleet, it is necessary to repair the cracking in both in-core and near-core structural components. Conventional welding methods, such as the gas tungsten arc (GTA) method, have attempted to fix these cracks [1,2]. The helium generated from nuclear transmutation reactions with the boron and nickel contained in the base metal increases as neutron fluence accumulates [3,4]. The accumulated helium (He) over the operating range of the reactor raises a concern for He-induced cracking close to or along the weld boundary [5–8]. Because of the heat input and thermal stress from the conventional welding approach, the heat affected zone (HAZ) of the repaired welds is a vulnerable area for more extreme cracking. This exacerbated cracking is caused by He coalescence into bubbles, which complicates the whole welding repair process over various operating conditions with different levels of dose rates and He concentrations.

To fulfill the demand of extended irradiation service, welding technologies should address this knowledge gap. Thus, an adaptive welding method—laser beam welding—should be adopted for repairing the LWR internals with different He concentrations and distributions. The low-energy input laser welding is proposed to minimize the stresses driving cracking and He coalescence at the weld boundary. Austenitic stainless steels (SSs) are the workhorse alloys and comprise most of the structural materials in the current fleet of LWRs. The mechanical integrity of these structural materials after long-term irradiation can lead to possible irradiation embrittlement and premature cracking. Given the potential for deterioration of He-induced cracking in the HAZ, the deformation mechanisms across the laser weldment need to be further assessed before they can finally be applied to the nuclear industry for actual laser welding repairs. Thus, a wide range of dose and He conditions are necessary for the validity of this technique. Moreover, at a fundamental scientific level, understanding the role of irradiation and laser welding on the deformation mechanisms is a central step toward tailoring the mechanical property via neutron and ion irradiation.

The objective of this study is to determine the deformation mechanisms of the laser weld repairs on neutron irradiated 304 SS. A combination of microstructural characterization and mechanical

testing have been performed as a pre-characterization for the weldments. The follow-up characterization of the pre-deformed microstructure will be coupled with current deformation models to unveil the underlying mechanisms corresponding to each dose and He conditions. Chapter 2 of this dissertation focuses on the relevant background information, including details about the tested specimen, literature survey on the results of microstructure and mechanical properties of similar materials after neutron and ion irradiation, and current understanding of deformation mechanisms in austenitic stainless steels with and without respect to irradiation. Chapter 3 outlines the objective of this dissertation, and Chapter 4 includes a detailed description of the experimental procedures. Chapter 5 presents the results of the microstructural evolution between the irradiated and post laser-welded regions. Chapter 6 presents the results of the mechanical testing and shows the post-deformed microstructure. Chapter 7 reviews and discusses the experimental results and interprets the deformation mechanisms based on the post-deformed microstructure under irradiation and laser welding conditions. Finally, Chapter 8 provides a series of conclusions and recommends future work.

2. BACKGROUND

2.1 Significance of laser welding

2.1.1 Laser beam welding

Laser welding [9–14] has been widely accepted in various industries in recent years for its capability to obtain high-precision joints of materials with the least degree of mechanical/thermal distortion. In general, laser beam welding is equipped with a high-energy laser source to cause localized melting [15]. This method has been validated for dissimilar materials joints [12,13,16–18], such as hydraulic valves [10], auto manufacturing [19], advancements in the nuclear industry [6], and electronics and medical industries with micro-precision fabrications.

A common laser beam welding technique is the Neodymium-doped Yttrium Aluminum (Nd-YAG) laser beam welding. The filler wire is melted by the laser beam. The small size of the laser limits the penetration and formation of the heat affected zone (HAZ). A schematic diagram of the laser weldment is depicted in Fig. 2.1. The weld pool is controlled by a certain thermal gradient [14,16,20]. This is crucial to maintain a smaller size/thickness of the HAZ, which has been demonstrated as an advantage over traditional welding techniques such as gas tungsten arc welding (GTAW) and electron beam welding [16,17,21]. Hence, crack formation during the weld quenching is suppressed locally due to reduced heat input [22]. The reduced heat input also generates a single boundary between the base and fusion zone [9,23,24]. This is different from the high-heat-input welding process possessing a multilayered HAZ [9,11,17,18,24]. As a result, the size of the HAZ is determined by thermal cycles [9] and the forming dendrites have a finer structure [22,25] during resolidification of the welding melt [23,26]. The formation of dendritic grains also helps stabilize a deep-penetration and relatively tapered weld [11,12,14,16,18,20]. A majority of the efforts to understand the microstructure-property relationship between the mechanical performance and the microstructure of the weld [11,12,22,27] have demonstrated a strengthening mechanism in the HAZ.

To further meet industrial demands, and despite past focus on the mechanical and metallurgical properties [9,16,26] and microstructure [9,16], other physical properties such as chemical

composition, heat transfer, corrosion, fatigue, creep, and weld pool geometry are also worthy of studying to understand the underlying physics of the laser welding process. Although a reduced HAZ is generated by laser welding, the thermodynamics such as phase transformation can behave in a complex manner. The corresponding microstructure, which has undergone a phase transformation such as austenite to martensite, can change the solidification mode [16]. Multiple factors can affect the mode: (1) the major composition of Ni and Cr can change the formation portion of the δ ferrite [28]; (2) localized cooling rate and temperature, which is usually faster than 10^3 K/s, can alter the liquid-solid transition [17]; and (3) the minor chemical composition of the material such as the content of Nb, Mo, Si, and Co can affect the martensitic transformation [29]. Characterization and quantification of the HAZ have only been studied with a few reports [22,28].

2.1.2 Helium-induced cracking

Within the context of extreme environments such as high-temperature and irradiation, laser beam welding has not yet been validated as an effective way to prevent Helium (He) -induced cracking. He-induced cracking of welds (see Fig. 2.2 as an example) was first observed in stainless steel tanks holding tritium-containing water. Mobile tritium diffused into the steel, then decayed to immobile ^3He , especially at grain boundaries, contributing to failed attempts at weld repairs. Since then, numerous incidences of He-induced cracking of welds have occurred during attempts to repair cracks in boiling water reactor (BWR) shrouds in commercial [30] and research reactor vessels [31]. Now, as the nuclear industry progressively moves toward plant life extension involving higher irradiation damage dose and helium accumulation, the Nuclear Regulatory Commission has mandated management plans requiring detailed surveillance inspections to ensure that all postulated failure mechanisms are identified to avert catastrophic consequences. Cracking of critical in-core or near-core components are amongst the postulated failure mechanisms. Further BWR shroud cracking is a grave concern, but there is also a long-term concern that pressurized water reactor (PWR) baffle-former plates may also crack, allowing bypass flow of coolant and potential structural instability of the assembly.

The importance of weld integrity to safe reactor operation has spurred extensive research leading to an understanding of the He-induced cracking mechanism. He is found in stainless steel nuclear reactor internals through a variety of reactions. During a long-term reactor operation, ^4He can be

produced through fast neutron reactions with relatively small cross-sections for all iron (Fe), chromium (Cr), and especially nickel (Ni) isotopes. More importantly in thermalized neutron spectra, thermal neutron (n, α) reactions with very large cross sections occur with ^{10}B , which is limited in concentration, but especially through the two-step reaction sequence: (1) $^{58}\text{Ni} (n, \gamma)$; (2) $^{59}\text{Ni} (n, \alpha)$. The latter reaction sequence is the most important contributor in LWRs, scaling directly with nickel content and non-linearly with thermal neutron fluence and producing hundreds of appm He at higher PWR-relevant exposures. Since He is insoluble in the metal matrix, He atoms usually coalesce into several nm diameter bubbles in the grain interior and on dislocations and grain boundaries [32]. These bubbles are especially problematic during weld repairs of the steel, because the heat of welding releases He from various microstructural traps, followed by He agglomeration into larger bubbles and almost two-dimensional puddles, primarily situated along grain boundaries along the weld melt boundary. Next, thermal stresses from the welding process cause micro-creep of the metal between bubbles, causing further bubble growth and eventually producing a dimpled fracture surface [32]. The macroscopic result is intergranular fracture in and around the HAZ of the weld [33]. The progression from He bubble formation to fracture of grain boundaries is shown schematically in [Fig. 2.3](#).

Westinghouse Materials Center of Excellence (MCOE) has a strong history in weld repair research and development. In 1986, Westinghouse MCOE was contracted to repair stress corrosion cracks of a 304 SS nuclear reactor vessel at the Savannah River Site. The weld repair was conducted using an autogenous and wire-fed gas tungsten arc (GTA) remote welding system. The repair failed in the HAZ of the 304 SS. A failure analysis identified He embrittlement of the highly irradiated 304 SS as a primary cause of the failure [31]. Subsequently, Westinghouse MCOE participated in the development of a low-penetration gas metal arc (GMA) overlay technique for welding irradiated stainless steel reactor vessel internals. The welding process minimized heat input, which in turn minimized He-induced cracking [34–36]. In the years since, the Electric Power Research Institute (EPRI), Oak Ridge National Laboratory (ORNL), and Westinghouse MCOE have investigated advanced techniques to weld irradiated materials, such as friction stir [37–39] and laser welding. These techniques are especially relevant to the DOE-NE LWR Sustainability (LWRS) and Next Generation Nuclear Plant (NGNP) base programs. Herein, we propose to focus our work on low power laser welding, for which encouraging results have been obtained in the archival literature.

2.1.3 Weldability of irradiated materials

Laser beam welding is hypothesized to inhibit further He-induced cracking. Nd-YAG laser beam welding techniques have been shown to improve the weldability of stainless steel reactor internals that have been neutron irradiated to as high as 7 dpa, and which contain measurable He concentrations as high as 50 appm [2,5,6,40–42]. Laser techniques can create a weld using reduced heat input compared to conventional welding techniques, which minimizes stresses on the workpiece and thus reduces the risk of cracking. Laser welding utilizes a solid state, gas, or fiber laser as a source of highly concentrated heat to rapidly form deep, narrow welds. The localized heat input results in a minimal HAZ, due to the rapid heating and cooling rates. Consequently, laser weldments often exhibit a well-defined border between the base metal and fusion zone, without the multi-layered HAZ often produced by other welding techniques. During laser welding, a keyhole is formed by the equilibrium between the surface tension of the liquid metal and the plasma pressure inside the keyhole. This requires the weldment to reach temperatures in excess of the boiling points of Ni and Cr (2732°C and 2672°C, respectively), giving rise to temperature gradient-driven fluid flow within the melt [15]. Resolidification of the melt typically produces a dendritic grain structure oriented parallel to the thermal gradient (Fig. 2.4), often perpendicular to the weld borders. A centerline is found where dendrites from both sides of the weld meet during solidification.

Even though Fig. 2.5 shows an example of the reduction of applied stress resulting from the suppression of surface cracking after GTA welding at a lower He concentration level [43,44], the reduced heat input is a significant factor in the improved performance of laser welding in irradiated materials. Conventional GTAW, also known as tungsten inert gas (TIG) welding, has a heat input of about 20 kJ/cm. At a distance 100 μm from the weld fusion line, such a large heat input produces a 225-1500°C temperature increase sustained for more than 30 seconds. Meanwhile, a heat input of 1 kJ/cm, typical of laser welding, produces a ~1500°C temperature spike for < 3 seconds [5]. In 304 SS containing 50 appm He, reducing the laser weld heat input from 20 kJ/cm (Fig. 2.6a) to 4 kJ/cm (Fig. 2.6b) eliminates surface cracking and minimizes sub-surface defects [5]. Even with a fixed heat input, laser welding outperforms conventional GTAW [6]. Morishima et al. [6] used GTAW and laser welding, both with a 2 kJ/cm heat input, on 316L SS irradiated in the Advanced Test Reactor (ATR) and containing ~9 appm He. GTAW produced significant intergranular

microcracking (Fig. 2.6c), while no defects were observed in the laser welded specimens (Fig. 2.6d).

Besides heat input, numerous welding parameters affect the propensity of laser weld repairs to experience He-induced cracking. Nishimura et al. [40] found that cracking increases in irradiated, He-containing 304L and 316L SS with increasing laser power (wattage). To the author's knowledge, no known studies have examined the effects of process parameters such as weld traverse speed in irradiated materials. But in unirradiated joints of ferritic AISI 430F to martensitic AISI 440C, Khan et al. [45] found that increasing laser weld speed decreased the weld width and penetration depth, which had implications on the mechanical performance of the weld. Another study showed that excessive weld speeds produced asymmetries, excess fractures, and gas porosity [46] in an unirradiated oxide dispersion strengthened steel. Thus, heat input alone does not govern weld cracking behavior, and factors such as weld power and travel speed must also be considered.

ASME standard [47] heat input for laser welding is given by

$$Q_{in} = \frac{P_{WP}}{v_{TS}} \quad (2.1)$$

where Q_{in} (J/cm) denotes the effective heat input (unit length); P_{WP} (w) is the time weighted average power input for the weld process; v_{TS} (cm/min) is the time weighted average weld process travel speed. Recently, EPRI and ORNL have formulated an expression for the effective laser weld heat input, which accounts for the numerous process parameters that influence cracking propensity in irradiated, He-containing materials [42]. Unlike theoretical heat input, their expression for effective heat input incorporates: (1) laser heat used to melt added filler material, and (2) heat loss to the atmosphere due to reflection of laser power. The effective heat input, Q_{eff} (kJ/cm), is given by:

$$Q_{eff} = \frac{\mu_{HT} P_{WP}}{v_{TS}} - \frac{\tau v_{WFS} P_{WP} A_{wire}}{v_{TS}} \quad (2.2)$$

where μ_{HT} is the heat transfer efficiency factor of arc/laser beam during welding (laser absorption efficiency); τ (kJ/cm³) denotes the heat required to melt a volume of filler metal; v_{WFS} (cm/min) is the time weighted average wire feed speed and A_{wire} (cm²) is the cross-sectional area of the wire. After assembling GTAW and laser weld repair data from the archival literature (Fig. 2.7a for 304 SS and Fig. 2.7b for 316 SS [47]), it becomes evident that the effective weld heat input provides a

threshold for He-induced cracking. Welds made with effective heat inputs below the threshold (dashed line) for a given He concentration (appm) consistently do not crack (green symbols), whereas welds made with effective heat inputs above the threshold exhibit a greater propensity to crack (red symbols). This body of results convincingly illustrates that laser weld repairs can be made to avoid He-induced cracking even in materials containing a few 10s of appm He, which is an unprecedented improvement over GTAW techniques, for which severe He-induced cracking occurs in 316L SS containing as little as ~1 appm He [2].

2.2 Neutron irradiated AISI 304L stainless steel hex blocks

A complication in the study of weld repairs is that LWR internals span a range of irradiation damage levels and He concentrations, so weld technologies must be adaptable to a variety of conditions. BWR shrouds, for example, experience a low irradiation damage accumulation rate with a high thermal-to-fast neutron ratio, resulting in a higher He/dpa ratio with little cavity swelling. PWR baffle-former plates, on the other hand, experience greater thermal stresses, damage rates almost two orders of magnitude higher than BWRs, and lower thermal-to-fast neutron ratio and He/dpa ratio. But, PWR baffle-former plates also experience increased internal temperatures due to higher gamma heating levels, which, when combined with the higher damage rates, will lead to increased cavity swelling and radiation-induced segregation. These microstructural factors are all known to impact post-weld cracking. It is obviously difficult to extract irradiated material from a BWR shroud or PWR baffle plate for welding studies without affecting the integrity of the operating reactor. So previous attempts to critically examine post-weld cracking have involved one of two lengthy and expensive testing procedures. The first involves the costly “tritium trick”, in which pressurized tritium was introduced to the material, and subsequently decayed into ^3He [48]. The attraction of hydrogen isotopes to grain boundaries leads to a significant partition of helium to grain boundaries, but the resulting helium distribution is not representative of neutron-produced uniform helium distributions [48]. The second technique involves irradiation of specimens in a test reactor with a higher-than-prototypic thermal-to-fast neutron ratio, which accelerates He production but presents difficulty in reaching the doses characteristic of the swelling regime. This approach also requires small specimen volumes for irradiation in test reactors, which are not large enough for subsequent welding studies. Furthermore, this approach produces much more radioactivity via both the higher power of thermal neutrons to

cause transmutation and radioactivation and because there is insufficient time for decay to reduce exposure to researchers.

However, there is a third alternative to provide specimens for welding studies, which is the most cost-effective and time-efficient approach proposed herein. This study will utilize AISI 304 SS hexagonal blocks, which have been irradiated in the experimental breeder reactor II (EBR-II) reflector. These hex blocks are ideal for this study because they were produced using technology typical of the period during which the baffle-former plates in current PWRs were produced. Each block contains a range of swelling and precipitation microstructures typical of that expected in LWR operation, even though these microstructures were produced in a fast rather than thermalized neutron spectrum characteristic of LWRs. Their microstructure is well-characterized [49–51], their He concentrations span the critical range over which conventional welding techniques will produce He-induced cracks, and they have manageable radioactivity. These considerations enable this laser welding to proceed quickly and with a lower cost. The materials chosen for this study are particularly relevant to the defined mission. The AISI 304 SS hex blocks were in a stack of six blocks in Row 8 of EBR-II, serving as a reflector assembly. The blocks were originally ~240 mm tall with face-to-face diameter of 52 mm, but currently exist in a wide variety of sizes and shapes. The thin 304 SS hex duct surrounding this stack was of similar composition and was one of the five ducts used to establish the currently employed flux dependent AISI 304 SS swelling equation for the U.S., Japanese, and French LWR programs. This assembly was chosen because its range of dpa rates matched those of PWR baffle-former plates. These blocks have been selected due to their well-known irradiation history, well-characterized swelling and microstructural distribution, He concentrations, and especially for the relatively large volume of materials available. A limited amount of archive material is also available and has been used in previous characterization of radiation-induced changes in properties. Given the broad applications of 304 SS in vessel internals and cooling systems, a comprehensive understanding of these materials has the potential for high impact by significantly enhancing reactor performance and safety margins.

2.3 Microstructural characterization

We will review the characterization methods and typical microstructure of the hex blocks as well as similar post-irradiated 304 SS materials. A combination of various instruments is used for

characterization of the post-irradiated laser welds. Scanning electron microscopy (SEM) is used for observing surface topology and small features on the laser weld. Electron backscatter diffraction (EBSD) is applied to characterize the grain sizes and grain orientations. Focused ion beam (FIB) is used as a sample preparation tool, for instance, with transmission electron microscopy (TEM) lamella. Irradiated samples prepared by FIB are too small to be detected by handheld monitors (below instrument detectable limit). TEM is used for characterizing the microstructure of the neutron irradiated 304L SS and the corresponding welds. Scanning TEM (STEM) is used to provide secondary phase mapping of the sample. Atom probe tomography (APT) is used to investigate processes such as small precipitation and grain boundary chemical segregation. All these electron microscopy techniques will advance our understanding of the microstructural evolution due to laser welding effects on irradiated materials.

2.3.1 Grain structures

The previous studies have observed finer grains in the HAZ [22,25]. Grain structures of the laser weld on neutron irradiated 304 SS can also be identified using EBSD, obtaining a grain orientation map, an image quality map, or a phase map. [52,53].

Figure 2.8 shows a Grain Reference Orientation Deviation (GROD) map of non-irradiated 304 SS at different strains (1-9%). The color scale of the strain level varies from blue to red. We can see the localized strain concentration increasing from 1% to 9%. Under the room-temperature tensile straining, the grain boundaries tend to have higher strain concentration than the inner grains. The relationship between the GROD and strain level can also be obtained in Fig. 2.8d. In comparison with irradiated 304 SS with 4.4 dpa, the non-irradiated steel is less sensitive to the local misorientation near the grain boundaries.

2.3.2 Dislocations

Huang et al. [54] performed TEM characterization of the hex block with dose ~0.4-28 dpa and swelling rate ~0.08-2.7% irradiated at ~414-448 °C. Dislocation networks and faulted interstitial Frank loops are representative features we learned from these irradiated hex blocks. They also studied the microstructure of the original hex blocks (unirradiated archival hex-block) prior to neutron irradiation. Figure 2.9 shows the microstructure of block 3 with 28 dpa. The images use

both bright-field imaging ($\vec{g} = [220]$) and dark-field imaging ($\vec{g} = [200]$). High-density dislocation networks surround the interior low-density dislocation cells with dislocation cell-walls. Since the block was previously under ~5-10% cold work [55], the deformation twinning bands can also be seen here. It is difficult to clearly see all the dislocation loops with the two-beam condition in such a high-defective and high-density area. Alternative methods such as rel-rod [56] and the weak-beam dark-field [57] method can also be applied to image the dislocation loops. The traditional two-beam method usually requires at least three conditions of \vec{g} vectors to meet the invisibility criteria. The Rel-rod method requires tilting the sample at four different $\{111\}$ family planes with respect to the imaging conditions. Therefore, we introduce the loop imaging method in bright-field STEM mode noted by Parish et al. [58], which can cover all the loops at a certain imaging zone axis. For our current work, 304 SS has a face-centered-cubic (fcc) structure where the loops commonly reside in the $\{111\}$ plane. Detailed methods for identifying the interstitial and vacancy loop with inside-out approach can be found in [59,60]. APT is an alternative approach which visualizes dislocation loops with detailed elemental distribution inside and outside the loops[61]. Cavities and precipitates also exist, and they will be covered in the next few sections of this chapter.

2.3.3 Cavities

Prior work on cavity microstructure was performed on block 3 and block 5 [54,61]. [Figure 2.10](#) shows bright-field TEM images of the cavities of different specimens from block 3 with 28 dpa. The diameter of the cavity varies from 18.0 to 28.3 nm and the cavity density ranges from $1.67\text{--}3.1 \times 10^{23}/\text{m}^3$. The swelling rate of the block 3 samples is 1.18-2.76%. Cavities in block 3 and block 5 do not show any preferential location whereas a relatively uniform cavity distribution is observed over the entire area of the TEM specimens. The cavity imaging method is based on changing the under/over-focus conditions which show the Fresnel contrast [62,63].

Another useful technique to imaging cavities is using backscattered electrons (BSE) in a SEM [64,65]. This method provides a large-area scanning of the surface with a depth up to around 1 μm to obtain the cavity structures such as cavity shape, size, and distribution. [Figure 2.11](#) is a successful application of this method of imaging cavities over an area of $2 \mu\text{m} \times 2 \mu\text{m}$ in the same material as shown on the hex block of 28 dpa, 8 appm irradiated at 418°C in [Figure 2.10](#). This method gives validation to the large cavities with diameters around 30-40 nm, but the cavities that

are smaller than 20 nm cannot be easily resolved using this method. Thus, more efforts are needed to improve this imaging technique.

By calculating the cavity density and distribution, we can obtain the cavity swelling rate of the irradiated material. Sun et al. [63,66] has performed measurements on two different AISI 304L SS: coarse grains and ultrafine grains. [Figure 2.12](#) shows the comparison of the cavity swelling of these 304L SSs. The tests show that the suppression of cavity nucleation results from the injected interstitials, and the ultrafine grain 304L SS has a different transition compared with the coarse grain 304L SS, indicating higher resistance to void swelling. The ion damage profile calculation is done by the SRIM program [67]. For our study, the neutron irradiation does not have a damage profile, and the swelling rate is dependent on factors such as dose rate, He concentration level, and temperature, based on theories of interstitial/vacancy reaction/diffusion controlled mechanisms [68,69]. He/dpa is hypothesized as an important variable for the cavity properties in our laser weld repairs that are performed on the neutron irradiated 304L SS.

2.3.4 Precipitation

Precipitation is a common occurrence after neutron irradiation, and regarding the hex blocks 3 of 28 dpa, 8 appm irradiated at 418°C and 5 of 1 dpa, 0.2 appm irradiated at 416°C, precipitates such as $M_{23}C_6$ carbide [54,61], γ' (Ni_3Si) [54,61,70], P enriched precipitates [61] and $M_6Ni_{16}Si_7$ G-phase [61] and ferrite [61] have been observed. It should be noted that G-phase and ferrite form only under high dose conditions. These secondary phase precipitates can be observed using standard TEM, selected area diffraction (SAD), high resolution TEM (HRTEM) or STEM modes [54,61,63,71]. However, for nanoscale precipitates such as γ' (Ni_3Si), APT is an optimal option to quantitatively resolve these features and provide information about chemical composition and nanoclustering [72]. [Figure 2.13](#) demonstrates the APT data of γ' (Ni_3Si) precipitates for two different dose conditions of low 0.4 dpa ([Fig. 2.13a](#)) and high 28 dpa ([Fig. 2.13b](#)). The segregation behaviors of the Fe, Cr, Ni, and Si in [Fig. 2.13\(c-f\)](#), have similar profiles for two cases of either depletion or enrichment, but the high dose has a sharper concentration at the boundary of the precipitates (radiation induced segregation will be discussed later in this chapter). Despite the advantages using APT, the process for manufacturing these atom probe tips is challenging due to the high-cavity density of the hex block specimens. Ion irradiation specimens can emulate to the

neutron irradiation [73]. [Figure 2.14](#) shows evidence of $M_{23}C_6$ carbide after Fe ion irradiation in the coarse grain 304L SS, illustrating the phase instability after irradiation can accelerate the precipitation of secondary phases. [Figure 2.14b](#) shows that carbides have minor diffraction spots between the major spots on the matrix. [Figure 2.14\(c-d\)](#) shows the microstructural evolution after Fe ion irradiation, indicating the existence of irradiation-induced cavities and carbides in the coarse grain 304L SS. It also shows that the ultrafine grain 304 L SS has a superior radiation resistance because the advanced grain boundary sinks dissolve defects ([Fig. 2.14\(e-f\)](#)) [63]. More grain boundaries accelerate the absorption of irradiation-induced defects such as cavities and precipitates.

2.3.5 Radiation Induced Segregation

Irradiation can also induce microchemical changes such as chemical segregation at the grain boundary. In austenitic steel, Cr depletion and Ni enrichment are expected [74–78] at the grain boundary after irradiation. Energy dispersive x-ray spectroscopy (EDS) in STEM and APT can both characterize the radiation induced segregation (RIS) at the grain boundaries, dislocation loops, and precipitates [78]. Except for the one study on RIS behavior in hex blocks shown in [Fig. 2.13](#), similar 304 SSs under neutron irradiation have also been examined to illustrate such expected RIS behavior in the hex blocks [70,79]. [Figure 2.15](#) also shows a representative grain boundary RIS with APT for Fe, Ni, Cr, Mn, Si, P, and C of the neutron irradiated 304 SS with 24 dpa, consistent with a previous study performed by Edwards et al [80]. Despite the nature of irradiation-induced chemical segregation, laser welding might further affect post-weld microchemistry.

2.3.6 Role of He/dpa ratio

As we have seen through the microstructural evolution of the irradiated materials, it should be noted that the dose serves as an important factor contributing to the overall microstructural change. An example is given as a pre-planted He 304 SS irradiated with Si ion shown in [Fig 2.16 \(a-b\)](#) [81]. The fraction of the dislocation loops increases as the He level increases. The average radius of the cavities increases as the dose increases. He level does not have a strong effect on the size of the cavities. But this does not imply the weak role of He in relation to the materials research and development under extreme conditions.

In fact, He generation alters the microstructural evolution path of irradiated materials, causing the formation of dislocation loops, cavities and precipitates [73]. As we have already discussed in the previous section (2.1.2), He-induced cracking can deteriorate the welding repairs of the reactor's inner components. As the He bubbles accumulate on the grain boundary [82], they can severely embrittle the materials at elevated temperatures such as the reactor's operational conditions. At low temperatures, the He bubbles can also induce hardening and further embrittlement of the structural materials. Therefore, understanding the combined roles of He and dpa is a key to materials design and novel welding repair techniques.

2.4 Micromechanical testing

Miniature mechanical testing techniques have matured in recent years, and many have been applied to irradiated materials, including nanoindentation [83,84], micropillar compression testing [85,86], microcantilever bending testing [87], and microtensile testing [88]. For this study, these techniques are complementary to one another and provide different insights into the material behavior that will collectively inform the mechanical performance of the weld under deformation.

Nanoindentation (Figure 2.17a) is a simple but effective technique to quantify the hardness and modulus across the laser weld, which gives us the yield strength and work hardening as a result of neutron irradiation and laser welding [22]. Plasma Focused Ion Beam (PFIB) with Xenon Plasma is used to remove bulk portions of a sample. PFIB is ten times faster than a conventional Gallium FIB [89]. This is beneficial to micromanufacture the micropillars (Figure 2.17b) and microcantilevers (Figure 2.17c).

Micropillars can provide relatively accurate measurements of yield stress, critical resolved shear stress (CRSS) and hardness along different crystallographic orientations or at certain grain boundaries using EBSD. Pillars can be fabricated by PFIB to approximate dimensions with cylindrical or cuboid type to maintain a constant strain rate [90].

Notched microcantilevers will be machined to observe real-time cracking development and propagation. This technique enables us to understand the microscopic cracking and mechanisms

in highly irradiated weld repairs due to the welding-induced annealing and irradiation-induced embrittlement.

The microtensile test is very similar to the macroscale tensile test. The lengthy fabrication process and complicated calibration limit us to obtain large quantities of mechanical data from these tests within a decent amount of time.

The relatively mature small-scale techniques have been evaluated based on the inverse proportional relationship between sample preparation and post-experimental effort in Fig. 2.17d [91]. The microtensile test has the highest amount of sample preparation but least amount of time for data analysis. Nanoindentation has opposite attributes, as it has the least amount of efforts for experimental testing, but the data analysis and modeling are time costly. Micropillar compression and microcantilever bending require relatively intermediate efforts. Our study will focus on nanoindentation and microcompression pillar tests, so this section will summarize key findings and implications on experimental testing of irradiated materials.

2.4.1 Nanoindentation

Nanoindentation can evaluate the mechanical properties of the materials at a small scale [92–94]. Using the legendary Oliver and Pharr method [95], the elastic modulus and hardness can be obtained and conversion between Berkovich and Vickers hardness can be found in literature [96,97]. Recently, high-temperature indentation has shown to be an effective tool to enable the understanding of creep behavior and temperature dependency [92,98,99]. Three major areas, including the hardness after irradiation, grain orientation dependency, and size effect are still lacking the knowledge gap regarding the laser weld on neutron irradiated 304L SS.

2.4.1.1 Irradiation hardening

Pokor et al. [100] have developed a mechanistic model accounting for the loop strengthening effect (dislocation loops have been discussed in section 2.3.2):

$$\Delta\sigma = MGb[\alpha_{FL}\sqrt{\rho_{FL}\phi_{FL}} + \alpha\sqrt{\rho_D} - \alpha\sqrt{\rho_0}] \quad (2.3)$$

where $\Delta\sigma$ is the yield strength increase; M is the Taylor factor; α is the dispersed barrier length by forest dislocations; b is the Burgers vector; α_{FL} is the Frank loop obstacle length; ρ_{FL} is the average loop density; ϕ_{FL} is the loop diameter; ρ_D is the post irradiation dislocation density; and ρ_0 is the initial dislocation density after cold work.

Was [78] described a simplified empirical model for the irradiation hardening:

$$\sigma_{rad} = \sigma_0 + K\sqrt{\text{dpa}} \quad (2.4)$$

where σ_{rad} denotes the post-irradiation yield stress; σ_0 is the unirradiated yield stress; K is a fitting parameter; and dpa is the irradiation dose level.

2.4.1.2 Grain orientation dependency

The small-volumetric indentation tip enables the nanoindentation to explore the crystallographic orientation, which impacts on the hardness and modulus data of the materials [92,101–103]. [Figure 2.18](#) is an example of using nanoindentation to probe the orientation-dependent modulus ([Fig. 2.18a](#)) and hardness ([Fig. 2.18b](#)) plotted in the inverse stereographical pole coordinates [104]. Three grains {000}, {101} and {111} have been selected for the comparison of the statistical distribution of the modulus ([Fig. 2.18c](#)) and hardness ([Fig. 2.18d](#)).

[Figure 2.19](#) shows a recent work [101] highlighting the hardness of modulus dependent on two different orientations of $\langle 111 \rangle$ and $\langle 113 \rangle$ for an ion-irradiated 800H. Nanoindentation experiments from room temperature to 300°C have been performed, which indicate the softening and degradation of mechanical properties under high temperature. The irradiated 800H also exhibit higher hardness than the unirradiated samples.

[Figure 2.20](#) [105] is another example of nanoindentation on two different grains versus the intersecting grain boundary, where we can observe the increase of the hardness and modulus of a weld material at the grain boundary compared with those inside the grains (square symbols represents the hardness and rhombus symbols represents the modulus).

2.4.1.3 Indentation Size Effect

Experimentally, the indentation size effect is a concern for the precise measurement of the hardness and modulus at varying indentation depths, which is due to the size of the plastic zone [92–94,98,101,106]. It is important to distinguish the true hardness of the bulk material from the surface properties. The Nix and Gao model [107] is adopted for considering the Indentation Size Effect (ISE):

$$H = H_0 \sqrt{1 + h^*/h} \quad (2.5)$$

where H is the indentation-depth dependent hardness; H_0 is the infinite-depth hardness; h^* is the characteristic length and h is the indentation depth. The size of the plastic zone is commonly known as $5h$ [83]. Different ISE behaviors at different temperatures and grain orientations can also be seen from Fig. 2.19. As the temperature increases, the effect of ISE decreases; the hardness and modulus also decrease. This is an indication of an acceleration of dislocation movement as a result of an expansion of the plastic zone and larger volume of storing geometrically necessary dislocations (GNDs) [101]. Irradiation-induced dislocation channeling might also affect the deformation behavior [101]. Figure 2.21 shows experimental hardness profiles with the ISE correction versus simulations of 316 SS with He ion irradiation from 1-3 MeV. Unlike the unirradiated 316SS, the plastic zone does not steadily flow with increasing irradiation doses due to the transverse crack propagation at a macroscopic level.

2.4.2 Micropillar compression

Uchic et al [108] first introduced the micropillar compression test, which overcame the shortcomings of ISE from nanoindentation. From the micropillar compression test, we can acquire valuable mechanical properties deriving from materials such as elastic properties [109,110], yield stress [111], and strain hardening [112]. Compared with the microtensile bar test [88,113,114], the micropillar compression test takes much less time to complete. This technique has a wide range of applicability, from single crystals and individual grain boundaries [115–118] to multilayered systems [119–121], thin films, and interfaces [122–124].

The straining hardening can be predicted using Ludwik's equation [125,126]:

$$\sigma = K_1 + K_2 \cdot \varepsilon_p^n \quad (2.6)$$

where K_1 and K_2 are parameters fitted by the true stress-strain curve corresponding to the initial strain hardening and strain hardening due to plastic strain as $\varepsilon_p = 1$, respectively; n represents the strain hardening exponent.

The backstress can be calculated using the model from Yang et al. [127]:

$$\sigma_b = \frac{\sigma_r + \sigma_u}{2} \quad (2.7)$$

where σ_r and σ_u are the reload and unload yield stress, respectively. Several examples will be given for unirradiated and irradiated materials regarding the microcompression responses.

Irradiated 304 SS has been studied using micropillar compression testing [91,128]. The dose effect on the yield stress is shown in Fig. 2.22. The slip planes for Fig.2.22 is determined as (111) and ($\bar{1}\bar{1}\bar{1}$) planes. The 10 dpa pillar with proton irradiation exhibits irradiation hardening behavior as yield stress increases in the range of ~600 MPa. Reichardt et al. [128] characterized the crystal-orientation-dependent yield stress for the micropillars, and the formation of dislocation channels in the neutron irradiated 304 SS raised localized deformation while the unirradiated 304 SS does not show any preferential slip systems. These results strongly suggest that the applicable work of orientation-dependent micropillar compression tests can be completed on the dose studied in this thesis.

Moreover, we can probe individual grain boundaries such as large-angle grain boundaries versus twin boundaries, for example coherent $\Sigma 3$ {111} twin boundaries [112,129,130]. This will help us establish an in-depth knowledge of the slip transfer mechanisms. Imrich et al. [130] has shown the results of the activation of slip systems unconstrained by twin boundaries. The twin boundary is not a barrier or obstacle for dislocation movements, as no evidence of dislocation pileups at the grain boundary has been found. But dislocation multiplication is a major factor for the

strengthening across the twin boundaries [129]. The dislocation-grain-boundary interaction mechanisms can be further detected in regards to the direct slip transfer, grain boundary as dislocation source, dislocation pileups, and non-conservation dislocation motions [112].

The plastic deformation of the micropillar consists of basal slip and twinning. [Figure 2.23](#) shows a study on the deformation mechanism of single-crystal magnesium. Liu et al. [131] concluded that the basal slip favored direction is along the $\langle 2\bar{1}\bar{1}3 \rangle$ and the twinning favored direction is along the $\langle 10\bar{1}0 \rangle$. The computed CRSS values are 6 MPa for the basal slip and 29 MPa for twinning. The incipient basal slip is affected by the pillar size. As a result, the measured yield stress of micropillar with a diameter larger than 10 μm is equivalent to the value of the bulk magnesium. The twin resolved shear stress (TRSS) for two different twins are also given for the explanation of the twin growth based on different tip positions: where the twinning feature is magnified near the top surface of the micropillar due to the stress perturbations by the indenter tip. They also presented the simulation results for the local stress distribution under the indentation using fast Fourier transform (FFT). This provides insight into probing these two types of deformation mechanisms and crystal plasticity [132] after neutron irradiation versus using laser welding. Since the dislocation channel might form during the pillar compression, the activation of the slip systems or twinning would vary based on the dpa and He concentration levels. Resulting temperature changes during compression on these deformation mechanisms can also be considered when conducting meaningful experiments.

2.5 Deformation mechanisms

Numerous deformation mechanisms are possible in austenitic SSs, and these mechanisms interact in a complex manner [133]. In the presence of irradiation damage, localized deformation becomes a dominant factor influencing the overall deformation of SSs [134–136]. Previous studies have determined that localized deformation can occur through several mechanisms, including dislocation channeling [137], slip [128], twinning [138], and phase transformation [139,140]. These deformation mechanisms can be affected by irradiation dose, irradiation/testing temperature, strain rate, and stacking fault energy (SFE) [136,141,142]. Post-irradiation annealing, including thermal annealing induced by welding processes, can further affect the possible mechanical response of irradiated SSs. Understanding deformation mechanisms in irradiated austenitic SSs is

critical because this class of alloys comprises most structural materials in the current fleet of light water nuclear reactors (LWRs). We will review the current understandings of deformation mechanisms in austenitic steels prior to and after irradiation.

2.5.1 Dislocation glide

Dislocations are one of the important driving mechanisms used to control the plastic deformation in austenitic SSs [133], specifically, dissociation of perfect dislocations into Shockley partials. This can be written as the following form [143]:

$$\frac{a}{2}[1\bar{1}0] = \frac{a}{6}[2\bar{1}\bar{1}] + \frac{a}{6}[1\bar{2}1] \quad (2.8)$$

where a is the lattice constant. In a face-centered-cubic (fcc) metal, a total of twelve slip systems ($\{111\} a/2\langle 110\rangle$) follows the minimum strain energy principle to dissociate into partials. These partials can further impact the twinning and martensitic transformation as a variation of the slip-controlled mechanism for plasticity in fcc metals. The leading partials ($\langle 211\rangle$) and trailing partials ($\langle 112\rangle$) do not align with the fcc lattice vectors. The leading partial leaves the stacking faults of $\{111\}$ planes, while the trailing partials recover the stacking faults. The repulsive force between these partials can be described by

$$F = \frac{Gb^2}{4\pi d} \quad (2.9)$$

where G is the shear modulus, b is the Burgers vector of the partials, and d is the separation distance between the partials. At an equilibrium state, considering the Peach-Koehler formulation [144], Byun [145] derived the force balance equations for separation distance between the partials (See Fig. 2.24).

$$d = \frac{Gb^2 \cos \theta_1 \cos \theta_2 + \frac{\sin \theta_1 \sin \theta_2}{1-\nu}}{\pi(2\gamma - \tau_{zx}b|\sin \theta_2 - \sin \theta_1|)} \quad (2.10)$$

where θ_1, θ_2 represents the angle between the Burgers vector of the leading and trailing partials and the line direction of the perfect dislocation, respectively. γ is the stacking fault energy. τ_{zx} is the largest shear stress component among the stress-tensor components. ν is the Poisson's ratio.

Eq. 2.10 tells the dependence of the separation distance on SFE, Burgers vectors and the stress field. At $\theta_1 = -30^\circ$ and $\theta_2 = 30^\circ$ (screw dislocation $\theta = 0$), the separation distance has a largest stress as

$$\tau_{zx,crit} = \frac{2\gamma}{b} \quad (2.11)$$

In this case, the critical resolved shear stress (CRSS) ($\tau = \sigma \cos \phi \cos \lambda$, where $m = \cos \phi \cos \lambda$ is the Schmid factor (SF); ϕ corresponds to the angle between the normal vector of the glide plane and the applied stress σ ; λ corresponds to the angle between the glide direction and the applied stress) can produce infinite separation distance, leading to extended stacking faults up to the grain size (see Fig. 2.25 as an example).

As we see the stress-controlled separation of partials, the applied stress can also activate certain slip systems as a certain SF reaches the maximum value. Table 2.1 gives the maximum SFs for fcc slip systems (for partials we only consider the cases when the SF of the leading partial is higher than the trailing partials). We choose three high-symmetry orientations ($\langle 100 \rangle$, $\langle 101 \rangle$ and $\langle 111 \rangle$) with a larger number of slip systems as well as the low-symmetry orientation ($\langle 123 \rangle$) with a smaller number of slip systems. However, experiments have observed much fewer systems activated [146–150]. Several works can explain these deviations [147,149,151]: (1) interaction of collinear Burgers vectors with the dislocations prevents multiple activation of one slip system along with its cross-slip system [152]; (2) fluctuation misorientation of grains can rotate the crystal from high-symmetry to low-symmetry directions [151]. It should be noted that the CRSS in fcc metals have crystallographic orientation-dependent behavior. For instance, fcc pure Cu exhibits higher CRSS for $\langle 111 \rangle$ grains than $\langle 101 \rangle$ and $\langle 100 \rangle$ grains with respect to the tensile axis [153]. Low strain usually allows dislocation to form slip bands [154–156], while high strain produces strain-hardening preferentially in $\langle 111 \rangle$ grains or orientation-dependent dislocation patterns [157–159]. More accurate models and theories on the role of dislocation dynamics are essential to be developed for a clear understanding of the origins of the low-strain slipping bands and dislocation patterns at a high-strain hardening period.

Another important factor in Eq. 2.10 is the SFE. The SFE is essential to alter the deformation mechanisms. Table 2.2 is given to show the correlations of SFEs of fcc austenitic SSs. The

experimental values of the SFE can be measured by X-ray diffraction [160,161], neutron diffraction [162], and TEM [163,164]. Diffraction methods focus on the interrelationship between volumetric chemical composition and SFE. TEM focuses on measuring the separation distance of dissociated partial dislocations. Due to the uncertainty during the experimental measurements, theoretical methods such as first-principle calculations [164–166] can provide a fundamental understanding of each individual element's discrepancies. For example, generalized SFE (GSFE) describes the fault energy that evolves along with the shear amplitude [167] shown in Fig. 2.26 [166]. Each energy peak in Fig. 2.26 has different physical representation: γ_{us} is the unstable SFE (USFE); γ_{isf} is the intrinsic SFE which is the SFE we utilized in our context; γ_{max} is the maximum energy. These peaks depend on each alloy's composition and the USFE- γ_{us} , rather than the commonly accepted SFE- γ_{isf} . Temperature also has an impact on SFE [161,167]. As SFE increases, deformation mechanisms change from phase transformation (low SFE) to twinning (intermediate SFE) to dislocation glide (high SFE) [161,167–169].

2.5.2 Deformation twinning

In an fcc metals twinning system $\{111\}\langle 112\rangle$, deformation-induced twins can generate along the $a/6\langle 211\rangle$ partials. Figure. 2.27 shows how the austenite fcc lattice-ACBACB stacking transforms into twinning planes under shear as-ACBA/BCAB stacking. The twinning shear is given as $1/\sqrt{2}$ ($a/6\langle 211\rangle$ /reciprocal spacing of $\{111\}$ plane). The twinning undergoes nucleation and growth. The nucleation of twins generates from the embryo of stacking faults [165] or pre-existing dislocations [170], even though no clear nucleus of twinning has been reported. A majority of the twinning nucleation mechanism [171–174] focuses on establishing heterogeneous nucleation on pre-existing defects. Their proposed initiation of twinning nucleation depends on the twinning stress level. The critical twinning stress for the incipient twinning increases as the SFE increases [165,172,174]. For localized stress concentration, such as grain boundaries, pileups of dislocations are easier to trigger the dislocation glide motion as multiple evidences have validated the multi-slip-system activation for twinning [175–177]. After the nucleation of twinning, the twins start the process of growth. The growth of twins is governed by the overlapping of stacking faults with arrays of partials [178]. The further thickening of twins is not clearly understood.

At low strain, the deformation-twinning in austenitic SSs shows orientation dependency (Fig. 2.28a), with a preference to $\langle 111 \rangle$ tensile direction [176]. This is due to the activation of the larger Schmid factors of leading partials. Hence, the smaller Schmid factors for trailing partials are unlikely to form extended stacking faults [145], and smaller Schmid factors for the perfect dislocations [176] are also disabled for slip events. In addition, $\langle 111 \rangle$ grains have more slip systems to activate the twinning at low strain. However, for the high strain, we see more twins occurring in the $\langle 111 \rangle$ - $\langle 001 \rangle$ in Fig. 2.28b. This can be explained by the grain rotation and strain hardening [179–181] and generally require a minimum of two twinning systems. The generated interfaces between the twin and the matrix inhibit the dislocation movement [182] in the matrix, and dislocations in the twins are more likely to behave similarly to the dislocation forest with sessile dislocations [174]. As the fraction of twins increases, the twinning-induced hardening can immobilize the dislocation glide. Even though the contributed strain from twinning is relatively small, the strain hardening leads to exceptional mechanical-properties alloys such as twinning-induced plasticity (TWIP) steels [183].

2.5.3 Deformation-induced martensitic transformation

Martensitic transformation has been attractive to the materials community with a long history due its significance in fundamental science and engineering applications. Tailoring this important phase transformation not only facilitates materials design and innovation such as microstructure optimization [184], thermal conductivity [185,186], mechanical properties [187,188], and electromagnetics [189], but it also helps bio cell control [190] and geology exploration [191].

A schematic diagram of the martensitic transformation is given in Fig. 2.29. In steels, different pathways of the martensitic transformation [192,193] (shown in Fig. 2.30) include face centered cubic (fcc) γ austenite to twin structure and then to a body centered cubic (bcc)/body centered tetragonal (bct) α' martensite ($\gamma \rightarrow T \rightarrow \alpha'$); γ austenite directly transforms into α' martensite ($\gamma \rightarrow \alpha'$); and γ austenite to a metastable hexagonal close-packed (hcp) ϵ martensite and then to α' martensite ($\gamma \rightarrow \epsilon \rightarrow \alpha'$). The latter two pathways are emphasized by Bogers and Burgers [194], using their hard-sphere model and further furbished by Olson and Cohen [195] with a shearing-intersection model during the plastic deformation. This model is known as the classical Bogers-Burgers-Olson-Cohen (BBOC) model. Atomistic observation of the $\gamma \rightarrow \epsilon \rightarrow \alpha'$ transformation

has been demonstrated by combined High Resolution Transmission Electron Microscopy (HRTEM) and Molecular Dynamics (MD) simulations [196–198]. Despite the intrinsic complexity of the martensitic transformation in the unirradiated steels, the role of irradiation and localized deformation have not been fully understood [134–136]; nevertheless, the further post-weld annealing may affect the pathways of this phase transformation. Deformation-induced martensitic transformation can occur during tensile tests of 300 SSs at cryogenic [199,200], low, [201] and room temperatures [192]. The volume fraction of the martensite follows a similar trend: an increase of α' , an increase of ε to a maximum volume, and then a decrease.

The earlier argument about the dependence of SFE on the transition of deformation mechanisms partially explains the pathways of martensitic transformation in austenitic SSs [164,178,202,203]: (1) low SFE $< 20 \text{ mJ/m}^2$ yields martensitic transformation/slip dominant plasticity; (2) intermediate $20 \text{ mJ/m}^2 < \text{SFE} < 50 \text{ mJ/m}^2$ favors the twinning/slip dominant plasticity; (3) high SFE $> 50 \text{ mJ/m}^2$ shows the slip dominant plasticity. The interplay among $\gamma \rightarrow T$, $\gamma \rightarrow \varepsilon$, and $\gamma \rightarrow \alpha'$ has not been well understood. Fig. 2.31 shows the change of deformation modes of shear bands (SBs), stacking faults (SFs), ε , and twins by variation of the concentration of Ni in Fe-Cr-Ni [204]. As the SFE increases, the dominant deformation mode transits from martensitic transformation to twinning. Only one model attempted to distinguish between the twinning and ε transformation: ordering the stacking faults by decreasing temperature or SFE can lower the emission of partials, which contribute to the arranged ε structure instead of twinning [205]. Moreover, the strain rate also changes the transition: (1) a lower strain rate increase of stress level and nucleation sites favors the nucleation of α' [206] rather than twins/ ε at low stress [207]; (2) a higher strain rate reduces the nucleation of α' [208,209], but twins/ ε are not well understood [210,211].

2.5.4 Effect of irradiation

As we discussed in section 2.3, the irradiation-induced microstructural evolution in austenitic SSs has been widely studied. However, the effect of irradiation on the deformation mechanisms has not yet been well understood. A typical stress-strain that curves on austenitic steels is shown in Fig. 2.32 [100]. After irradiation, the elongation has decreased and necking almost occurs directly after yield point. The tensile properties are also affected by irradiation dose and temperature [212,213].

The interactions of dislocations and irradiation-induced defects (loops, cavities, precipitates) can further affect the deformation [133]. Lee et al. proposed a phenomenological model based on the types of interactions between loops and partials to illustrate the interlink between pileups, stacking faults, and defect-reduced channels [214]. Atomistic simulations also show the dynamic interactions between dislocation and loop [215], stacking fault tetrahedron (SFT) [216,217] and cavity [218,219]: as shearing, absorption, or pileup of dislocations can control the deformation. Twinning and martensitic transformation are also affected by SFE [220] similar to the unirradiated case. Irradiation-induced defects can further alter the deformation mode by providing more active nucleation sites for twinning and martensitic transformation. More importantly, dislocation channeling occurs by an unfauling of sessile loops as a clear path of removing irradiation-induced defects [53,134,135,221]. The clear transition criteria between irradiation, slip, phase transformation, and dislocation channeling has not been developed. Byun et al. [222] developed a deformation mode map of 316 SSs in terms of dose and true stress at room temperature. At lower dose < 0.1 dpa, large stress can cause the transition from dislocation tangles to stacking faults and further induce plastic instability stress (PIS) and channels. At higher dose > 1 dpa, large stress is more likely to produce channels and the threshold of PIS has been raised. To sum up, the deformation mechanisms of irradiated austenitic SSs are dependent on the localized mechanical state (stress, strain and strain rate), testing temperature, irradiation condition, and SFE.

Table 2.1 Schmid factors (SFs) for perfect and Shockley partial dislocations in fcc slip systems.

Grain orientation	Largest SF (number of systems)	Leading/ trailing partials (number of systems)
<111>	0.27 (6)	0.31/0.16 (6)
<101>	0.41 (4)	0.47/0.24 (4)
<100>	0.41 (8)	0.24/-0.24 (8)
<123>	0.14 (1)	0.30/0 (1), 0.47/0.13 (1), 0.47/0.34 (1), 0.27/0.24 (1), 0.27/0.03 (1)

Table 2.2 Stacking fault energy (SFE) for fcc alloys (elemental composition in wt%).

Authors	System	SFE formulation (mJ/m ²)
Brofman et al. [223]	Fe-Ni-Cr-C	$\gamma = 16.7 + 2.1 \text{ Ni} - 0.9 \text{ Cr} + 26 \text{ C}$
Lu et al. [164]	Fe-Ni-Cr-Mn-C-Si-S-N-Al-O	$\gamma = [F_{hcp} + 2F_{dhcp} - 3F_{fcc}]/A_{2D}^{*1}$
Meric de Bellefon et al. [224]	Fe-Cr-Ni-Mo-Si-Mn-C-N	$\gamma = 2.2 + 1.9 \text{ Ni} - 2.9 \text{ Si} + 0.77 \text{ Mo} + 0.5 \text{ Mn} + 40 \text{ C} - 0.016 \text{ Cr} - 3.6 \text{ N}$
Ojima et al. [225]	Cr-Ni-Mn-N	$\gamma = 5.53 + 1.4 \text{ Ni} - 0.16 \text{ Cr} + 17.10 \text{ N}$
Pickering [226]	Fe-Cr-Ni-C-Si-Mn-N	$\gamma = 25.7 + 2 \text{ Ni} - 13 \text{ Si} - 1.2 \text{ Mn} + 410 \text{ C} - 0.9 \text{ Cr} - 77 \text{ N}$
Qi-Xun et al. [227]	Fe-Cr-Ni-Mn-Mo	$\gamma = [36, 42] + 1.59 \text{ Ni} - 5.59 \text{ Si} + 15.21 \text{ Mo} + 0.06 \text{ Mn}^2 - 1.34 \text{ Mn} + 40 \text{ C} + 0.01 \text{ Cr}^2 - 1.75 \text{ Cr} - 60.69 (\text{C} + 1.2 \text{ N})^{0.5} + 26.27 (\text{C} + 1.2 \text{ N})(\text{Cr} + \text{Mn} + \text{Mo})^{0.5} + 0.61 [\text{Ni}(\text{Cr} + \text{Mn})]^{0.5}$
Rhodes et al. [228]	Ni-Cr-Mn-Si	$\gamma = 1.2 + 1.4 \text{ Ni} - 0.6 \text{ Cr} + 17.7 \text{ Mn} - 44.7 \text{ Si}$
Saeed-Akbari et al. [229]	Fe-Mn-Al-Si-C	$\gamma = 2\rho\Delta G^{\gamma \rightarrow \varepsilon} + 2\sigma^{\gamma/\varepsilon} \text{ *2}$
Schramm et al. [230]	Fe-Cr-Ni-Mn	$\gamma = -53 + 6.2 \text{ Ni} + 0.7 \text{ Cr} + 3.2 \text{ Mn} + 9.3 \text{ Mo}$
Yonezawa et al. [231]	Fe-Cr-Ni	$\gamma = -7.1 + 2.8 \text{ Ni} - 0.49 \text{ Cr} + 0.75 \text{ Mn} - 2 \text{ Si} + 2 \text{ Mo} - 5.7 \text{ C} - 24 \text{ N}$

*1: F_{hcp} is the free energy of the hcp lattice; F_{dhcp} is the free energy of the double hcp lattice; F_{fcc} is the free energy of the fcc lattice; A_{2D} is the interface area.

*2: ρ is the molar surface density; $\Delta G^{\gamma \rightarrow \varepsilon}$ is the free energy for the phase transformation and $\sigma^{\gamma/\varepsilon}$ is the γ/ε interfacial energy.

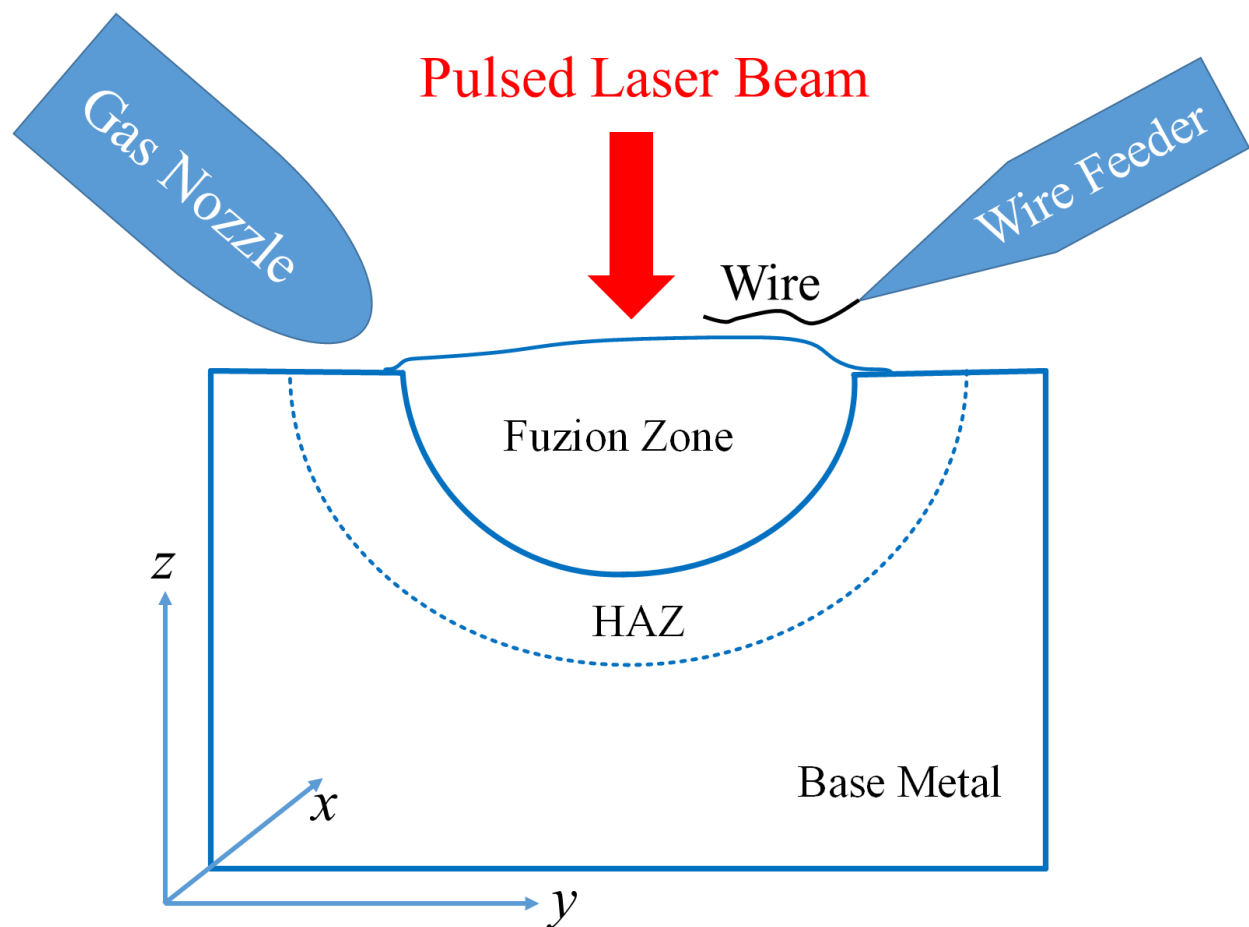


Figure 2.1 Schematic diagram of the laser weldment.

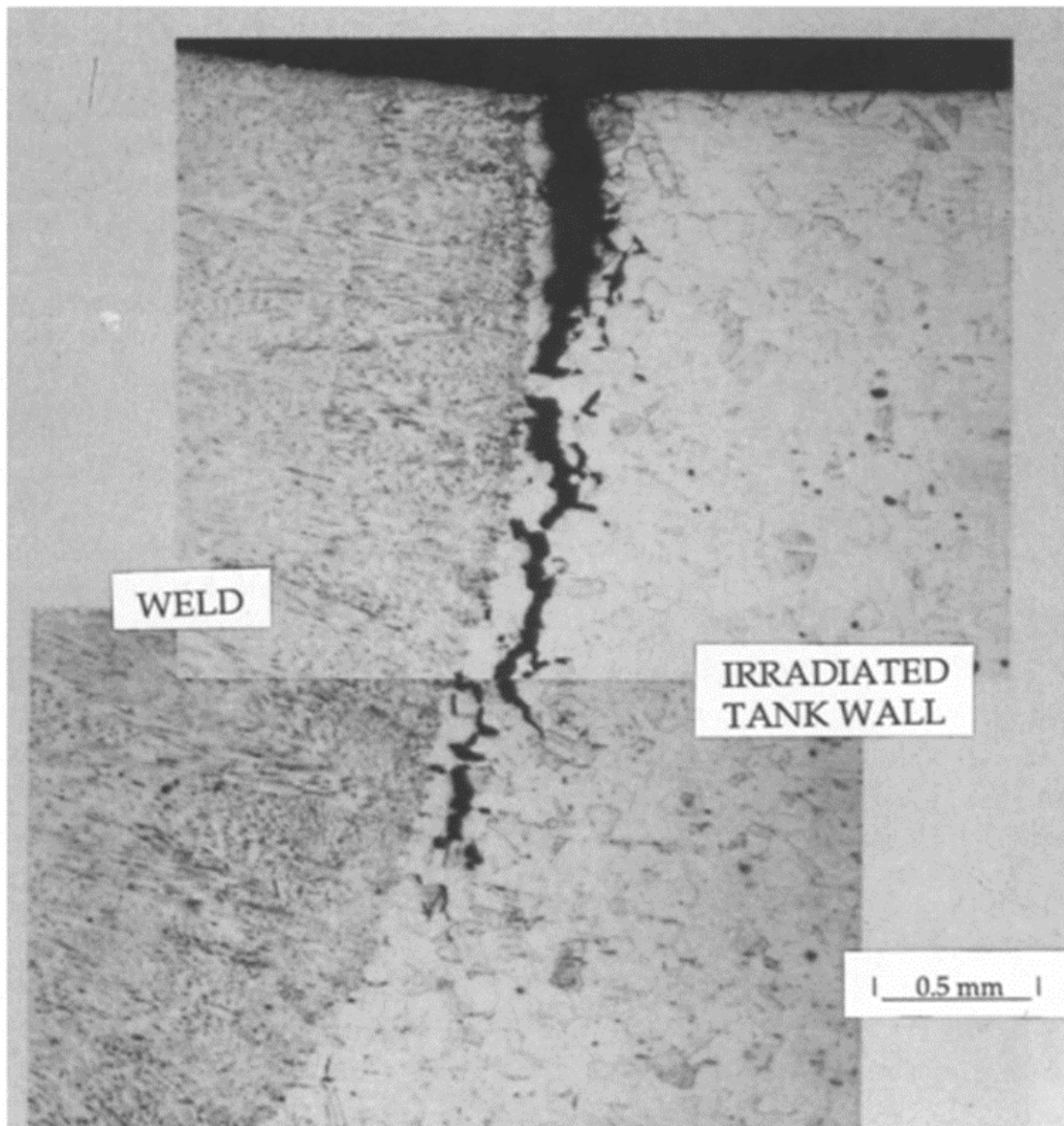


Figure 2.2 Conventional gas tungsten arc weld on irradiated 304 SS containing 1.5 appm helium [44].

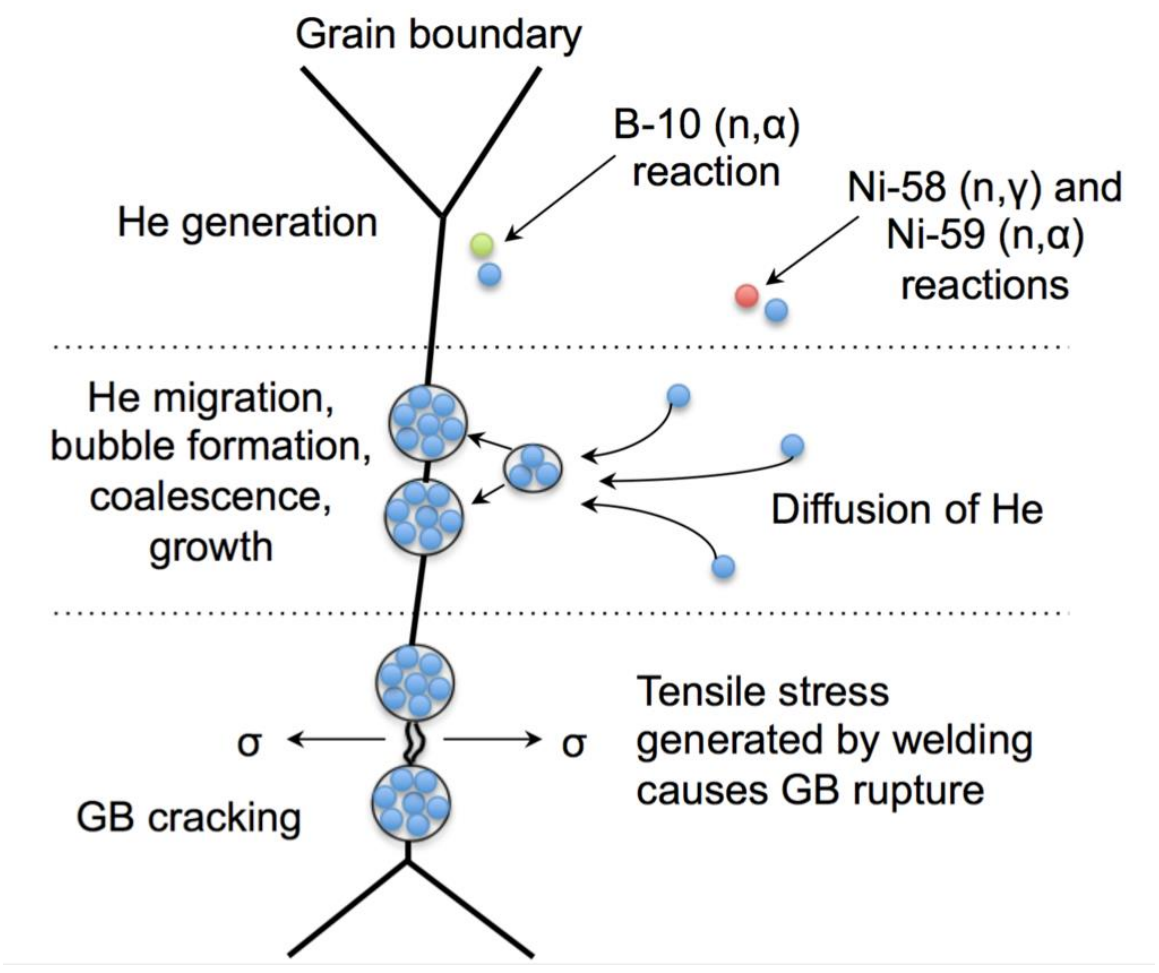


Figure 2.3 Schematic diagram showing the progression of He generation, He bubble formation, and grain boundary fracture.

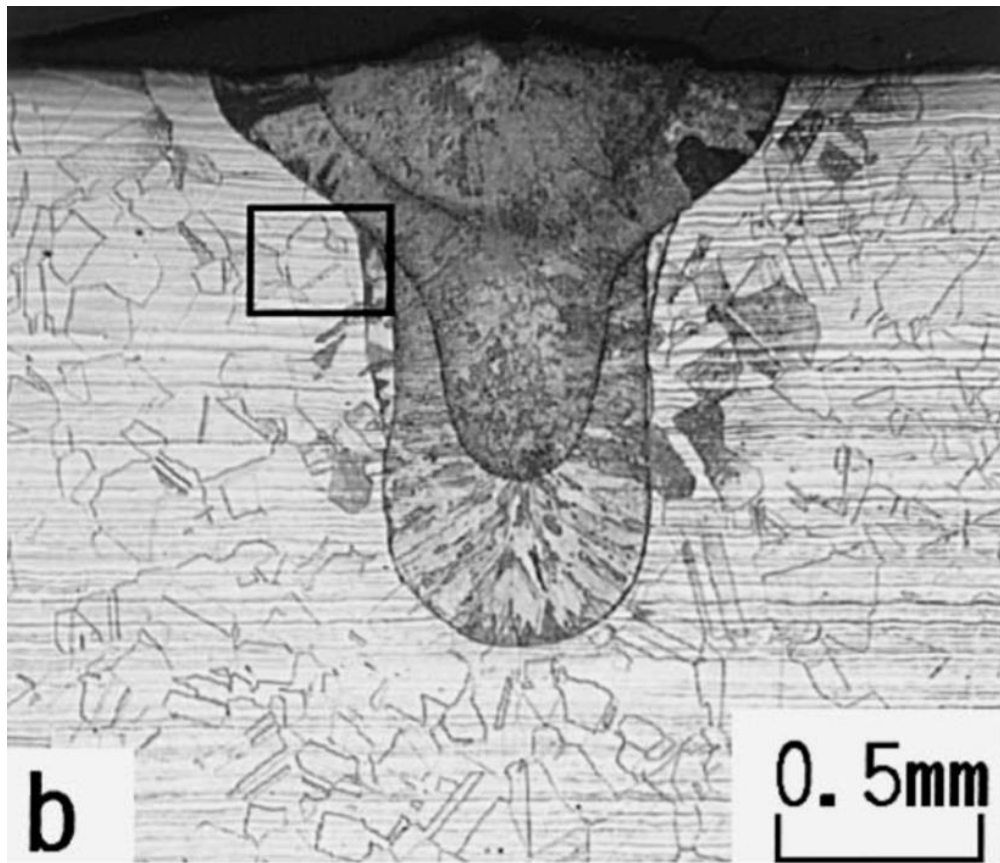


Figure 2.4 Typical laser weld cross-section with dendritic grain structure and centerline [40].

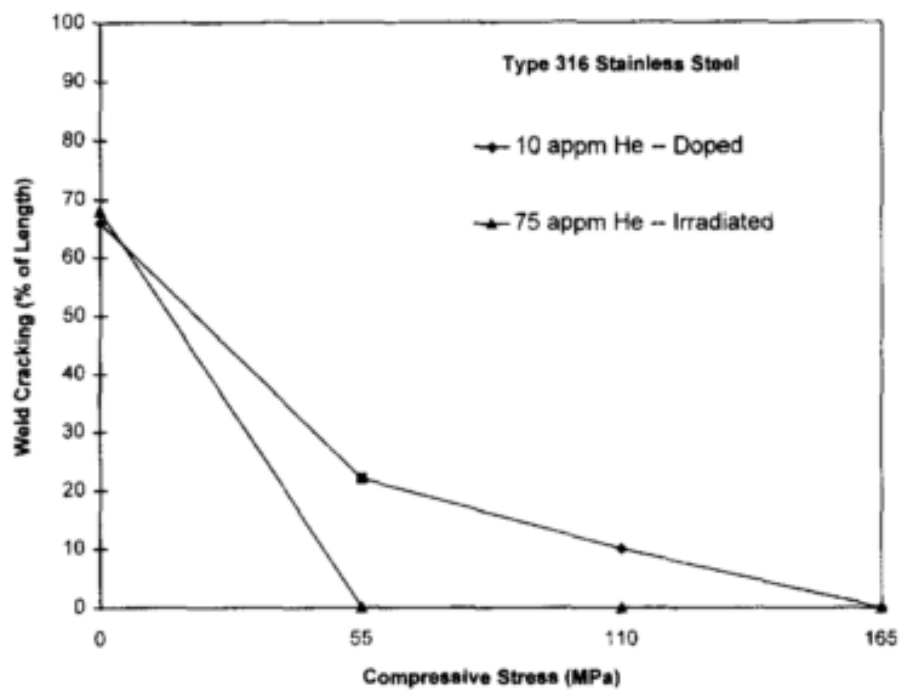


Figure 2.5 Comparison of weld cracking in He doped and irradiated 316 SS [43].

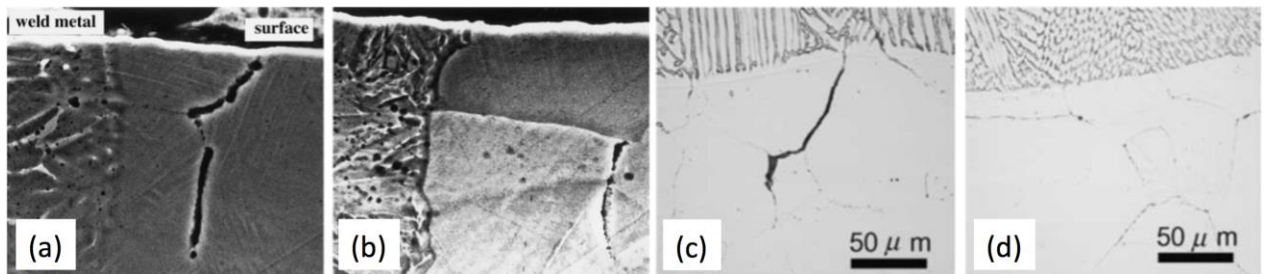
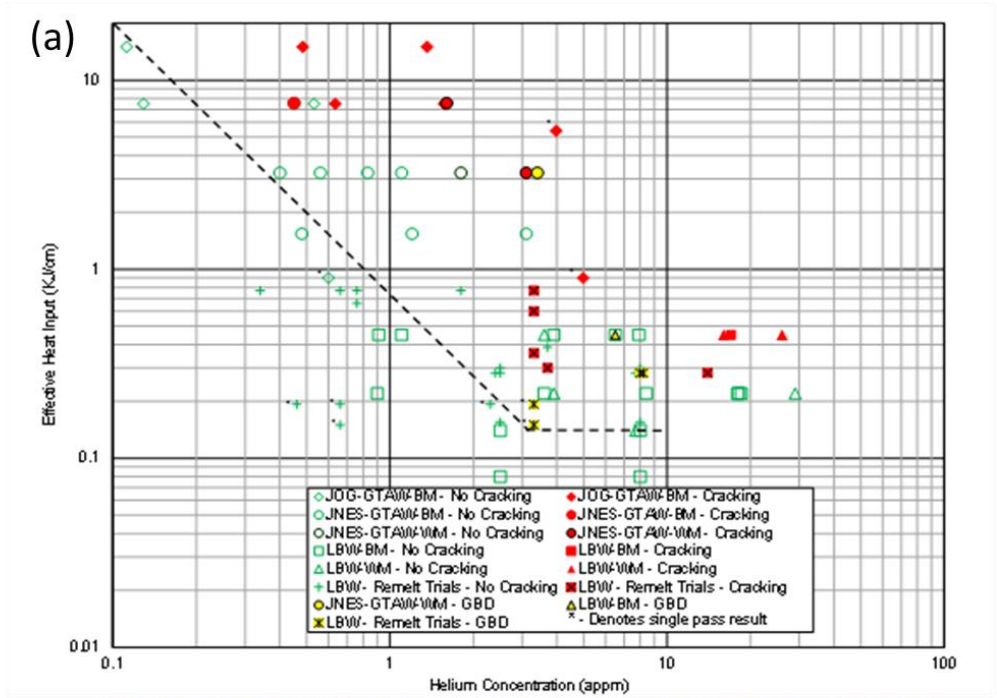
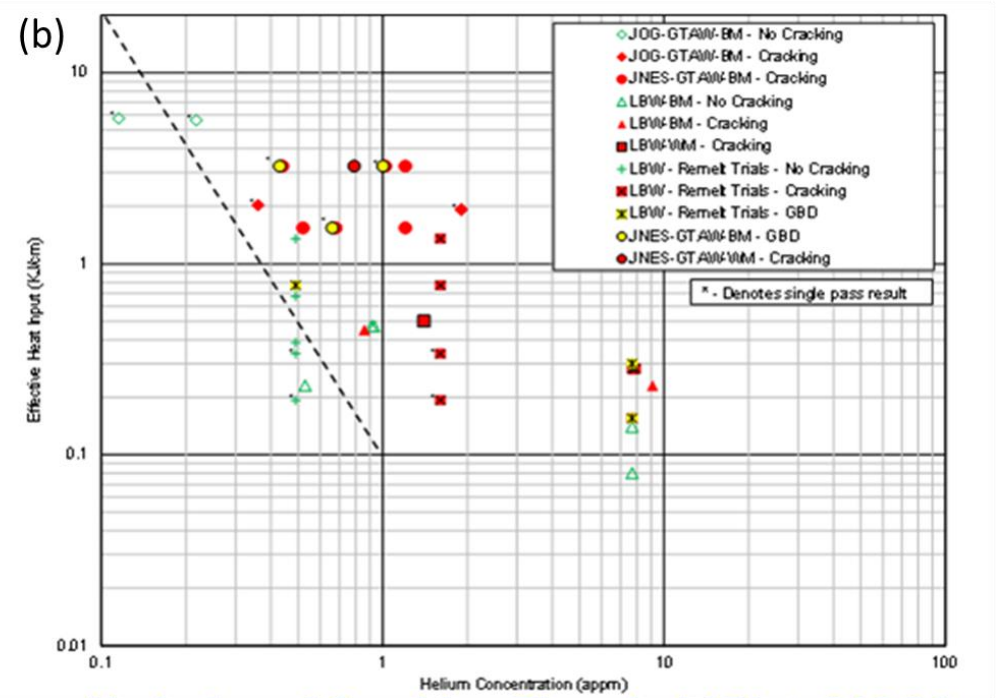


Figure 2.6 Reduction of cracking in laser welded 304 SS containing 50 appm He when heat input is reduced from (a) 20 kJ/cm to (b) 4 kJ/cm [5]. With a fixed heat input of 2 kJ/cm in 316L SS, GTAW produces microcracking (c), while (d) laser welding does not [6].



He-Induced Cracking Threshold Plot: 304 SS



He-Induced Cracking Threshold Plot: 316 SS

Figure 2.7 Effective laser weld heat input threshold of (a) 304SS and (b) 316SS (dashed line) as a function of He concentration. Below the threshold, welds do not produce He-induced cracks (green), but above the threshold, welds do produce He-induced cracks (red) [47].

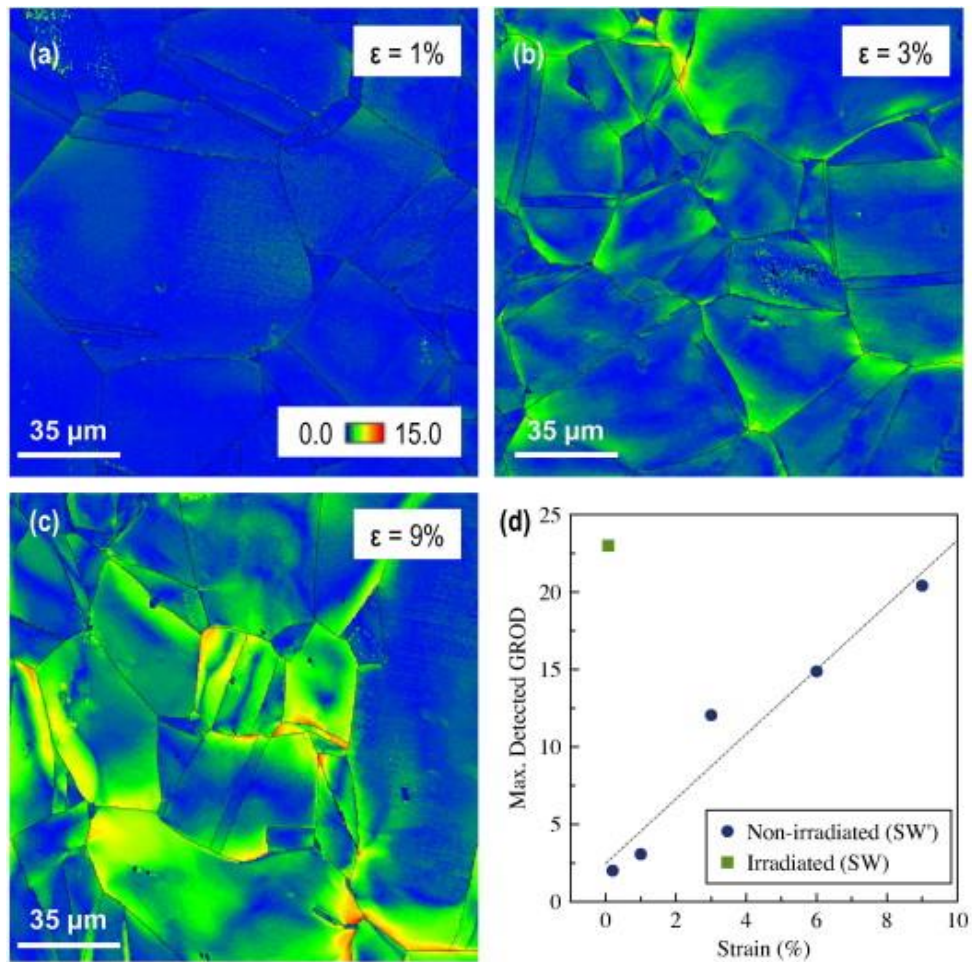


Figure 2.8 Planar EBSD GROD maps for the deformed unirradiated specimens (SW) and a relationship between the maximum observed GROD value and strain level [53].

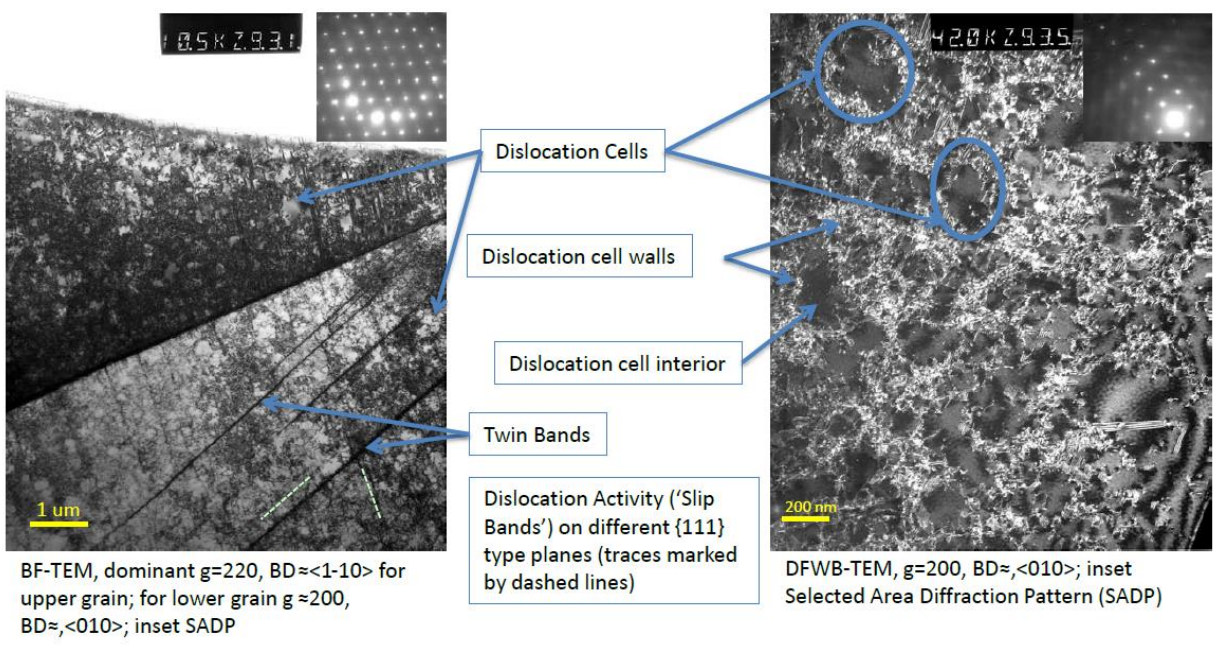


Figure 2.9 Microstructure of unirradiated archive hex-block observed using electron microscopy, derived at a depth in the middle of the block, showing dislocation and slip structure characteristic of ~5% cold-work [54].

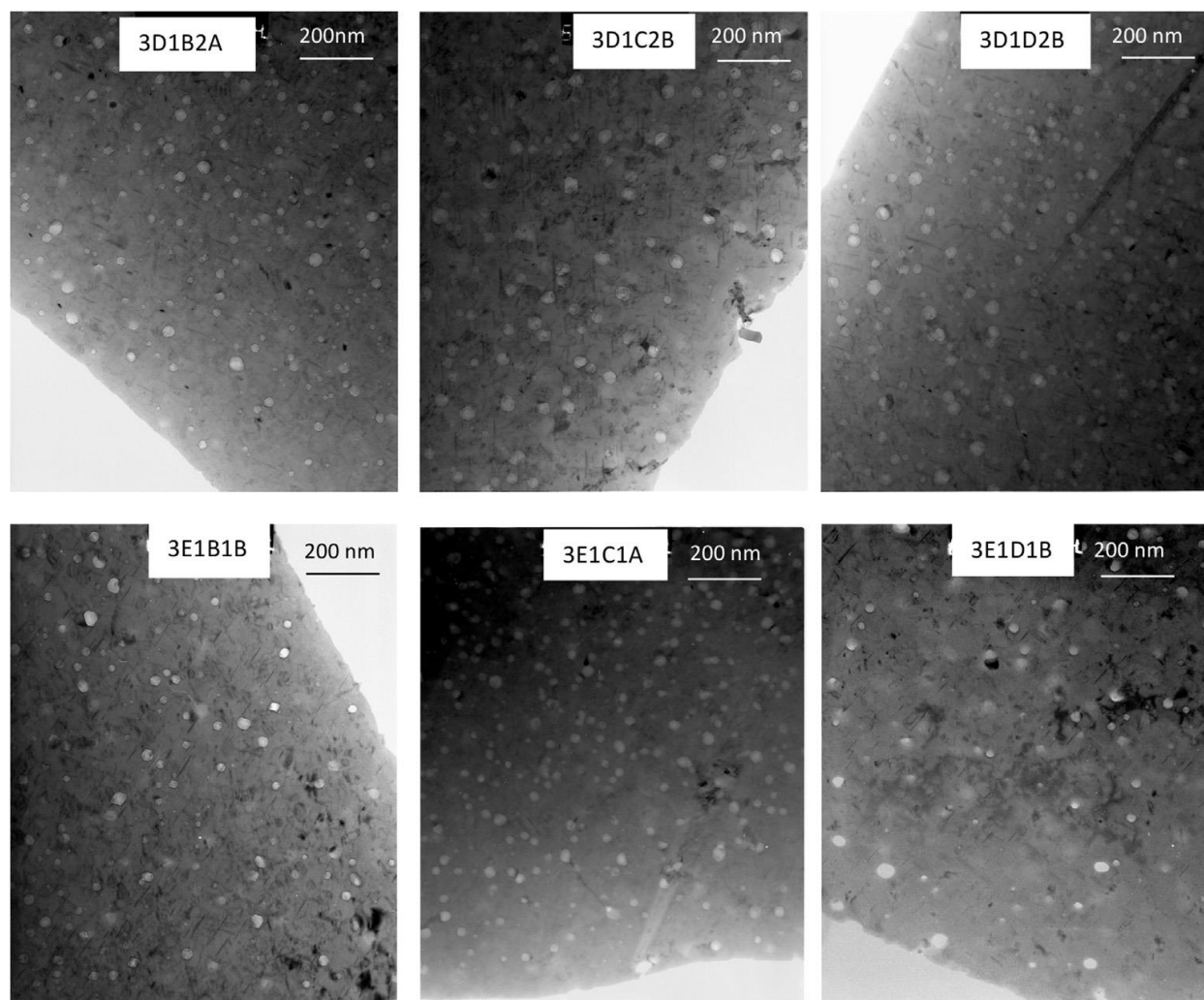


Figure 2.10 Bright-field TEM imaging of cavities from different specimens from hex-block 3D-28 dpa, 8 appm irradiated at 418°C and 3E-29 dpa, 8 appm irradiated at 420°C [54].

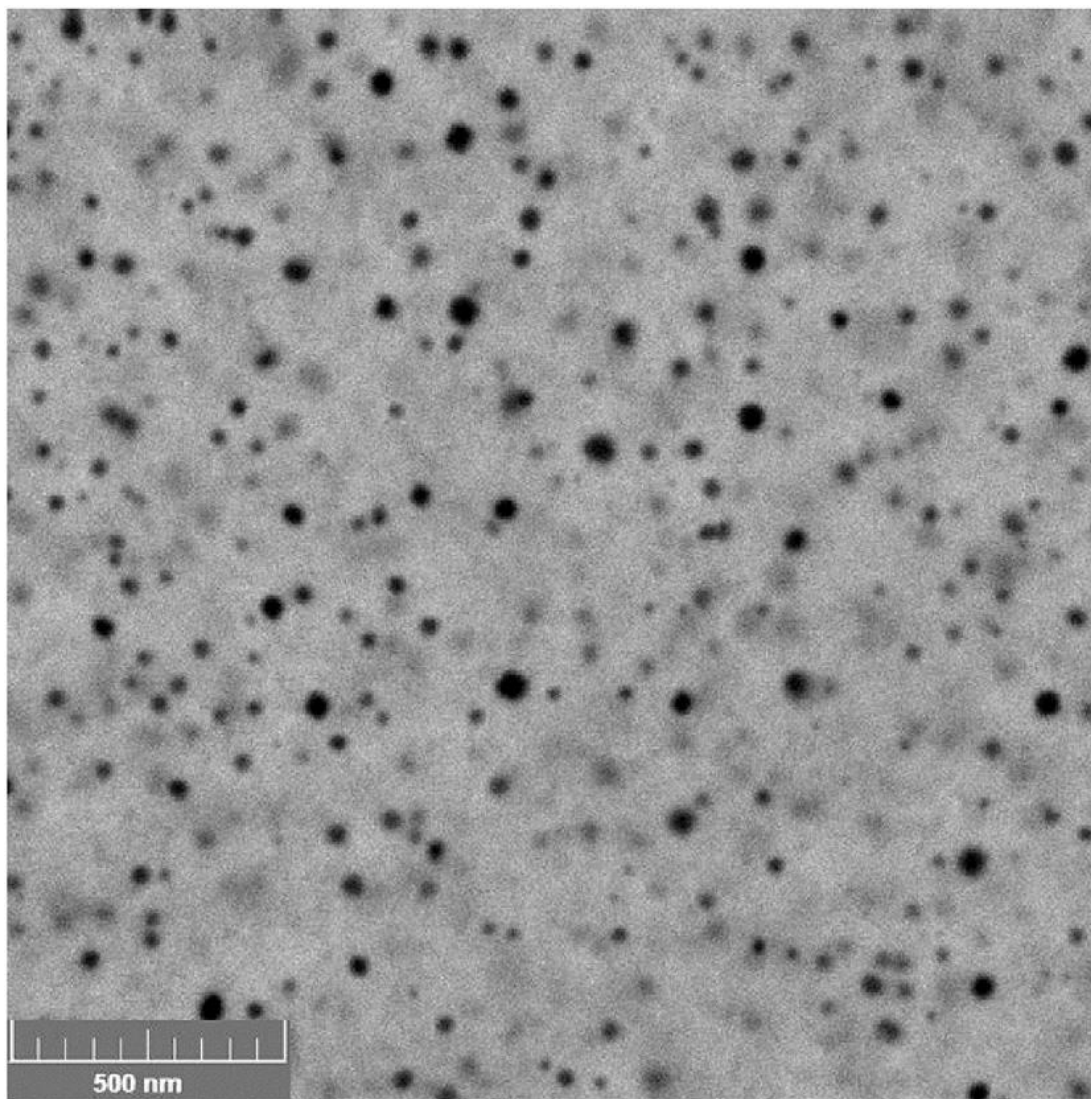


Figure 2.11 Backscattered electron (BSE) scanning microscopy imaging of cavities in hex-block of 28 dpa, 8 appm irradiated at 418°C shown in [Figure 2.10](#) [64].

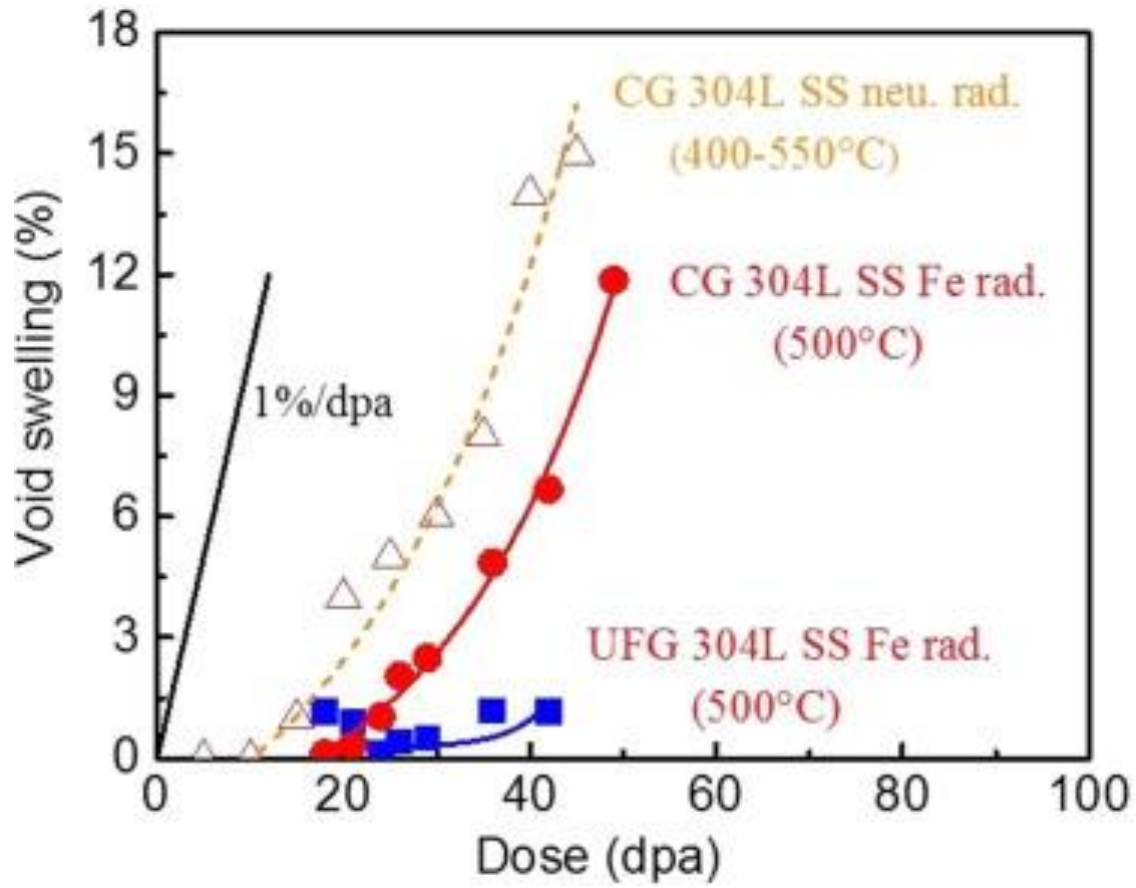


Figure 2.12 Comparison of void swelling of Fe ion irradiated 304L SS with neutron irradiated 304L SS with different grain sizes [66].

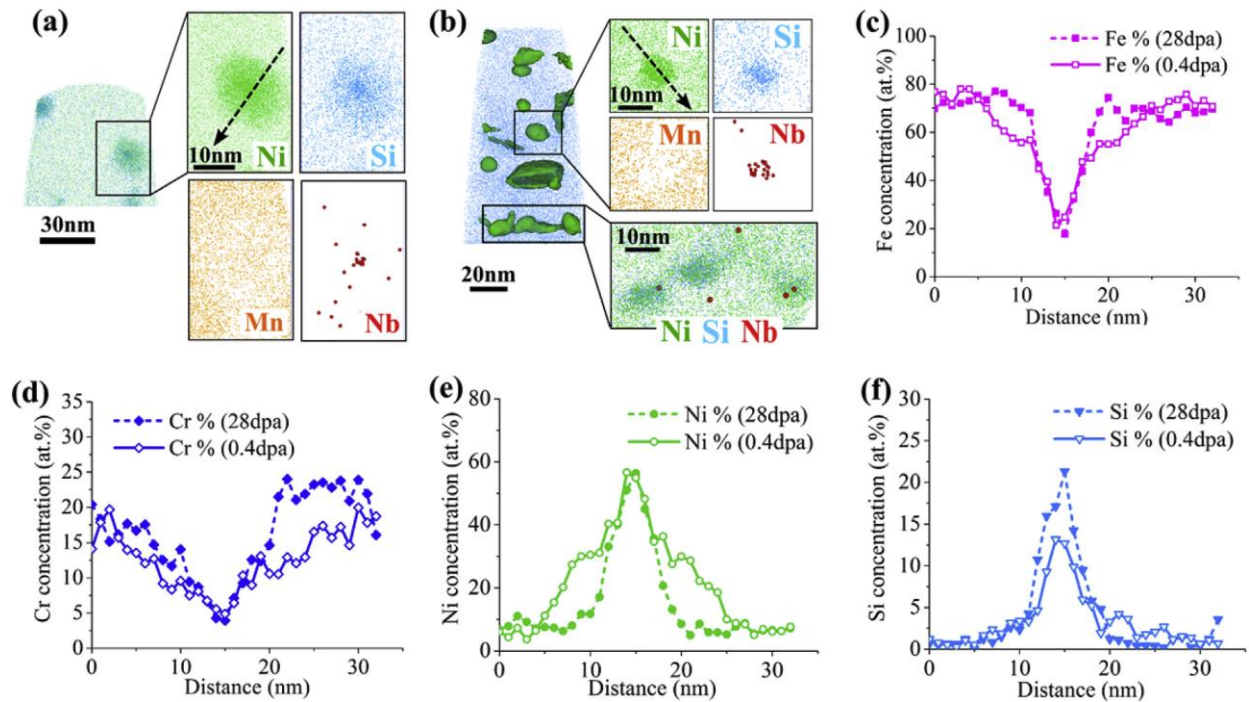


Figure 2.13 Ni and Si rich precipitates in (a) 0.4 dpa material and (b) 28 dpa material; (c) to (f): line profiles measured by placing a 10 nm diameter cylinder along the arrows indicated in (a) and (b) [61].

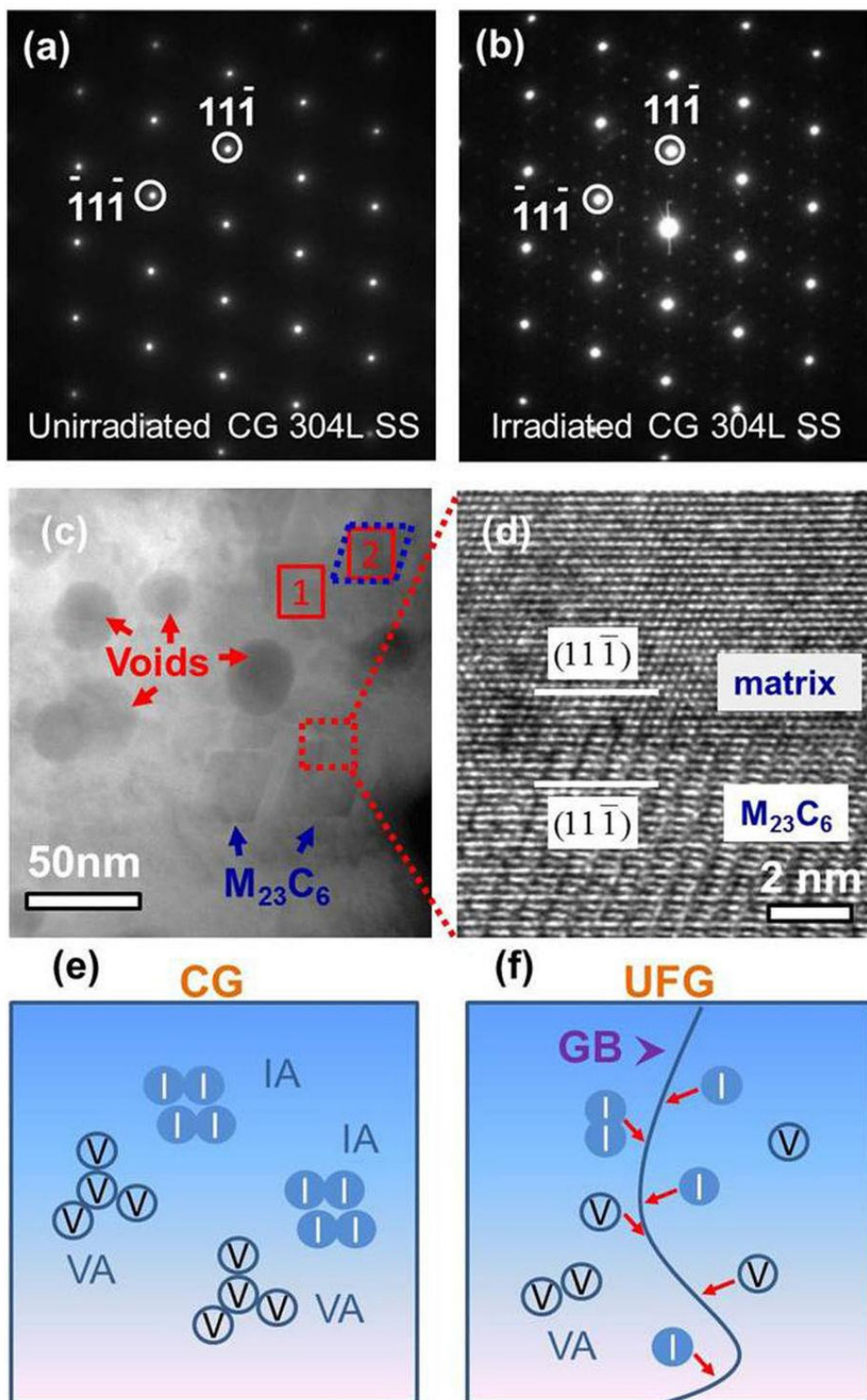


Figure 2.14 Fe ion irradiation-enhanced $M_{23}C_6$ precipitation in CG 304L SS [63].

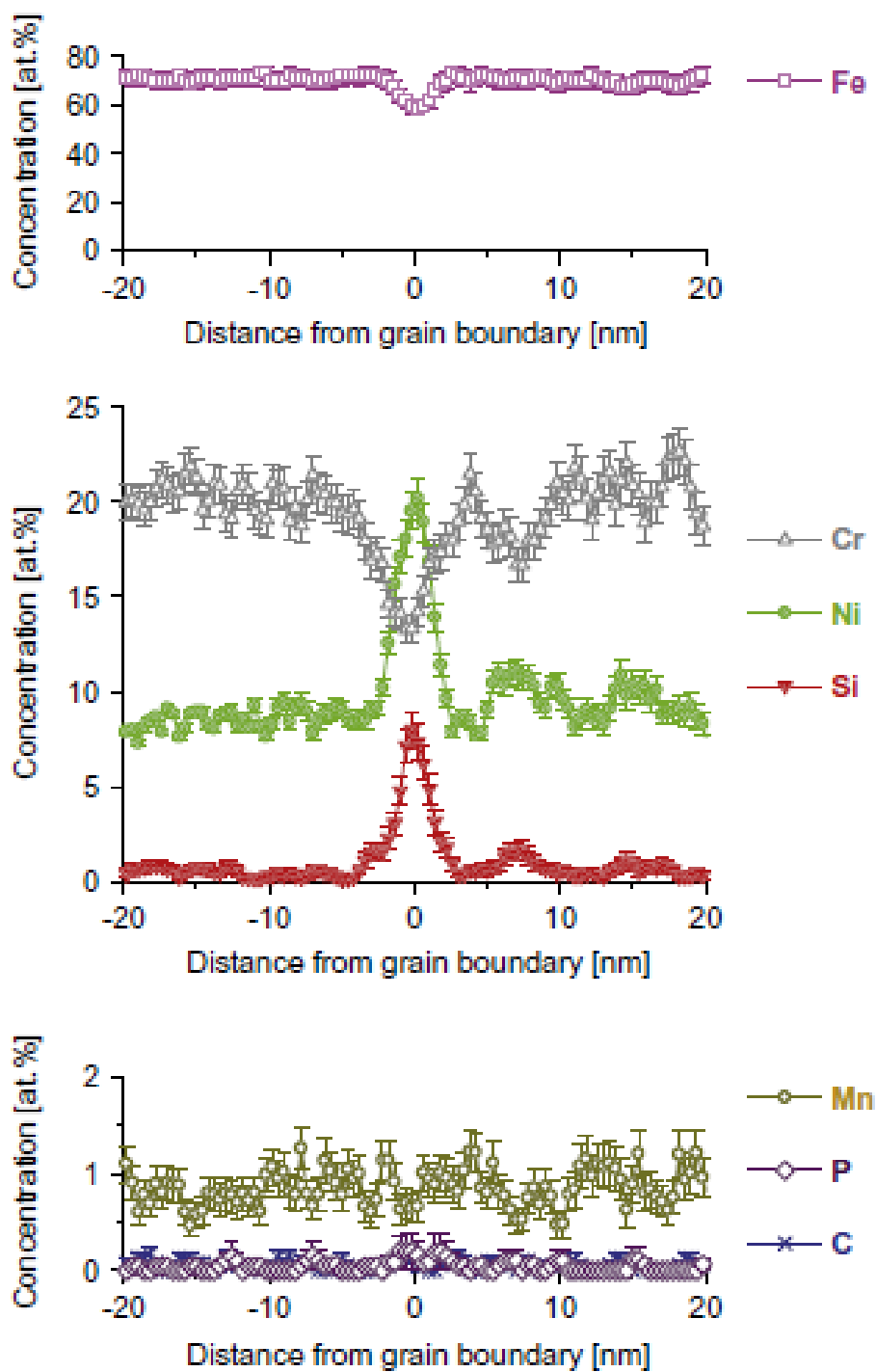


Figure 2.15 APT data of concentration of elements through the grain boundary of 304 SS of 24 dpa [79].

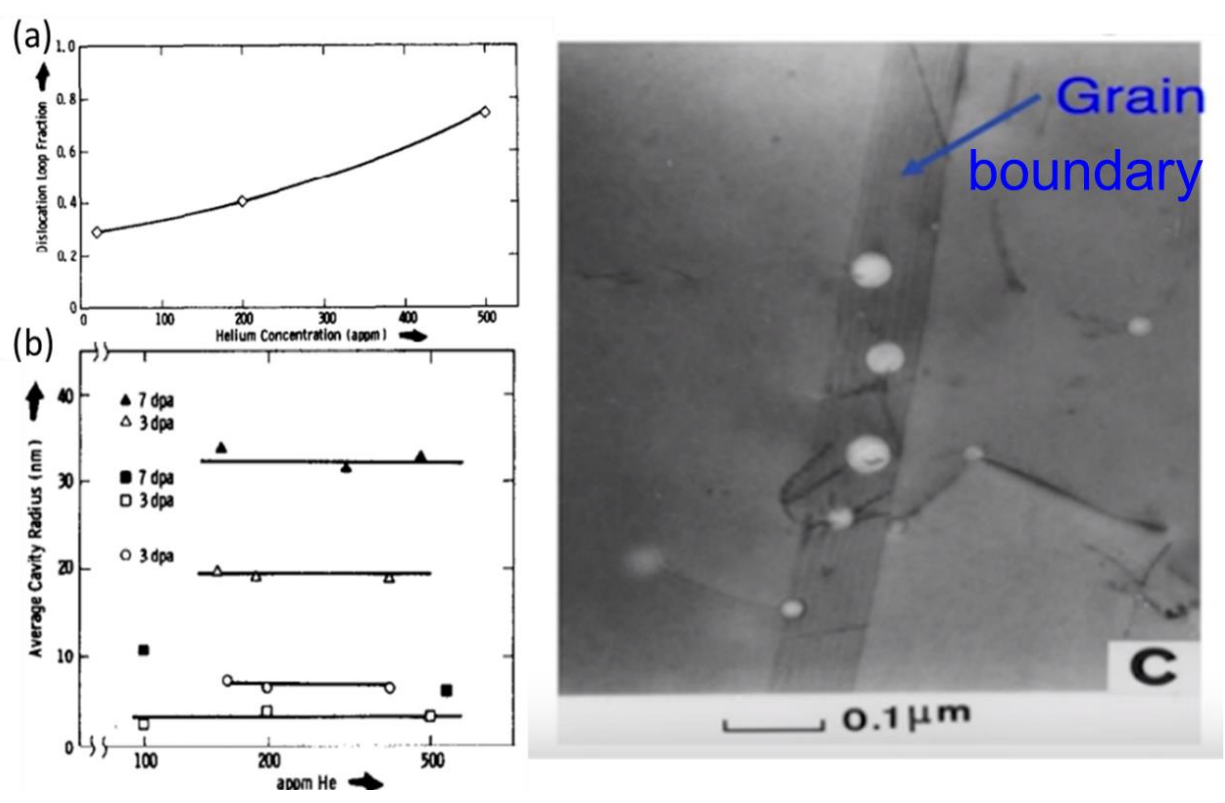


Figure 2.16 (a-b) Si ion irradiated 304 with pre-planted He indicates (a) loops increase as He increases and (b) cavity grows as dpa increases [81]. (c) He bubbles on a grain boundary [82].

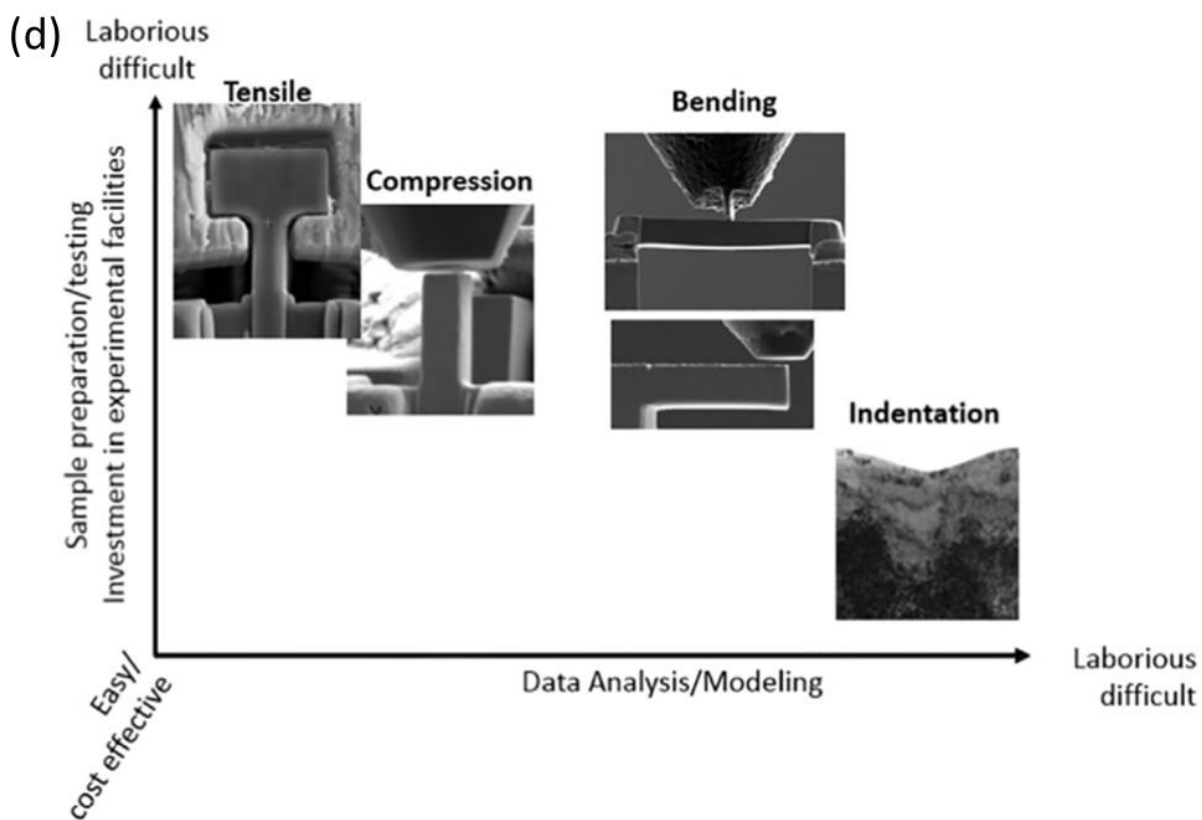
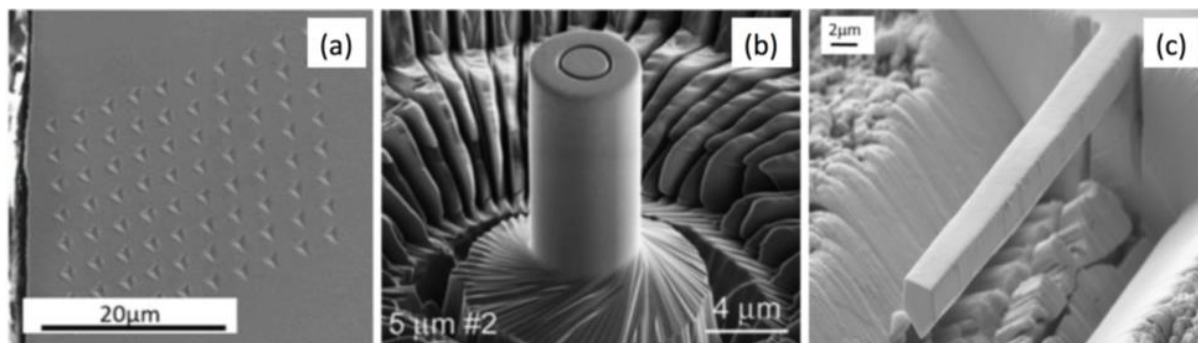


Figure 2.17 (a) Array of nanoindentations on an irradiated alloy [89]; (b) microcompression pillar [108]; (c) microcantilever on an irradiated alloy [87]; and (d) levels of difficulty in small-scale mechanical testing in the plane of experimental and data analysis [91].

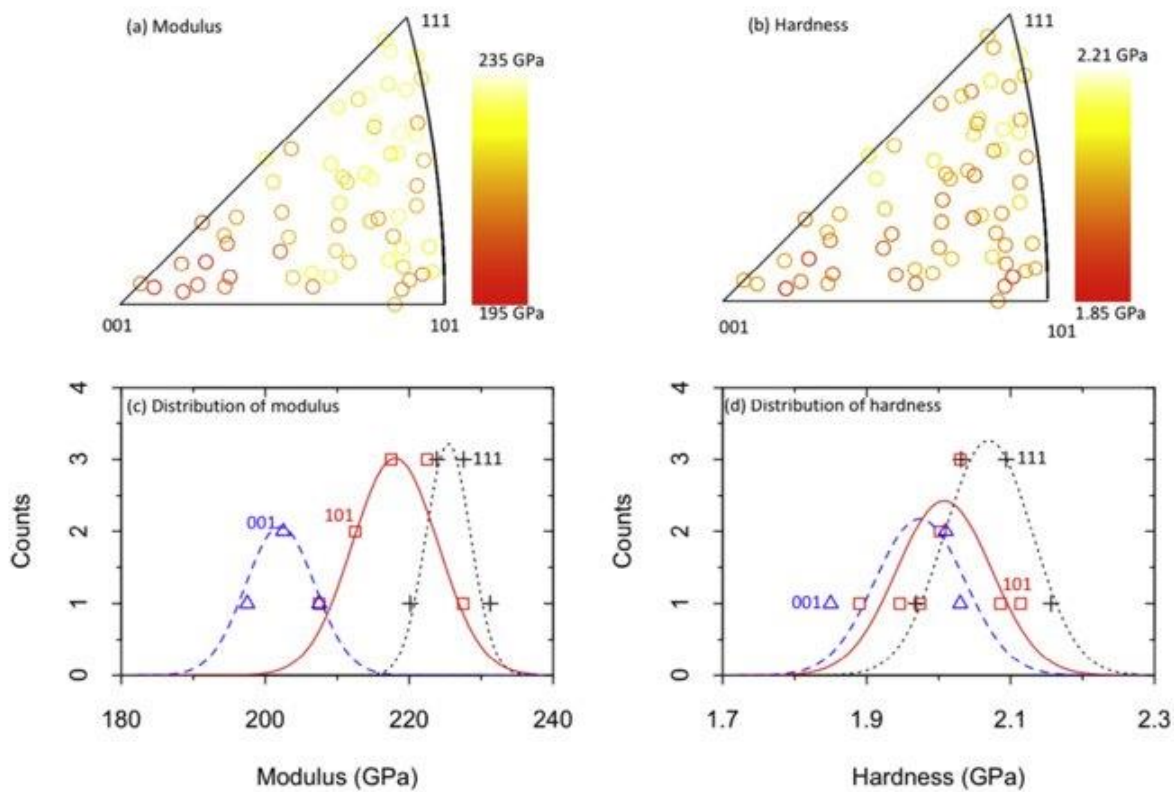


Figure 2.18 Fe-20Cr-25Ni: color-coded standard stereographic triangles (SST) and distributions of elastic modulus and hardness of the indents close to {001}, {101}, and {111} grains [104].

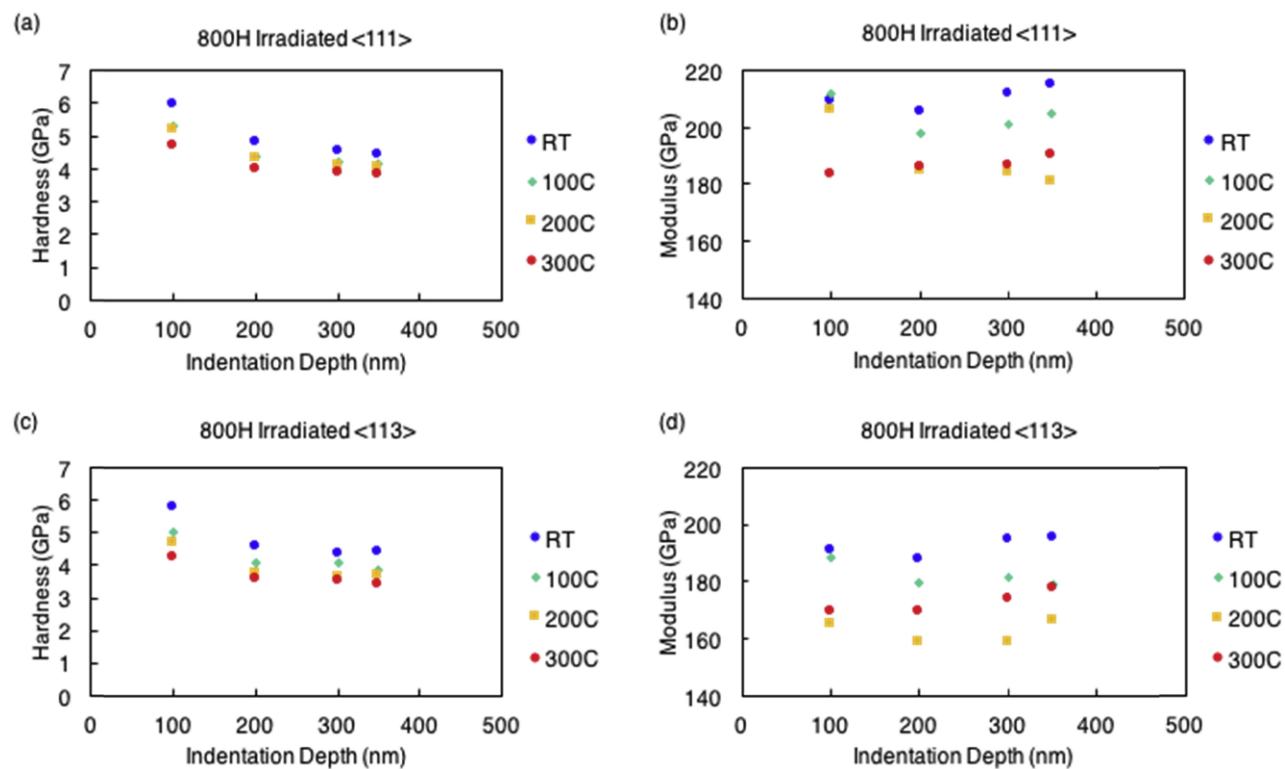


Figure 2.19 Irradiated 800H: hardness and modulus profiles as a function of depth and temperature of grains of (a-b) <111> and (c-d) <113> orientations [101].

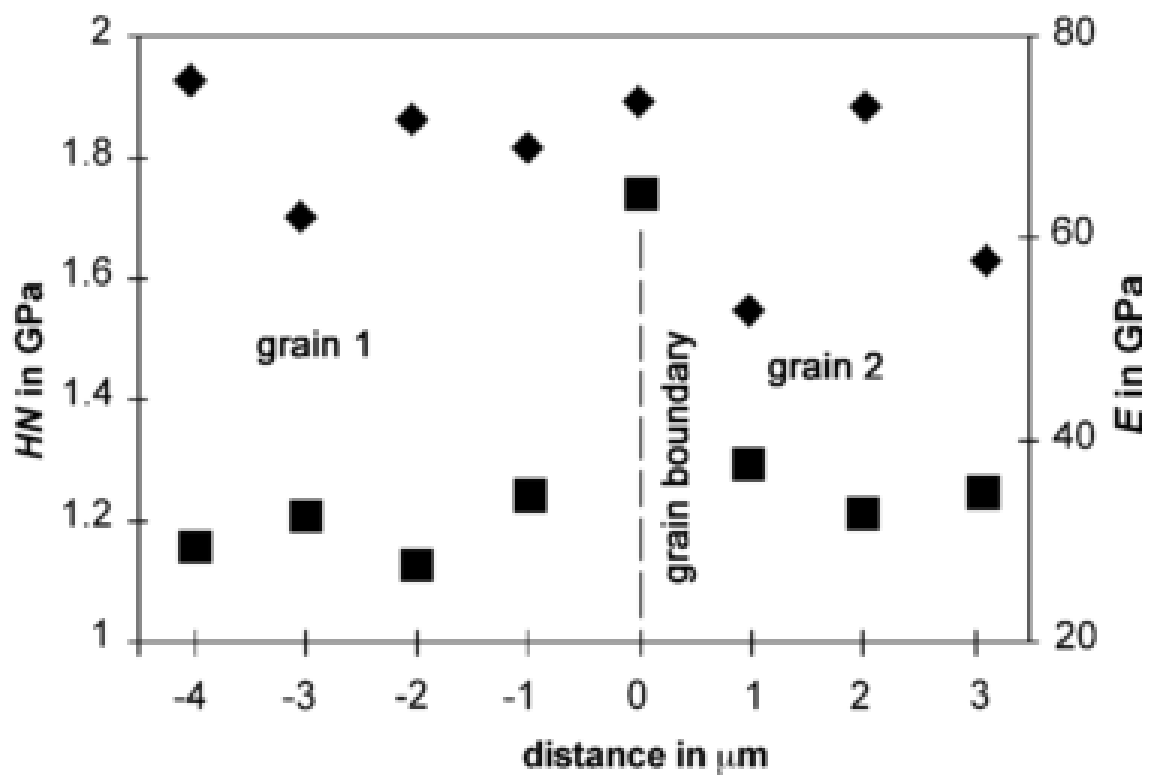


Figure 2.20 Nanoindentation data for hardness and modulus in two different grains and at grain boundary for an iron-based material [105].

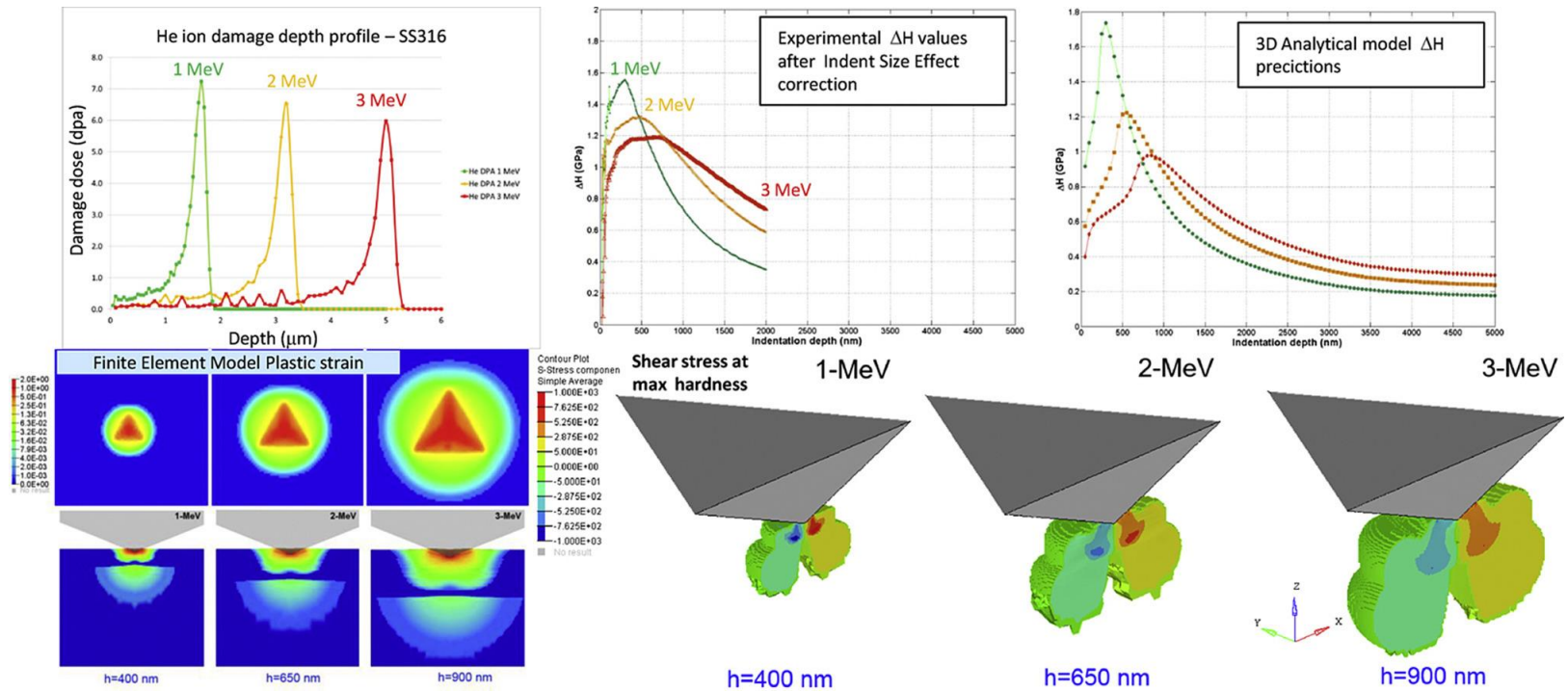


Figure 2.21 Relationship between damage and hardness profiles in ion irradiated SS316 using nanoindentation – experiments and modelling [98].

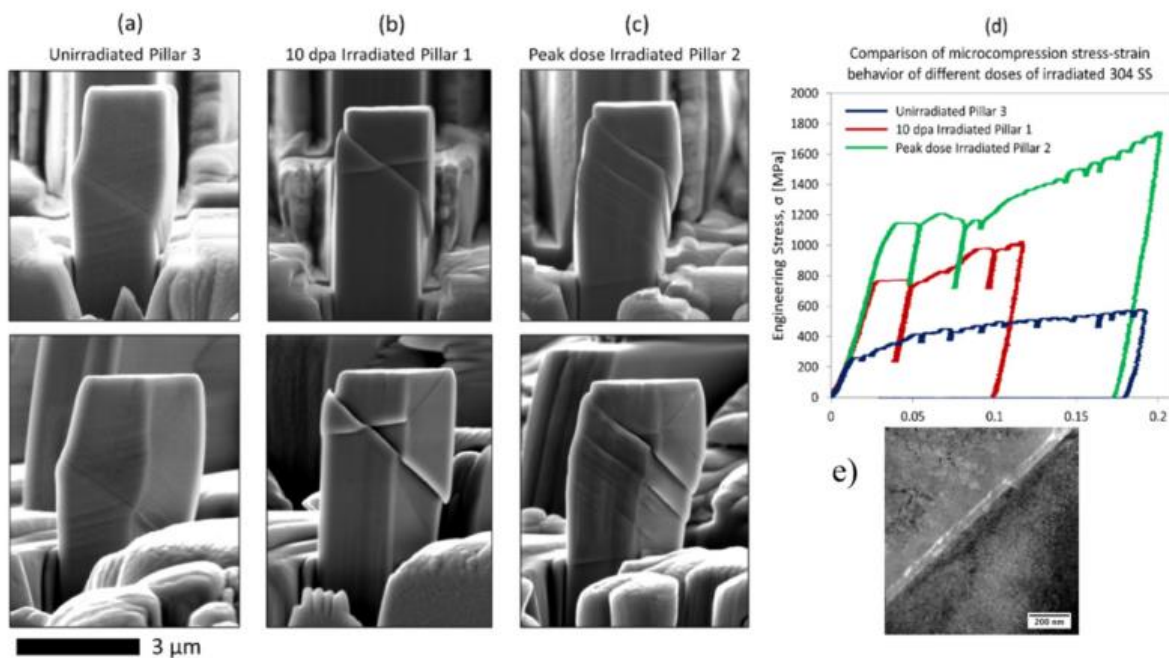


Figure 2.22 SEM image of ion beam irradiated 304 SS (a-c) and (d) the engineering stress-strain curve with (e) TEM image of the post-compression irradiated sample [127].

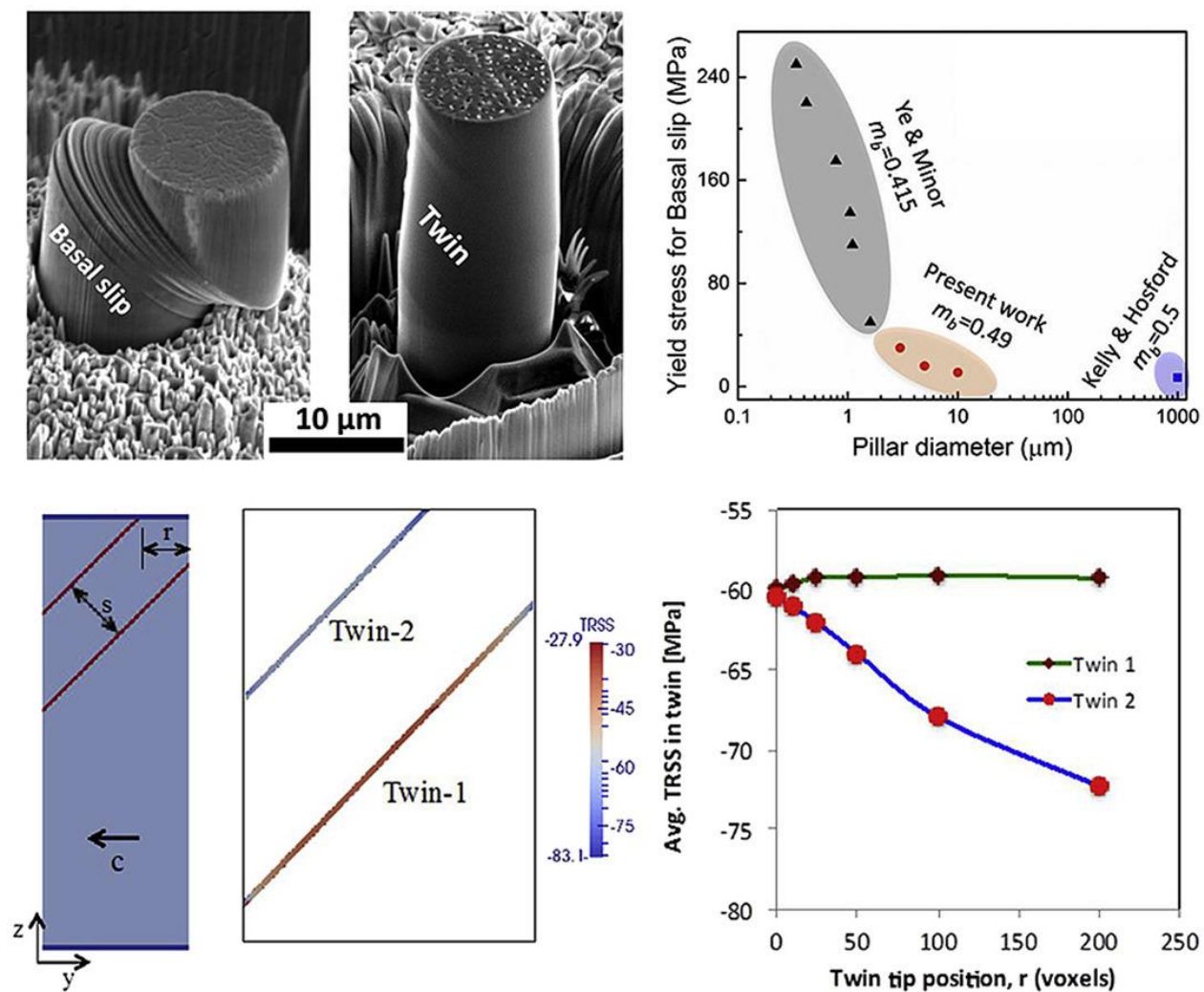


Figure 2.23 Experimentally quantifying critical stresses associated with basal slip and twinning in magnesium using micropillars [131].

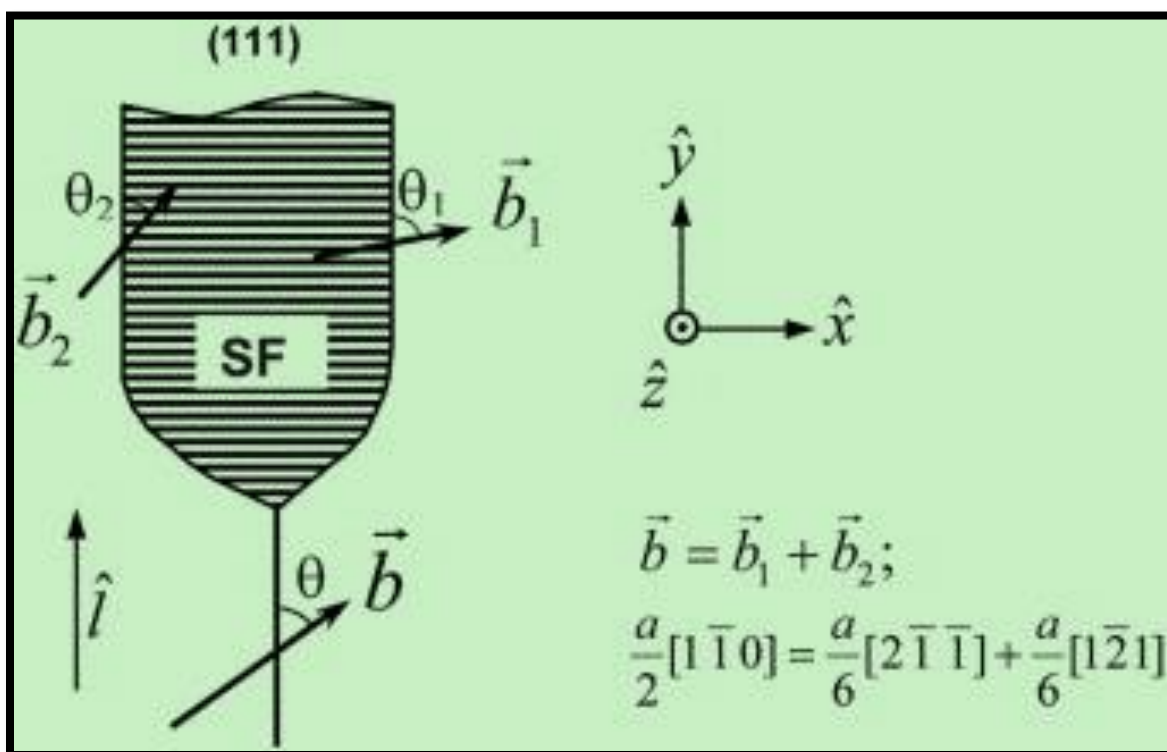


Figure 2.24 Schematic diagram of a perfect dislocation \hat{l} into leading partial with Burgers vector \vec{b}_1 and trailing partials with Burgers vector \vec{b}_2 [145].



Figure 2.25 Stacking faults of 316LN SS after 8% strain deformation from disk bending at 150 °C [232].

Fault Energy

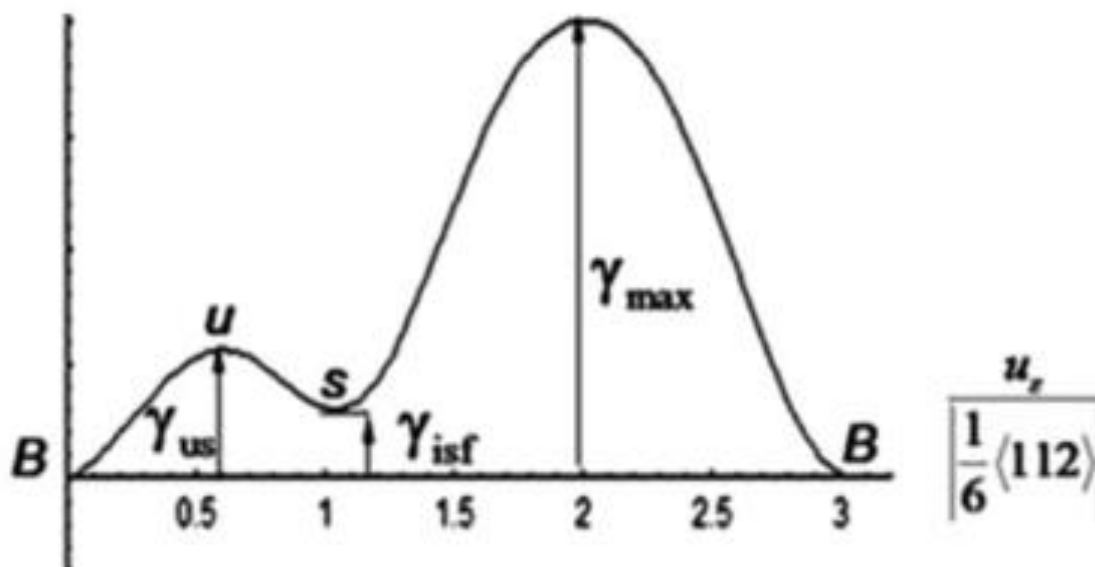


Figure 2.26 Fault energy evolution in terms of the distance of partial $\langle 112 \rangle$ direction [166].

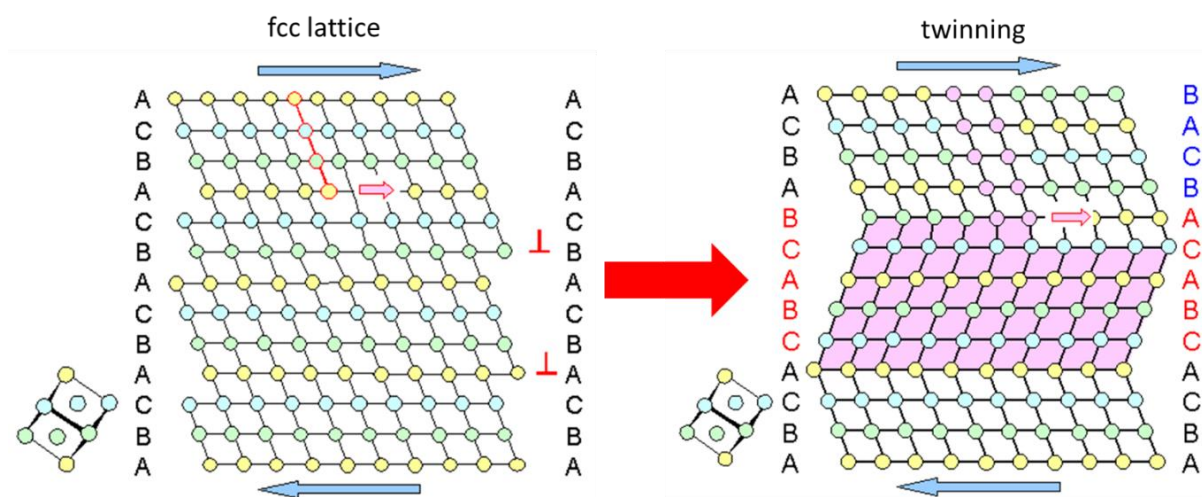


Figure 2.27 Schematic diagram of twinning in an fcc lattice [233].

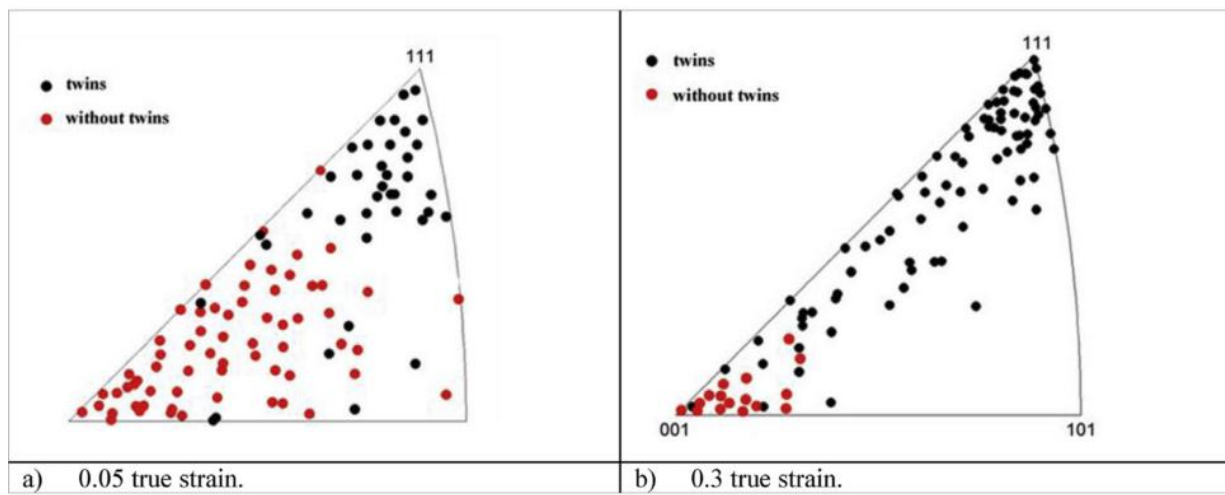


Figure 2.28 Effect of grain orientation on twinning of Fe-Mn: (a) 0.05 and (b) 0.3 true strain [176].

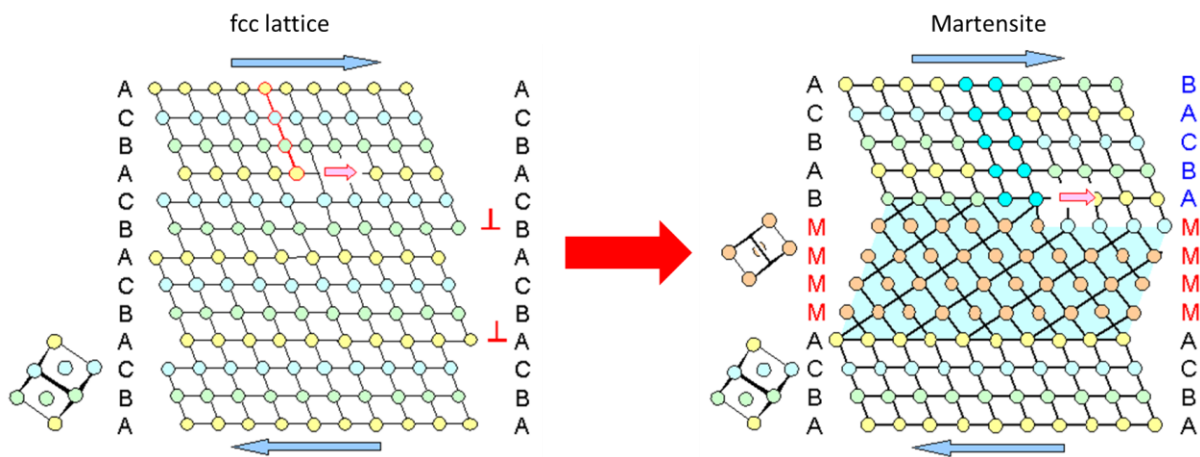


Figure 2.29 Schematic diagram of martensitic transformation in an fcc lattice [233].

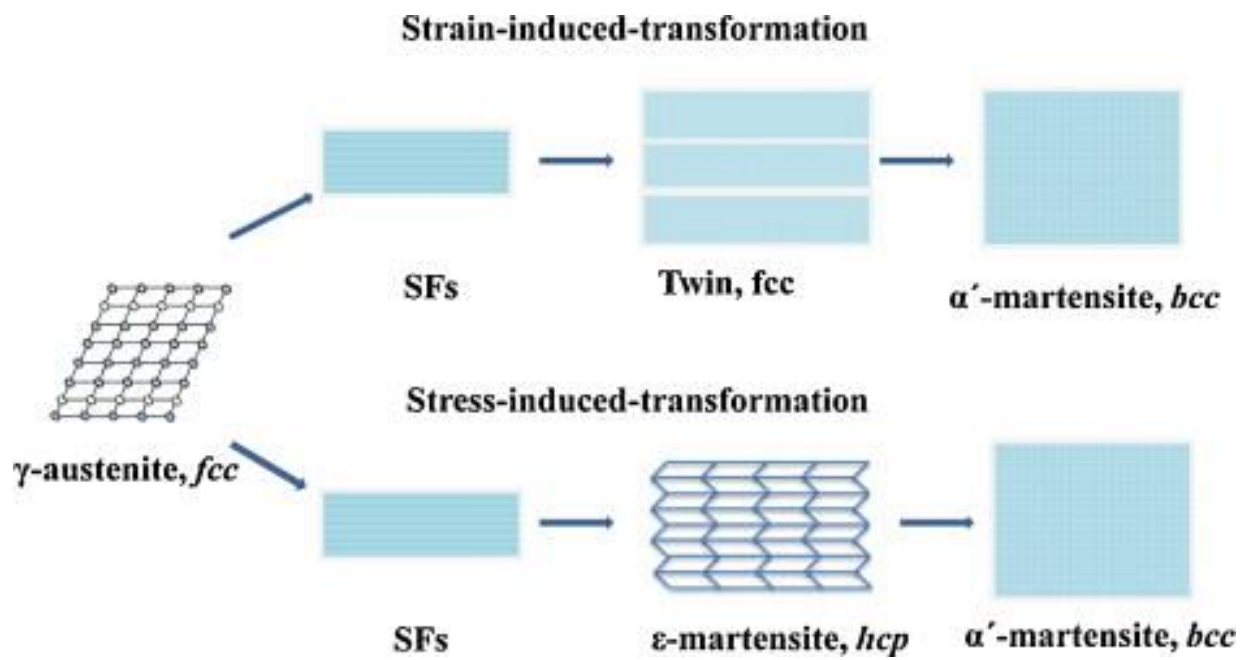


Figure 2.30 Schematic diagram of martensitic transformation in 304 SS [192].

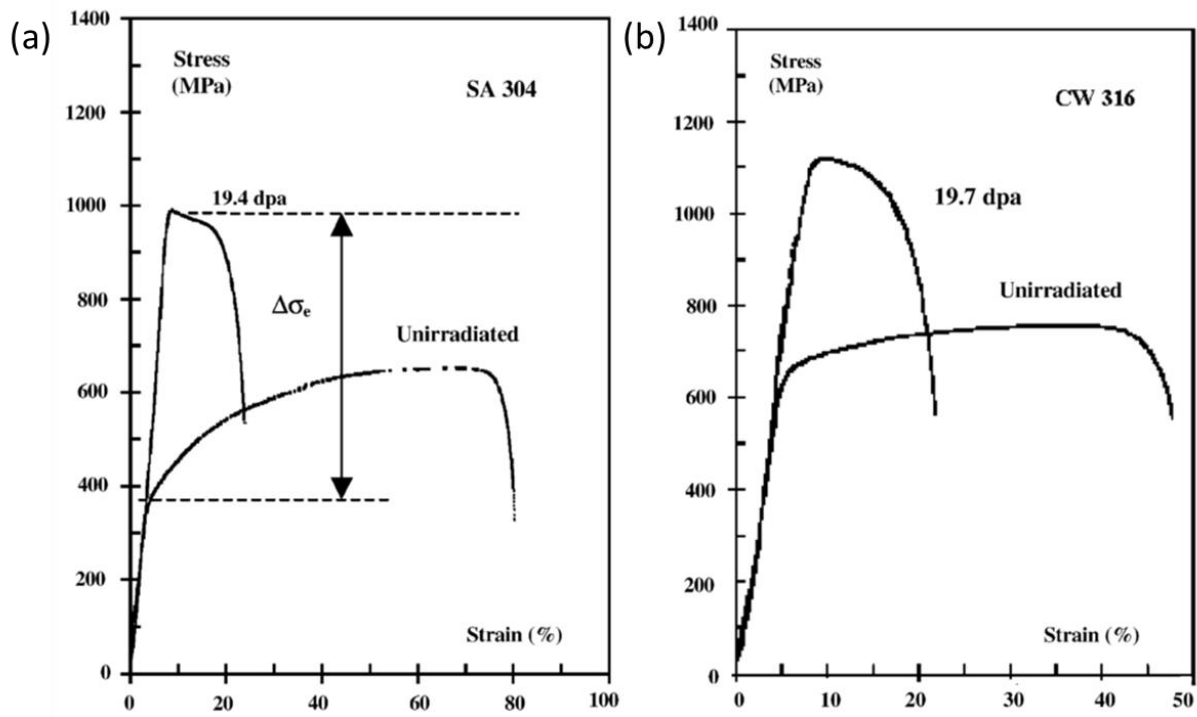


Figure 2.32 Engineering stress versus strain curves of unirradiated and irradiated steels (a) solution annealed (SA) 304 at 19.4 dpa and (b) cold worked (CW) 316 at 19.7 dpa [100].

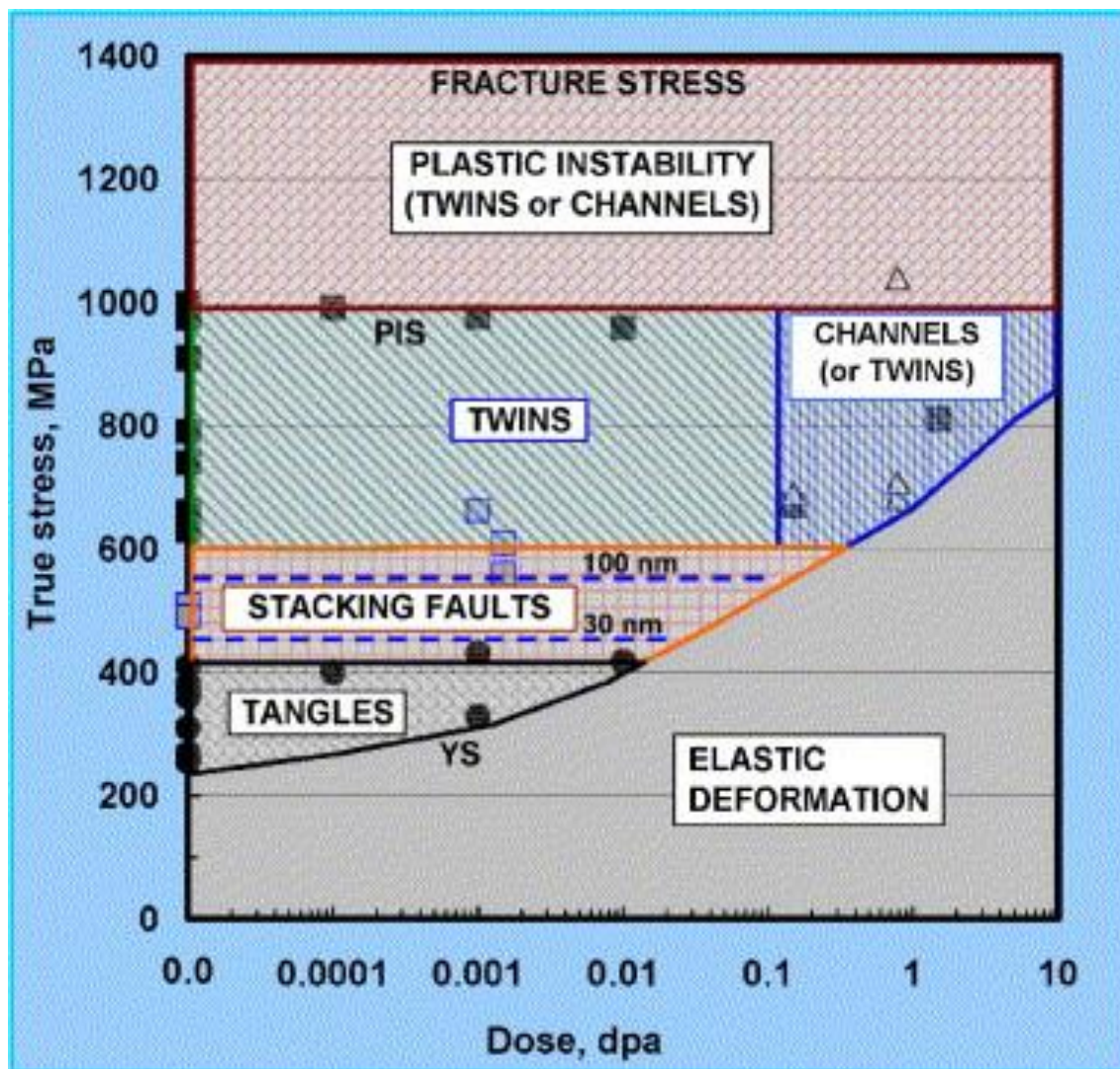


Figure 2.33 Deformation mode map of 316 SSs in terms of true stress and dose [222] domain.

3. OBJECTIVE

The objective of this dissertation is to determine the influence of irradiation and laser-welding on the deformation mechanisms of neutron irradiated austenitic stainless steels. Three steps are implemented to achieve this objective: (1) characterization of the microstructure prior/after laser welding; (2) induce plastic deformation in the laser weldment, then characterize the deformed microstructure; and (3) correlate the deformation mechanisms to the pre/post-deformed microstructure. This thesis will evaluate the overall mechanical integrity of the laser welded irradiated austenitic stainless steels, and it will demonstrate that deformation mechanisms are influenced by both the irradiation-induced defects and the effect of laser weld-induced microstructural evolution over a range of dose and He concentration levels.

Irradiated AISI 304L stainless steels have been selected over a range of doses ~ 1 -28 dpa, He concentration 0.2-8 appm and swelling $\sim 0.5\%$ -2.5%. As we discussed in Chapter 2, previous studies on similar materials have been conducted. Direct measurements of size and density distribution of irradiation-induced defects such as loops, cavities and precipitates will be performed. The results will be directly compared to the existing literature. Unirradiated archive AISI 304L SS is also used as a control for the dependence of irradiation. We will then make laser welds on the irradiated steels. The microstructure of the weld HAZ will be compared to the base metal. The microstructure prior to mechanical deformation will be the key to the response of the subsequent micromechanical tests.

Room-temperature micromechanical testing will be performed on the samples using *ex-situ* and *in-situ* methods. Nanoindentation will measure the orientation-dependent mechanical properties of the laser weldment. SEM *in-situ* microcompression pillar testing enables us to visualize the microstructural evolution during the compression. These two techniques will be employed for the direct comparison between the base metal and the HAZ. The archive material before neutron irradiation is also tested as a control. Relevant data such as modulus, hardness and stress-strain curves will be provided for the evaluation of the mechanical integrity of the laser weldment. The microstructure-property relationship will be evaluated between the base metal and the HAZ. The size of the HAZ will then be estimated compared with the grain structure obtained from EBSD

orientation imaging microscopy (OIM) mapping. The irradiation-induced defects will be considered for calculation of the irradiation hardening mechanism. The laser weld-induced annealing will also be compared for the post-weld softening mechanism. The overall mechanical properties of the laser weldment at different combinations of dose and He concentration levels will be revealed.

After the mechanical deformation, the post-deformed microstructure will be carefully examined by TEM. This process includes FIB preparation of TEM lamellae from the indentation plastic zone and the compressed micropillars. A detailed description of the deformation mechanisms such as dislocation slip, twinning, and martensitic transformation in irradiated austenitic stainless steels will be provided. The deformation modes between the base metal and the HAZ will be revealed. Based on the observation of the deformation process, a deformation map will be established to predict the critical twinning stress for fcc metals and alloys. In addition, the pre-deformed microstructure involving the irradiation-induced cavities will be emphasized as an important role of changing the localized deformation of the irradiated austenitic stainless steels. Finally, a phenomenological model will also be covered to develop the criteria of the incipient twinning versus martensitic transformation.

The unprecedented results from this dissertation will provide new insights into irradiation-tailored deformation by modulating the irradiation conditions to induce deformation mechanisms that are usually only achievable at larger strain or lower temperature conditions. The predictive criteria for the deformation in fcc metals and alloys establishes a crucial scientific foundation for candidate materials for advanced nuclear reactors and other applications, research, and development at extreme environments.

4. EXPERIMENTAL

4.1 Hex-block materials

The materials we have selected are rectangular samples of highly activated AISI 304L stainless steel (SS). The samples, dimensions of approximately 25.4 mm thickness \times 10.2 mm length per side, had been cut from sections previously obtained from two hexagonal-shaped neutron reflector blocks. These so-called “hex blocks” are U.S. Department of Energy owned material and were irradiated in the Experimental Breed Reactor II (EBR-II), a sodium cooled fast reactor, from 1982 until 1995 [51,54,61] (see Fig. 4.1). The chemical composition of an unirradiated archive hex-block AISI 304L SS was found to be Fe-19.26Cr-8.81Ni-1.57Mn-0.43Si-0.056C-0.03S-0.027P in wt%, determined by energy-dispersive X-ray spectroscopy (EDX) and performed by a field-emission gun equipped with a Zeiss SEM operating at 20 kV, and by an inductively coupled plasma (ICP) analysis [54,61]. Hex blocks were cold worked prior to neutron irradiation. The surfaces of these hex blocks have \sim 10% cold work, while the internals have \sim 5% cold work [61]. Due to the rarity of these archival materials, they epitomize the valuable non-irradiation reference state.

Five hex blocks were stacked vertically in the reflector region of EBR-II, with blocks 1-5 stacked in numerical order from bottom to top of the core (Figure 4.1(a)). Block 3 was vertically nearest the core, and thus received the highest irradiation fluence and temperature. Block 5 was vertically the furthest from the core, and thus received the lowest irradiation fluence and temperature. The dose range and dose rate range of blocks 3 and 5 are \sim 0.4-33 dpa and \sim 3.6×10^{-7} dpa/s. Through numerous other studies over the years, the hex blocks have been sliced into hexagonal “coins”, labeled x A, x B, x C, and so on, where x represents the block number (Figure 4.1(a)). Coins have also been sliced into three sections, e.g. 5D1, 5D2, and 5D3 (Figure 4.1(d)), in which the section $xy1$ is a rectangular prism, and sections $xy2$ and $xy3$ are so-called “triangles,” although they are technically pentagon-shaped segments. A library of works [51,54,241,242,61,234–240] can be referenced by the readers to learn more about the details of the hex blocks as well as their sectioning methods.

To prepare specimens for welding specifically for this project, the sections xy_2 and xy_3 are each further sliced into a plate and a true triangle (Figure 4.1(h-j)). Figure 4.2 shows the schematic diagram of the process of obtaining the weld coupons from the hex blocks. A rectangular section from a hex coin triangle was sliced off with approximate dimensions of 2.5 cm \times 5 cm \times 0.6 cm (1 inch \times 2 inch \times 0.25 inch). The two large opposing faces on each rectangular coupon were then milled in-cell to obtain flat and parallel surfaces and to provide surfaces suitable for welding. Milling of the coupon surfaces and the final appearance of the surfaces after milling is shown in the photographs in Fig. 4.3.

The plates are used for welding, which was performed in the Westinghouse High Level Hot Cells. The three plate samples selected for welding are from hex block sections 5D2, 3A2, and 3E3. These samples have nominal damage doses of approximately 1, 23, and 28 dpa with corresponding helium contents of approximately 0.2, 3 and 8 appm helium, respectively (see Table 4.1). The He concentration is determined by an isotope dilution gas mass spectroscopy method, which is similar to the neutron activation [49]. These hex block materials had been studied previously by various teams of researchers, including detailed microstructural characterization of the radiation-induced defect structures as a function of damage dose and irradiation temperature [54,61,64,71,243–247].

4.2 Laser welding and metallographic preparation

Bead-on-plate laser welds were made on the 3 rectangular coupons using a TruPulse 556 Nd-YAG laser welding system housed in the Westinghouse High Level Hot Cells. The BEO D70 laser welding head is outfitted with a video feed, air knife, and multi-axial positioning system. The system was operated remotely in a hot cell such that welds can be made on highly radioactive materials.

Figure 4.4 provides images of the hot cell laser welding system. Multiple wire fed welds were made on each of the three rectangular coupons to support the contingency plans for extra welded specimens. The welds made to support this dissertation discussed herein consisted of single-pass wire fed welds.

Most of the welds utilized for this thesis were prepared using a consistent set of weld parameters referred to as Weld Parameter Set 1 (WPS1). [Table 4.2](#) summarizes key weld parameters for WPS1. It should be noted that the 308L SS weld wire composition is Fe-19.88Cr-9.79Ni-2.13Mn-0.52Si-0.021C-0.007S-0.023P in wt%. [Figure 4.5](#) provides a Keyence digital microscope image showing the typical appearance of a pulsed laser weld where the image shown is for the single-pass weld made on coupon 5D2, 3A2 and 3E3.

As depicted by the sketches in [Fig. 4.6](#), preparation of small cross-sectional weld samples suitable for electron microscopy was a three-step process. The first step (henceforth referred to as “Step 1”) was to cross section the welds of interest into thin plates with approximate dimensions of 6.5 mm × 6.5 mm × 1 mm thick. The second step (“Step 2”) was to further reduce each thin plate to remove excess unnecessary base material to obtain a sample which contained only weld metal and a very limited amount of surrounding base metal. This reduced sample geometry was approximately 3 mm × 2 mm × 1 mm. The third step (“Step 3”) was to further reduce the thickness of each sample by grinding and polishing each sample to a final thickness of approximately 250 to 500 μm.

Steps 1 and 2 are shown in [Figs. 4.7-4.8](#). [Figure 4.7](#) provides images showing the Step 1 process of precision cutting thin plates from welds of interest. [Figure 4.8](#) provides images showing the Step 2 process of further reducing the thin plates to produce samples which contain only the weld and a very limited amount of surrounding base metal. [Figure 4.9](#) shows the general appearance of the weld samples after Step 2.

As mentioned in the previous section, each small weld sample slice was ground and polished to a final thickness of approximately 250–500 μm (i.e., Step 3). Each of the small, thin reduced geometry plates were ground and polished outside of the cell. After polishing, each sample was lightly swab etched. To grind and polish the extremely small radioactive samples, Westinghouse developed a method for temporarily mounting each small sample in Crystalbond 509 mounting adhesive. After the polishing was completed, the small sample was removed from the Crystalbond mount and etched. The method for temporary Crystalbond mounting, grinding, polishing, and removal from the Crystalbond mount is described as follows:

- Put a very thin layer of vacuum grease onto a Micarta surface. Place the weld sample into the vacuum grease (with the surface to be polished face down). Push flat; the sample will stick onto the grease. Place a plastic mold ring around the specimen and push it down into the grease.
- Heat a hot plate to 255°F and use a thermocouple to monitor the temperature. In a Pyrex container that has a pour spout, place a piece of the Crystalbond stick that is approximately the same height as the mold ring. Allow approximately 10 minutes for the Crystalbond to melt and become pourable.
- Using tongs, remove the Pyrex container from the hot plate and pour directly into the mold ring with the weld sample placed inside the ring (with the surface to be polished face down). Fill mold. After pouring, start immediately cooling the specimen with air. When the Crystalbond cools completely (approximately 15 minutes), it will harden and be ready for grinding and polishing.
- Place the mounted samples into a sample holder ring if appropriate. On a grinding wheel with a constant water feed, and using 220 grit silicon carbide paper, chamfer around the edge of the mold on the face down edges. Remove and discard the 220 grit paper. Using 1200 grit silicon carbide paper on the wheel, constant water feed, and a force of 15 newtons, grind the samples for 15 seconds.
- Rinse with water and/or clean with mild detergent and a cotton ball. Transport the samples to the polisher. Utilize the following polishing method:
 - a. Force 25 N.
 - b. MD Allegro-(300 mm) for 90 seconds with 9 μm DT spray applied with DT blue, continuous drip.
 - c. MD Dur-(300 mm) for 90 seconds with 3 μm DT spray applied with DT blue, continuous drip.
 - d. MD Dac-(300 mm) for 90 seconds with 1 μm DT spray applied with DT blue, continuous drip.
 - e. MD Nap-(300 mm) for 180 seconds with pour of OPS then to continuous drip and water flood at end.

- f. Between each step, mounts are cleaned with water and/or mild detergent and a cotton ball.
 - g. Dry with air.
- After the mounts are polished, fill a concave plate with acetone. Place the mount (polished face down) into the acetone to dissolve the Crystalbond and free the welded sample. After the sample is free, clean the sample (to remove any remaining Crystalbond) by repeatedly placing it into acetone and spraying with canned air to dry. Repeat until clean.

Note that as described in the above method, only one side of each of the small weld samples was ground and polished. Once the weld sample was removed from the temporary Crystalbond mount and thoroughly cleaned, the polished surface was etched using a 5 to 15 second Marble's swab etch.

Figure 4.10 provides images of the small thin weld samples obtained from welds prepared using WPS1 weld parameters on coupons 5D2, 3A2 and 3E3, respectively. From the micrographs, we can clearly see the impact of the He on the completed surface of the cross-sectional weldments. At lower He concentration (< 1 appm), the welded surface is relatively clean and no obvious cracking has been observed. At intermediate He concentration (~ 3 appm), laser weld-induced pores have occurred (marked by red arrows) and micro cracks have appeared. At a higher He concentration (~ 8 appm), we still see that the weld-induced pores and the cracks have grown (enveloped by red ovals). These are indications of the He impact on the quality of the welds.

4.3 Electron Microscopy

4.3.1 Grain orientation

We utilized EBSD to obtain the grain structure of the laser weldment. The EBSD detector was used inside a FEI (now Thermo Fisher Scientific) 3D FEG dual-beam scanning SEM/FIB for the OIM mapping. The voltage of the SEM was set at 30 kV. The current of the electron beam was 2 nA. The dwell time of the EBSD scan was 100 μ s. The step size was ~ 0.1 - 0.3 μ m/pixel. The neighboring confidence index (CI) was 0.05. The neighboring grain tolerance angle was $\sim 3^\circ$. The EBSD scanning was conducted across the laser weldment including the base metal, the HAZ, and

the weld region. The OIMDC 7.1.0 version software was used for the collection of the EBSD mapping data. The obtained OIM maps were then referred to the mechanical testing using grain-orientation specific fabrication of micropillars and location selection of nanoindentation experiments.

4.3.2 FIB lift outs

We utilized two types of FIB microscopes for the lift-out for transmission electron microscopy (TEM) lamellae preparation. A Tescan LYRA-3 GMU FIB/SEM (dual beam FIB with an Orsay Physics Canion FIB column) at Westinghouse and a FEI Quanta 3D FEG dual beam (SEM/FIB) at the Microscopy and Characterization Suite (MaCS), Center for Advanced Energy Studies (CAES) were used for FIB lift-outs from the laser welds on the irradiation AISI 304L SS. Six (6) FIB lift outs were obtained from locations identified as an example shown in [Fig. 4.11](#). In particular, the following specific lift-outs were prepared:

- 2 from the base metal.
- 2 from the HAZ.
- 2 from the weld metal + HAZ.

A standard FIB lift-out method [248] was used. Firstly, the FIB carbon (C) deposition of $\sim 1 \mu\text{m}$ was used to define regions of interest and to protect the surface from spurious FIB milling. Another $\sim 1 \mu\text{m}$ -thick platinum (Pt) was also deposited as a following protection layer. Specimens were removed with an Omniprobe via *in-situ* lift out and secured to the “V” in an Omniprobe grid on both sides using a $1 \mu\text{m}$ thick C/Pt deposition at the bottom ends of each specimen, i.e., 2 carbon pads deposited per specimen on both sides of the grid, therefore 4 carbon deposited pads per specimen. The “usable” portion of each specimen (i.e., within the C deposited pads) was approximately $8\text{-}15 \mu\text{m}$ length \times $8\text{-}12 \mu\text{m}$ depth. [Figure 4.12](#) contains a series of images documenting the steps of the weld, the HAZ, and the weld + HAZ FIB lift outs and grid positions. In lieu of thinning the thick lift-out lamellae, a final cleaning step was adopted at 2 kV running at 1-2 minutes at each side to remove the FIB-induced damage of the sample. The final thickness of a lift-out TEM lamellae is $\sim 30\text{-}150 \text{ nm}$. [Figure 4.13](#) provides an image documenting the FIB lift-out positions for the weld specimen from 5D2 hex block.

4.3.3 Microstructure characterization

We utilized two types of transmission electron microscopes to characterize the microstructural features such as dislocations, loops, precipitates, twins, and martensite laths. The original microstructural characterization and post-deformed microstructure under the plastic zone of the indent was performed by a FEI Tecnai TF30-FEG STWIN scanning TEM (STEM) at CAES MaCS. This microscope has a point resolution of 0.2 nm and a line resolution of 0.102 nm. The STEM has a high angle annular dark-field detector (HAADF) with a resolution of 0.19 nm. The camera length varies between 80 mm and 4500 mm. Analytical analysis of the chemical composition of the grain boundaries, precipitates and matrix were performed by the energy dispersive X-ray spectroscopy (EDS) in the STEM mode. The EDS detector has a solid angle of 0.13 sr. The dwell time for each point of the drift-corrected line scan was ~ 10 s. The thickness of a TEM lamellae was measured by electron energy loss spectroscopy (EELS). The mean free path of the EELS was calculated at ~ 90 nm. The second microscope, JEOL 2100 TEM, at Electron Microscopy Laboratory (EML), was only used to characterize the specimens after microcompression. As we have already discussed in Chapter 2, both bright-field STEM technique [58] and rel-rod method [57] were applied for imaging dislocation loops. The rel-rod method specifically targets faulted interstitial Frank loops. Dislocations in the archive sample were imaged under a two-beam $\vec{g} \rightarrow 3\vec{g}$ condition. The Burgers vector was determined by the invisibility criteria. Precipitates were characterized with the dark-field TEM. STEM HAADF imaging mode was used for characterizing irradiation-induced cavities [234]. The quantification of each type of defect N_i was determined as follows.

$$N_i = \frac{n_i}{A_i t_m} \quad (4.1)$$

where n_i is the number of defect type (loops, cavities, and precipitates) in a selected area. A_i is the area of a micrograph. t_m is the measured thickness of the specimen (dislocation line does not count for the thickness). Multiple micrographs were included for statistical analysis of the average and standard deviation of each defect feature.

4.4 Mechanical testing

Figure 4.14 is a flow chart showing the sequence of conducting mechanical testing and the corresponding post-analysis of the mechanically deformed microstructure of the base metal versus the HAZ of the laser weldment on the neutron irradiated AISI 304L SS. We use two different methods as nanoindentation and microcompression experiments based on the OIM maps of the selection of grains of interest, i.e., {100}, {101} and {111}. The location of the HAZ was determined also based on the OIM mapping [22]. After we induced the plastic deformation into the sample, we follow the steps in section 4.3 for the TEM lamellae preparation to fabricate FIB lift-outs from the post-indented plastic zones and post-compressed micropillars. TEM analyses were then performed on these TEM specimens to identify the post-deformed microstructure.

4.4.1 Ex-situ Nanoindentation

Nanoindentation was conducted to measure the strength of the base metal and the HAZ. A Bruker-Hysitron TI-950 Triboindenter with a Berkovich tip (250 nm tip radius) at MaCs, CAES was used at room temperature. At least an 8×8 indentation matrix was performed on both base and HAZ of the laser weldments on each condition with a separation distance of 25 μm . An unirradiated specimen was also evaluated as a control. The locations of the indents are compared with the OIM maps after nanoindentation to determine the mechanical properties along specific grain orientations. All measured indents were located at least 10 μm away from grain boundaries to minimize the grain boundary effect [249]. Indentations were carried out in a load-controlled mode with a constant loading rate of ~ 5 mN/s, a maximum indentation depth of ~ 1500 nm, and a holding time at the peak load of 5 s. Shallower indentation at depths of ~ 200 nm (~ 0.25 mN/s) and 400 nm (~ 0.5 mN/s) were also conducted. The Oliver-Pharr method [95] was used for calculating the hardness and elastic modulus with the assistance of the TriboScan MP 9.3.13.0 software.

The Herzian elastic solution is given by [250–253]:

$$P = \frac{4}{3} E_r \sqrt{Rh^3} \quad (4.2)$$

where P is the load, R is the tip radius of the nanoindenter, h is the corresponding indentation depth, and E_r is the reduced modulus as

$$\frac{1}{E_r} = \frac{1-\nu_i^2}{E_i^2} + \frac{1-\nu_s^2}{E_s^2} \quad (4.3)$$

where ν_i and ν_s are the Poisson's ratio, and E_i and E_s are the Young's modulus of the indenter tip ($E_i = 1141$ GPa and $\nu_i = 0.07$ [22]) and sample, respectively. For a specific (hkl) plane, the anisotropic modulus can be calculated as [254,255]:

$$E_{hkl}^* = [m + n(A - A_0)^B] \frac{E_s}{1-\nu_s^2} \quad (4.4)$$

where m , n , A_0 , and B are functions of Poisson's ratio of the (001) plane, and A is the shear anisotropy factor. These values can be found in [250,255–257].

The radius of the plastic zone is usually described by the $R_{pz} = f \cdot R_c$, where R_c is the radius of the nanoindenter and f is the scaling factor which can be estimated using a well-known equation [258] for the normalized size of the plastic zone:

$$f = \left(\frac{2E}{3\sigma_y} \right)^{1/3} \quad (4.5)$$

For the 5 mN/s loading rate, the calculated scaling factor is 5.08 and 5.12 for the unirradiated and irradiated sample, respectively. For the 0.5 mN/s and 0.25 mN/s loading rates, the normalized scaling factors are 4.84 and 4.93. It should be noted that the expansion of the plastic zone is based on the spherical indenter geometry.

The nanoindentation experiment is modeled using an axisymmetric 2-D finite element mesh built in ABAQUS/CAE 6.14-1. The indentation area is $1 \times 1 \mu\text{m}$ with the finest mesh spacing nearest the indent and gradually larger further away from the indent. A non-penetrating hard contact is assumed normal to the indent. Measured yield strength and modulus are adopted as input parameters. Load is applied to the indent in 0.5 mN increments over 40 s for each step. More details in the finite element modeling can be found in [259].

4.4.2 *In-situ* micropillar compression

Single grains ($\{111\}$, $\{101\}$, $\{221\}$, $\{331\}$ etc.) were selected for micropillar testing in both the base metal and the HAZ; while several grain orientations have been tested, the $\{101\}$ grain orientation was systematically studied in both the base metal and the HAZ and will thus be the central focus of this thesis. FIB was employed to mill 2-4 pillars of dimensions $4 \times 4 \times 8 \mu\text{m}$ per grain orientation, and a 0.1 nA beam at 30kV was used for final cleaning to minimize surface ion damage [260]. Each pillar was compressed with a flat punch in the Bruker Hysitron PI-88 depth-sensing *in-situ* SEM mechanical testing holder (see Fig. 4.15), operating at ambient temperature. The compression was carried out in a displacement-controlled mode with a strain rate of $\sim 10^{-3} \text{ s}^{-1}$. The maximum strain is $\sim 20\%$. Engineering stress-strain curves were converted based on the original pillar dimensions and the load-displacement data recorded by the PI-88. Yield strength was determined using the 0.2% plastic strain offset. The modulus was calculated as a secant modulus. The frame grabber is used to capture the videos that the SEM charge coupled device (CCD) screen outputs. All videos were captured at 15 frames per second and each video file has approximate 118583 kbps total bitrate.

Table 4.1 Hex coin triangles selected for removal of rectangular coupon for welding.

Coin/Triangle	He (appm)	Dose (dpa)	Temperature (°C)
5D2	0.2	1	415
3A2	3	23	430
3E3	8	28	415

Table 4.2 Summary of weld parameters used to prepare welds.

Weld Parameter Set	Weld Parameter Set 1 (WPS1)
Approximate Weld Length	1.5 inches
Number of Pulses	300
Lens-to-Work Distance	200 mm
Travel Speed	2.5 inch/min
Weld Wire	Wire supplied by EPRI
Wire Alloy	Turboalloy 308L
Wire Specification	AWS A5.9-06 Class ER308L
Wire PO	EP501-0000039717
Wire SN	742049
Wire Heat	510676
Wire Lot	433550
Wire Diameter, in	0.02
Wire Feed Speed	17 inches/min
Power	1400 W
Pulse Duration	38.00 ms
Frequency	8.00 Hz
Energy	53.20 J
Average Power	425.60 W
Utilization	99.30%
Bead Overlap	N/A

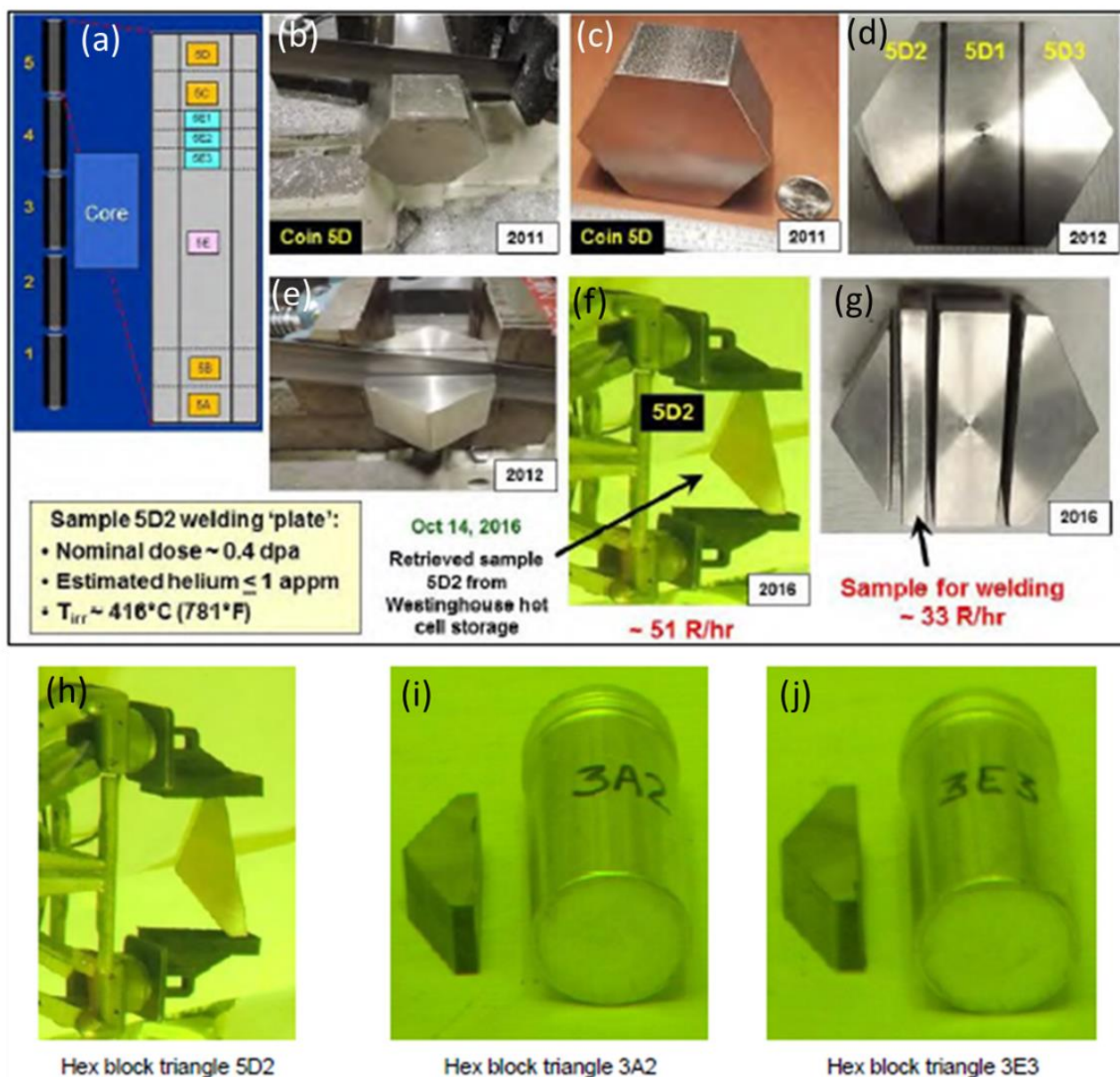


Figure 4.1 Rectangular coupons were sectioned from 3 hex-block “triangles” to obtain 3 welding coupons. (a-g) Example showing selection of left triangle 5D2 (previously obtained from Coin 5D in 2012 of 1 dpa and 0.2 appm He) and sectioning of rectangular coupon from this triangle to obtain 1 of the 3 needed welding coupons. (h-j) Three hex-block triangles selected for welding studies.

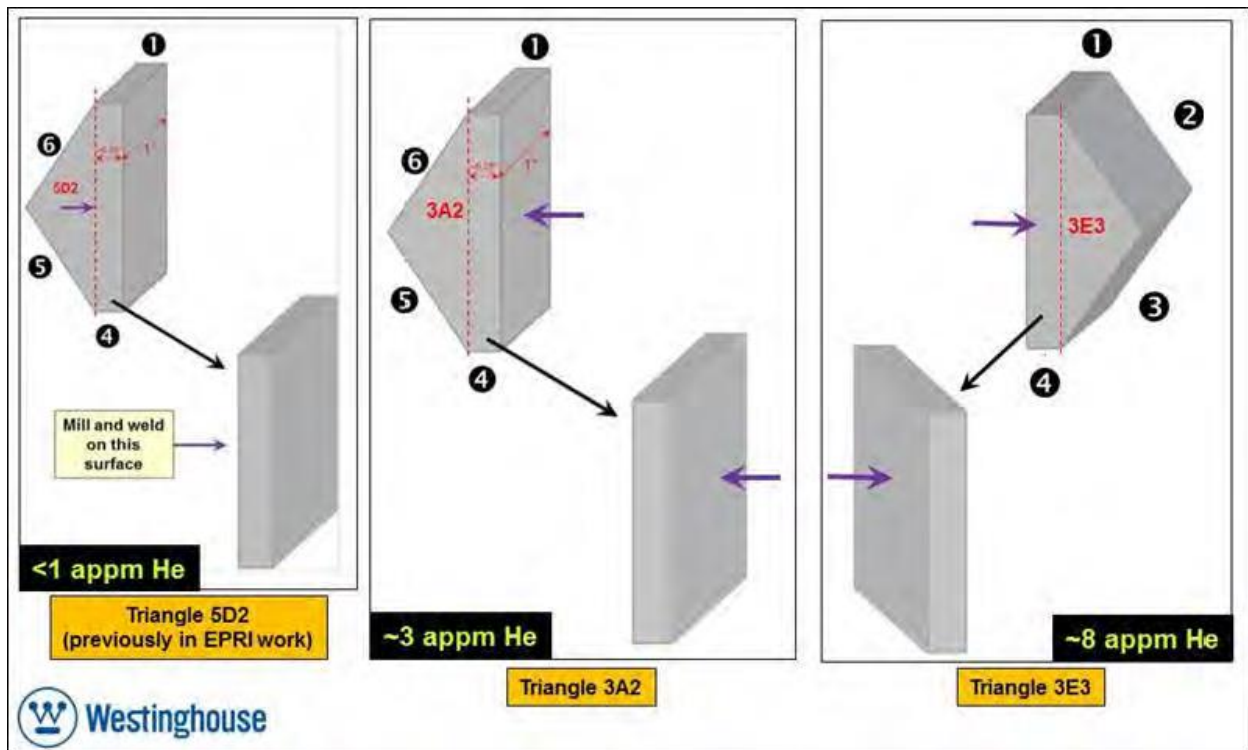


Figure 4.2 Sketches showing how rectangular coupon was removed from 3 different hex-block triangle samples to obtain 3 welding coupons.

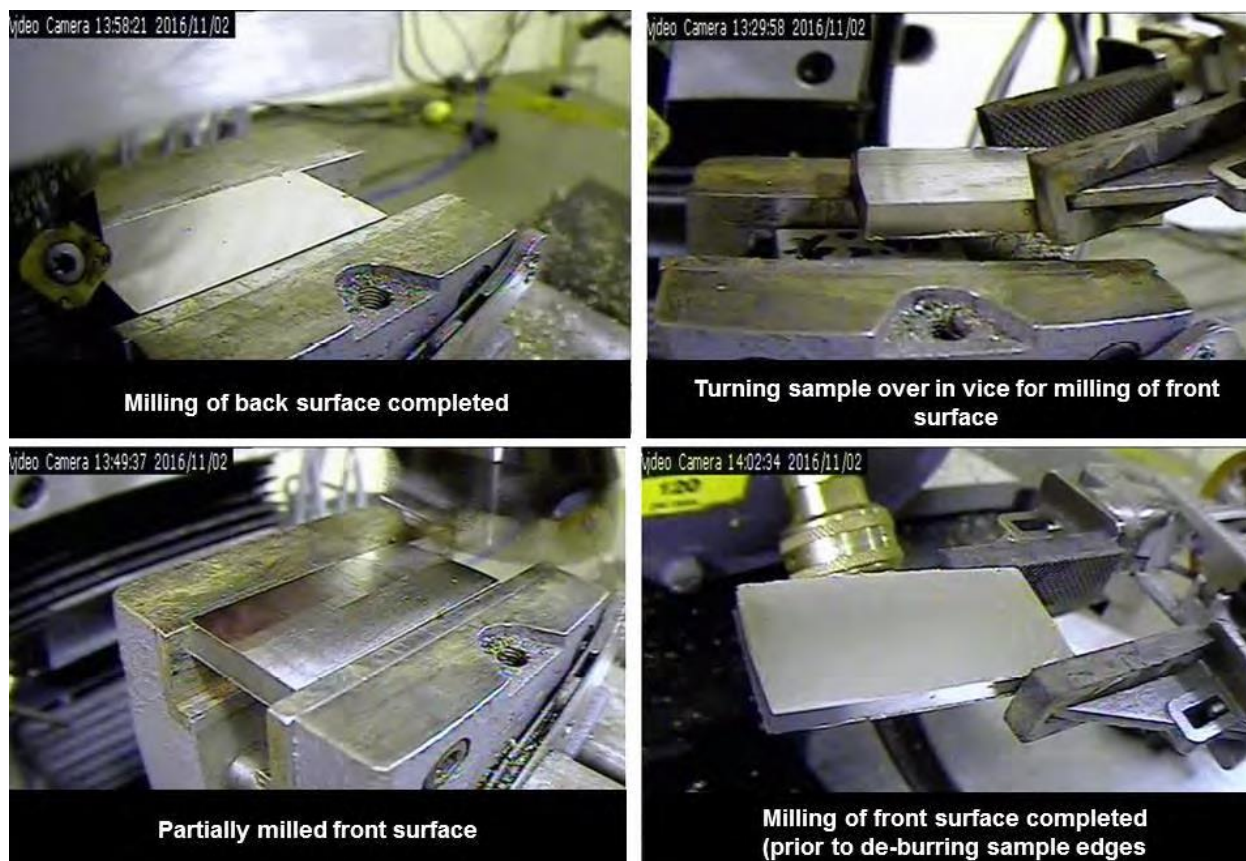


Figure 4.3 Example of in-cell process used to section rectangular coupon from hex-block triangle: photographs from inside the Westinghouse High Level Hot Cell showing milling of the surfaces on the rectangular plate removed from hex-block triangle 5D2 in preparation for subsequent welding.

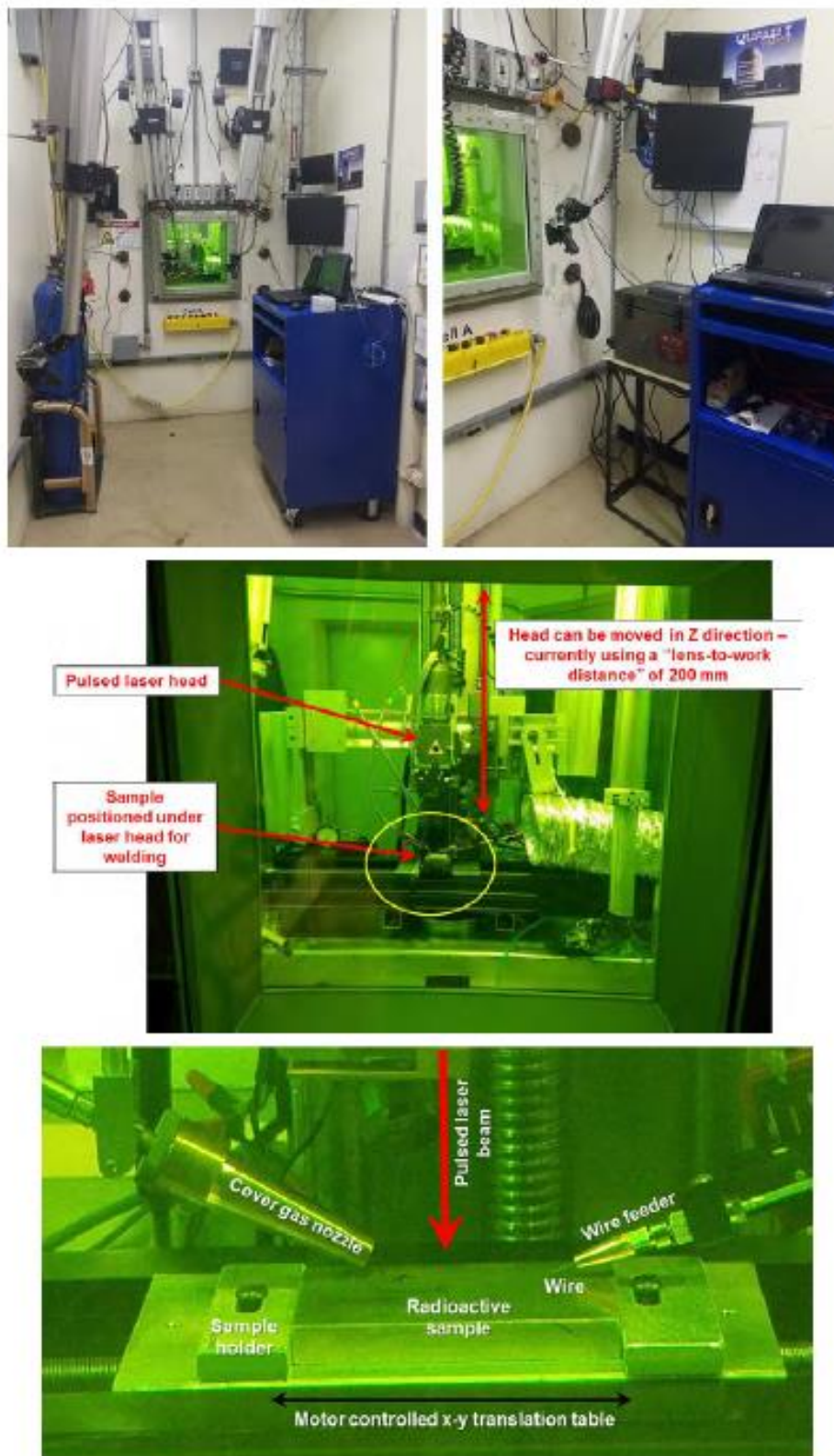


Figure 4.4 Hot-cell pulsed laser welding equipment set-up.

**Weld Coupon
5D2**



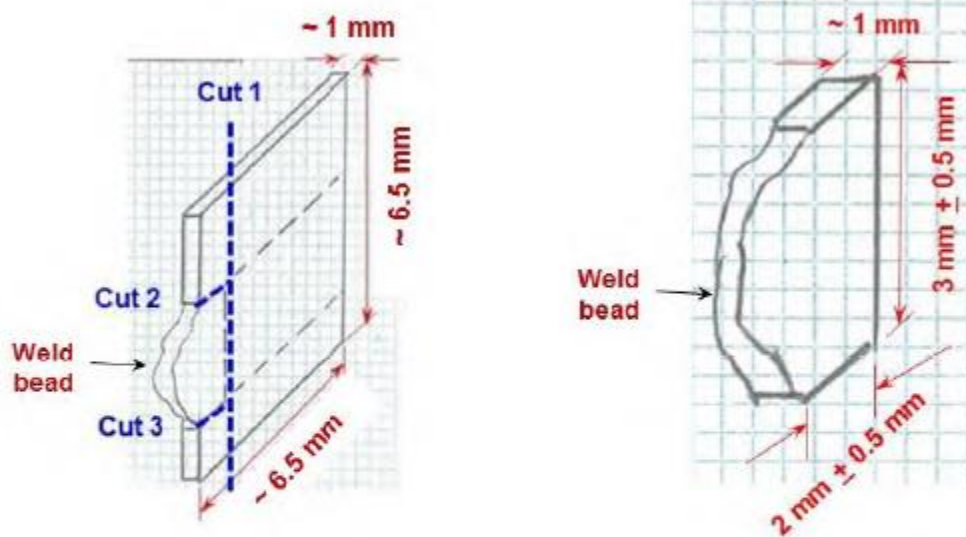
**Weld Coupon
3A2**



**Weld Coupon
3E3**



Figure 4.5 Keyence digital microscope images showing the typical appearance of the WPS1 pulsed laser weld.



STEP 1: Cross section welds to obtain thin plates of approximately 0.25 inch x 0.25 inch x 0.04 inch thick.

STEP 2: Further reduce the thin plate (as shown by Cut 1, Cut 2 and Cut 3) to remove excess unnecessary base material.

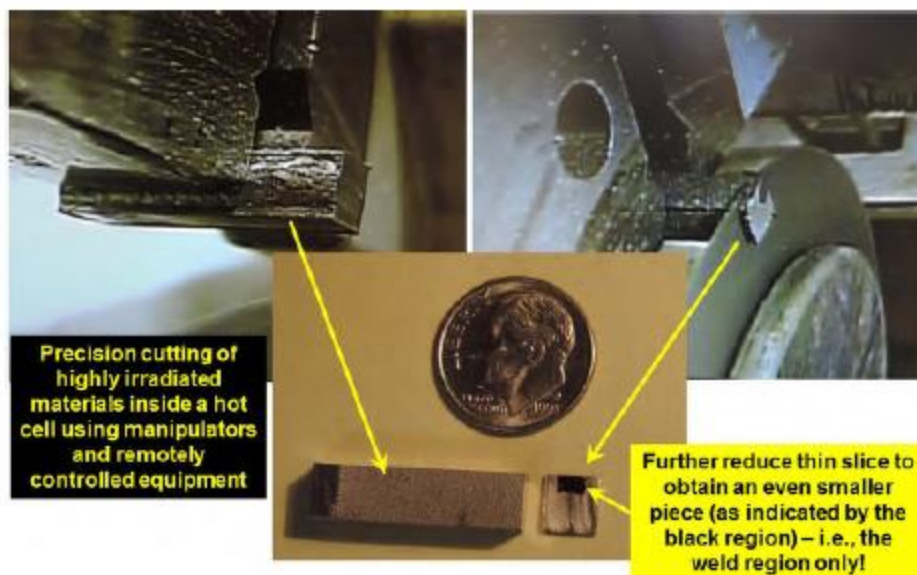
Reduced sample geometry: Sketch showing the further reduced piece which includes the weld and a very limited amount of surrounding base material. The reduced sample geometry was approximately 3 mm x 2 mm x 1 mm thick.

STEP 3: Grind and polish this sample to an optimum thickness of approximately 250 – 500 μm .

Figure 4.6 Sketch of cross-sectional weld sample geometries.

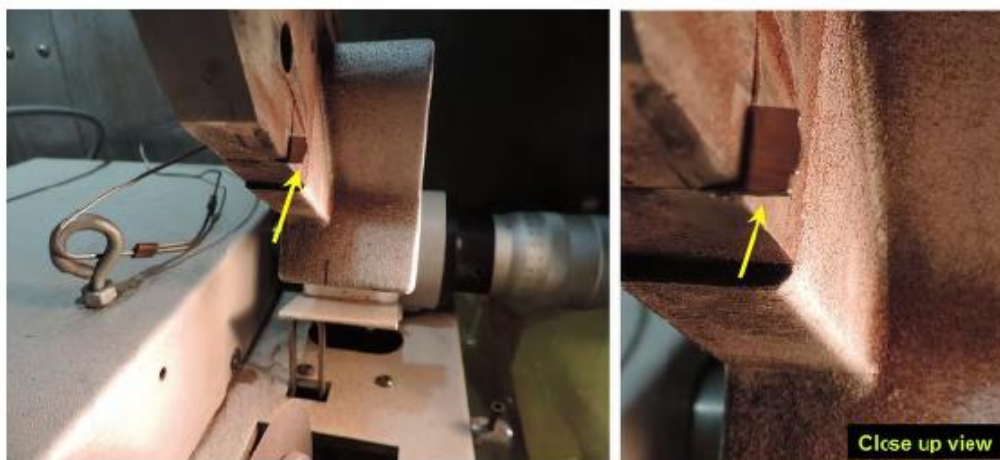


Thin cross sectional slice being cut off weld using ultra thin specialty blade - the thin slice (marked with a yellow arrow) is nearly complete.



Dime shown in photograph to give a sense of scale. The removed thin slice must be further reduced to a smaller size which is represented by the black colored area shown on the slice.

Figure 4.7 Photographs illustrating Step 1: cutting of thin cross-sectional slices through welds of interest.



Thin slice obtained from irradiated weld sample 5D2 mounted in slow speed programmable saw with ultra thin wafering blade in preparation for cutting out the weld from the thin slice.



Cutting in progress of thin slice obtained from irradiated weld sample 5D2 – cutting to remove weld portion of the thin slice.

Figure 4.8 Photographs of Step 2: further reduction of thin plate, include only the weld and a very limited amount of surrounding base material.

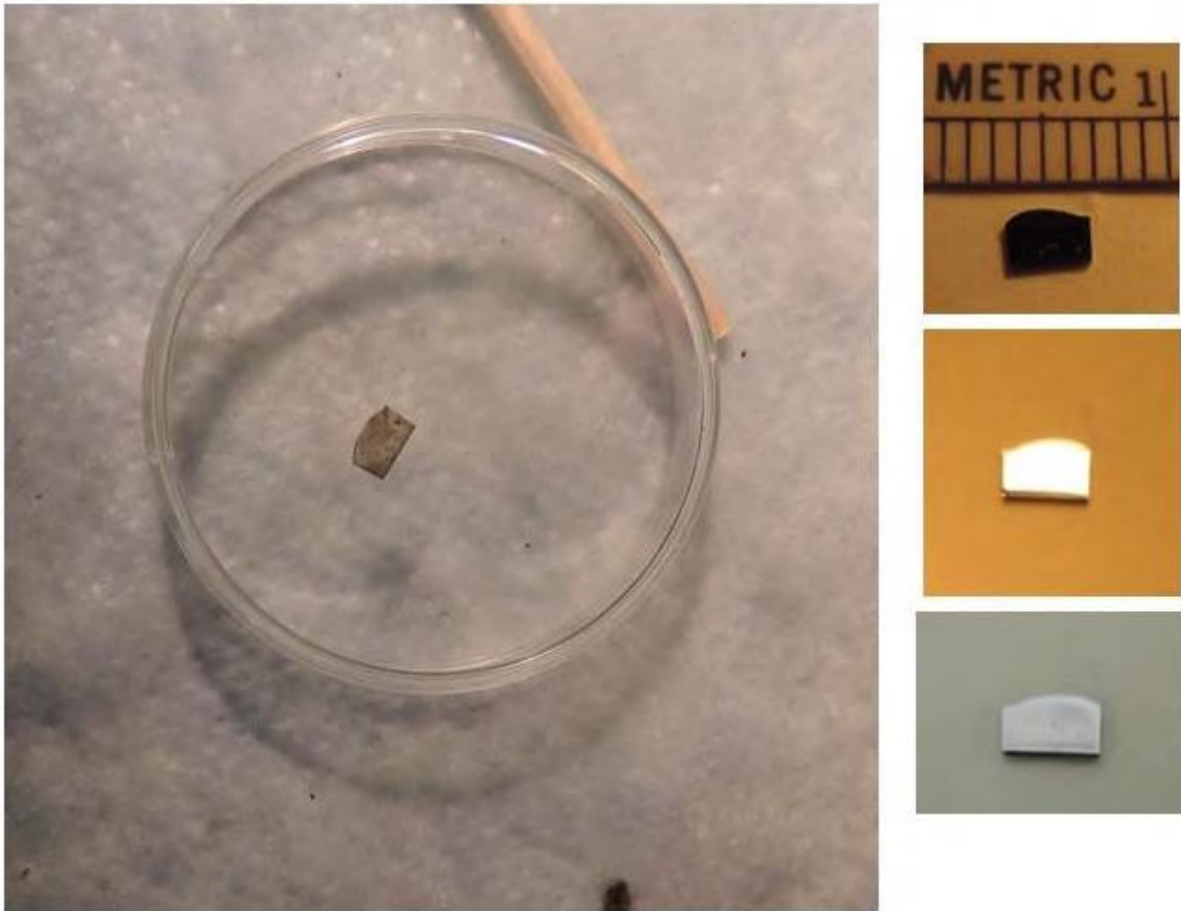


Figure 4.9 General appearance of further reduced weld cross sections with approximate dimensions of $3 \text{ mm} \times 2 \text{ mm} \times 1 \text{ mm}$ (i.e., after Step 2 completed).

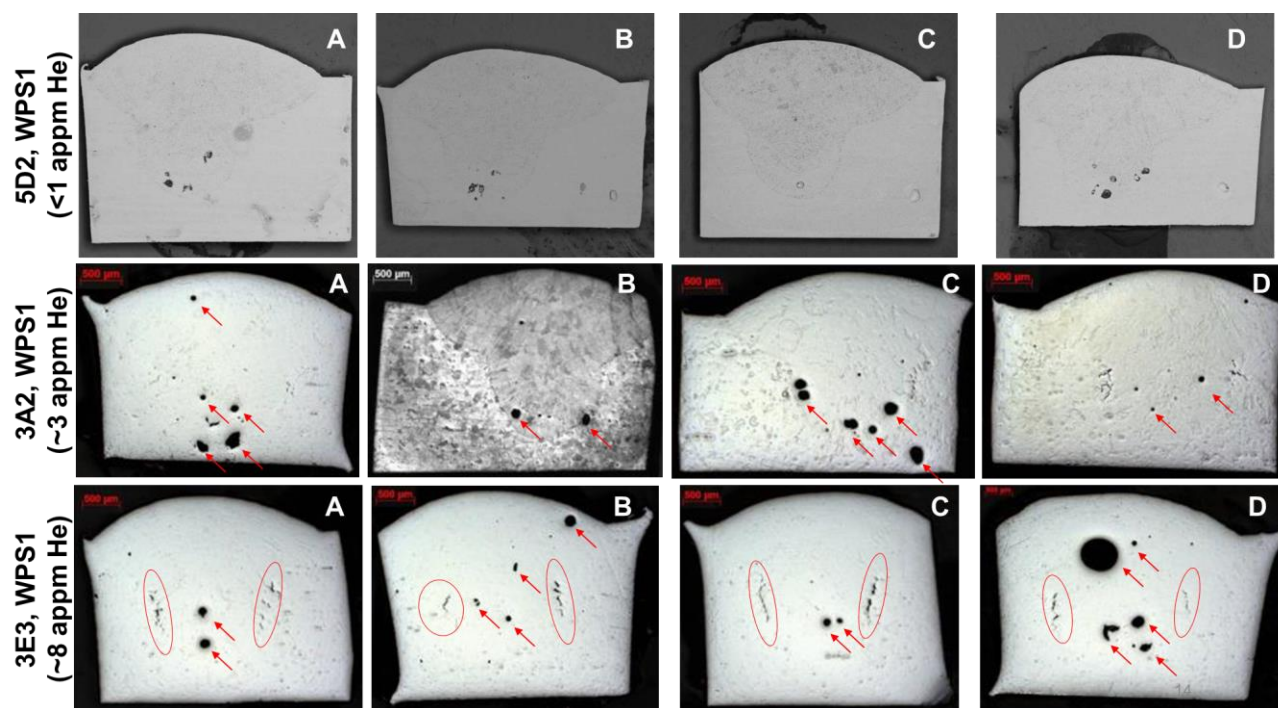


Figure 4.10 Light optical microscope images of selected weld samples obtained from weld coupon (post-etch images shown). Red arrows indicate laser weld-induced pores and red circles represent laser weld-induced cracks.

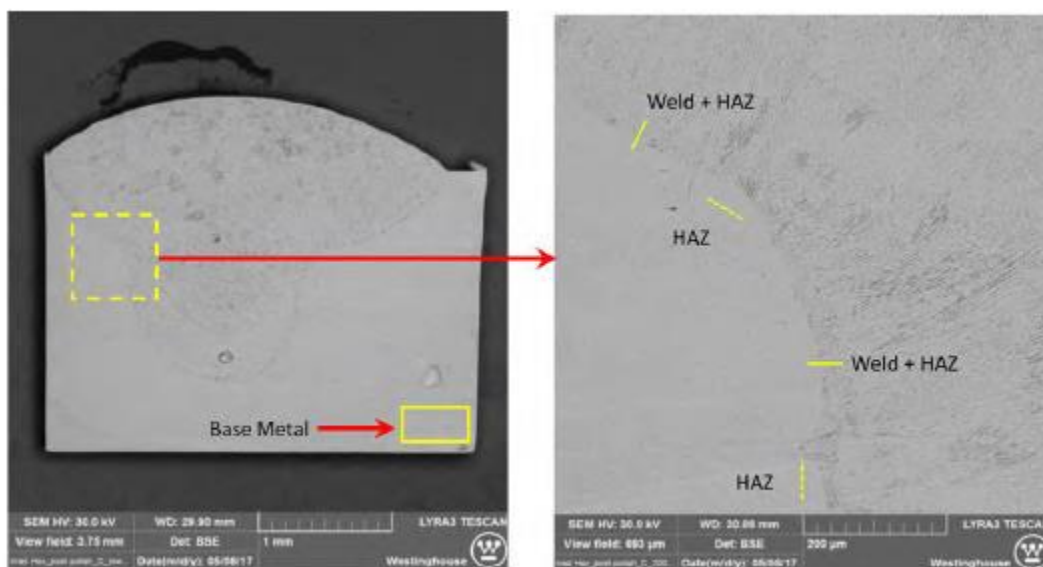
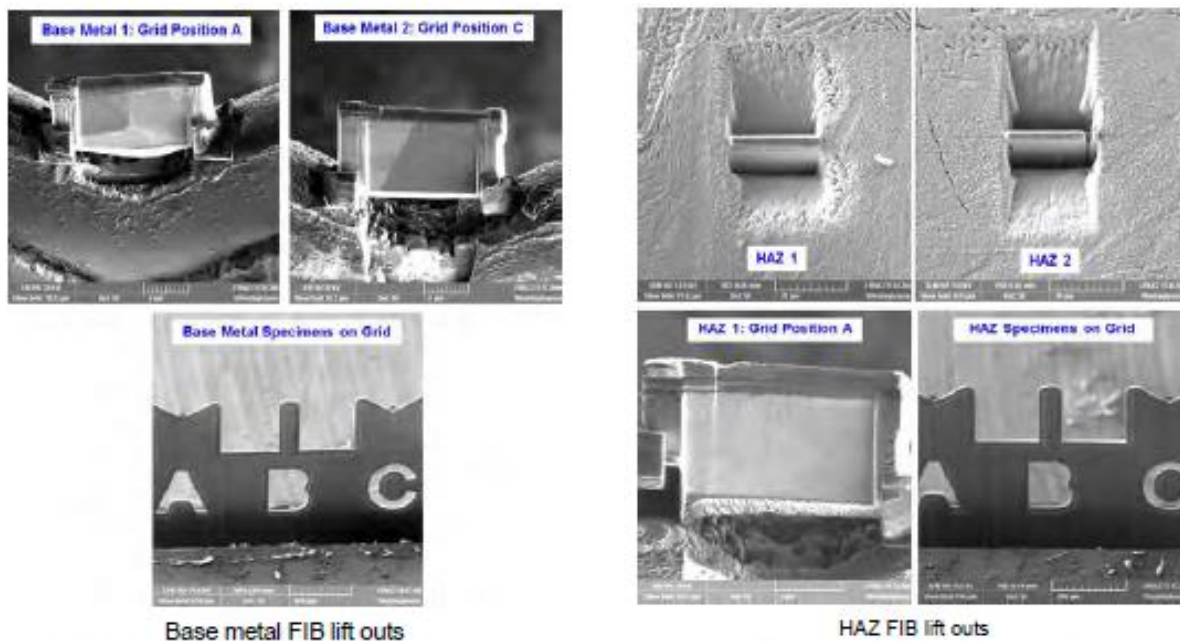


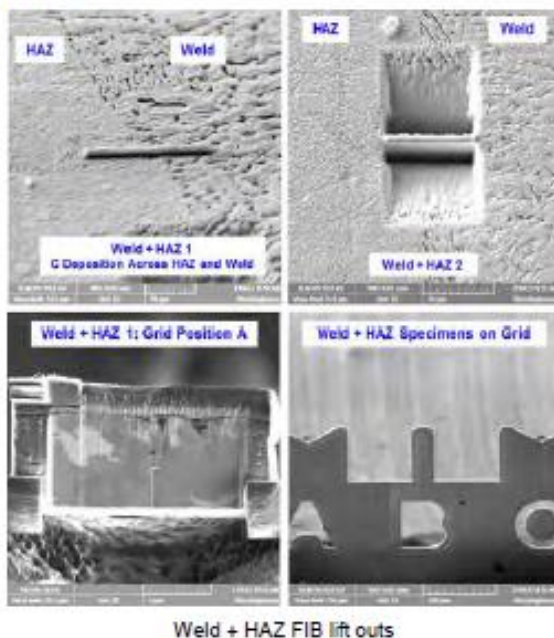
Figure 4.11 Images indicate locations for FIB lift-outs from laser welded specimen of 1 dpa, 0.2 appm He from 5D2 hex block.



Base Metal 1: Omniprobe grid position A
 Note: mounted $\sim 10^\circ$ from vertical, i.e., from grid plane
Base Metal 2: Omniprobe grid position C

HAZ 1: Omniprobe grid position A
HAZ 2: Omniprobe grid position C

Note that both base metal specimens include a grain boundary approximately centered in the specimen.



Weld + HAZ 1: Omniprobe grid position A
Weld + HAZ 2: Omniprobe grid position C

Figure 4.12 Images document weld, HAZ, and weld + HAZ FIB lift-outs and grid positions from laser weldments shown in Fig. 4.11.

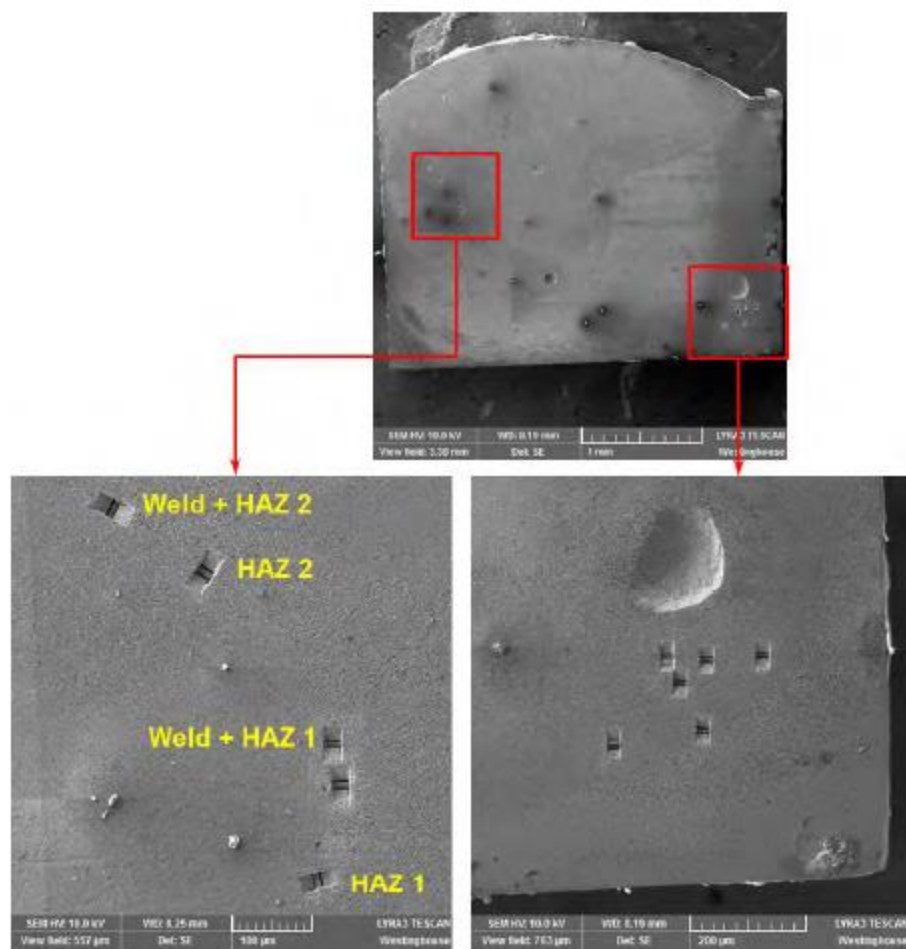


Figure 4.13 Images document different FIB lift-out locations in the base metal, weld, and HAZ from laser weldments shown in Fig. 4.11.

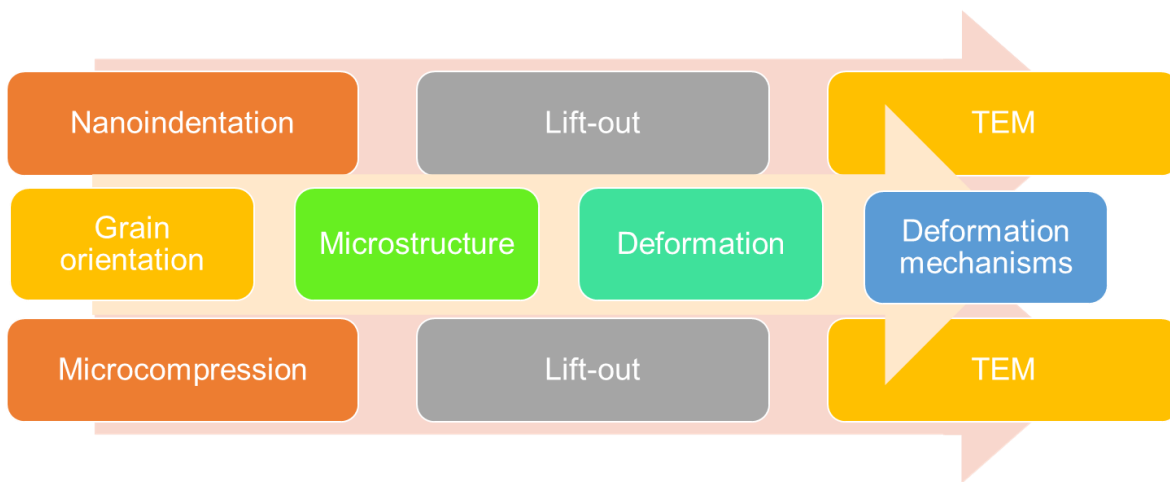


Figure 4.14 Schematic diagram of the mechanical testing and the follow-up post-deformed microstructural analysis on deformation mechanisms.

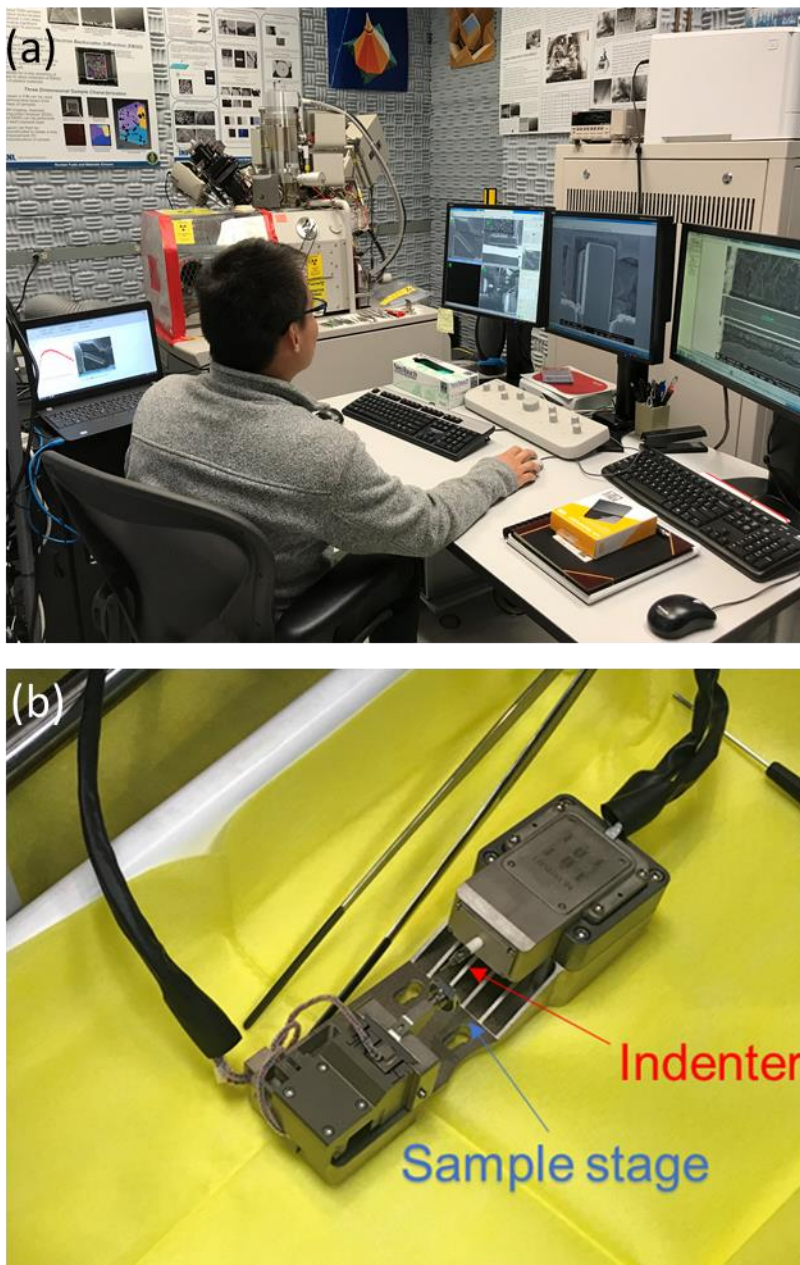


Figure 4.15 Hysitron PI-88 in-situ SEM mechanical testing system at Electron Microscopy Laboratory (EML) at Materials and Fuels Complex (MFC) in Idaho National Laboratory (INL).
(a) PI-88 in operation and (b) holder.

5. MICROSTRUCTURAL RESULTS

5.1 Irradiated microstructure

Irradiation-induced defects have been characterized for each condition. [Figure 5.1](#) shows an example of the typical microstructure before and after neutron irradiation. Before irradiation, the dislocations are clearly seen by bright-field TEM imaging in [Fig 5.1 \(a\)](#). The density of the dislocations is $(0.68 \pm 0.70) \times 10^{14} \text{ m}^{-2}$. No loops and cavities have been observed in the unirradiated archive sample. The neutron irradiation has induced defects including cavities, loops, precipitates, and clusters; an example of the irradiated microstructure is shown in [Fig. 5.1 \(b\)](#) from the 23 dpa, 3 appm He specimen. The dark-field TEM micrograph with $\vec{g} = [200]$ indicates a combination of networks of irradiation induced-defects. Considering the nature of characterizing irradiation-induced defects as mentioned in chapter 2, different imaging techniques are employed to capture the corresponding microstructure. Throughout this chapter, micrographs will be shown only for the 23 dpa, 3 appm He specimen, for the purposes of brevity. However, a summary of all quantitative microstructural data is provided in [Table 5.1](#) for all irradiation and weld conditions. Micrographs from all other conditions are provided in [Appendix](#).

5.1.1 Dislocation Loops

Dislocation loops have been observed under the bright-field STEM condition in [Fig. 5.2\(a\)](#). The micrograph of the loops is taken on the $[001]$ zone axis. Red arrows point out the all the possible faulted loops under the on-zone STEM condition. The average diameter of the loops is 29.4 ± 9.5 nm. The counted loop density is $(3.22 \pm 0.70) \times 10^{21} \text{ m}^{-3}$. [Figure 5.2 \(b\)](#) shows the size distribution of the loops. The overlaid Gaussian distribution is also presented. The peak loop diameter matches the Gaussian distribution. Despite the strong contrast of dislocations under the STEM condition, the high-density networking of dislocations, loops, precipitates, cavities and clusters are still apparent. Hence, the rel-rod technique is also adopted to image the interstitial Frank loops. The nature of the loops (faulted versus unfaulted and interstitial versus vacancy) can be determined by the inside-outside approach. The direction of the incident beam is close to $[\bar{1}\bar{1}3]$ or $[\bar{1}10]$. The small excitation error s_g is larger than zero. The Burgers vectors of the Frank loops are $\vec{b} =$

$\pm 1/3 \langle 111 \rangle$ by the invisibility criterion. Figure 5.3 shows the Frank loops of the 23 dpa and 3 appm He sample. The precipitates are also visible under the rel-rod condition.

5.1.2 Cavities

Irradiation-induced cavities have also been characterized by a STEM HAADF detector shown in Fig. 5.2(a). The cavities are observed for the irradiated AISI 304L SS with 23 dpa dose and 3 appm He. The diameter distribution of the cavities is given in Fig. 5.2(b). The average diameter of the cavities is 19.3 ± 7.6 nm. The average number density of the cavities is $(1.33 \pm 0.33) \times 10^{21} \text{ m}^{-3}$. The overlaid Gaussian distribution indicates that the real peak of the diameter of the cavities is slightly deviating to a smaller value. A majority of these irradiation-induced cavities lie on the $\{111\}$ planes. They typically have truncated octahedral geometry but are not saturated to grow as helium bubbles. One of the cavities is boarded by a dashed rectangle. The morphology of this cavity is revealed by high resolution TEM (HRTEM) using different focusing conditions (Fig. 5.4(c)-overfocus and Fig. 5.4(d)-underfocus). The inset patterns are given as the fast Fourier transformations. This clearly shows the boundary between the cavity and the matrix as an incoherent interface. The void swelling can also be calculated with $\Delta V / (V - \Delta V)$. The estimated void swelling is $1.67 \pm 0.43\%$, consistent with the original reported value of $\sim 1.5\%$.

5.1.3 Precipitates

Irradiation-induced precipitates have also been characterized using a simple stab of the minor diffraction patterns taken at a certain zone axis. Examples of precipitates are given in Fig. 5.1(b) and Fig 5.3(a-b). These dark-field TEM micrographs indicate the existence of precipitate groups, dislocations decorated with precipitates and single precipitates. Existing works on similar precipitates such as carbide, Ni_3Si , and G-phase in identical alloys have already been summarized in Chapter 2. Under the TEM resolution, it is very difficult to distinguish the type of each precipitation. The average size of the precipitates is 14.67 ± 1.14 nm. The number density of the precipitates is $(1.44 \pm 0.54) \times 10^{21} \text{ m}^{-3}$.

5.2 Post-welded microstructure

Laser weld-induced microstructural evolution is presented with respect to the change of loops, cavities, and precipitates. We focus on the characterization of these defects in the HAZ.

5.2.1 Loops

Dislocation loops have been observed under the bright-field STEM condition in Fig. 5.5. The micrographs of the loops were taken on the $[\bar{1}\bar{1}3]$ zone axis shown in the inset diffraction patterns. Red arrows point out the all the possible loops. Two different conditions of dose and He are given in Fig. 5.2(a)-23dpa, 3 appm He and Fig. 5.2(b)-28dpa, 8 appm He, respectively. For the 3 appm case, the average diameter of the loops is 22.3 ± 8.7 nm and the counted loop density is $(8.03 \pm 3.11) \times 10^{21} \text{ m}^{-3}$. For the 8 appm case, the average diameter of the loops is 19.3 ± 7.9 nm and the counted loop density is $(12.80 \pm 2.09) \times 10^{21} \text{ m}^{-3}$. Despite the strong contrast of dislocations under the STEM condition, the high-density networking of dislocations, loops, precipitates, cavities, clusters, and black dots are still apparent. We thus also apply the rel-rod technique to image the interstitial Frank loops. The direction of the incident beam is close to $[\bar{1}\bar{1}3]$ or $[\bar{1}10]$. The small excitation error s_g is larger than zero. The Burgers vectors of the Frank loops are $\vec{b} = \pm 1/3 \langle 111 \rangle$ by the invisibility criterion. Figure 5.6(a-b) shows the Frank loops along with precipitates of the 23 dpa, 3 appm He sample and the 28 dpa, 8 appm He sample, respectively.

5.2.2 Cavities

The HAADF STEM imaging technique is also employed to characterize irradiation-induced cavities in the HAZ as shown in Fig. 5.7(a) for 23 dpa, 3 appm He, and Fig. 5.7(b) for 28 dpa, 8 appm He, respectively. In the 23 dpa, 3 appm He sample, the counted average diameter of the cavities is 16.2 ± 4.4 nm, and the number density of the cavities is $(1.36 \pm 1.21) \times 10^{19} \text{ m}^{-3}$. In the 28 dpa, 8 appm He sample, the counted average diameter of the cavities is 22.2 ± 4.2 nm, and the number density of the cavities is $(1.45 \pm 1.29) \times 10^{19} \text{ m}^{-3}$. The cavities have been annealed during the laser welding in the HAZ, indicating a lower density number and smaller size of these cavities.

5.2.3 Precipitates

Figure 5.6 shows the Franks loops with precipitates. We also applied weak-beam dark-field (WBDF) imaging technique to observe the irradiation-induced precipitates (see Fig. 5.8). In addition, we have observed laser weld-induced precipitates in the HAZ much larger than the irradiation-induced precipitates. For instance, at 23 dpa, 3 appm He, the Cr enriched precipitate has appeared in the HAZ (Fig. 5.9). The EDS line scan shows the increase of Cr from 19 at% in the matrix to 30 at% in the precipitate. At a lower condition, 1 dpa, 0.2 appm He, the number

density of precipitates has increased as shown in Fig. 5.10(a). The inset selected area diffraction (SAD) pattern in Fig. 5.10(b) indicates the precipitate has a bcc structure on the [001] zone axis while the matrix is on the fcc [111] zone axis, which is also distinguishable from the HRTEM image of the matrix/precipitate interface. Fig. 5.10(c) shows the increase of Cr content of the precipitate compared to the matrix.

5.3 Comparison of microstructural trends

5.3.1 Grain structure

An SEM image is given in Fig. 5.11(a) showing the cross-section of the laser weld of the neutron irradiated AISI 304L SS at 23 dpa dose and 3 appm He concentration. The straight green box shows the interface at the welding boundary with an optical microscope. The HAZ is extended into the base metal. Laser weld-induced pores have also been observed, represented by red arrows. The dotted oval indicates smaller cracks in the HAZ. The dashed red box has been selected for the EBSD scan. The OIM map in Fig. 5.11(b) shows the transition from dendritic grains in the weld fusion zone to equiaxed grains in the base metal. The HAZ is an intermediate region with a combination of both elongated and circular grains. The average grain size of the base metal and the HAZ is $52.1 \pm 25.4 \mu\text{m}$, while the weld metal is $30.7 \pm 18.5 \mu\text{m}$. Figure 5.12 gave the micrographs of light optical microscope of selected weld cross-sections with the 1 dpa, 0.2 appm He sample and the 23 dpa, 3 appm sample. The cracks have been observed in the 23 dpa, 3 appm sample. The outlined crack area is $\sim 1081 \mu\text{m}^2$.

5.3.2 Comparison of loops and cavities

Figure 5.13 gives a summary of the microstructure comparison between the base metal and HAZ for dose level of 1, 23, and 28 dpa and He concentration 0.2, 3 and 8 appm. At a low He concentration, no cracking has been observed. At a higher He concentration ~ 3 appm, laser weld-induced cracking has been generated. Laser weld-induced pores have also been observed at higher He conditions. The laser weld removes the cavities in the HAZ. The loops are relatively smaller, but the population has not been greatly reduced quantitatively. The trends of the loops and cavities are given in Fig. 5.14(a-b) for both the base metal and the HAZ. The number density of the cavities increases with the dose level and He concentration. The size of the cavities also increases with the dose level and He concentration. After laser welding, the number density of the cavities in the

HAZ has reduced to two orders of magnitude smaller than the base metal. The loop densities of the base metal and the HAZ increase as the dose level and He concentration go up. The number density of loops in the base metal is still comparable to the HAZ with respect to the order of magnitude. The size of the loops decreases the dose level and He concentration rise because the loops saturate at certain irradiation level [56]. A summary of the microstructural features including loops, cavities and grains is listed in [Table 5.1](#).

5.3.3 Comparison of radiation-induced segregation

Radiation-induced segregation (RIS) has been given by conducting an EDS line scan at the grain boundary in the laser welds. The base metal of the 1 dpa, 0.2 appm He is shown in [Fig. 5.15\(a\)](#), with a concentration of Ni, depletion of Cr, and a slight decrease of Mn at the grain boundary, which is consistent to the report in Chapter 2. After the laser welding, the HAZ of the 0.2 appm exhibits the decrease of RIS at the grain boundary for Ni, Cr and Mn at the grain boundary (see [Fig. 5.15\(b\)](#)). The same trends can also be found in the 23 dpa, 3 appm and 28 dpa, 8 appm HAZ ([Fig. 5.15\(c-d\)](#)). The oscillations of the concentration profiles might be related to the dislocation motion [261].

Table 5.1 Summary of microstructure features in the laser welds of all conditions.

Condition	Void Density [m⁻³]	Void Diameter [nm]	Loop Density [m⁻³]	Loop Diameter [nm]	Grain Size [μm]
0.2 appm, 1 dpa Base	$0.10 \pm 0.078 \times 10^{21}$	16.3 ± 6.1	$1.54 \pm 0.75 \times 10^{21}$	41.7 ± 13.4	47.5 ± 2.3
0.2 appm, 1 dpa HAZ	$5.00 \pm 2.38 \times 10^{19}$	11.4 ± 3.9	$2.40 \pm 0.77 \times 10^{21}$	22.8 ± 4.5	49.2 ± 4.1
3 appm, 23 dpa Base	$1.20 \pm 0.29 \times 10^{21}$	20.9 ± 7.7	$8.03 \pm 3.11 \times 10^{21}$	22.3 ± 8.7	52.0 ± 1.5
3 appm, 23 dpa HAZ	$1.38 \pm 1.21 \times 10^{19}$	16.2 ± 4.4	$5.77 \pm 2.11 \times 10^{21}$	14.2 ± 3.9	52.7 ± 5.3
8 appm, 28 dpa Base	$1.36 \pm 7.03 \times 10^{21}$	24.9 ± 8.7	$12.8 \pm 2.09 \times 10^{21}$	19.3 ± 7.9	51.6 ± 6.2
8 appm, 28 dpa HAZ	$1.42 \pm 1.29 \times 10^{19}$	22.2 ± 4.2	$12.5 \pm 1.62 \times 10^{21}$	8.9 ± 1.9	46.9 ± 7.4
Archived	-	-	-	-	52.0 ± 17.7

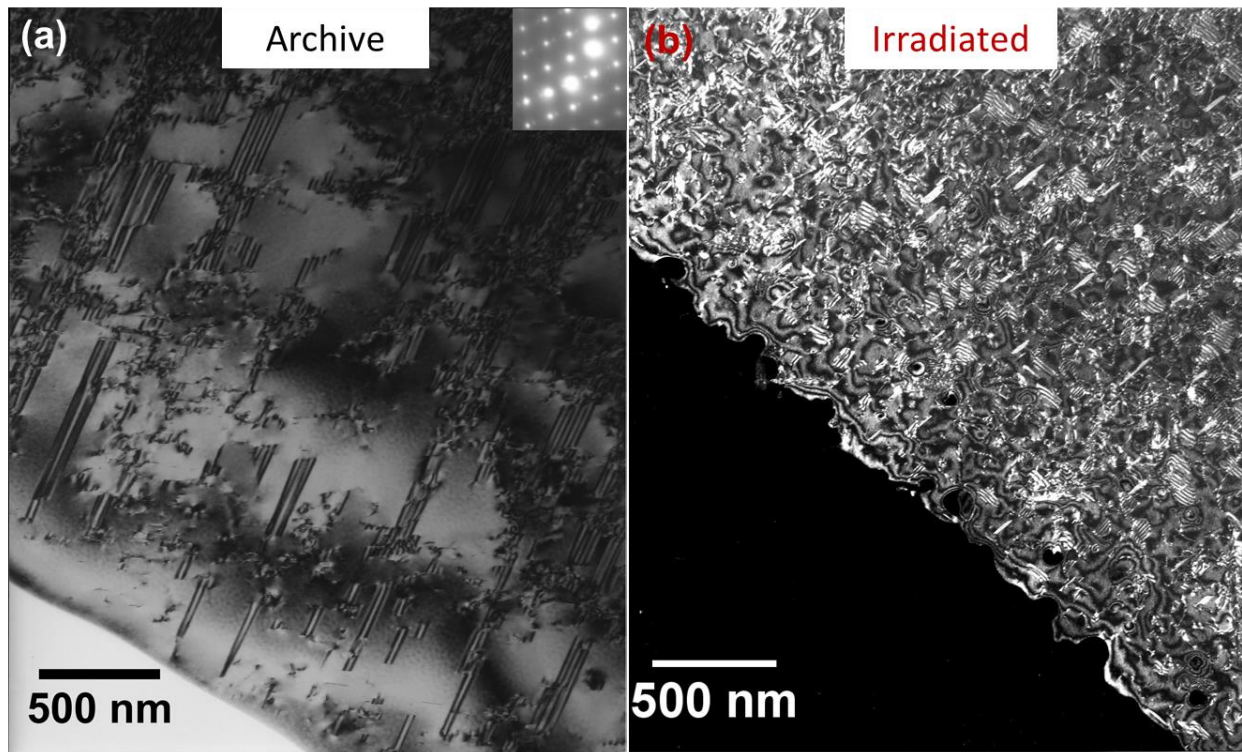


Figure 5.1 Comparison of microstructure before and after neutron irradiation. (a) Dislocations in the archive AISI 304L SS and (b) defect networks in irradiated AISI 304L SS at 23 dpa and 3 appm He under dark-field TEM mode with $\vec{g} = [200]$.

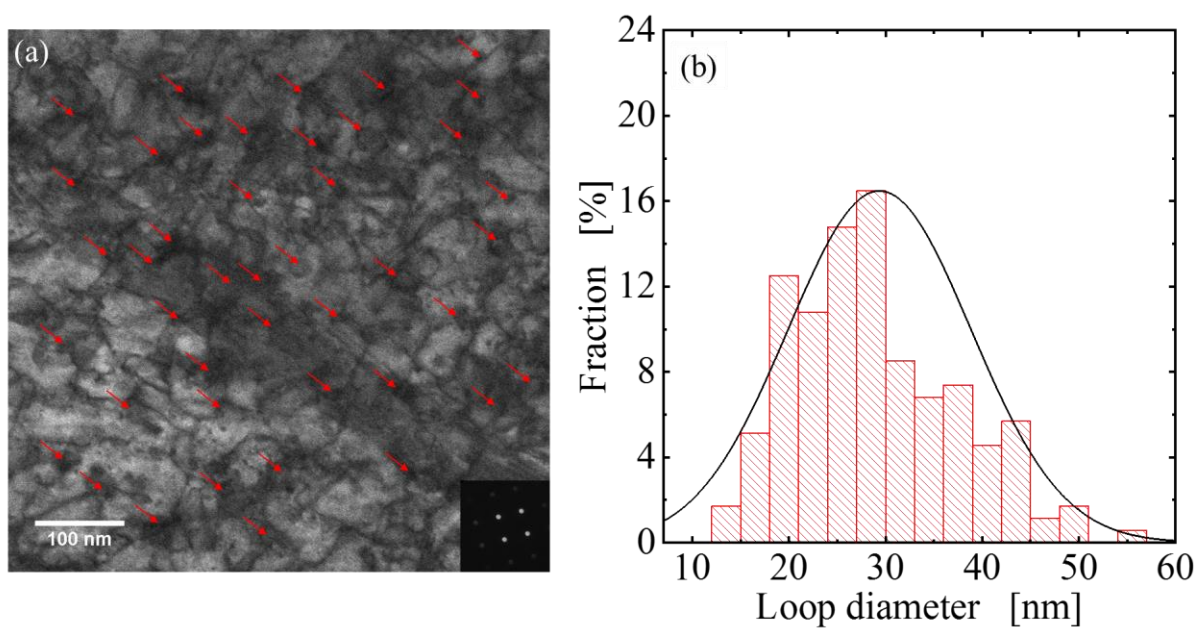


Figure 5.2 Dislocation loops in the irradiated AISI 304L SS with 23 dpa and 3 appm He under the bright-field STEM mode. (a) Bright-field STEM imaging of dislocation loops on [001] zone axis (inset diffraction pattern). (b) Loop size distribution in (a) with overlaid Gaussian distribution.

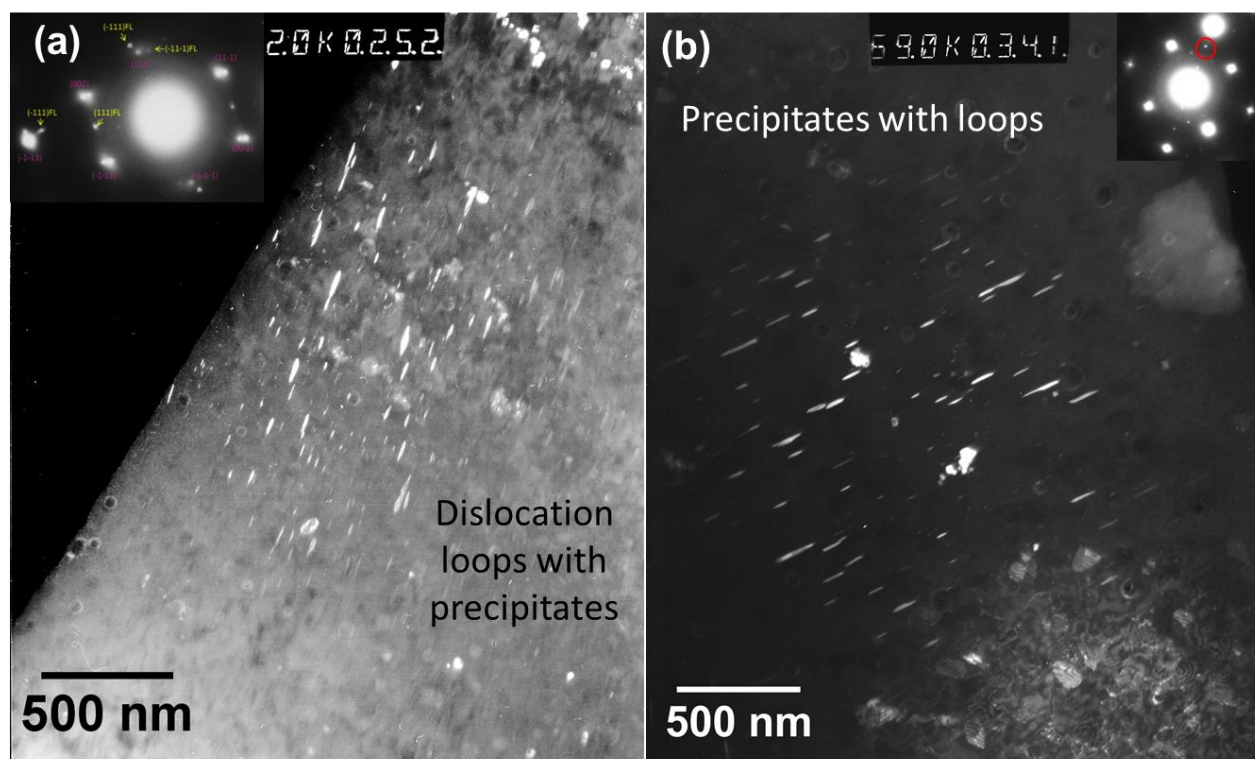


Figure 5.3 Rel-rod method of imaging Frank loops. (a-b) Frank loops with precipitate groups and single precipitates of neutron irradiated AISI 304L SS of 23 dpa and 3 appm He condition.

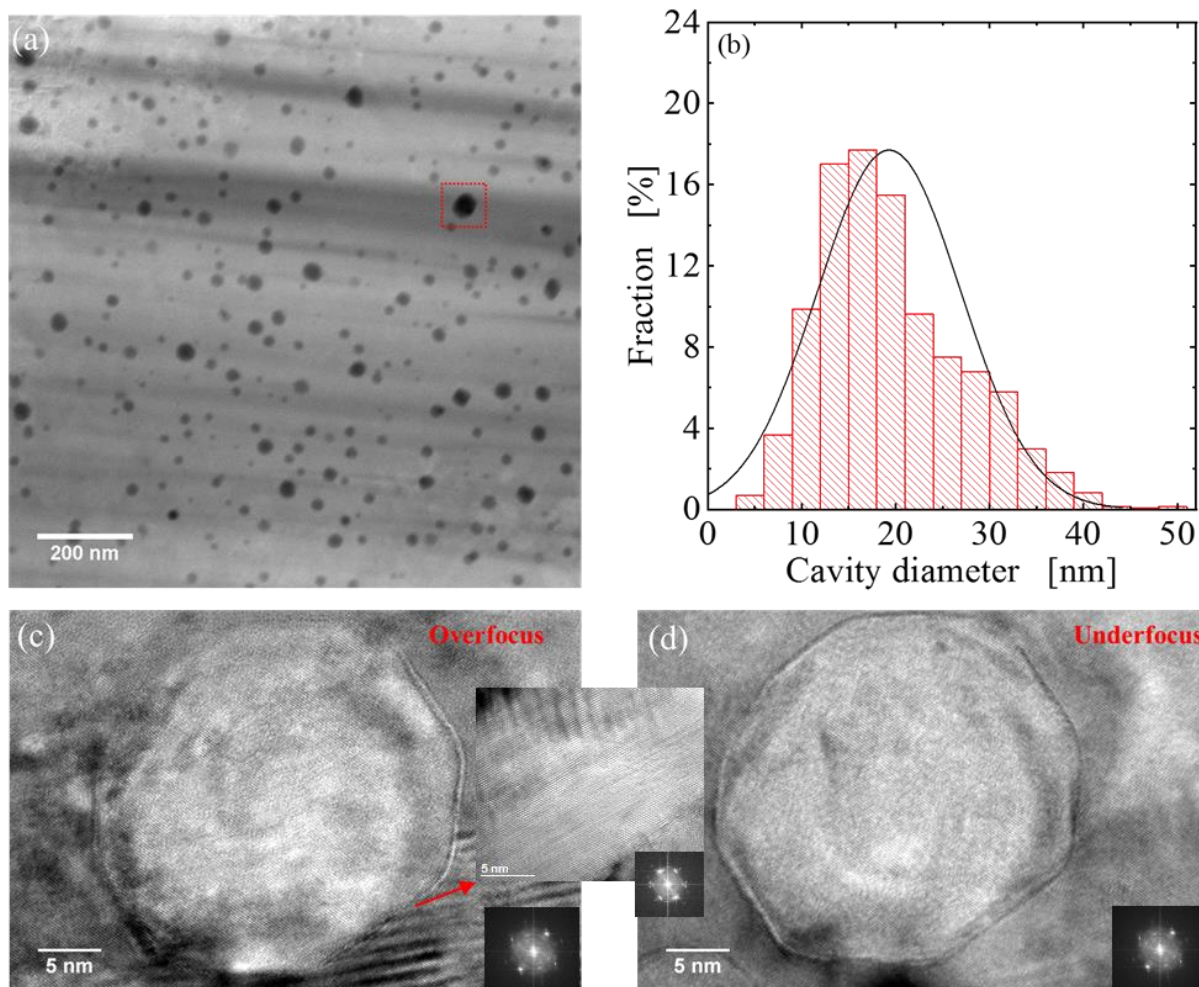


Figure 5.4 Detailed microscopy and statistical analysis of irradiation induced-cavities on the irradiated AISI 304L SS of 23 dpa and 3 appm He. (a) HAADF STEM imaging of cavities. (b) Size distribution of cavities overlaid with a Gaussian distribution. (c-d) HRTEM (with inset FFTs) of a cavity enveloped by the dashed rectangle in (a) shows the incoherent interface between the cavity and the matrix under different focusing conditions: (c) overfocus and (d) underfocus.

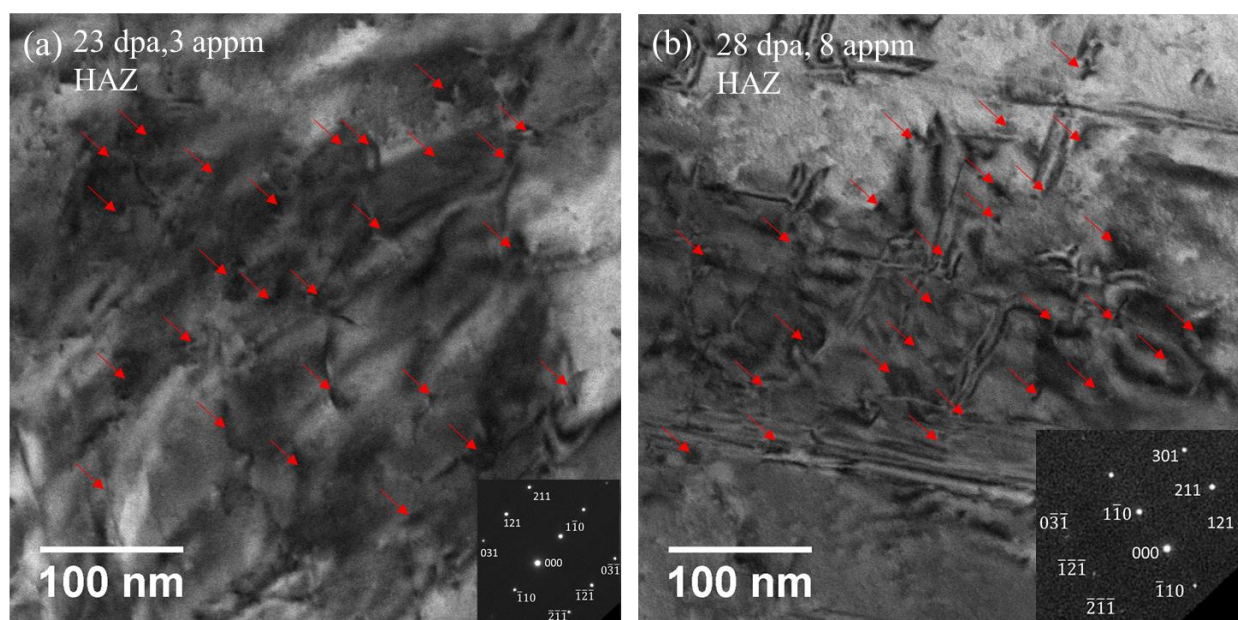


Figure 5.5 Bright-field STEM images of loops in the HAZ on $[\bar{1}\bar{1}\bar{3}]$ zone axis with inset diffraction patterns. (a) 23 dpa, 3 appm He and (b) 28 dpa, 8 appm He.

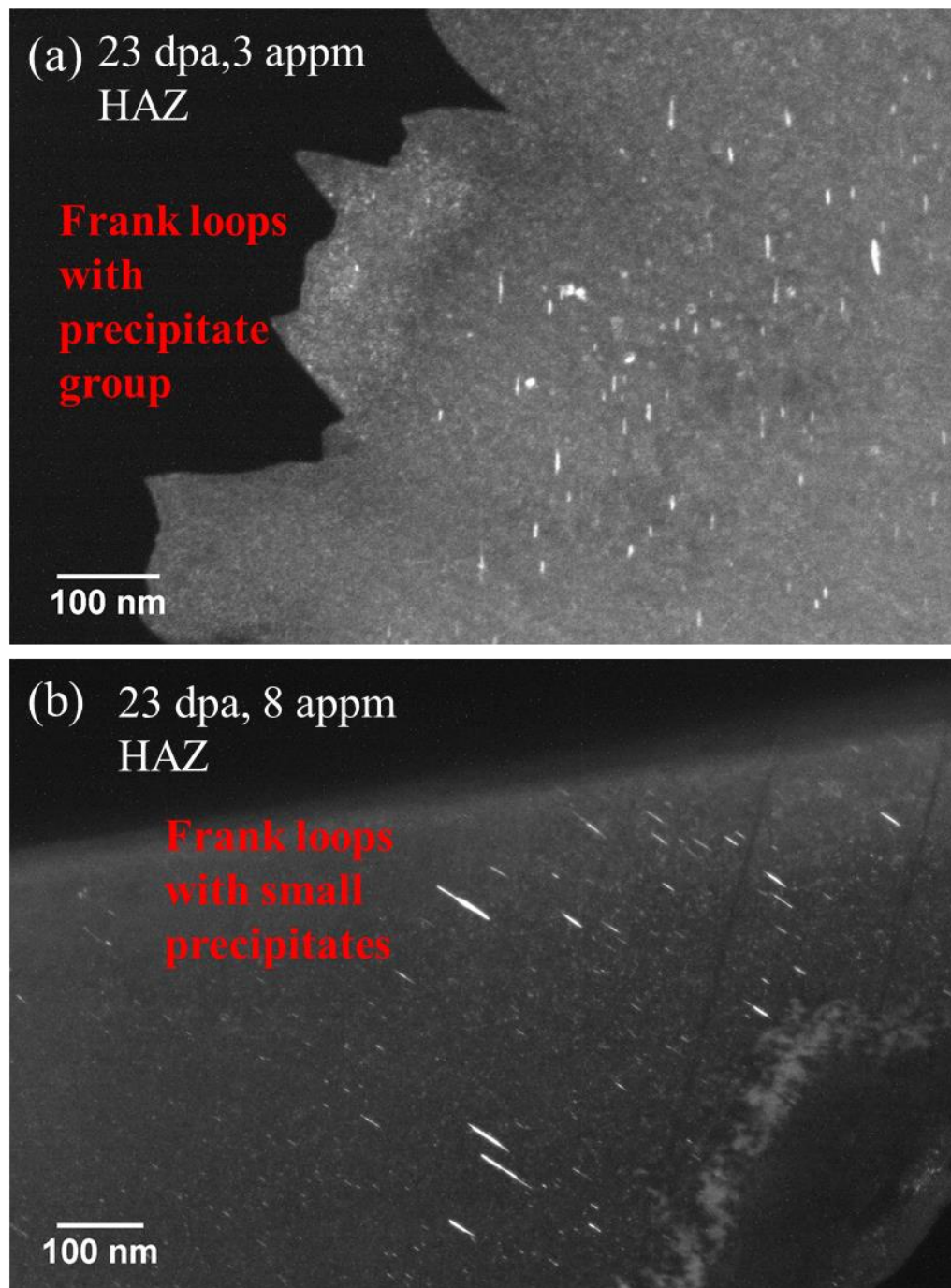


Figure 5.6 Rel-rod images of interstitial Frank loops in the HAZ: (a) 23 dpa, 3 appm He and (b) 28 dpa, 8 appm He.

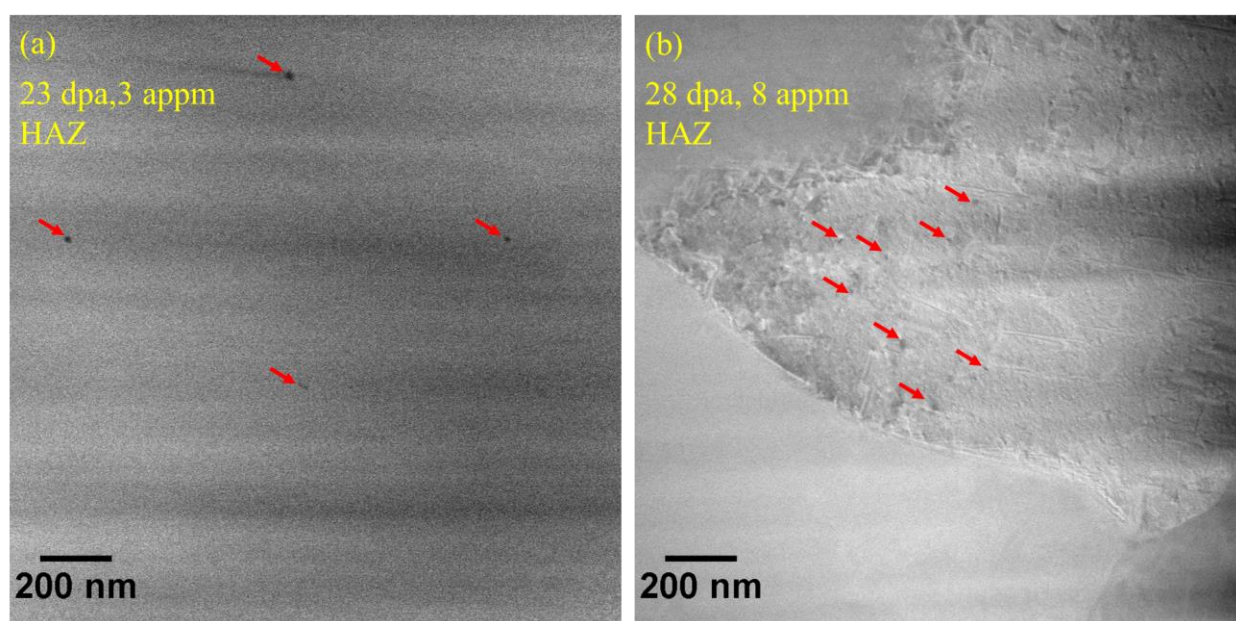


Figure 5.7 HAADF of cavities in the HAZ: (a) 23 dpa, 3 appm He and (b) 28 dpa, 8 appm He.

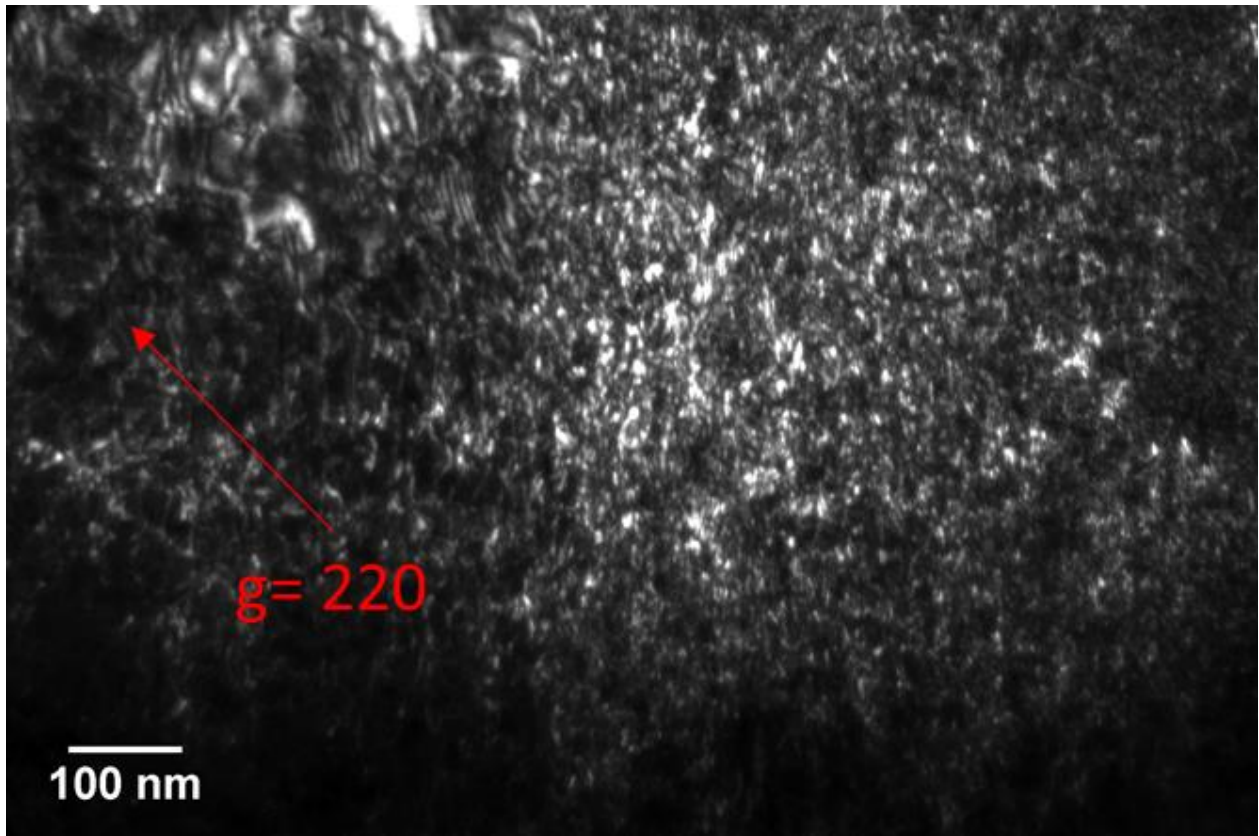


Figure 5.8 Weak-beam dark-field image of precipitates in the HAZ of a 28 dpa, 8 appm He sample.

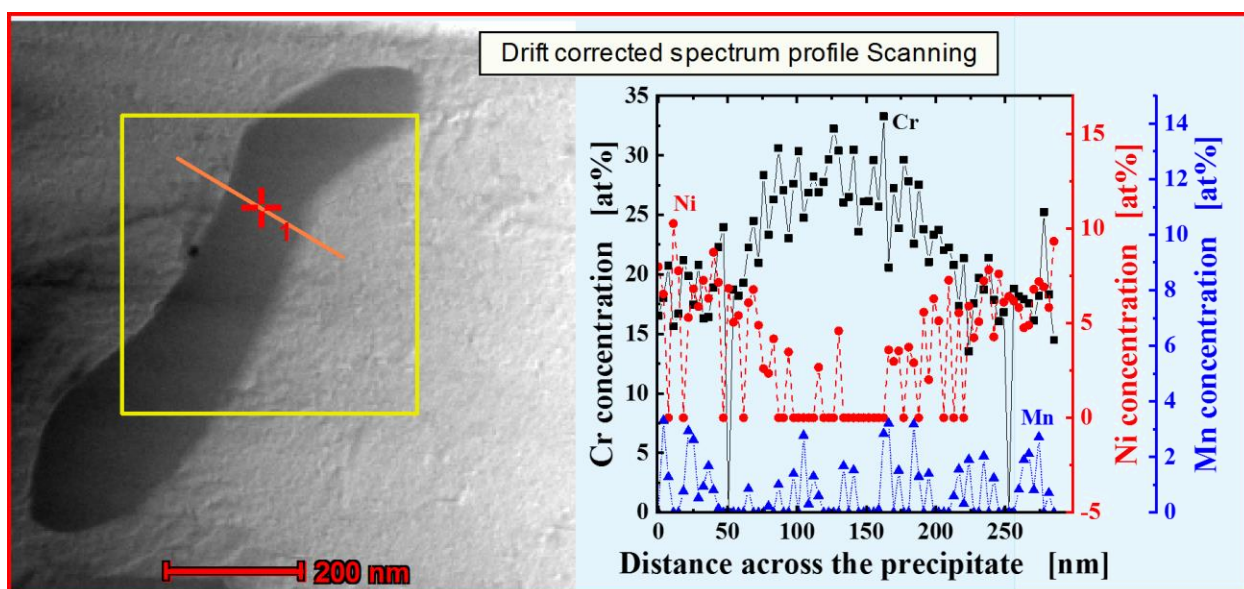


Figure 5.9 Cr enriched precipitate in the HAZ of the 23 dpa, 3 appm He sample. EDS line scan across the boundary shows Cr enrichment in the precipitate compared with the matrix.

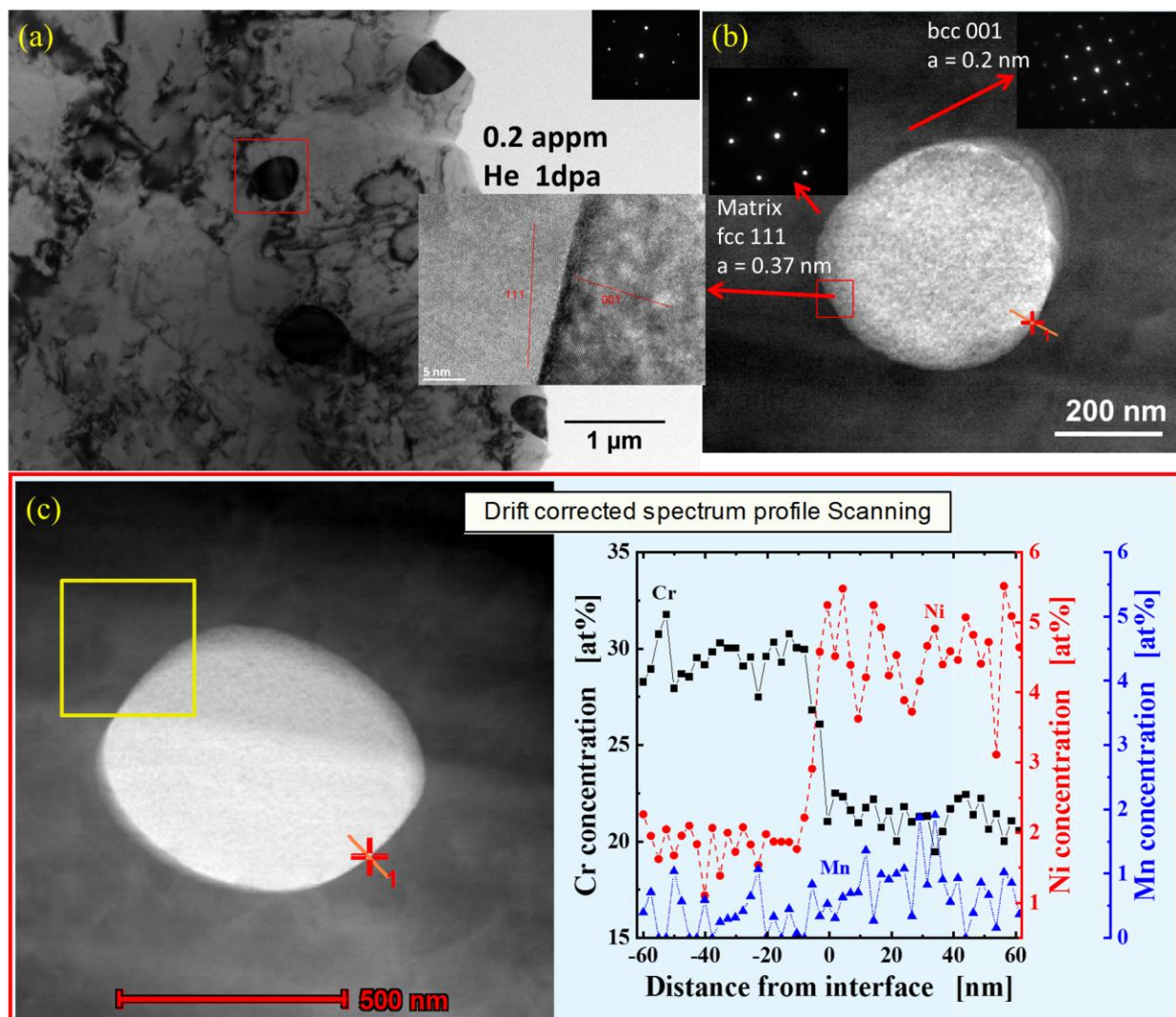


Figure 5.10 Detailed analysis of the Cr enriched precipitate in the HAZ. (a) Laser weld-induced precipitates in the 1dpa, 0.2 appm He sample. (a) SAD of the matrix versus the precipitate with inset of HRTEM image of the interface between the interface and the precipitate. (c) EDS line scan across the boundary shows Cr enrichment in the precipitate compared to the matrix.

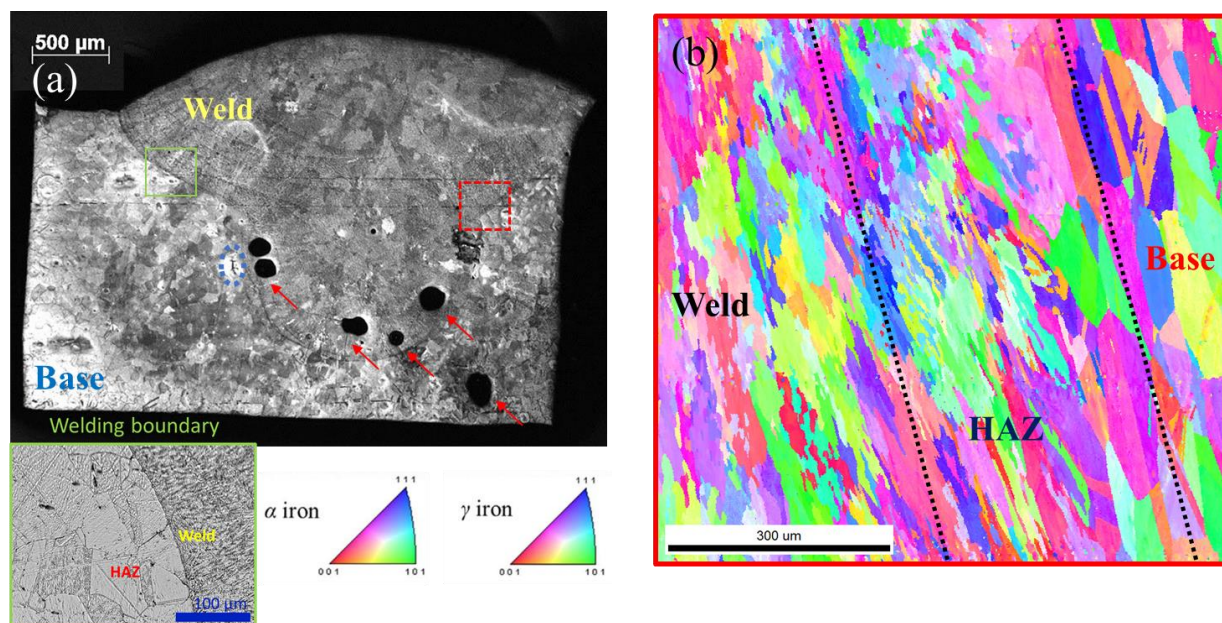
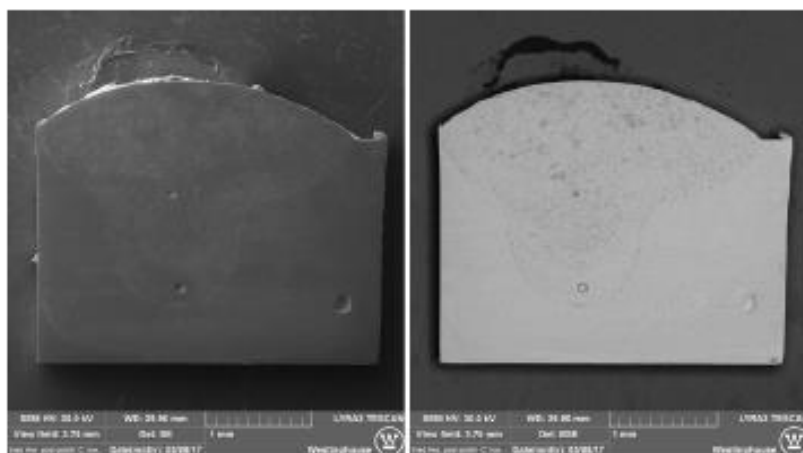
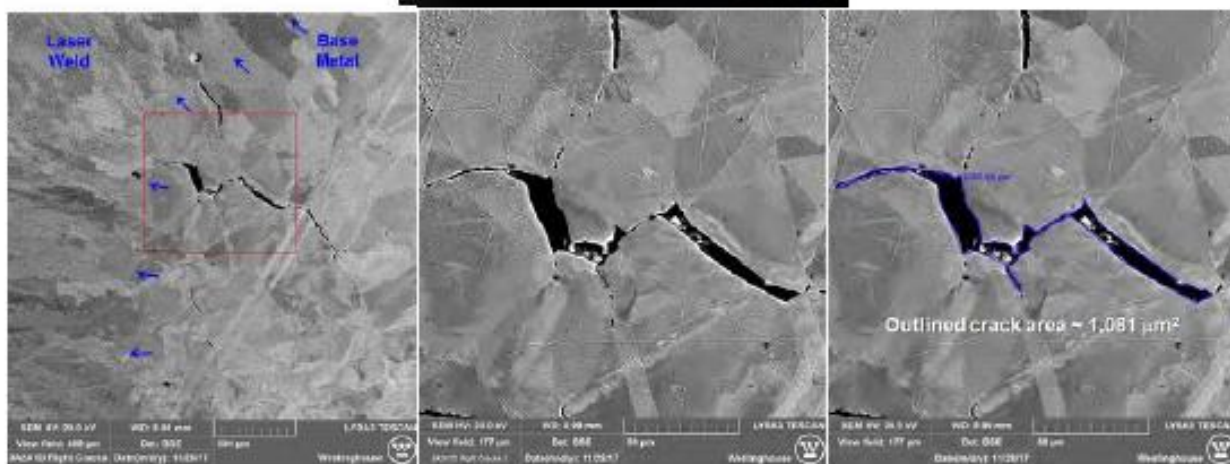


Figure 5.11 Laser weldment of a neutron irradiated AISI 304L SS of 23 dpa and 3 appm He. (a) SEM micrograph of the finished laser weld cross-section. Red arrows indicate weld-induced pores. Straight green box shows the interface of the weld boundary between the weld and the HAZ. Dotted blue oval represents the laser weld-induced cracking in the HAZ. (b) OIM maps of the weldment cross-section of the dashed red rectangular box in (a): transition from elongated dendritic grains in the weld region to the equiaxed grains in the base metal and the HAZ has a combination of both dendritic and equiaxed grain structure.



SEM secondary electron (left) and backscatter electron (right) images of weld sample LW-12C (note, FIB lift outs were later obtained from this particular sample).



Light optical image of weld sample 3A1A1D with yellow circle indicating cracking on the right of the weld. SEM backscattered images of the same cracked region.

Figure 5.12 Selected 23 dpa, 3 appm He laser welds-SEM imaging and crack analysis.

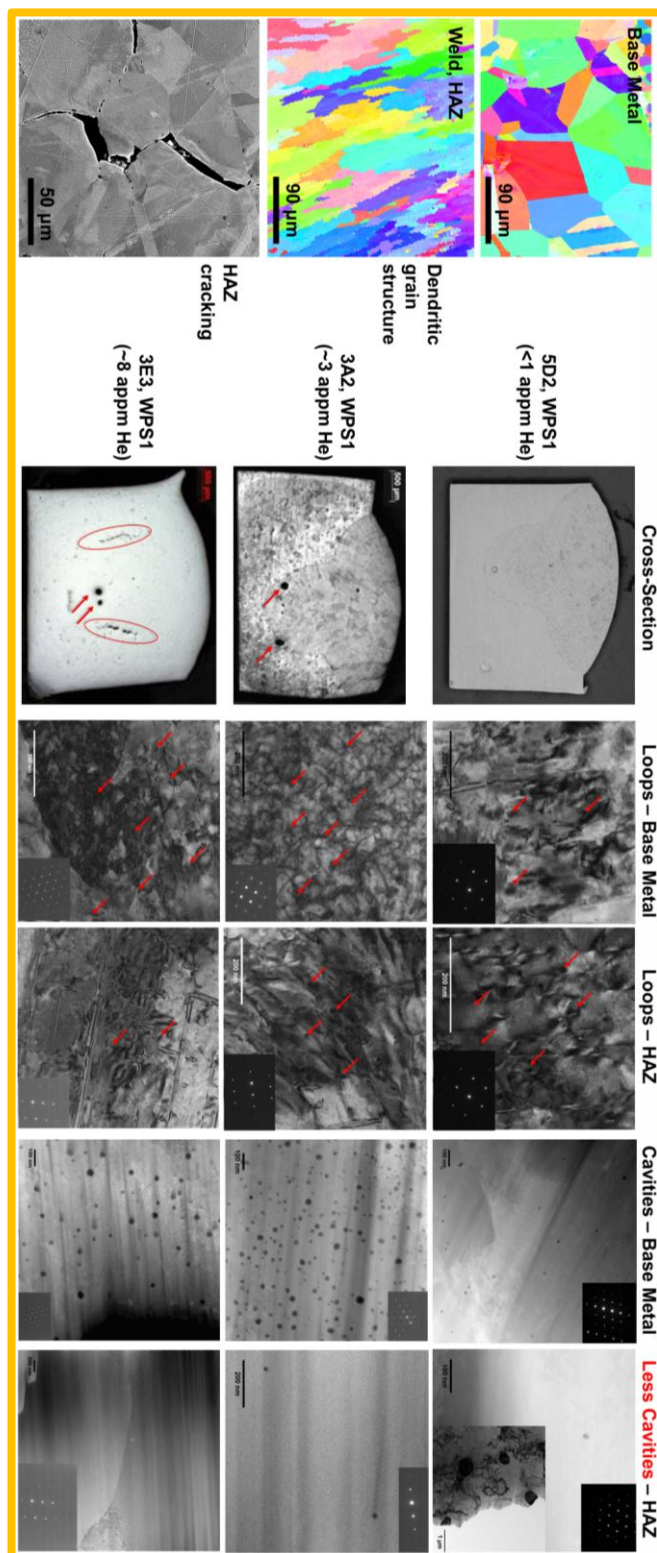


Figure 5.13 Summary of microstructure of the laser welds of neutron irradiated AISI 304L SS at different dose levels (1, 23, 28 dpa) and He (0.2, 3, 8 appm) concentrations: grain structure with OIM mapping, HAZ cracking, images of the loops and cavities in the base metal and HAZ.

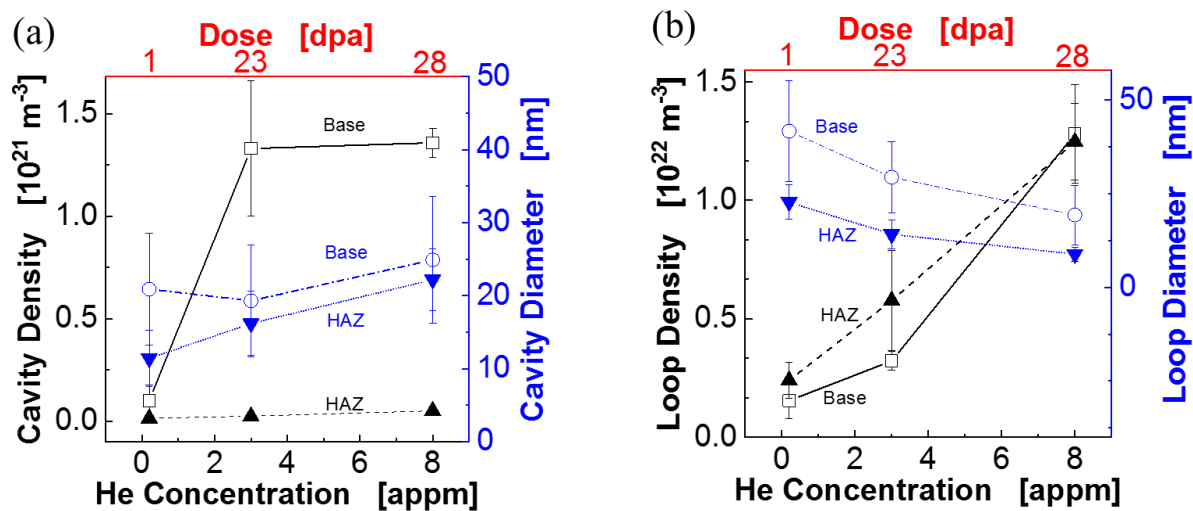


Figure 5.14 Microstructural evolution in the base metal and HAZ versus the dose level He concentration. (a) Average cavity density and diameter and (b) average loop density and diameter.

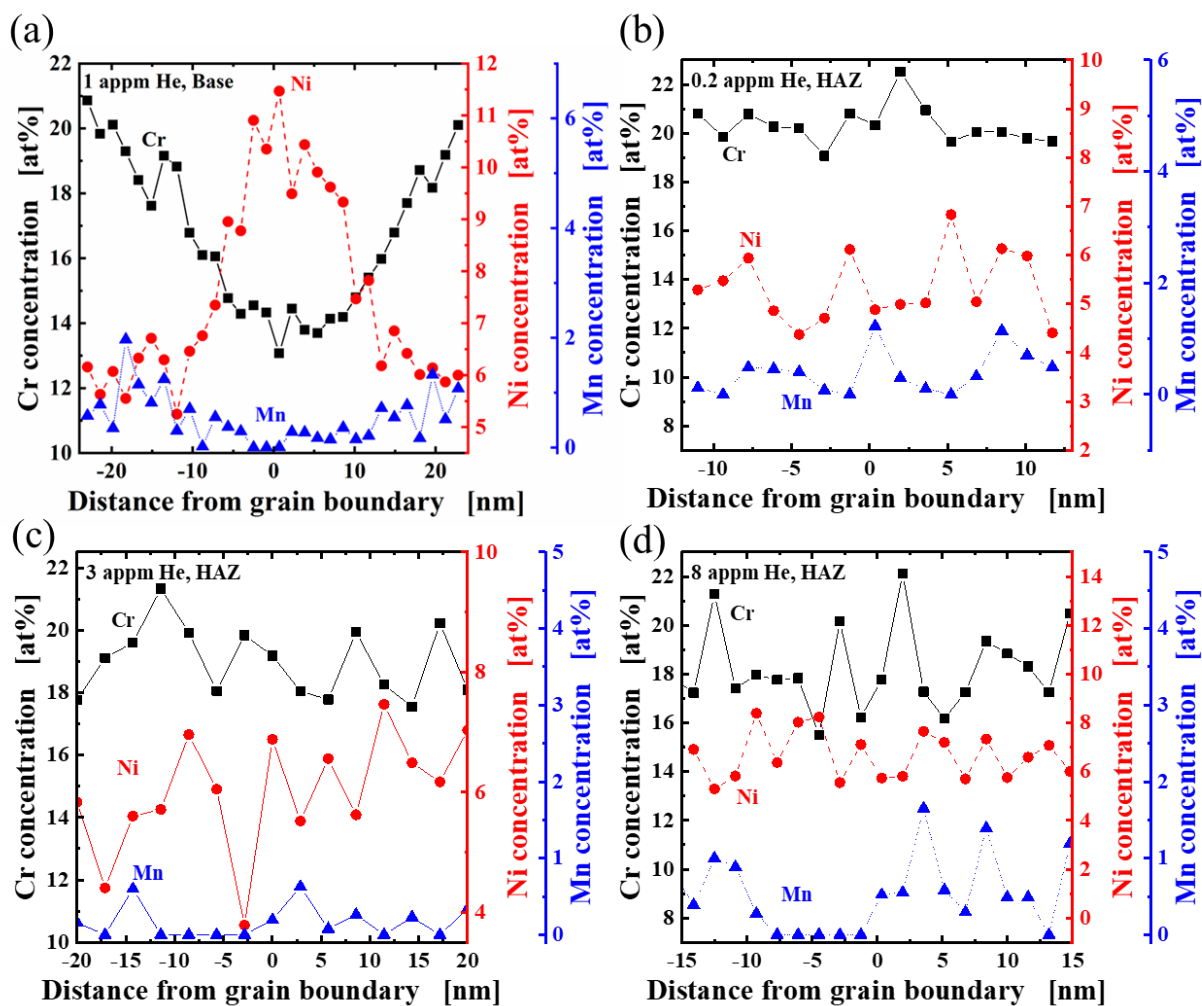


Figure 5.15 Radiation-induced segregation (RIS) at the grain boundary of the laser weld for Cr, Ni, Mn: (a) 1 dpa, 0.2 appm He in the base metal, (b) 1 dpa, 0.2 appm He in the HAZ, (c) 23 dpa, 3 appm He in the HAZ, and (d) 28 dpa, 8 appm He in the HAZ.

6. MECHANICAL TESTING RESULTS

This chapter will cover the mechanical testing, including nanoindentation and micropillar compression tests, on the laser weldment of irradiated AISI 304L SS. The outcome of these tests includes not only the hardness and modulus data, but also the mechanically induced deformation, which we will subsequently study in Chapter 7 to confirm the deformation modes. All the test conditions have been listed in [Table 6.1](#).

6.1 Mechanical properties by nanoindentation

Nanoindentation experiments have been performed in both the base metal and the HAZ. [Figure 6.1](#) shows a typical example of the load versus displacement curve during the nanoindentation. The Berkovich tip has been captured during the indentation of $\{111\}$ grains in the base metal of the 1 dpa, 0.2 appm He AISI 304L SS sample in [Fig. 6.1 \(a-d\)](#). The ductility of the sample makes the *in-situ* nanoindentation difficult to discern the brittle fracture around the corner areas covered by the Berkovich tip. The *ex-situ* nanoindentation still provides useful information such as hardness and elastic modulus. This has been demonstrated in [Fig. 6.1 \(e-f\)](#), showing the indentation marks with the corresponding grain structure under light optical microscopes. The irradiated AISI 304L SS sample is 23 dpa and 3 appm He with base metal in [Fig 6.1 \(e\)](#) and the HAZ in [Fig. 6.1 \(f\)](#). The TEM lift-out marks under the indents of $\{101\}$ grains can also be seen in [Fig. 6.1 \(e-f\)](#).

6.1.1 Hardness and elastic modulus

Hardness and moduli were probed specifically to the $\{100\}$, $\{110\}$, and $\{111\}$ grains in [Fig. 6.2\(a-b\)](#). Nanoindentations were conducted along the top-down direction consistent with the OIM grain orientation map as shown in [Fig. 6.2\(c-d\)](#) (archive and base metal) and [Fig. 5.11\(b\)](#) (HAZ). These EBSD maps provide the precise location for grain orientation-specific nanoindentation experiments. The number of data points collected for the $\{100\}$, $\{110\}$, and $\{111\}$ grains are 18 and 15, 55, and 9, and 10 and 13 for the unirradiated and irradiated AISI 304L SS sample with 23 dpa, 3 appm He, respectively. Average hardness values in the $\{100\}$, $\{110\}$, and $\{111\}$ directions are 2.93 ± 0.12 GPa, 3.23 ± 0.22 GPa, and 3.24 ± 0.12 GPa for the archive 304L and 3.39 ± 0.19 GPa, 3.87 ± 0.22 GPa, and 3.76 ± 0.25 GPa for the irradiated sample with 23 dpa, 3 appm He,

respectively. The corresponding average moduli are 171 ± 6 GPa, 179 ± 7 GPa, and 184 ± 5 GPa for the archive AISI 304L and 208 ± 3 GPa, 222 ± 9 GPa, and 226 ± 13 GPa for the irradiated sample with 23 dpa, 3 appm He, respectively. The mechanical properties of the archive and base metal are summarized in [Table 6.1](#). For the HAZ, 33, 19, and 41 data points are taken for each orientation plane ([Fig. 1\(c-d\)](#)). The base has a hardness range of 3.4-3.8 GPa and a modulus range of 208-225 GPa. The HAZ has a decrease of anisotropy in both hardness, which decreased to 2.5 GPa, and modulus, which decreased to a range of 201-203 GPa. $\{101\}$ grains have exhibited the largest change of hardness before and after the laser welding. The hardness and modulus versus distance along the indentation have also been given in [Fig. 6.3\(a-b\)](#). The decrease of hardness and modulus implies that the HAZ is softened by the laser welding. Average hardness and moduli with the measurement errors are also listed in [Table 6.2](#).

These results reveal weak grain orientation dependence of hardness and modulus in both the archive and irradiated specimens. However, the irradiation-induced increases in hardness and modulus on $\{110\}$ planes are relatively larger than those on $\{100\}$ and $\{111\}$ planes. Statistical distributions of the hardness and modulus from all 204 indents taken on each specimen (i.e. archive and irradiated 23 dpa, 3 appm He) are shown in [Fig. 6.4\(a-b\)](#). These distributions indicate that the neutron irradiated AISI 304L SS of 23 dpa, 3 appm He exhibits higher hardness and modulus compared to its unirradiated counterparts. Given the weak anisotropy in hardness in both the archive and neutron irradiated AISI 304L SS of 23 dpa and 3 appm He, the average mechanical properties (over all grain orientations) may be a representative indicator of the irradiation effect. The average values of the hardness and modulus are 3.16 ± 0.23 GPa and 178 ± 7 GPa for the archive 304L SS, and 3.70 ± 0.31 GPa and 214 ± 14 GPa for the neutron irradiated AISI 304L SS of 23 dpa and 3 appm He, indicative of irradiation hardening and embrittlement. The HAZ has less anisotropy, thus the average values of the hardness and modulus are also indicative factors of the laser welding annealing. All mechanical quantifications are summarized in [Table 6.2](#).

6.1.2 Post-nanoindentation microstructure

After nanoindentation, TEM lamellae from $\{101\}$ grains were prepared for the archive, base metal and HAZ in the 23 dpa, 3 appm He sample. We will present the archive and base metal first and then follow up with the HAZ.

6.1.2.1 Archive versus irradiated AISI 304L SS

The post-indentation microstructures under the indent are shown in Fig. 6.5(a-b) for archive and neutron irradiated AISI 304L SSs of 23 dpa and 3 appm He. Typical load versus displacement ($P-h$) curves were shown in Fig. 6.5 (c) for both archive and neutron irradiated AISI 304L SSs of 23 dpa and 3 appm He samples along [101] orientation.

For the post-indented archive material, dislocation networks, slip bands and twinning are observed without notable phase transformation (Fig. 6.6(a)). However, in the neutron irradiated specimen of 23 dpa and 3 appm He, a high density of martensite laths was observed, extending from the indentation depth to 10 μm underneath the indenter tip (Fig. 6.6(b)).

In addition, two pop-ins (i.e., load drops or displacement bursts and discontinuities enveloped by two dashed red circles) were observed in the load-displacement curve at indentation depths ~ 410 and ~ 433 nm. The load drops at depth of ~ 410 and 433 nm correspond to the austenite-to-martensite phase transformation, as the martensite phase was not observed at the depth lower than 400 nm (see Fig. 6.7). The pop-ins associated with austenite-to-martensite phase transformation were not present in the load-displacement curve of the unirradiated specimen, suggesting the absence of austenite-to-martensite phase transformation. Assuming the indenter tip is nearly spherical at shallow depth, we can compare the experimental data with the Hertzian elastic contact solution [250,251], also shown in Fig. 6.5(c) (see Chapters 2 and 7).

Bright-field TEM micrographs taken from the indent plastic zone, in Fig. 6.6, show that deformation twins form in the archive specimen, while martensite laths form in its neutron irradiated counterparts. The TEM micrographs of the indented archive specimen taken along $[1\bar{1}1]$ zone axis show $[111]\langle 112\rangle$ twins. The diffraction pattern of neutron irradiated AISI 304L SS of 23 dpa and 3 appm He taken along $[1\bar{3}1]$ zone axis reveals the existence of the fcc γ -Fe austenite phase and the bcc α' martensite phase. The measured lattice constants of the archive and neutron irradiated AISI 304L SS of 23 dpa and 3 appm He are 3.75 ± 0.07 Å and 3.73 ± 0.07 Å, respectively. The measured lattice constant of the α' martensite is 2.83 ± 0.12 Å. The orientation relationship follows the Pitsch model [262], and the transformation follows the Bain deformation rules [262–

264], indicating the plane parallel $(10\bar{1})_\gamma // (21\bar{1})_{\alpha'}$, direction parallel $[0\bar{1}0]_\gamma // [0\bar{1}\bar{1}]_{\alpha'}$, and

Bain distortion strain is type 1 as
$$\begin{bmatrix} 0.75 & 0 & 0 \\ 0 & 1.41 & 0 \\ 0 & 0 & 1.41 \end{bmatrix}.$$

6.1.2.1.1 Bain transformation

The Bain transformation shown can be expressed in the following three Bain strains [265] depending on the compression axis:

$$B_1 = \begin{bmatrix} \beta & 0 & 0 \\ 0 & \alpha & 0 \\ 0 & 0 & \alpha \end{bmatrix}, B_2 = \begin{bmatrix} \alpha & 0 & 0 \\ 0 & \beta & 0 \\ 0 & 0 & \alpha \end{bmatrix}, B_3 = \begin{bmatrix} \alpha & 0 & 0 \\ 0 & \alpha & 0 \\ 0 & 0 & \beta \end{bmatrix}. \quad (6.1)$$

where $\alpha = \sqrt{2}a/a_0$ and $\beta = c/a_0$. The term a_0 is the lattice parameter of the fcc phase, $c \geq a$ is the lattice parameter of the bct phase, and $c = a$ for the bcc structure. The rigid body rotation R can lead to the transformation from fcc to bct/bcc, given as:

$$T = RB_i \quad (6.2)$$

The detailed mathematical derivation of the transformation strain operation can be found in ref. [266]. Typical orientation relationship is listed in Table 6.3 [256,264,267]. In this paper, we adopt the Pitsch model for illustrating the orientation relationship. The corresponding orientation relationship of the plane parallel and direction parallel has been given as:

$$(110)_\gamma // (\bar{1}\bar{1}\bar{2})_{\alpha'} \text{ and } [001]_\gamma // [1\bar{1}0]_{\alpha'} \quad (6.3)$$

Based on the parallels from determining the conjugation of the strain variants, we can also use [268]:

$$(010)_\gamma // (101)_{\alpha'} \text{ and } [101]_\gamma // [\bar{1}11]_{\alpha'} \quad (6.4)$$

All the Pitsch orientation relationships and the corresponding transformation strain have been summarized in Table 6.4.

In the neutron irradiated 304L SS, the irradiation-induced cavity structure is embedded with deformation-induced α' martensite, as shown in Fig. 6.8(a) at a depth of $\sim 10 \mu\text{m}$ under the indenter

tip. Red arrows identify martensite laths on the $[\bar{1}\bar{3}1]$ zone axis. Fig. 6.8(b) shows that the cavities and martensite laths coexist without interfering each other. High resolution TEM (HRTEM) of the martensite-lath tips reveals an incoherent martensite-matrix interface, Fig. 6.8(c), indicating the difference in lattice structure between the matrix and the martensitic phases. HRTEM of the interface between a martensite needle and a void, Fig. 6.8(d), reveals the incoherent interface between the matrix and the void, showing a lattice misfit ~ 0.24 where the matrix is the fcc γ phase at the $[\bar{1}\bar{3}1]$ orientation, whereas the martensite is the bcc α' phase at the $[\bar{1}\bar{3}1]$ orientation. The martensitic phase has a stronger contrast in HRTEM compared with the matrix and the void, due to the HRTEM phase-contrast effect.

6.1.2.2 Base metal versus HAZ

After laser welding, we have observed softening in the HAZ compared with the irradiated base metal. Figure 6.9 directly compares the post-indentation microstructure of the base metal and the HAZ. Two different pathways are observed between these two regions. In the base metal, the deformation-induced martensite laths (Fig. 6.9(a)) have been confirmed with the diffraction pattern (Fig. 6.9(b)). The bright-field TEM micrograph in Fig. 6.9(a) is captured along the $[\bar{1}\bar{3}1]$ zone axis in the matrix –fcc γ austenite phase (lattice is depicted by a straight white box). The minor diffraction spots are the martensite laths-bcc α' martensitic phase (lattice is depicted by a dashed red box). The orientation relationship follows the Pitsch shear model [268] with an orientation parallel $[001]_{\gamma} // [\bar{1}01]_{\alpha'}$ and plane parallel $(\bar{1}\bar{1}0)_{\gamma} // (\bar{1}\bar{2}\bar{1})_{\alpha'}$. Martensite laths have also been observed across the irradiation-induced cavity in Fig. 6.9(c). The HAZ has undergone a different path as the $\gamma \rightarrow \varepsilon \rightarrow \alpha'$ transformation. The schematic diagram is shown in Fig. 2.30. The bright-field TEM of Fig. 6.9(d) shows the formation of hcp- ε shear bands beneath the indent. The diffraction pattern in Fig. 6.9(e-f) further reveals the crystallography structure of these two plates. Fig. 6.9(f) indicates the two hcp- ε plates intersect and emerge into α' martensite in the intersection.

The orientation relationship of this $\gamma \rightarrow \varepsilon \rightarrow \alpha'$ transformation can be referred to as the Kurdjumov-Sachs (K-S) model [269]. The orientation parallel is $[\bar{1}10]_{\gamma} // [11\bar{2}0]_{\varepsilon} // [1\bar{1}1]_{\alpha'}$ and the plane is $(111)_{\gamma} // (0002)_{\varepsilon} // (011)_{\alpha'}$. The classical BBOC model can be referred to in order to illustrate the dislocation behavior during this transformation (more information can be found in Chapter 7). The two ε plates have two arrays of $a/6\langle 112 \rangle$ partial dislocations on every second and

every third $\{111\}_\gamma$ plane. The ε_1 (T/2) has an average of 1/2 of the twinning shear whereas the ε_2 (T/3) has an average of 1/3 of the twinning shear. The resulting prismatic bcc structure with a closed-packed direction parallel $\langle 110 \rangle_\gamma // \langle 111 \rangle_{\alpha'}$ forms at the intersection of these two hcp- ε plates.

To determine the stress dependency of the deformation-induced martensitic transformation, post-indentation microstructures at different stress levels are shown in Fig. 6.10. Since the size factor between the base metal and the HAZ does not drastically deviate from each other, we used an average value of the hardness and modulus for the finite element modeling for simplicity. The stress-dependent deformation mechanisms have been found by variation of the indentation depths. At a shallower indentation depth of ~ 200 nm (Fig. 6.10(a-b)), we have not seen any phase transformation but only dislocation dissociation in both the base and the HAZ. Figure 6.10(c) simulates the Von Mises [258] stress map. Regions in red and orange represent the plastic zone (magenta box) corresponding to the microstructures in Fig. 6.10(a-b). At a larger indentation depth of ~ 400 nm (Fig. 6.10(d-e)), we can see the two different modes of martensitic transformation in the base metal and the HAZ. This time, the magenta box in Fig. 6.10(f) at approximately 500 nm beneath the indent is no longer the plastic zone. From the depth controlled nanoindentation in Fig. 6.7 and Fig. 6.10, the increased stress level reveals the martensitic transformation is indeed induced by stress. In the base metal, α' martensite laths have been observed. The HAZ has two hcp- ε plates formed. Compared to the largest ~ 1500 nm depth indent, there is no nucleation of α' martensite at the intersection of the ε plates. The archive material has only experienced twinning under the same loading conditions.

6.2 Mechanical properties by micropillar compression

Microcompression experiments are conducted on both the base metal and the HAZ along the same orientation, enabling a direct comparison of the deformation mechanisms across the weldment of irradiated AISI 304L SS of 1 dpa, 0.2 appm He. The deformation mechanism of the neutron irradiated weldment is studied using transmission electron microscopy.

6.2.1 Hardness and modulus

Stress-strain curves from the micropillar compression tests on $\{101\}$ grains in both the base metal and the HAZ are presented in Fig. 6.11(a-b). The base metal has an average yield stress of 999 ± 54 MPa, while the HAZ has a lower average yield stress of 828 ± 144 MPa. The effective modulus, Y_{eff} , is calculated from the secant modulus from the stress-strain curve (Fig. 6.11(c-d)). The average modulus of base metal $\{101\}$ grains is 48 ± 21 GPa, whereas the average modulus of the HAZ $\{101\}$ grains is 31 ± 17 GPa. Stress-strain curves from other grain orientations can be found in Fig. 6.12; similar trends revealing laser weld-induced softening are observed across all grain orientations.

From the stress-strain curves (Fig. 6.11(a-b)) of the $\{101\}$ grains, load drops can be observed during compression tests on the HAZ (marked by arrows in Fig. 6.11(b)). However, no such events are observed in the base metal. The ductile slip during compression in the base metal is more predominant than the HAZ shown in Fig. 6.11(c). These load drops are believed to correspond to twinning events, which can be categorized into three regions as shown in Fig. 6.11(d): incipient twinning (twinning nucleation), twinning migration, and twinning hardening (twin-twin interaction) [270]. Confirmation of the twinning process is obtained through post-compression TEM characterization and will be presented later in this chapter.

6.2.2 Post-compression microstructure

Figure 6.13 compares representative *in-situ* SEM microcompression tests on $\{101\}$ grains from the base and the HAZ. In the base metal, the slip initiates at a strain of ~ 0.07 (Fig. 6.13(b)); the slip planes become evident in Fig. 3(b-d), marked by blue arrows. The final strain reached is ~ 0.25 (Fig. 6.13(d)). Post-compression TEM reveals dissociation of dislocations in Fig. 6.13(e), with a deformation-induced phase transformation in the base metal, Fig. 6.13(f). Specifically, the face centered cubic (fcc)- γ phase forms needles of the hexagonal close-packed (hcp)- ϵ martensite. The crystallographic orientation relationship of these two phases follows the direction parallel $[110]_{\gamma} \parallel [\bar{2}110]_{\epsilon}$ and plane parallel $(1\bar{1}1)_{\gamma} \parallel (0001)_{\epsilon}$ [271]. This finding is consistent with our previous studies of deformation-induced phase transformation by nanoindentation on the same irradiated AISI 304L SS base metal [140] and the nanoindentation results in section 6.1.2. No deformation-induced twins are found in the base metal. Fig. 6.13(g-j) shows a representative

micropillar compression on a (101) grain in the HAZ. Incipient twinning begins to occur at a strain of ~ 0.05 (Fig. 6.13(h), marked by red arrows). With continued loading, the deformation twins migrate; this phenomenon can be seen in the *in-situ* video [272] and in Fig. 6.13(i) as multiple twins merge with decreasing space between them. As the strain further increases, twinning hardening begins to dominate (Fig. 6.13(j)). The final strain is ~ 0.22 . These deformation twins are confirmed by bright field and dark field TEM characterization of the post-compression microstructure (Fig. 6.13(k-l)). The average twin spacing is 294 ± 46.1 nm. Microtwins have widths larger than 200 nm (Fig. 6.13(l)), while nanotwins have widths less than 20 nm (see Fig. 6.14). No deformation-induced martensite is observed in the HAZ. Deformation behavior in the unirradiated archive shows similar twinning as the nanoindentation (see Fig. 6.15). Figure 6.16 summarizes the deformation behavior of the base metal and HAZ in the 1 dpa, 0.2 appm He AISI 304L SS sample.

The observed slip/twinning planes are confirmed by reconstruction of the pillar geometry using the 3D SOLIDWORKS® software. Each of the four $\{111\}$ family planes is examined mathematically using the Euler angle rotation matrix to match the equivalent planes with the calculated normal vector of the planes observed in the *in-situ* SEM video. The plane observed in the base metal pillar corresponds to the $(11\bar{1})$ (S1) slip plane (Fig. 6.13(m)), while the HAZ pillar has two sets of twinning planes, (111) (T1) and $(1\bar{1}1)$ (T2), as shown in Fig. 6.13(n).

The Schmid factors (SFs) of the slip $\{111\}\langle 011\rangle$ and twinning $\{111\}\langle 112\rangle$ systems along the $[101]$ compression axis are 0.41 and 0.24, respectively. Table 6.5 summarizes the SFs for slip and twinning systems along the $[101]$ loading direction. The SFs are subsequently used to calculate the critical resolved shear stress (CRSS); a smaller SF indicates a lower CRSS on the deformation plane. In the specimens studied here, the base metal has a CRSS of 410 ± 22.2 MPa, while the HAZ has a CRSS on the twinning plane of 199 ± 34.6 MPa. The difference in the CRSS between the base metal and the HAZ is more significant than that difference in yield stress; this is attributed to twinning, which significantly reduces the CRSS in the HAZ. The Thompson tetrahedron (see Fig. 6.17) is used to visualize possible twinning systems in an fcc crystal. The closest-packed planes for twinning are represented by each face of the Thompson tetrahedron (i.e., BCD- α , ACD- β , ABD- γ and ABC- δ). The dashed lines represent the possible twinning directions for partial

dislocations, whereas the edges of the tetrahedron correspond to slip directions. For instance, δB and αC are the observed twinning systems, $(111)[\bar{2}11]$ and $(\bar{1}\bar{1}1)[2\bar{1}\bar{1}]$, respectively, confirming the SOLIDWORKS® rendering of the deformation planes.

Table 6.1 Mechanical testing on all conditions.

Coin/Triangle	He (appm)	Dose (dpa)	Temperature (°C)	Nanoindentation	Micropillar compression
5D2	0.2	1	415	Completed	Completed
3A2	3	23	430	Completed	Future
3E3	8	28	415	Completed	-

Table 6.2 Hardness and modulus measurement by nanoindentation of the laser welds of irradiated AISI 304L SS of 23 dpa, 3 appm He.

Mechanical properties		Unirradiated archive	Neutron irradiated base metal	HAZ
Hardness [GPa]	100	2.93 ± 0.12	3.39 ± 0.19	2.53 ± 0.24
	110	3.23 ± 0.22	3.87 ± 0.22	2.47 ± 0.11
	111	3.24 ± 0.12	3.76 ± 0.25	2.51 ± 0.18
	Average	3.16 ± 0.23	3.70 ± 0.31	201 ± 7
Modulus [GPa]	100	179 ± 7.07	208 ± 3.40	2.50 ± 0.20
	110	184 ± 4.56	222 ± 9.38	201 ± 7
	111	208 ± 3.40	226 ± 12.7	203 ± 8
	Average	178 ± 7.20	214 ± 14.2	198 ± 14
Deformation mode		Twinning	$\gamma \rightarrow \alpha'$	$\gamma \rightarrow \varepsilon \rightarrow \alpha'$

Table 6.3 Summary of the fcc-bcc orientation relationship.

Model	Plane parallel	Direction parallel	No. of variants
Bain [265]	$\{010\}_\gamma // \{010\}_{\alpha'}$	$\langle 001 \rangle_\gamma // \langle 101 \rangle_{\alpha'}$	-
Kurdjumov-Sachs(K-S)[269]	$\{111\}_\gamma // \{110\}_{\alpha'}$	$\langle 110 \rangle_\gamma // \langle 111 \rangle_{\alpha'}$	24
Nishiyama-Wassermann (N-W) [273,274]	$\{111\}_\gamma // \{110\}_{\alpha'}$	$\langle 011 \rangle_\gamma // \langle 001 \rangle_{\alpha'}$	12
Greninger-Troiano (GT) [275]	$\{111\}_\gamma \sim 1^\circ$ to $\{110\}_{\alpha'}$	$\langle 121 \rangle_\gamma \sim 2^\circ$ to $\langle 110 \rangle_{\alpha'}$	24
Pitsch [268]	$\{001\}_\gamma // \{101\}_{\alpha'}$	$\langle 110 \rangle_\gamma // \langle 111 \rangle_{\alpha'}$	12

Table 6.4 The Pitsch orientation relationships.

Variant No.	Plane parallel	Direction parallel	Bain Variant
1	$(01\bar{1})_{\gamma} // (\bar{1}2\bar{1})_{\alpha'}$	$[100]_{\gamma} // [10\bar{1}]_{\alpha'}$	B_2
2	$(\bar{1}01)_{\gamma} // (\bar{1}\bar{1}2)_{\alpha'}$	$[010]_{\gamma} // [\bar{1}10]_{\alpha'}$	B_3
3	$(1\bar{1}0)_{\gamma} // (2\bar{1}\bar{1})_{\alpha'}$	$[001]_{\gamma} // [0\bar{1}1]_{\alpha'}$	B_1
4	$(110)_{\gamma} // (12\bar{1})_{\alpha'}$	$[001]_{\gamma} // [101]_{\alpha'}$	B_2
5	$(0\bar{1}1)_{\gamma} // (1\bar{1}2)_{\alpha'}$	$[\bar{1}00]_{\gamma} // [\bar{1}\bar{1}0]_{\alpha'}$	B_3
6	$(\bar{1}0\bar{1})_{\gamma} // (2\bar{1}\bar{1})_{\alpha'}$	$[010]_{\gamma} // [01\bar{1}]_{\alpha'}$	B_1
7	$(\bar{1}\bar{1}0)_{\gamma} // (\bar{1}2\bar{1})_{\alpha'}$	$[001]_{\gamma} // [\bar{1}01]_{\alpha'}$	B_2
8	$(011)_{\gamma} // (\bar{1}\bar{1}2)_{\alpha'}$	$[100]_{\gamma} // [110]_{\alpha'}$	B_3
9	$(10\bar{1})_{\gamma} // (21\bar{1})_{\alpha'}$	$[0\bar{1}0]_{\gamma} // [0\bar{1}\bar{1}]_{\alpha'}$	B_1
10	$(\bar{1}10)_{\gamma} // (\bar{1}21)_{\alpha'}$	$[00\bar{1}]_{\gamma} // [\bar{1}0\bar{1}]_{\alpha'}$	B_2
11	$(0\bar{1}\bar{1})_{\gamma} // (\bar{1}\bar{1}2)_{\alpha'}$	$[100]_{\gamma} // [1\bar{1}0]_{\alpha'}$	B_3
12	$(101)_{\gamma} // (2\bar{1}1)_{\alpha'}$	$[010]_{\gamma} // [011]_{\alpha'}$	B_1

Table 6.5 Schmid factors (SFs) for slip and twinning systems along the [101] loading direction.

Slip	$(111)[01\bar{1}]$	$(111)[\bar{1}10]$	Twinning	$(111)[\bar{2}11]$	$(111)[11\bar{2}]$
SF	0.41	0.41	SF	0.24	0.24
Slip	$(1\bar{1}\bar{1})[011]$	$(1\bar{1}\bar{1})[\bar{1}\bar{1}0]$	Twinning	$(1\bar{1}\bar{1})[2\bar{1}\bar{1}]$	$(1\bar{1}\bar{1})[1\bar{1}\bar{2}]$
SF	0.41	0.41	SF	0.24	0.24

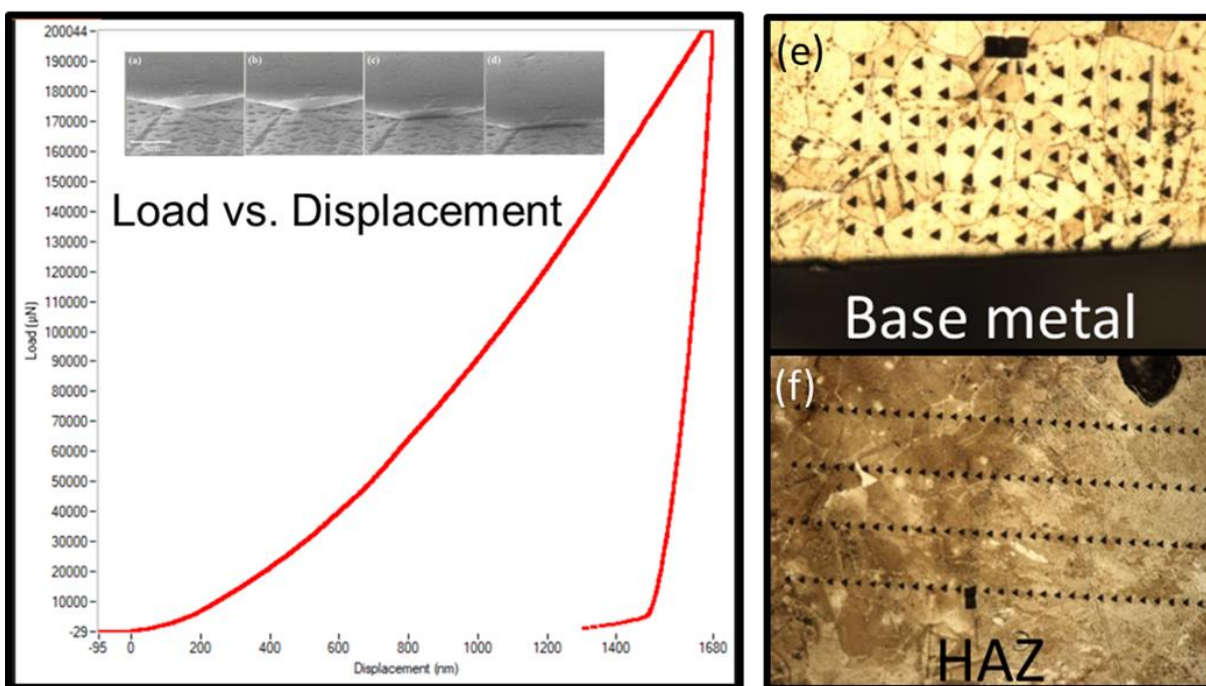


Figure 6.1 Typical load-displacement curve of the nanoindentation. (a-d) snapshots of the Berkovich tip indenting the (111) grain of the base metal in the 1dpa, 0.2 appm He sample. (e-f) Indentation mapping with the grain structure under light optical microscope. (e) Indentation marks with TEM lift-out in the base metal of the 23 dpa, 3 appm He sample. (f) Indentation marks with TEM lift-out in the HAZ of the 23 dpa, 3 appm He sample.

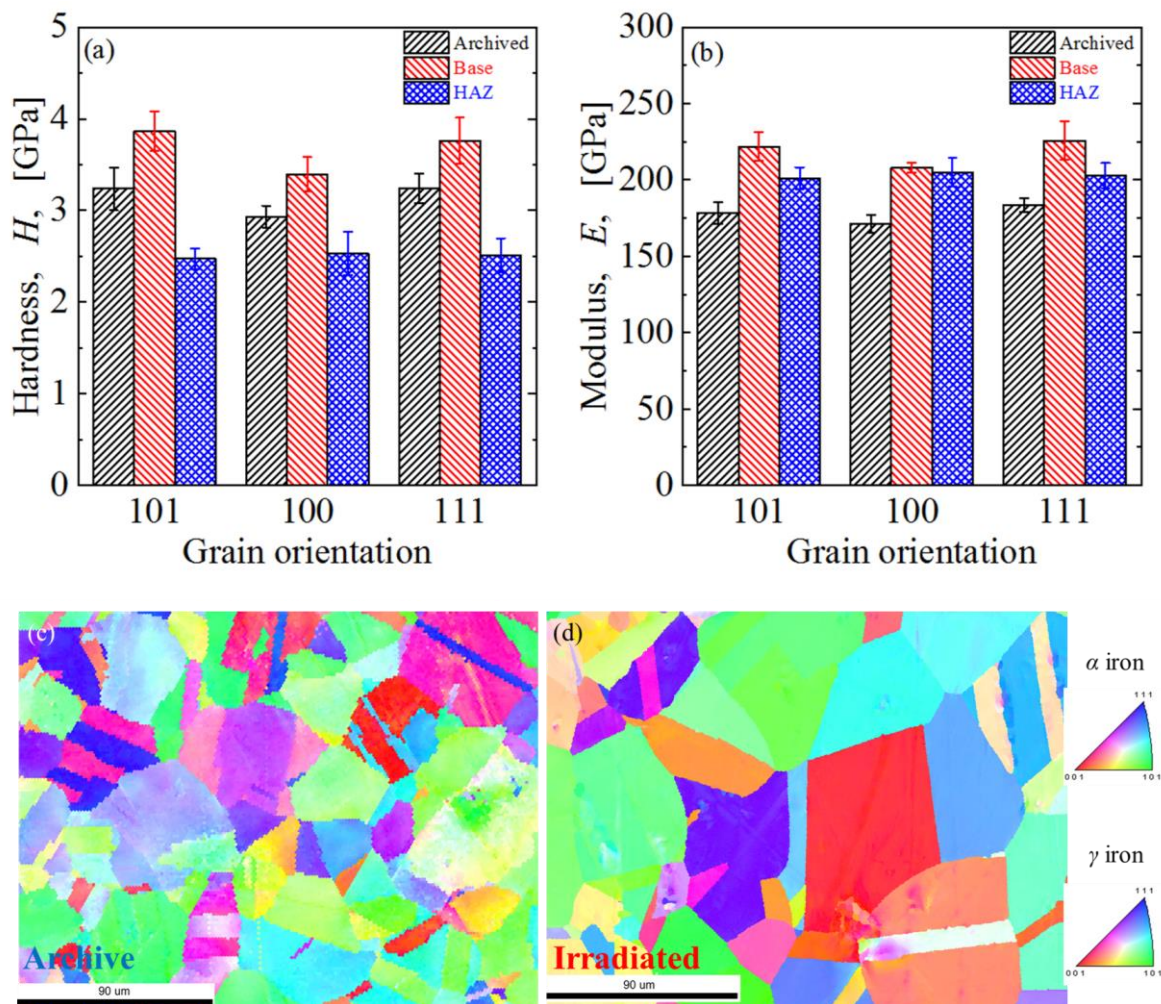


Figure 6.2 Nanoindentation measurements of (a) hardness and (b) modulus on $\{100\}$, $\{101\}$ and $\{111\}$ grains of the archive AISI 304L SS, base metal, and HAZ. OIM maps of area of the grains tested by the nanoindentation experiments. (c) Corresponding indenting area of the archive sample. (d) Corresponding indenting area of the irradiated base metal.

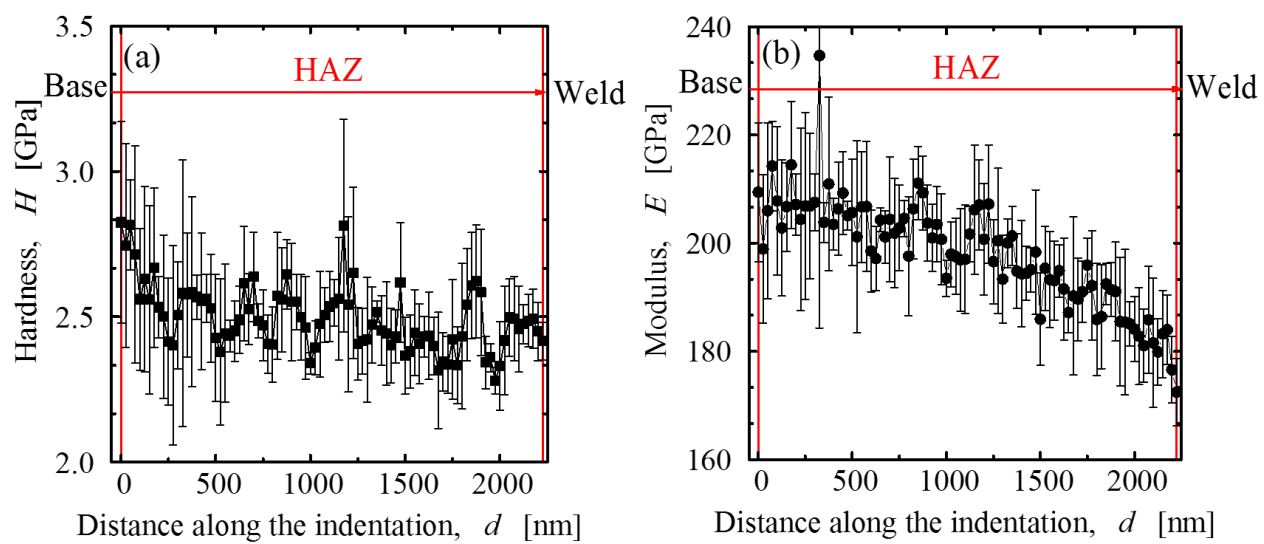


Figure 6.3 (a) Hardness and (b) modulus along the indentation across the HAZ.

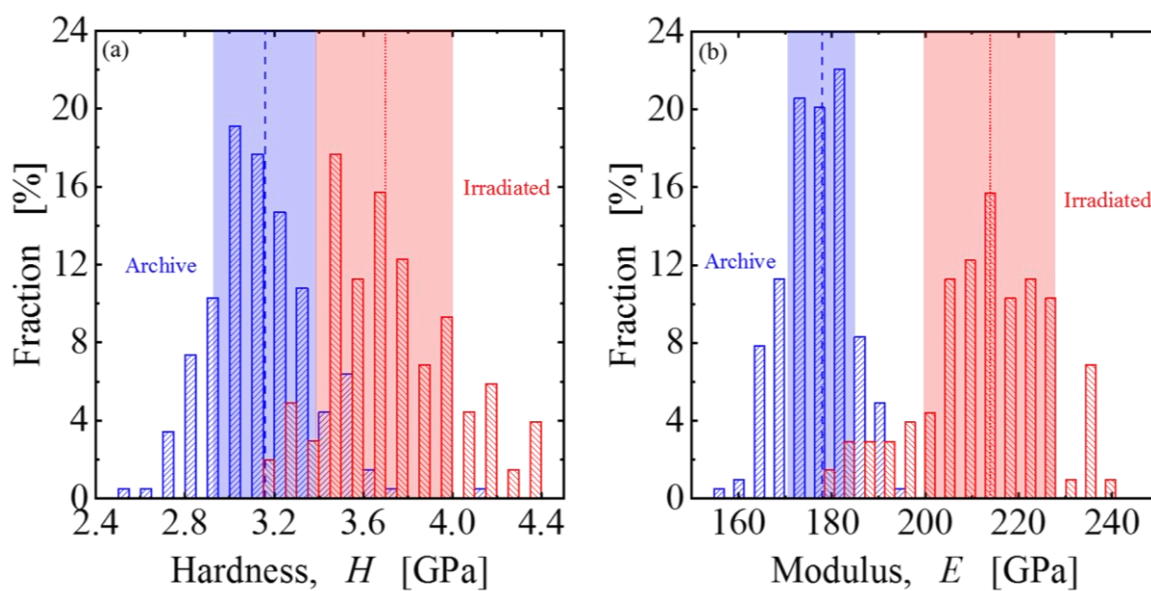


Figure 6.4 Comparison of hardness and modulus data from all indentation experiments in the archive and irradiated base metal of AISI 304L SS of the 23 dpa and 3 appm He condition. (a) Hardness histogram. (b) Modulus histogram.

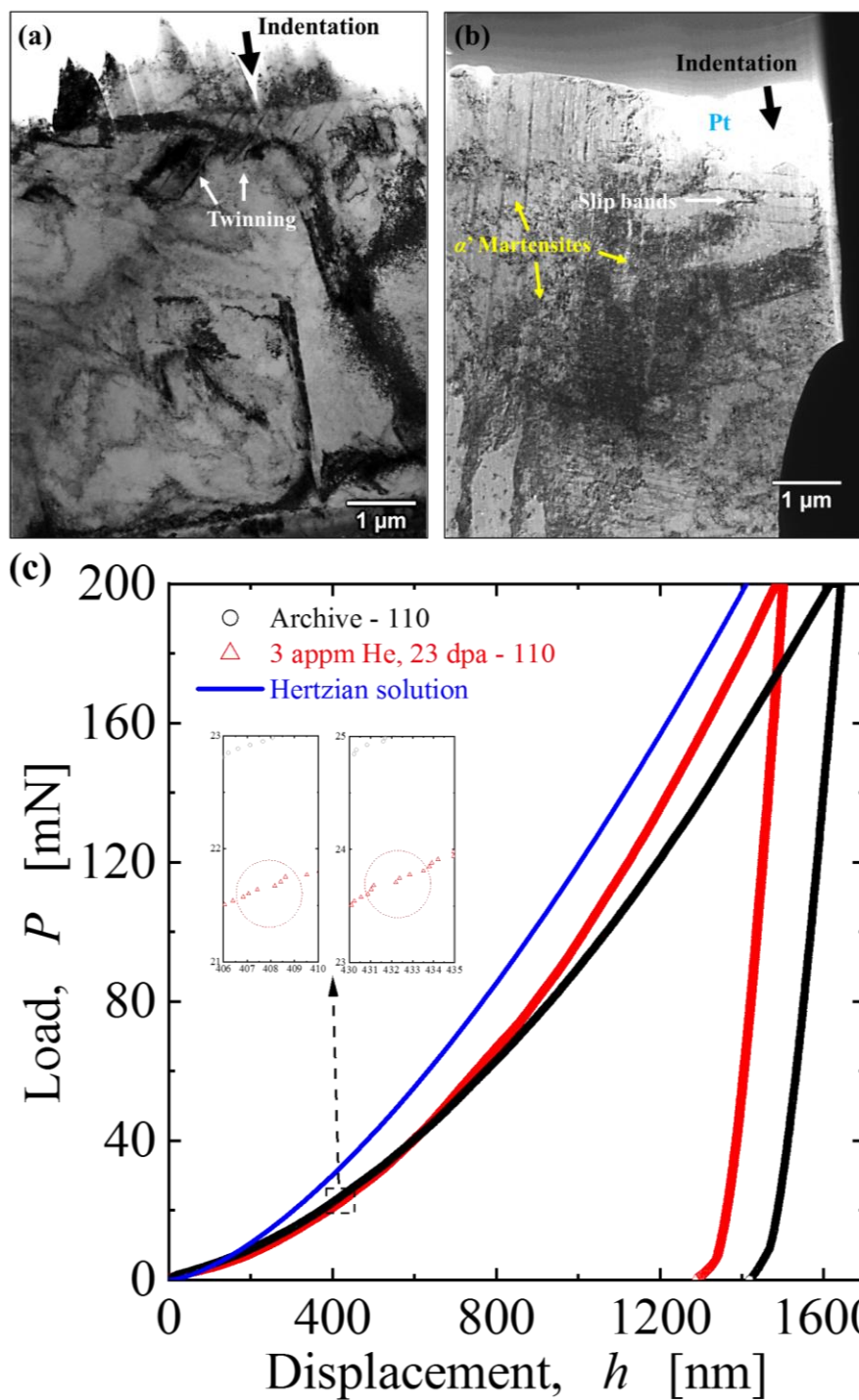


Figure 6.5 TEM micrographs of the post-indentation microstructure: (a) archive AISI 304L SS containing deformation twins, and (b) irradiated AISI 304L SS of the 23 dpa and 3 appm He containing martensite needles. (c) Comparison of load-displacement curves of the archive (black line) and irradiated (red line) AISI 304L SS on {110} grains with the Hertzian elastic solution (blue line). Dotted red circles indicate the initiation of pop-ins.

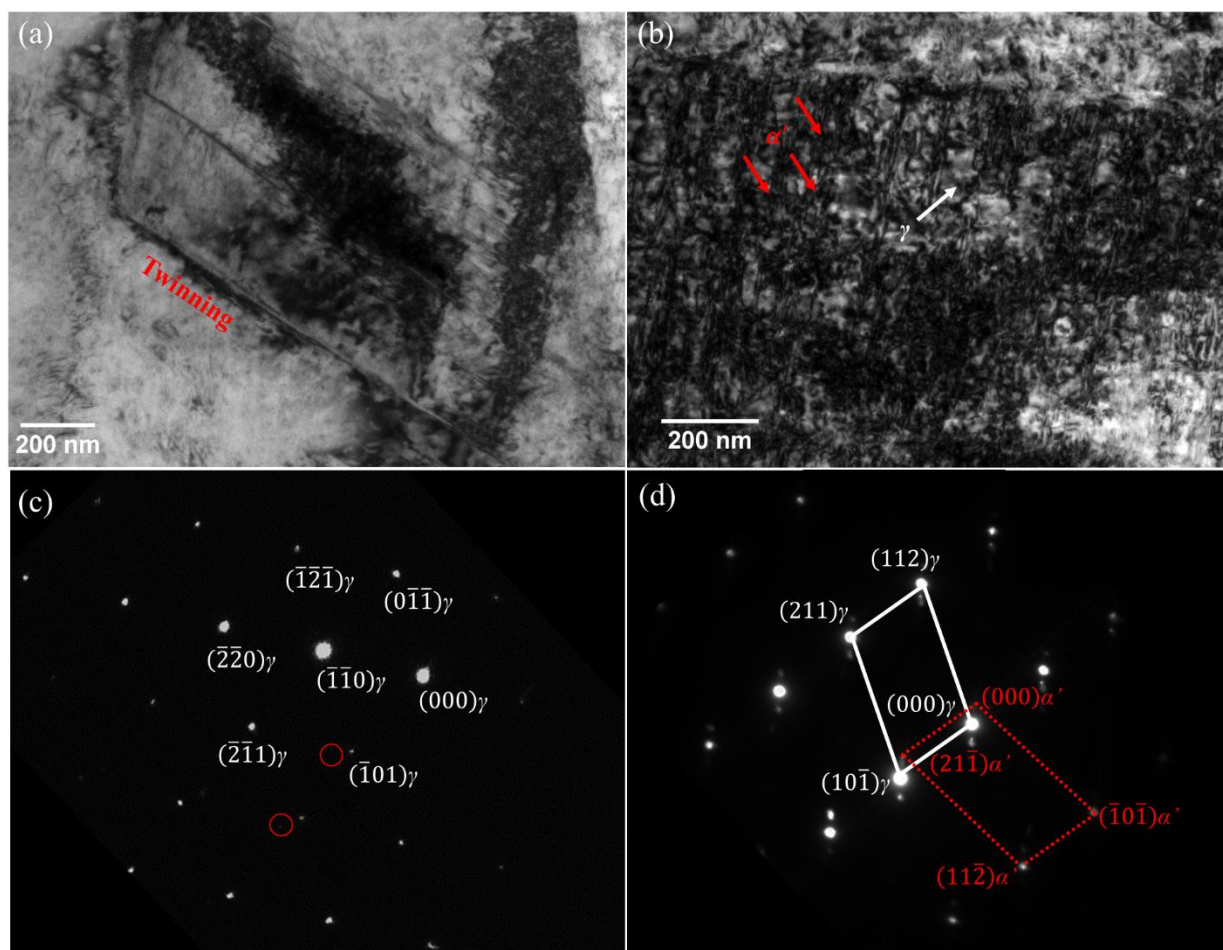


Figure 6.6 Bright-field TEM micrographs of the post-indentation microstructure of: (a) archive AISI 304L SS at $[1\bar{1}\bar{1}]$ zone axis and (b) neutron irradiated AISI 304L SS at $[1\bar{3}\bar{1}]$ zone axis. Diffraction patterns of (c) archive matrix, red circles represent the minor diffraction spots of the twins and (d) major spots indicate the matrix (solid white box) and the minor spots indicate the α' martensite laths (dashed red box).

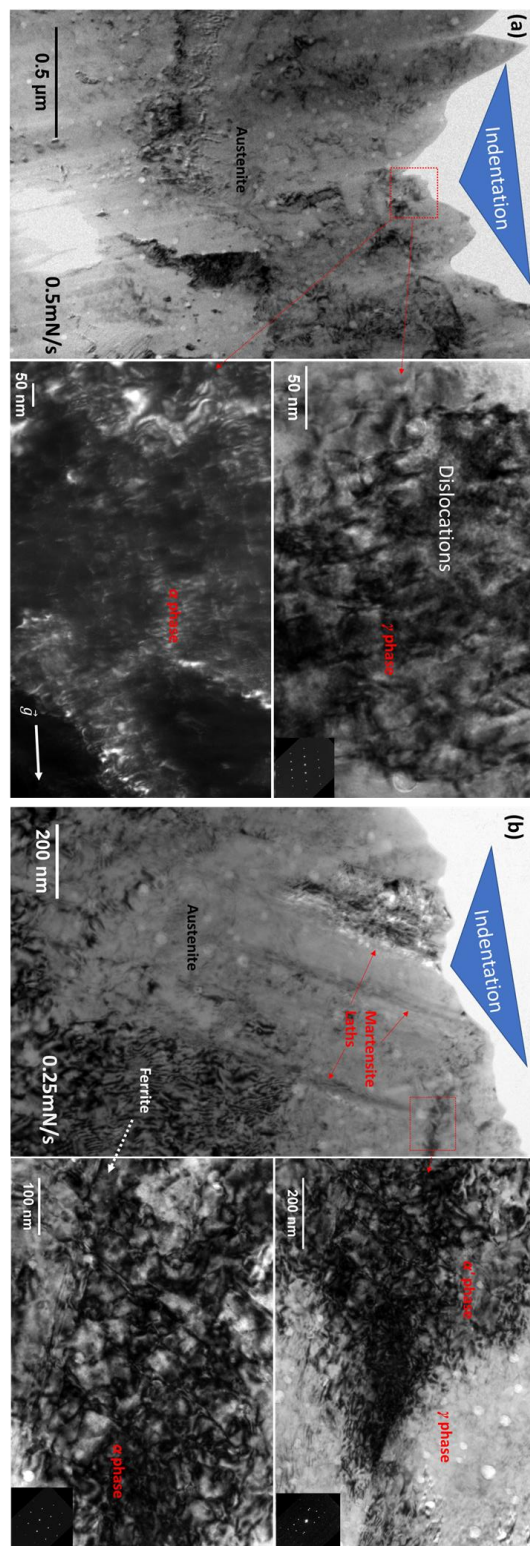


Figure 6.7 Comparison of post-indentation microstructure of neutron irradiated 304L SS under different load rates (a) ~200 nm (0.25 mN/s for 40s) with no phase transformation and (b) ~400 nm (0.5 mN/s for 40s) with martensitic phase transformation.

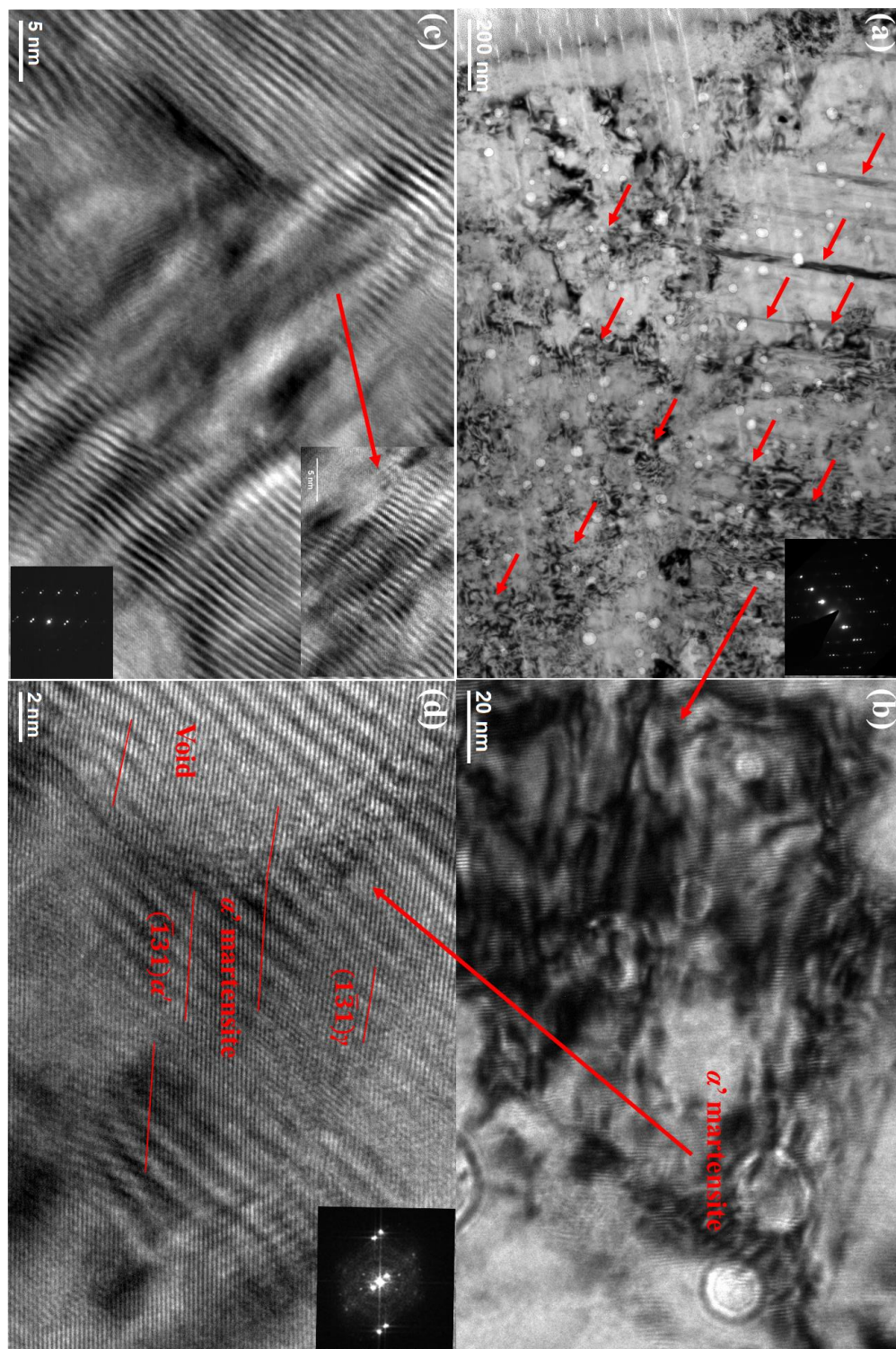


Figure 6.8 TEM micrographs of nanoindentation-induced α' martensite in irradiated AISI 304L SS; (a) bright-field TEM of martensite (red arrows) with cavities, (b) enlarged image of the martensite, (c) HRTEM of martensite and zoom-in image of the martensite tips, and (d) HRTEM of an incoherent void-martensite interface.

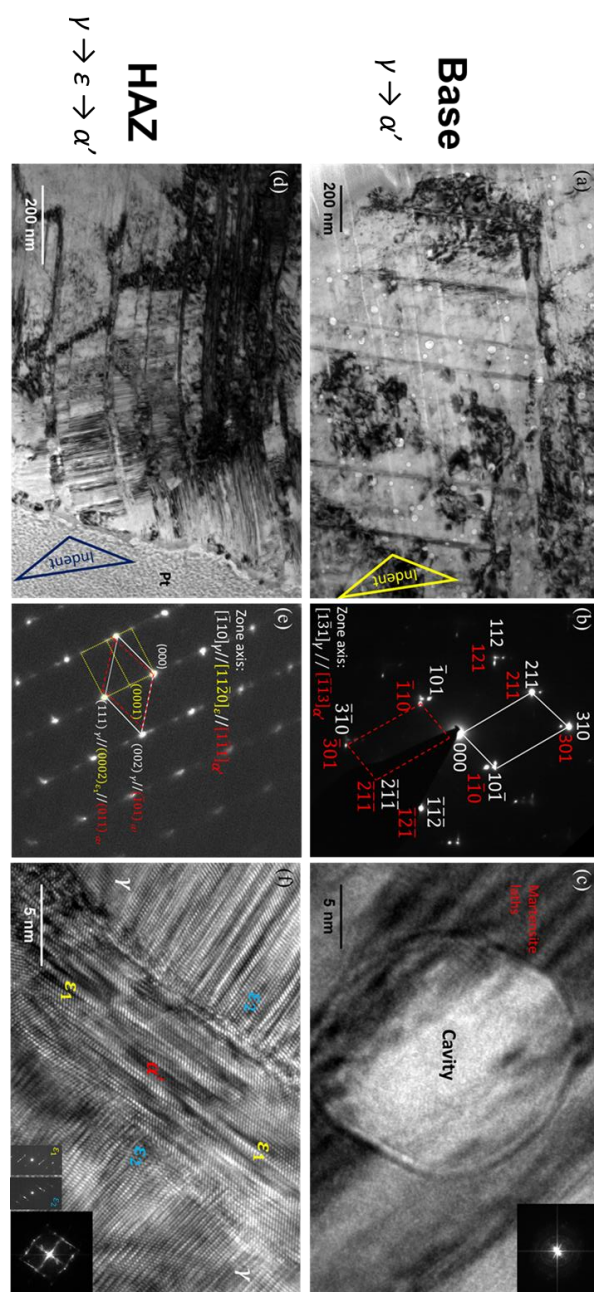


Figure 6.9 Comparison of post-indentation microstructure of the base (a-c) and the HAZ (d-f) with a loading rate of 5 mN/s and an indentation depth of 1500 nm. (a) BFTEM micrograph of martensite laths in the base metal. (b) Corresponding diffraction pattern in (a). (c) HRTEM image of martensite laths across the cavity. (d) BFTEM micrograph of martensite laths in the HAZ metal. (e) Corresponding diffraction pattern in (d). (f) HRTEM images of formation of bcc- α' at the intersection region of two hcp- ϵ plates. Solid white box represents the reciprocal lattice of fcc- γ matrix. Dashed red box represents the reciprocal lattice of the bcc- α' martensite. Dotted yellow box represents the reciprocal lattice of the hcp- ϵ martensite.

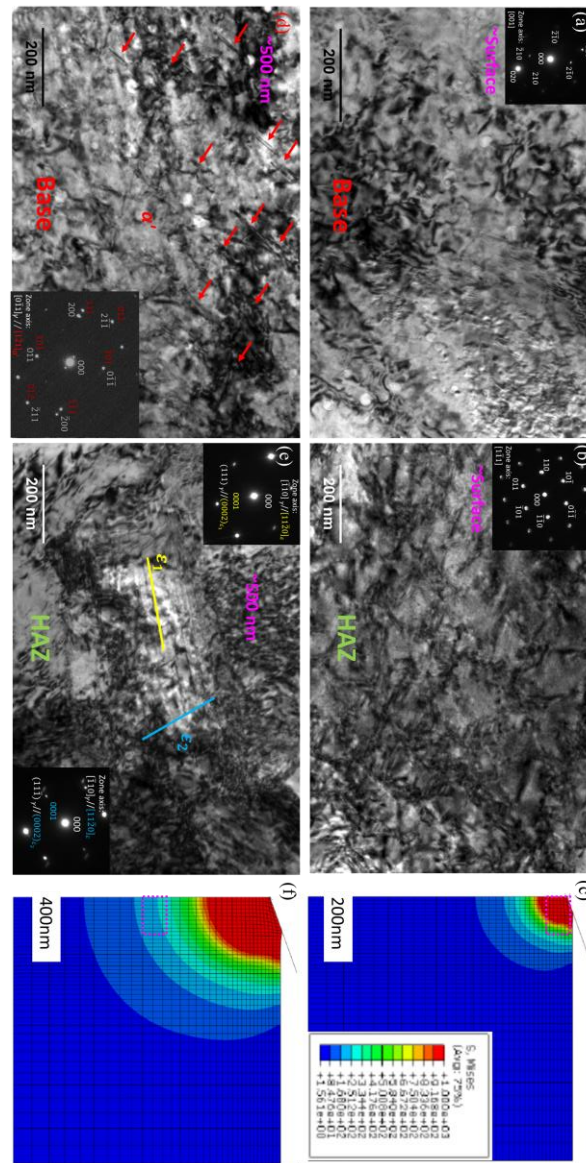


Figure 6.10 Formation of martensite laths at different indentation depths of 200 nm (a-b) and 400nm (d-e). (a) BFTEM micrograph of the dislocations near the surface under the indent in the base metal with a loading rate of 0.25 mN/s. (b) BFTEM micrograph of the dislocations near the surface under the indent in the HAZ with a loading rate of 0.25 mN/s. (c) FEM maps of the stress field under a 200 nm indent of the AISI 304L SS. (d) BFTEM micrograph of α' martensite laths at a depth of ~ 500 nm under the indent in the base metal with a loading rate of 0.5 mN/s (red arrows indicate the α' martensite laths). (e) BFTEM micrograph of the two hcp- ϵ martensite laths at a depth of ~ 500 nm under the indent in the HAZ with a loading rate of 0.5 mN/s. (f) FEM maps of the stress field under a 400 nm indent of the AISI 304L SS. Magenta box in (c) and (f) corresponds to the approximate depth in (a-b) and (d-e), respectively.

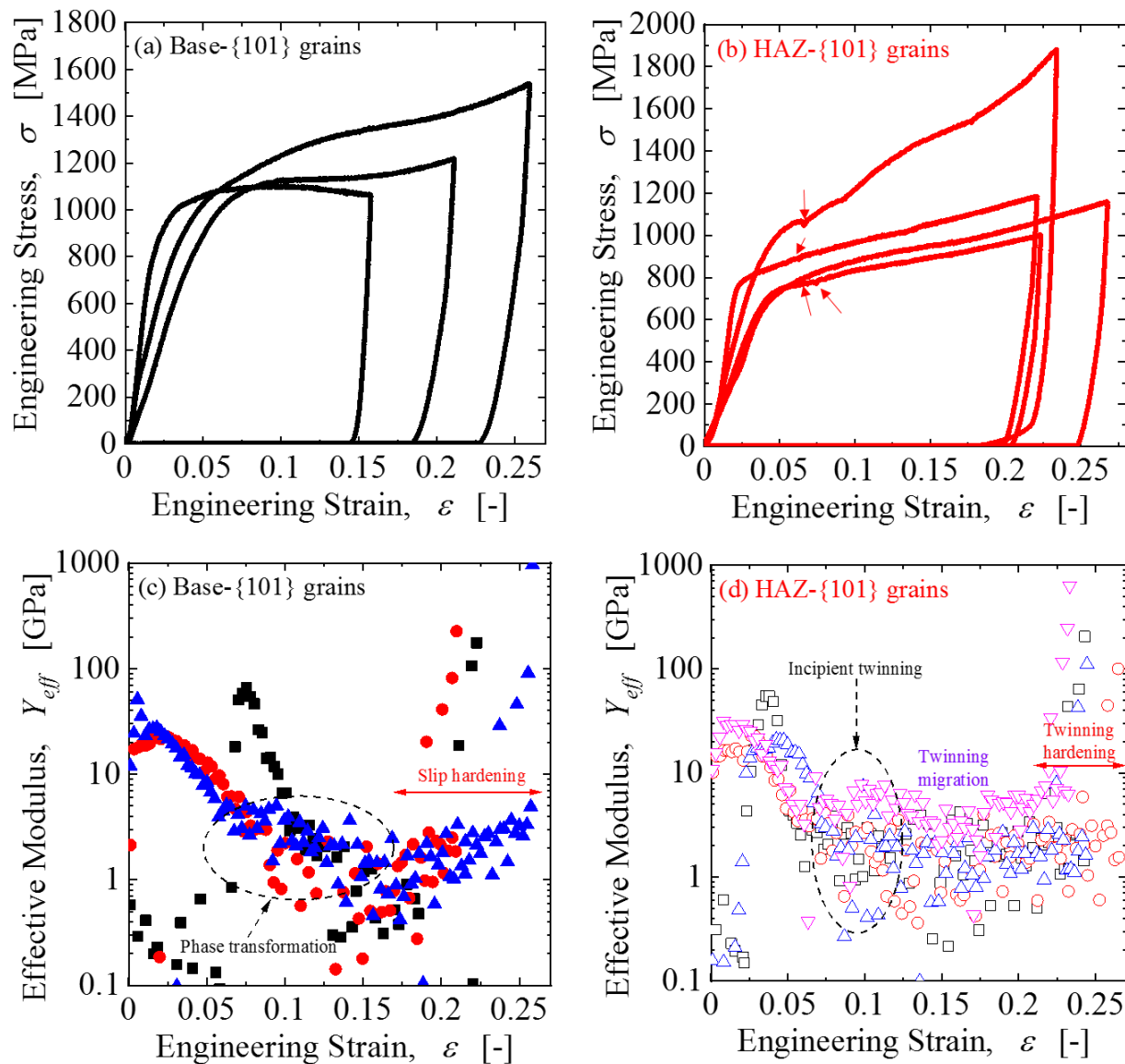


Figure 6.11 Micropillar compression engineering stress-strain curves for tests performed on AISI 304L SS welds of 1 dpa and 0.2 appm He along $\{101\}$ grains in (a) base metal and (b) the HAZ. Effective modulus, Y_{eff} , determined as secant modulus during the compression tests of (c) base metal and (d) HAZ.

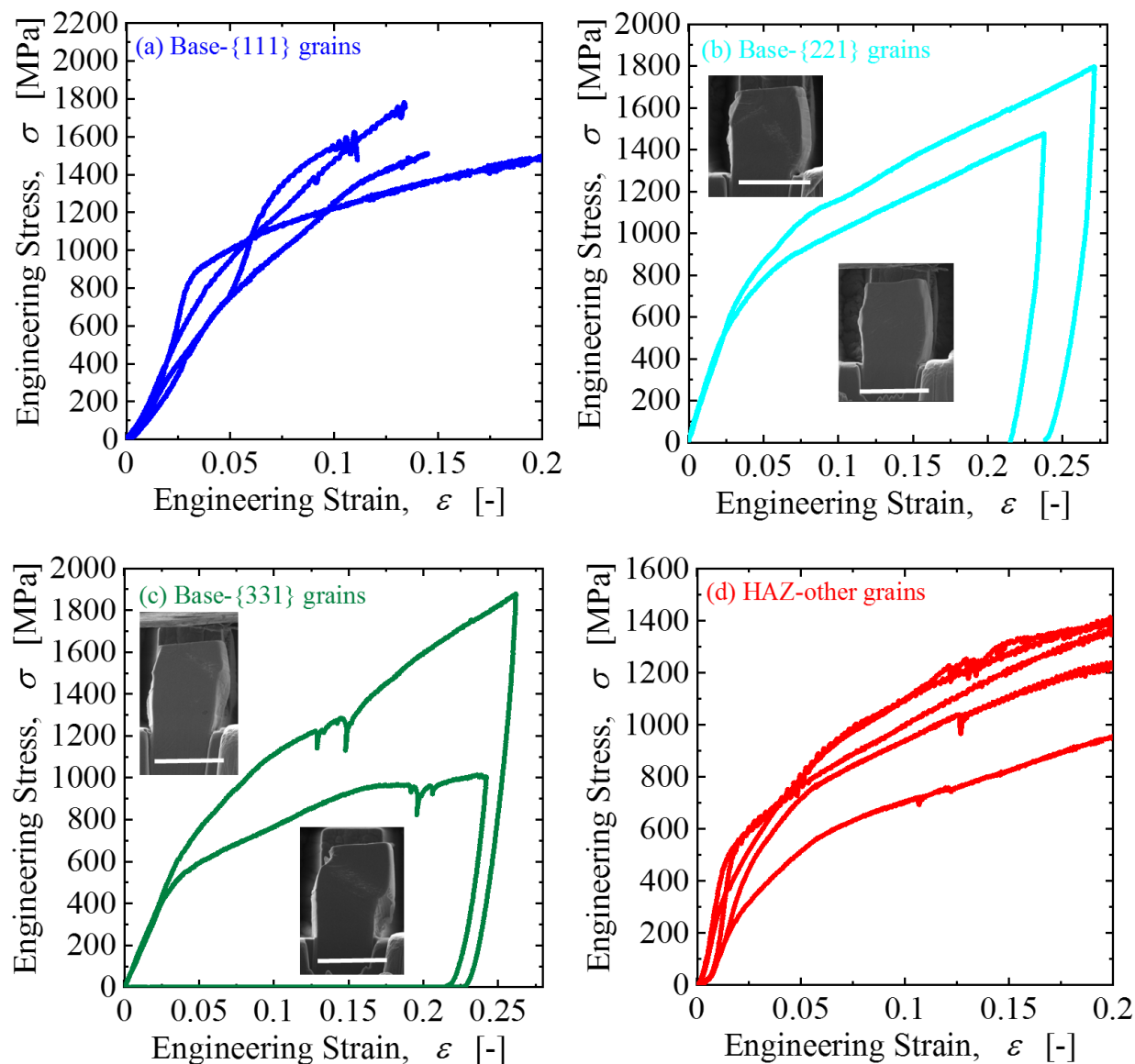


Figure 6.12 Additional stress-strain curves from pillar compression experiments of the laser welds of irradiated AISI 304L SS of 1 dpa, 0.2 appm He: (a) base metal $\{111\}$ grains (b) base metal $\{221\}$ grains with post-compression pillar images, (c) base metal $\{331\}$ grains with post-compression pillar images, in which load drops correspond to slip events, and (d) the HAZ random grain orientations.

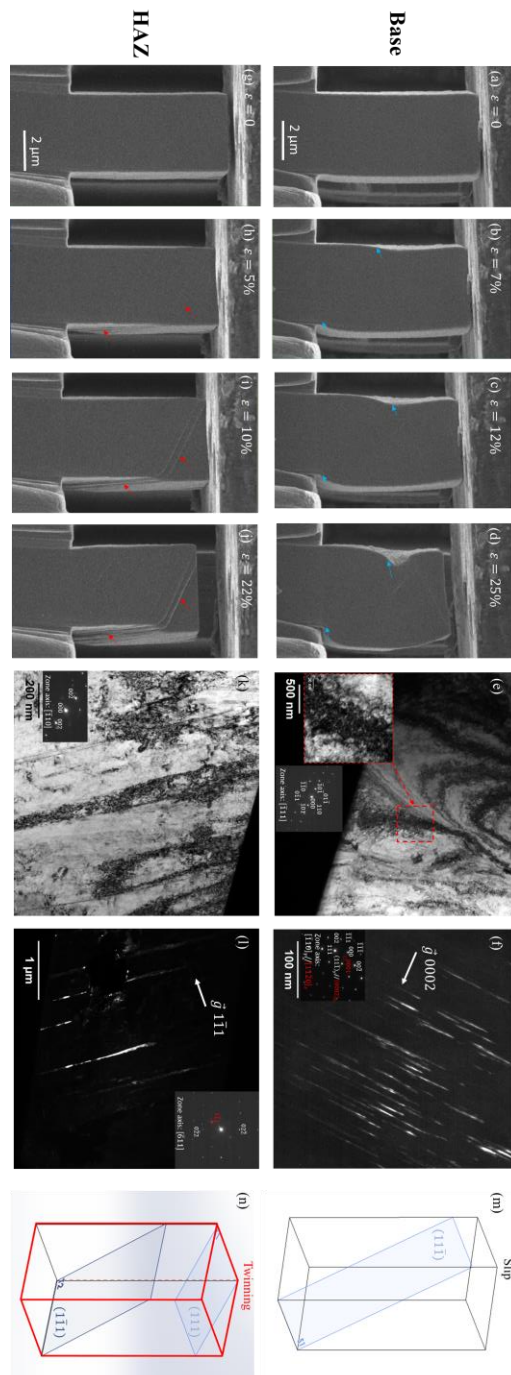


Figure 6.13 Snapshots of *in-situ* SEM micropillar compression tests of irradiated AISI 304 SS welds along $\{101\}$ grains at room temperature: (a-d) base metal at strains of 0, 7%, 12% and 25%, and (g-i) the HAZ at strains of 0, 5%, 10% and 22%. TEM micrographs of compressed pillars of the (e-f) base metal showing the formation of ϵ martensite. (k-l) the HAZ showing the formation of deformation twins and 3D SOLIDWORKS® modeling of (m) activated slip planes S1 ($11\bar{1}$) in the base and (n) twinning planes of T1 (111) and T2 ($1\bar{1}\bar{1}$) in the HAZ.

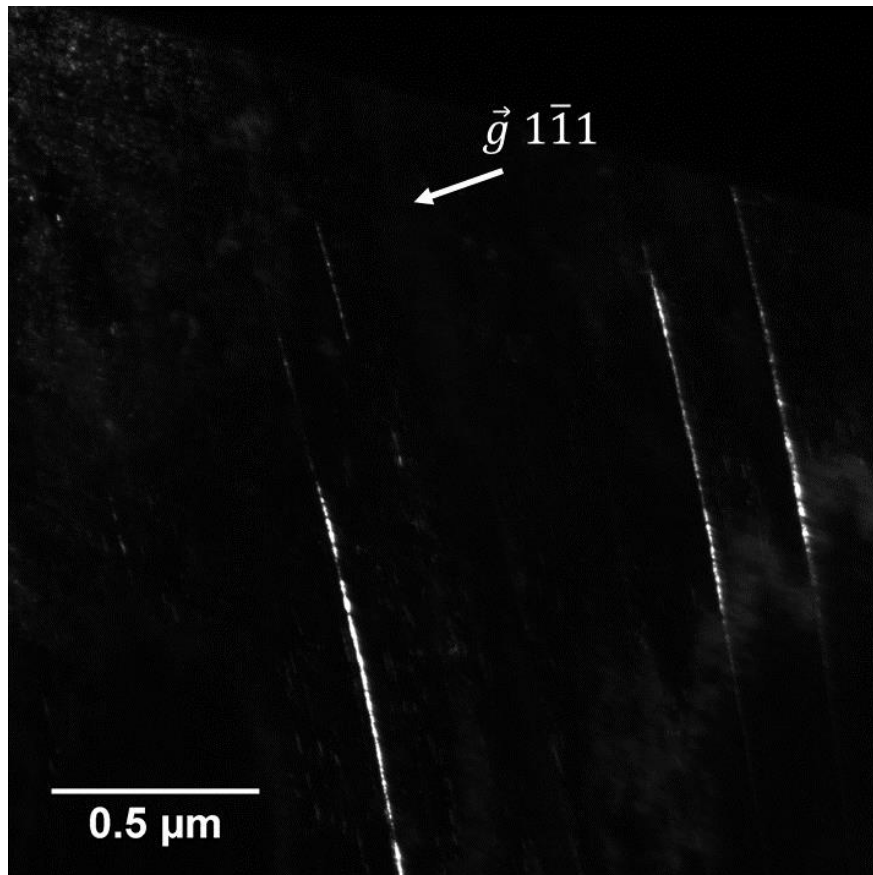


Figure 6.14 Nanotwins in the post-compression pillar of the (101) grain in the HAZ.

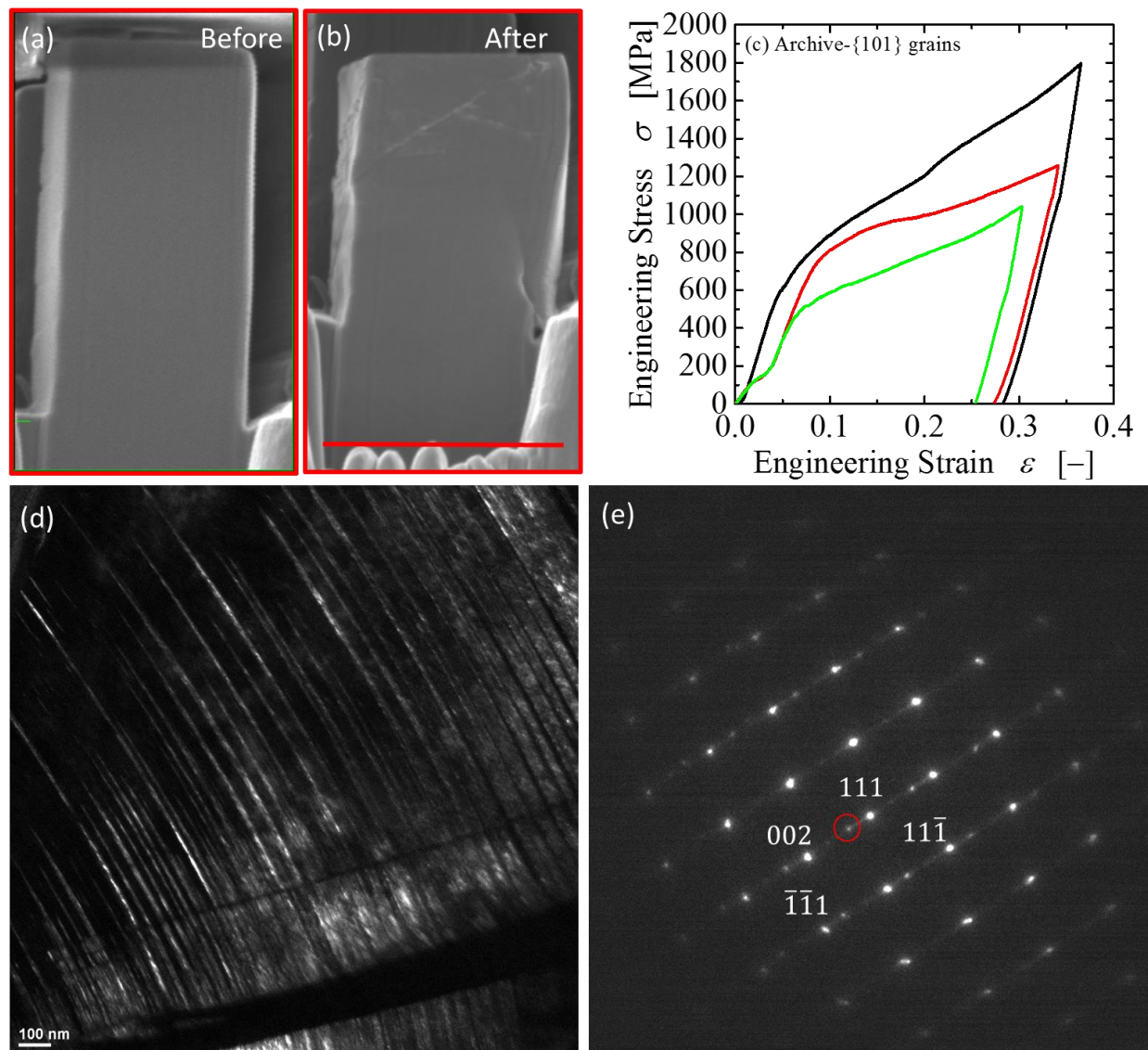


Figure 6.15 (a-b) Before/after snapshots of *in-situ* SEM micropillar compression tests of unirradiated archive AISI 304 SS welds along $\{101\}$ grains at room temperature: (c) stress-strain curves of different pillars from $\{101\}$ grains. (d) Dark-field TEM micrographs of compressed pillars showing the formation of twinings and (e) the corresponding selected diffraction pattern in (d).

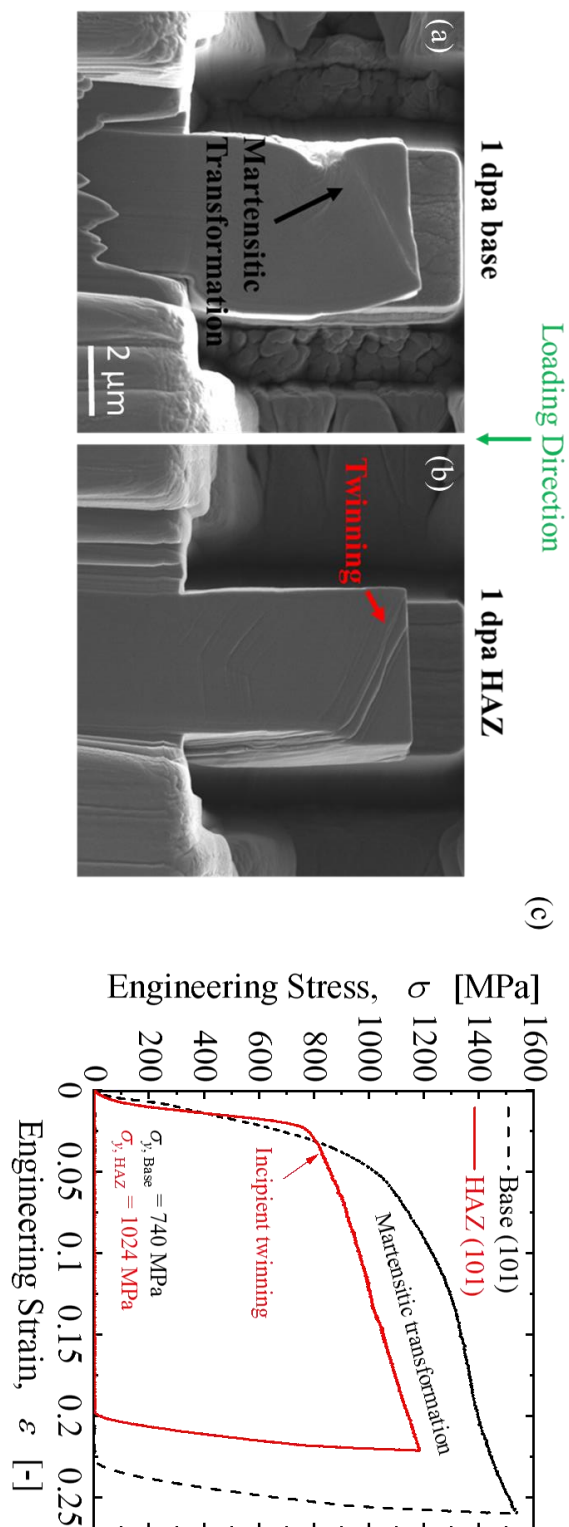


Figure 6.16 Final SEM micropillar compression video still-frame from $\{101\}$ grains in the base metal and the HAZ shown in greater detail in Fig. 6.13, showing: (a) $\gamma \rightarrow \epsilon$ martensitic transformation, and (b) twinning, with (c) the corresponding engineering stress-strain curves.

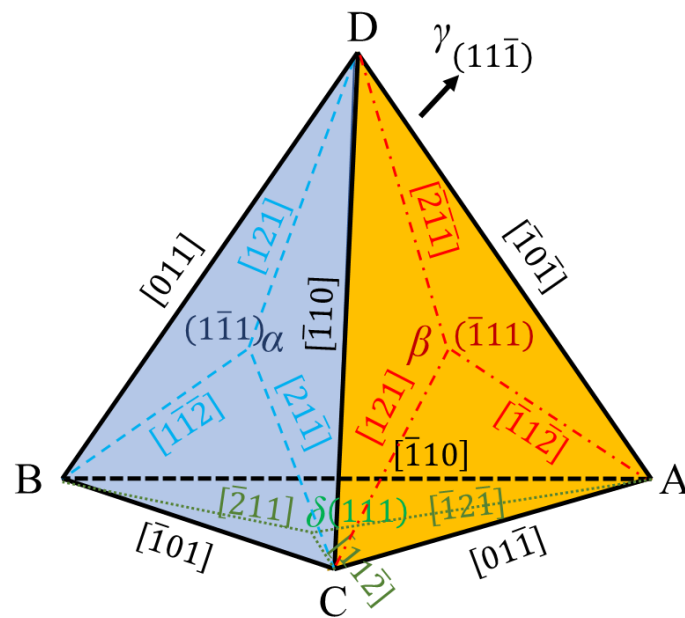


Figure 6.17 Thompson tetrahedron illustrates possible twin systems in an fcc crystal corresponding to [Table 6.5](#).

7. DISCUSSION

7.1 Comparison of mechanical properties

The archival literature covering experiments and simulations on fcc materials provides insight on the anisotropy mechanical behavior of materials under nanoindentation [249,252,253,276]. For the slip/twinning systems of $\langle 001 \rangle$, $\langle 110 \rangle$, and $\langle 111 \rangle$ compression directions, $\langle 001 \rangle$ has the largest Schmid factors at 0.41 for slip and 0.47 for twinning. Thus, the $\langle 001 \rangle$ is considered a “soft” orientation, whereas $\langle 110 \rangle$ and $\langle 111 \rangle$ are considered “hard” orientations. These directionally-dependent Schmid factors can affect the activation of slip/twinning systems as the stress increases during the nanoindentation loading.

Molecular dynamics (MD) simulations on fcc Fe-Cr-Ni pointed out that the formation of disassociated dislocations during indentation and the low stacking fault energy together support the mechanism of dislocation glide as Shockley partials [249]. The austenitic AISI 304L SS in our study has a relatively low stacking fault energy of $\sim 15 \text{ mJ/m}^2$ [277]. Moreover, it has been shown that the (001) plane tends to have the lowest dislocation density in an austenitic steel [249], suggesting that the dislocation density and the associated dislocation nucleation and emission on the $\{100\}$, $\{110\}$, and $\{111\}$ planes can also affect the hardness measurement by nanoindentation. Although the literature would suggest some anisotropy in hardness, the weak anisotropy observed in both the unirradiated and irradiated 304L SS could be attributed to the size of the nanoindentation plastic zone, which could extend beyond the grain of interest (see Chapter 4). Moreover, whereas theoretical calculations of directional anisotropy focus on isolated single crystals, the mechanical response of the grains studied herein is influenced by constraints imposed by neighboring grains with varying Schmid factors. However, even considering the expansion of the plastic zone, the reduction of anisotropy in the HAZ is clearly seen as we have shown in Chapter 6.

7.1.1 Irradiation hardening

Irradiation-induced defects such as clusters, loops, cavities, and precipitates cause irradiation hardening and embrittlement, as these defects are serving as obstacles that can impede the movement of dislocations. Irradiation hardening mechanisms can be categorized as either source

hardening (activation of dislocation slip by pinning on obstacles) or friction hardening (impediment of dislocation motion by radiation-induced defects) [278]. The increment of yield strength attributed to each type of obstacle can be predicted using the Orowan dispersed barrier hardening model [279] as:

$$\Delta\sigma_{y,i} = M\alpha_i\mu b\sqrt{N_i d_i} \quad (7.1)$$

where M is the Taylor factor, which is 3.06 for fcc Fe-Cr-Ni alloys [278,280], μ is the shear modulus, which is determined as ~75 GPa by the nanoindentation experiments herein, b is the magnitude of the Burgers vector, which is ~0.253 nm for 304L SS [22], N_i is the number density of defects of type i , d_i is the average size of defects of type i , and α_i is the barrier strength factor for defects of type i . If we use the irradiated AISI 304L SS of 23 dpa and 3 appm He, cavities and interstitial Frank loops are the primary microstructural features contributing to irradiation hardening. Their number densities and average diameters are on the same order of magnitude (see [Table 5.1](#)), which approximately corresponds to a strength factor $\alpha \approx 0.33$ for both obstacle types [213,279,281–283].

The strength factor α is dependent on types of the defects. Lucas [284] pointed out the defects fall into three categories: (1) strong barriers such as cavities and voids with $\alpha \approx 1$; (2) intermediate barriers, for instance, Frank loops and small precipitates $0.33 < \alpha < 0.45$; and (3) weak barriers like small voids/bubbles/loops $\alpha < 0.25$. A fitting method [213,283] can be used for obtaining the strength factor in the dispersed barrier hardening model:

$$\alpha = k_1 \ln(k_2 d) \quad (7.2)$$

where k_1 and k_2 are fitting parameters, and d is the size of the defects. We set $\alpha = 0.33$ for both loops and precipitates, and $\alpha = 1$ cavities strengthening in [Eq. \(7.1\)](#). The selected barrier strength factor for loops and precipitates ($\alpha = 0.33$) falls at the lower limit of their known values, representing a conservative approach that predicts the least amount of irradiation-induced hardening. Additionally, since the dislocation lines cannot be discerned from loops in the irradiated material, we make another conservative assumption by treating all lines as having the

same strengthening contribution as loops; this treatment limits the predicted amount of strengthening.

The total irradiation hardening of metallic alloys can be estimated using root-square summation over all microstructural features i that contribute to hardening, when the features or obstacles have similar strengths [73].

$$\Delta\sigma_y = \sqrt{\sum_i (\Delta\sigma_{y,i})^2} \quad (7.3)$$

Linear summation over all microstructural features i that contribute to hardening should be applied when obstacles have dissimilar strengths:

$$\Delta\sigma_y = \sum_i (\Delta\sigma_{y,i}) \quad (7.4)$$

We adopt linear summation for calculation of the total irradiation hardening. Because the irradiated microstructure contains dislocation-type defects (i.e., loops and lines considered together for conservatism), cavities, and precipitates that contribute to hardening, these three strengthening contributions are summed. However, to calculate irradiation hardening, the initial microstructure containing dislocations must be subtracted from the sum:

$$\Delta\sigma_y = \Delta\sigma_{y,loops\ irradi} + \Delta\sigma_{y,cavities\ irradi} + \Delta\sigma_{y,ppt\ irradi} - \Delta\sigma_{y,lines\ unirrad} \quad (7.5)$$

The conversion between the nanoindentation hardness and yield stress is given as an empirical correlation for fcc materials [22,259,285,286]

$$\Delta\sigma_y = 3.03\Delta H_V \quad (7.6)$$

in which $H_V = 94.495H_{Berkovich}$. The calculated hardening contribution for each type of defects of the base metal compared to the unirradiated archive AISI 304L SS is given in [Table 7.1](#).

The calculated total yield strength increase can be converted to a change in hardness of $\sim 0.71 \pm 0.54$ GPa. However, nanoindentation experiments ([Fig. 6.4\(a\)](#)) measured an increase in hardness of 0.54 ± 0.28 GPa. Numerically, these results indicate that within statistical confidence,

irradiation hardening is consistent between the dispersed barrier calculation and our nanoindentation measurement. However, the error bars on both the dispersed barrier and nanoindentation results are large, rendering it difficult to draw a meaningful comparison across the two approaches. The error bar on the nanoindentation measurement could be associated with factors such as grain orientation, active slip planes, and the empirical relationship used to estimate yield strength from nanohardness. Uncertainty on the dispersed barrier calculation is associated with limited counting statistics in the microstructural quantifications, but we must also consider potential heterogeneities (e.g., associated with in-reactor neutron irradiation dose and temperature gradients which are difficult to monitor and control).

It is also worth noting that the dispersed barrier calculation is conservatively low for two main reasons. First, the selected barrier strength factor for loops and precipitates ($\alpha = 0.33$) falls at the lower limit of their known values, representing a conservative approach that predicts the least amount of strengthening. Second, since loops and lines cannot be discerned in the irradiated micrographs (see Chapter 5), it is assumed that all dislocation lines remain in the microstructure (i.e., are not annealed with irradiation) and they are treated with the same strength factors as loops. This treatment further limits the predicted irradiation-induced hardening. Hence, distinguishing loops from lines and employing a less conservative approach could cause a statistically significant (i.e., outside of error bars) difference between the dispersed barrier calculation and the nanoindentation measurements. In such a case, accounting for the observed nanoindentation-induced phase transformation in the dispersed barrier calculation could explain the difference between measurements and calculations.

7.1.2 Laser welding softening

Void swelling and helium bubble embrittlement (we regard both voids and bubbles as cavities in this thesis) can deteriorate the long-term service in the nuclear reactor [278]. Post irradiation annealing has been reported in irradiated alloys that irradiation-induced cavities can be removed at elevated temperature [287–289]. Fig. 5.13 shows the High angle annular dark-field (HAADF) STEM images of the original microstructure of the base metal and the HAZ before nanoindentation experiments. The obvious difference between these two regions indicates the laser welding has annealed the irradiation-induced cavities in the HAZ. For the laser welded AISI 304L SS of 23

dpa and 3 appm He, the average number density of the cavities is $1.2 \pm 0.3 \times 10^{21} \text{ m}^{-3}$ in the base metal and $1.4 \pm 1.3 \times 10^{19} \text{ m}^{-3}$ in the HAZ. The average diameter of the cavities for the base metal is $20.9 \pm 7.7 \text{ nm}$ and $16.2 \pm 4.4 \text{ nm}$ for the HAZ.

After the laser welding, the irradiation-induced cavities have been reduced and shrunk. In addition, the softening happens as a result of the grain growth in the HAZ during the laser welding [290] as can be seen in Fig. 5.11(b). Hence, the softening of the HAZ is caused by the laser welding even through laser weld-induced heat.

We adopt linear summation to calculate the total laser weld-induced softening similar to what we have discussed in Section 7.1.1 of irradiation hardening. Because the laser weld-annealed microstructure contains dislocation-type defects (i.e., loops and lines considered together for conservatism), cavities, and precipitates (negligible due to the density) that contribute to hardening, two strengthening contributions by loops and cavities are summed. However, to calculate softening compared to the irradiated base metal, the initial microstructure containing dislocations must be subtracted from the sum:

$$\Delta\sigma_y = \Delta\sigma_{y,loops \text{ irradiated}} + \Delta\sigma_{y,cavities \text{ irradiated}} - \Delta\sigma_{y,lines \text{ unirradiated}} \quad (7.7)$$

in which the strengthening factor $\alpha = 0.25$ for the small loops in the HAZ.

The calculated total yield strength decrease of the HAZ compared to the base metal can be converted to a change in hardness of $0.89 \pm 0.26 \text{ GPa}$. However, nanoindentation experiments (Table 6.2) measured an increase in hardness of $1.20 \pm 0.21 \text{ GPa}$. Numerically, these results indicate that within statistical confidence, laser weld-induced softening is consistent between the dispersed barrier calculation and our nanoindentation measurement. However, the error bars on both the dispersed barrier and nanoindentation results are large, rendering it difficult to draw a meaningful comparison across the two approaches. The error bar on the nanoindentation measurement could be associated with factors such as grain orientation, active slip planes, and the empirical relationship used to estimate yield strength from nanohardness. Uncertainty on the dispersed barrier calculation is associated with limited counting statistics in the microstructural

quantifications but must also consider potential heterogeneities (e.g., laser welding cooling rate and temperature gradients, which are difficult to monitor and control).

It is also worth noting that the dispersed barrier calculation is conservatively low for two main reasons. First, the selected barrier strength factor for loops ($\alpha = 0.25$) falls at the lower limit of their known values, representing a conservative approach that predicts the least amount of strengthening, leading to the most amount of softening. Second, since loops and lines cannot be discerned in the irradiated micrographs (see Chapter 5), it is assumed that all dislocation lines remain in the microstructure (i.e., are not annealed with irradiation) and they are treated with the same strength factors as loops. This treatment further increases the predicted laser weld-induced softening. Therefore, distinguishing loops from lines and employing a less conservative approach could cause a statistically significant (i.e., outside of error bars) difference between the dispersed barrier calculation and the nanoindentation measurements. Thus, in such a case, accounting for the observed nanoindentation-induced phase transformation in the dispersed barrier calculation could explain the difference between measurements and calculations of the softening.

Figure 7.1 shows the calculated irradiation hardening and laser weld softening leading to the change of the yield strength in the laser weldment of neutron irradiated AISI 304L SS of 23 dpa, 3 appm He irradiated at 415 °C. The horizontal axis at the origin is the yield strength of the archive AISI 304L SS of 905 MPa. Each contribution of change in yield strength includes dislocation lines, loops, precipitates, and cavities. The net total values of the calculated hardening in the base metal and softening in the HAZ by the proposed model are the white rectangular columns with error bars. The measured total values of the irradiation hardening of the base metal versus the laser weld-induced softening in the HAZ has been shown as the yellow rectangular columns with error bars. To sum up, the phase transformation in general needs to be considered for the decrease in yield strength.

7.1.3 He/dpa effect

He and dose-dependent hardness on laser weldments of irradiated AISI 304L SS are given in Fig. 7.2. The base metal has a higher hardness from 3.22 ± 0.17 GPa to 3.94 ± 0.16 GPa than the HAZ, which has a hardness of 2.36 ± 0.08 GPa to 2.64 ± 0.18 GPa, in the range of dose from 1 dpa to

28 dpa and He from 0.2 appm to 8 appm. As the dose and He concentration increase, the hardness of both base metal and HAZ increase. The HAZ is softer than the base metal across all the corresponding dose and He conditions because of post laser weld annealing. The hardness of the archive AISI 304L SS is also measured as 3.16 ± 0.23 GPa. All the detailed values of the measured nanoindentation hardness have been summarized in [Table. 7.3](#).

7.2 Deformation-induced martensitic transformation in high He and dose condition

We will discuss the deformation pathways in the laser weldment of highly irradiated AISI 304L SS of 23 dpa and 3 appm He concentration.

7.2.1 Base metal

Applied stress causes the activation of nucleation sites for martensite embryos, leading to lattice deformation [263,291]. The probability P of martensite nucleation can be written as [263,264]:

$$P = -\frac{0.011}{24\bar{v}N_0\Delta S}(\Delta G + U) \quad (7.8)$$

where \bar{v} denotes the average volume per martensite, N_0 is the initial number of nucleation sites per unit in the austenitic matrix before nanoindentation, ΔS is the entropy change ($\partial\Delta G/\partial T$, T is the temperature) during the fcc to bcc phase transformation, and ΔG and U are the thermal and mechanical driving forces, respectively, for the martensitic transformation. Specifically, ΔG is the Gibbs free energy and U is the applied external stress on the sample which can be expressed as [250,264]:

$$U = \sigma_{ij} \cdot \varepsilon_{ij} \quad (7.9)$$

where σ_{ij} represents the applied external stress tensor on the sample and ε_{ij} is the strain tensor of the lattice deformation during the strain-induced martensitic transformation.

The strain-induced martensitic transformation is favored if the sum $\Delta G + U$ is greater than the critical free energy of the martensitic transformation, $\Delta G_c = 2100$ J/mol [264]. No martensite laths were observed in the unirradiated archive 304L SS sample under the same loading condition (i.e., the same U) that generated strain-induced martensite laths in the irradiated 304L SS sample. Hence, the neutron irradiation must sufficiently increase the Gibbs free energy such that $(\Delta G_{irrad} + U) \geq \Delta G_c$. Irradiation-induced defects, specifically cavities, are believed to enable the martensitic phase

transformation by accommodating the large surface area to volume ratio of the martensite in the plastic region affected by a nanoindent. The free energy of the martensitic phase transformation includes the surface energy contribution due to the creation of new martensite-matrix interfaces. Meanwhile, the cavities also create internal surfaces, which can compensate this surface energy contribution to the total free energy change during the phase transformation [292]. The cavity contribution to the Gibbs free energy is based on the energy required to form a cavity of n vacancies:

$$E_n = (36\pi\Omega^2)^{1/3}\gamma\left(\frac{4\pi R_V^3}{3\Omega}\right)^{2/3} \quad (7.10)$$

where Ω is the atomic volume of the fcc Fe $\sim 1.18 \times 10^{-29} \text{ m}^3$ [278], γ is the surface energy of fcc Fe $\sim 2.2 \text{ J/m}^2$, and R_V is the average cavity radius measured to be 9.65 nm (we use the 23 dpa and 3 appm He AISI 304L SS sample as an example). Thus, the total increase of Gibbs free energy by all the cavities in the irradiated 304L SS studied herein is calculated to be 24.28 J/mol, which contributes to the sum of $(\Delta G + U)$ exceeding the critical free energy. In the irradiated 304L SS specimen, the surface area of the martensite-matrix interface is measured as $3.98 \times 10^6 \text{ m}^2/\text{m}^3$ per lath while the surface area of cavities is $4.24 \times 10^6 \text{ m}^2/\text{m}^3$. The same order of magnitude of the martensite and cavity surface areas indicates the ability for cavities to compensate the surface energy necessary for the martensitic transformation. However, as can be seen in Fig. 6.8, martensite laths exist both coincidentally and non-coincidentally with cavities. Thus, irradiation-induced cavities are not necessarily the operative nucleation sites for the strain-induced martensite.

7.2.2 HAZ

In the laser welds of 23 dpa and 3 appm He AISI 304L SS, the remaining unresolved concern here is the cause of the different pathways between the base metal and the HAZ. In the presence of a high number density of cavities, the dislocation jogs will form by interactions with these cavities [293]. These jogs will lead the partial dislocations into dislocation climb. This process inhibits the dislocation glide into the twinning shear. Further, the stress concentration at these cavities eventually results in the phase transformation. Additionally, phase-field simulations have also been demonstrated to show that the stress-induced martensitic phase transformation occurs at the different shapes of nanovoids [294]. Previous studies have also pointed out that the surface tension of the cavities compensate the surface energy of the martensitic phase [140,292].

Thus, the large quantities of the irradiation-induced cavities provide abundant nucleation sites for the direct $\gamma \rightarrow \alpha'$ phase transformation in the base metal (Fig. 7.3(a)). For the HAZ, the reduction of cavities by two orders of magnitude compared with the base metal provides a different pathway for the dislocation motion. Less cavities correspond to a smoother way for the dislocation to slip (Fig. 7.3(b)). The nucleation of the metastable ε martensite involves the dislocation motion, for instance, the shear on $\{111\}_\gamma$ planes produces an hcp- ε plate by slip, twin, or highly stacking faults [295]. Thus, the BBOC model (Fig. 7.4) corresponding to the $\gamma \rightarrow \varepsilon \rightarrow \alpha'$ mode also requires the shear of partial dislocation at the intersection of the preformed two hcp- ε plates.

The competition between the normal dislocation slip and the direct nucleation of α' martensite laths at the cavities modulate the modes of the martensitic transformation between the base metal and the HAZ. Therefore, the pathways of the deformation-induced martensitic phase transformation have been changed in the HAZ by the laser-welding annealing of the irradiation-induced cavities. These results indicate the potential by maintaining a certain stress-level, and controlling the population of cavities by irradiation can tailor the martensitic transformations, which are commonly achievable at relatively low or cryonic temperatures or large strains [214].

7.3 Deformation twinning in low He and dose condition

We will discuss the deformation pathways in the laser weldment of lowly irradiated AISI 304L SS of 1 dpa and 0.2 appm He concentration.

It is known that twins can form from partial dislocations in fcc metals. The dissociation of a single perfect dislocation into two Shockley partial dislocations [143] is written as:

$$\frac{a}{2} [\bar{1}01] = \frac{a}{6} [\bar{2}11] + \frac{a}{6} [11\bar{2}] = \frac{a}{6} [21\bar{1}] + \frac{a}{6} [1\bar{1}\bar{2}] \quad (7.11)$$

where a is the lattice constant. Compared to trailing partials ($[11\bar{2}]$ or $[1\bar{1}\bar{2}]$), the leading partials ($[\bar{2}11]$ or $[21\bar{1}]$) are more likely to trigger the glide motion and initiate the nucleation of twinning [145,270]. The critical shear stress for twinning can be determined from the known CRSS measured on the twinning plane [183] using the empirical relationship:

$$\sigma_T = 3.06 * CRSS \quad (7.12)$$

Additionally, two criteria are established in the archival literature to predict the critical stress for twinning at room temperature from material constants. Stress-dependent twinning by separation of leading partials of a dissociated screw dislocation in Eq. 7.11 is governed by the Byun criteria [145]:

$$\sigma_T = 6.14 \frac{\gamma}{b_p} \quad (7.13)$$

where γ represents the SFE and Burgers vector of the partial $b_p = 0.147 \text{ nm}$ [183]. Classical twinning theories also predict the CRSS with respect to the SFE, according to the Naeita-Takamura criteria [296]:

$$\sigma_T = 1.53 \frac{\gamma}{b_p} \quad (7.14)$$

These two aforementioned criteria tend to bind the twinning behaviors of fcc metals and alloys, as shown on the deformation map in Fig. 7.5(a). A wide variety of fcc metals and alloys are included on the deformation map: austenitic steels 304L [192,297], 316L [145,297,298], 317L [298] (enlarged in Fig. 7.5(b)); pure metals Cu [299–301], Pb [299], Ag [299], Au [299], Ni [302]; superalloys TMS-82 [303], C2000 [304]; twinning induced plasticity (TWIP) steels [183] Fe-22Mn-0.5C, Fe-22Mn-0.6C, Fe-27Mn-2.5Si-3.5Al, Fe-22Mn-0.1C-1.2Al, Fe-17Mn-0.4C-1.3Al, Fe-18Mn-0.6C-1.5Al, Fe-15Mn-0.7C-2Al-2Si; high entropy alloys FeNiCoCrMn [270], CrMnFeCoNi [305]; nanocrystalline Al [306], Cu [307]; ultrafine grained Cu [307], orientation-dependent Cu grains [308] and polycrystalline Cu [309]; additively manufactured (AM) 316 [310]; and other alloys Cu-5Al [301], Cu-8Al [300], Cu-8.3Al [301], 70Cu-30Zn [297,298], 80Cu-20Zn [297,298], 90Cu-10Zn [297,298], Ag alloy [296], MP35N [298]. Results from the present work are also included. The Byun criteria (solid blue line, Fig. 7.5(a)) tends to fall in close agreement with austenitic steels and Cu alloys with low SFE. The Naeita-Takamura criteria (dashed green line, Fig. 7.5(a)) tends to agree well with metals and alloys having medium (TWIP, high entropy alloys) to high SFE (pure Cu, Ni, super alloys, Ni). In general, as the SFE increases, the critical twinning stress increases.

The SFE is well known to influence the mechanical properties and deformation mechanisms of metallic alloys [220]: i.e., under identical loading conditions, low SFE alloys are inclined to form twins and martensite, while higher SFE alloys tend to undergo a dislocation slip [214]. Austenitic 304L SS has a relatively low SFE of ~ 15 mJ/m² [140]. However, several different deformation mechanisms have been observed in unirradiated 304 SS depending on the strain level, including slip, dislocation dissociation, stacking faults, twinning, and martensitic transformation [192]. After irradiation, phase transformation [139] and dislocation channeling [145] have been observed to be the dominant plastic deformation mechanisms. Given that a variety of deformation mechanisms are inherently active in 304 SS, the observed difference in the deformation mechanisms between the base metal and the HAZ is unlikely caused by variations in the overall SFE. Fig. 7.5(a) also shows that the critical twinning stress does not simply increase monotonically with the SFE. Rather, microstructural considerations must also influence the deformation mechanism.

For 304L SS, the Byun criteria predicts a critical twinning stress of 600 MPa. This prediction is consistent with our measured twinning stress in the HAZ, $\sigma_{T, \text{HAZ}} = 608 \pm 114$ MPa (dashed horizontal red line in Fig. 7.5(a-b), determined using Eq. 7.12). But in the base metal, where no twinning is observed, the measured twinning stress is 1253 ± 68 MPa (dashed horizontal black line in Fig. 7.5(a-b), determined using Eq. 7.12); this is more than twice the predicted critical twinning stress. This quantitative comparison suggests that the microstructural differences between the HAZ and the base metal can rationalize the difference in twinning behavior. Microstructure is well known to influence twinning stress. For instance, grain size alone causes the twinning stress to shift; e.g., finer grained Cu tends to have a higher twinning stress than coarse grained Cu. Although the opposite is observed in the present results, in which the finer dendritic grains in the HAZ have a lower twinning stress than the base metal, we will also consider irradiation-induced cavities finer than the grain scale.

The population and nature of irradiation-induced cavities can explain the change in deformation mechanism from martensitic transformation in the base metal, to twinning in the HAZ. The effect of nanovoid surface tension on martensitic phase transformation has been demonstrated through phase field simulations [294]. Moreover, internal surfaces of cavities can compensate for the surface energy increase of the martensitic transformation, making the martensitic transformation

more energetically favorable in the presence of cavities (i.e., base metal) [140,292]. At the same time, the interaction of partial dislocations with larger cavities can result in recombination into perfect dislocations [293], which would suppress twinning in the base metal. Dislocations can also form jogs by absorbing vacancies from cavities; with increasing CRSS, leading partials will tend to climb over these jogs rather than to twin [219], thus further suppressing twinning in the base metal. In the HAZ, laser welding causes annealing of the irradiation-induced cavities, as well as formation of a dendritic structure with dislocations having Burgers vector $\vec{b} = \pm 1/2 \langle 110 \rangle$ in the HAZ (Fig. 7.6). These dislocations are noteworthy because they can further dissociate into partials and consequently induce incipient twinning.

The critical twinning stress for the HAZ aligns with the Byun criteria, but the critical twinning stress in the base metal exceeds the Byun criteria, which enables the material to undergo a deformation-induced martensitic transformation due to the higher number density of cavities compared to the HAZ. In summation, laser welding induces two major microstructural phenomena that govern deformation mechanisms: (1) welding decreases the number density of cavities, effectively reducing the number of nucleation sites for the martensitic transformation [263], and (2) welding produces partial dislocations that promote twinning.

7.4 Deformation transition criteria in austenitic stainless steels

We will discuss the transition criteria of deformation pathways in the laser weldment of irradiated AISI 304L SS as a function of dose level and He concentration. As we have discussed previously, the deformation mode is heavily affected by the presence of irradiation-induced cavities. In the coordinate of cavity density versus He/dose level, the deformation transition can be plotted as shown in Fig. 7.7. In the lower dose and He regime, twinning is more likely to occur as well as the generation of hcp- ϵ martensite plates with an increase of the cavity population. As the cavity density accumulates to a certain level, the nucleation of ϵ martensite phases starts to follow the BBOC model, inducing bcc- α' martensitic laths at the intersection of the two hcp- ϵ martensite plates. At a condition of very high density of cavities $\sim 10^{21} \text{ m}^{-3}$, direct transformation of $\gamma \rightarrow \alpha'$ is preferred as the lowest Gibbs free energy is supported to form the martensitic laths by the compensation of the internal surface energy of irradiation-induced cavities.

7.4.1 Direct austenite-to-martensite phase transformation

The distribution of the irradiation-induced cavities can be treated as the nearest neighbor distribution [311]. The mean inter-cavity distance can be calculated based on the Wigner-Seitz radius as follows [312]:

$$\lambda_{cav} = \left(\frac{3}{4\pi n} \right)^{1/3} \quad (7.15)$$

where n is the number density of cavities. When dislocations and dislocation junctions interact with irradiation-induced cavities, the localized stress concentration near the cavities can promote the volumetric change into martensitic transformation. The characteristic length of the direct martensitic transformation can be compared with the separation distance of the partial dislocations at equilibrium state [143]:

$$d_{eq} = \frac{\mu a^2}{16\pi} \left\{ \frac{2+\nu}{3(1-\nu)} \right\} \frac{1}{\gamma} \quad (7.16)$$

The derivation of the mechanical state of the dislocation glide has been discussed in Chapter 2. At equilibrium state, the separation distance between partials is calculated as ~14.12 nm for 304 SS. If we consider this as a critical resolved shear stress, the equilibrium separation distance is ~43.2 nm for the system. If the mean inter-cavity distance is smaller than the separation distance, the nucleation of direct $\gamma \rightarrow \alpha'$ is preferential.

7.4.2 Transition into hcp martensite

The hcp- ϵ plates usually occur as several layers of stacking faults pre-exist during the deformation. Unlike directly transformed into bcc- α' martensite phase, the hcp- ϵ phase forms in the presence of lower population of cavities. As described in Fig 7.3, the dislocation slip is more predominant than the nucleation of stress-induced martensite due to localized stress concentration near the cavities. Thus, the transformation of $\gamma \rightarrow \epsilon$ requires a larger characteristic length as the mean inter-cavity distance surpassing the separation distance of the partials. The lower density of cavities in this case will promote forming the hcp phase and further forms the $\gamma \rightarrow \epsilon \rightarrow \alpha'$ depending on whether the strain or geometrically necessary cavities (GNC) is sufficient for forming the bcc- α' martensitic laths. In addition, if the density of the GNC for martensitic transformation is high enough, then the direct austenite-to-martensite $\gamma \rightarrow \alpha'$ is favored. Otherwise, the strain level determines the $\gamma \rightarrow \epsilon \rightarrow \alpha'$ in terms of the BBOC model.

7.4.3 Transition into twinning

In fcc crystals, the dislocation motion is the predominant mechanism that governs the plasticity. The strain hardening behavior can be linked by the dislocation mean free path L_i [313]

$$\frac{1}{L_i} = \frac{\tau_{C,i}}{\mu b K_{hkl}} \quad (7.17)$$

where $\tau_{C,i}$ is the Taylor stress for the i -th slip system of dislocation forest density ρ_i in the form of $\tau_{C,i} = \mu b \sqrt{\sum_j a_{i,j} \rho_j}$ [314]. To simplify our problem instead of running large-scale dislocation dynamics simulations, we can refer to the average critical Taylor stress from Fig. 7.5 of ~1000 MPa. The orientation-dependent non-dimensional parameter K_{hkl} can also be treated as an average value of 35 with regards to fcc Cu [313]. Therefore, the average mean free path \bar{L} of dislocations is ~381 nm. If the mean inter-cavity distance exceeds this mean free path of dislocations \bar{L} , then the deformation twinning is more likely to be supported.

We can categorize the deformation transition criteria into three regimes:

1. $\lambda_{cav} \leq d_{eq}$: direct $\gamma \rightarrow \alpha'$ phase transformation;
2. $d_{eq} < \lambda_{cav} < \bar{L}$: intermediate $\gamma \rightarrow \varepsilon$ or $\gamma \rightarrow \varepsilon \rightarrow \alpha'$ depending on the strain level;
3. $\lambda_{cav} \geq \bar{L}$: twinning or strain hardening.

If we plot the mean cavity distance with respect to the He concentration shown in Fig. 7.8, the decrease of the mean inter-cavity distance dominates the transition from martensitic transformation to twinning. The horizontal green line is the average mean-free path of dislocations. The horizontal red line is the separation distance of partials at equilibrium state. In the intermediate regime between $d_{eq} < \lambda_{cav} < \bar{L}$, the two characteristic lengths, the hcp- ε martensitic plates are favored and can further extend to bcc- α' martensite laths based on the stress level.

Table 7.1 Quantitative analysis of the hardening contribution of the unirradiated and neutron irradiated AISI 304L SS (base metal) with 23 dpa and 3 appm He.

Microstructural features	Archive	Neutron irradiated	Strengthening factor α	ΔH [GPa]
Average grain size [μm]	52.0 ± 27.4	46.8 ± 17.9	-	
Dislocation Line [$\times 10^{14} \text{m}^{-2}$]	0.68 ± 0.70	-	0.33	0.56
Frank loop density [$\times 10^{21} \text{m}^{-3}$]	-	3.22 ± 0.39	0.33	0.66
Average Frank loop diameter [nm]	-	29.4 ± 9.46		
Cavity density [$\times 10^{21} \text{m}^{-3}$]	-	1.33 ± 0.33	1	0.30
Average cavity diameter [nm]	-	19.3 ± 7.64		
Precipitation density [$\times 10^{21} \text{m}^{-3}$]	-	1.44 ± 0.54	1	0.31
Average precipitation size [nm]	-	14.67 ± 1.14		
Total hardening	0.54 ± 0.28 (measurement) 0.71 ± 0.54 (calculation)			

Table 7.2 Quantitative analysis of the softening contribution of the base metal and HAZ of the laser weld of irradiated AISI 304L SS with 23 dpa and 3 appm He.

Microstructural features	Base	HAZ	Strengthening factor α	ΔH [GPa]
Average grain size [μm]	53.7 ± 18.5	71.7 ± 25.4	-	-
Frank loop density [$\times 10^{21} \text{ m}^{-3}$]	3.22 ± 0.39	2.15 ± 0.39	0.33 (base) 0.25 (HAZ)	0.66 (base) 0.28 (HAZ)
Average Frank loop diameter [nm]	29.4 ± 9.46	14.2 ± 3.90		
Cavity density [$\times 10^{21} \text{ m}^{-3}$]	1.33 ± 0.33	0.014 ± 0.013	1	0.30 (base) 0.097 (HAZ)
Average cavity diameter [nm]	19.3 ± 7.64	16.2 ± 4.40		
Precipitation density [$\times 10^{21} \text{ m}^{-3}$]	1.44 ± 0.54	-	1	0.31 (base)
Average precipitation size [nm]	14.67 ± 1.14	-		
Total softening	1.20 ± 0.21 (measurement) 0.89 ± 0.26 (calculation)			

Table 7.3 Nanoindentation hardness dependence on He and dpa level.

He and dpa level	Hardness [GPa]
0.2 appm, 1 dpa Base	3.22 ± 0.17
0.2 appm, 1 dpa HAZ	2.36 ± 0.08
3 appm, 23 dpa Base	3.7 ± 0.31
3 appm, 23 dpa HAZ	2.5 ± 0.2
8 appm, 28 dpa Base	3.94 ± 0.16
8 appm, 28 dpa HAZ	2.64 ± 0.18
Archived	3.16 ± 0.23

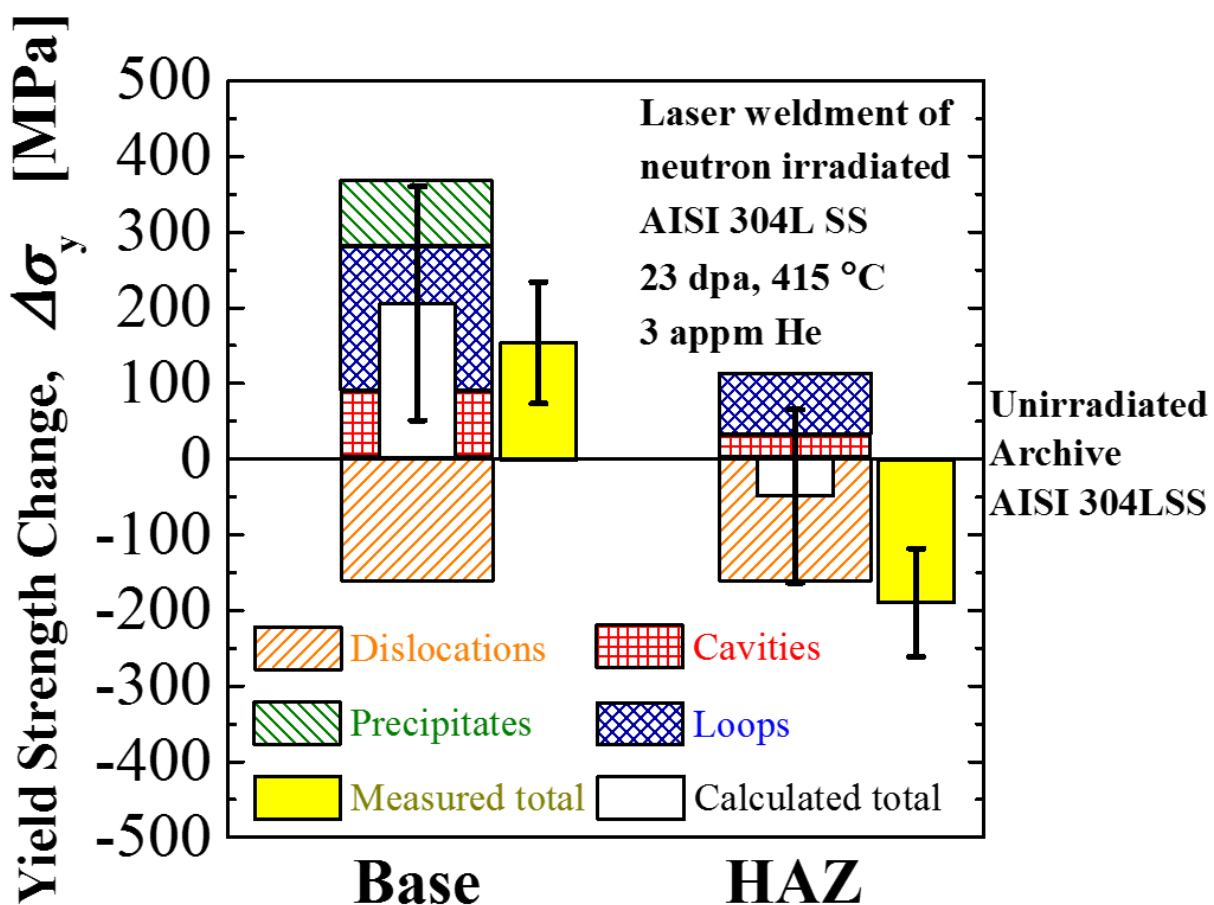


Figure 7.1 Calculated irradiation hardening and laser weld softening leading to the change of the yield strength in the laser weldment of neutron irradiated AISI 304L SS of 23 dpa, 3 appm He irradiated at 415 °C. The horizontal axis at the origin is the yield strength of the archive AISI 304L SS of 905 MPa. Each contribution of change in yield strength includes dislocation lines, loops, precipitates, and cavities. The net total values of the calculated hardening in the base metal and softening in the HAZ by the proposed model are the white rectangular columns with error bars. The measured total values of the irradiation hardening of the base metal versus the laser weld-induced softening in the HAZ has been shown as the yellow rectangular columns with error bars.

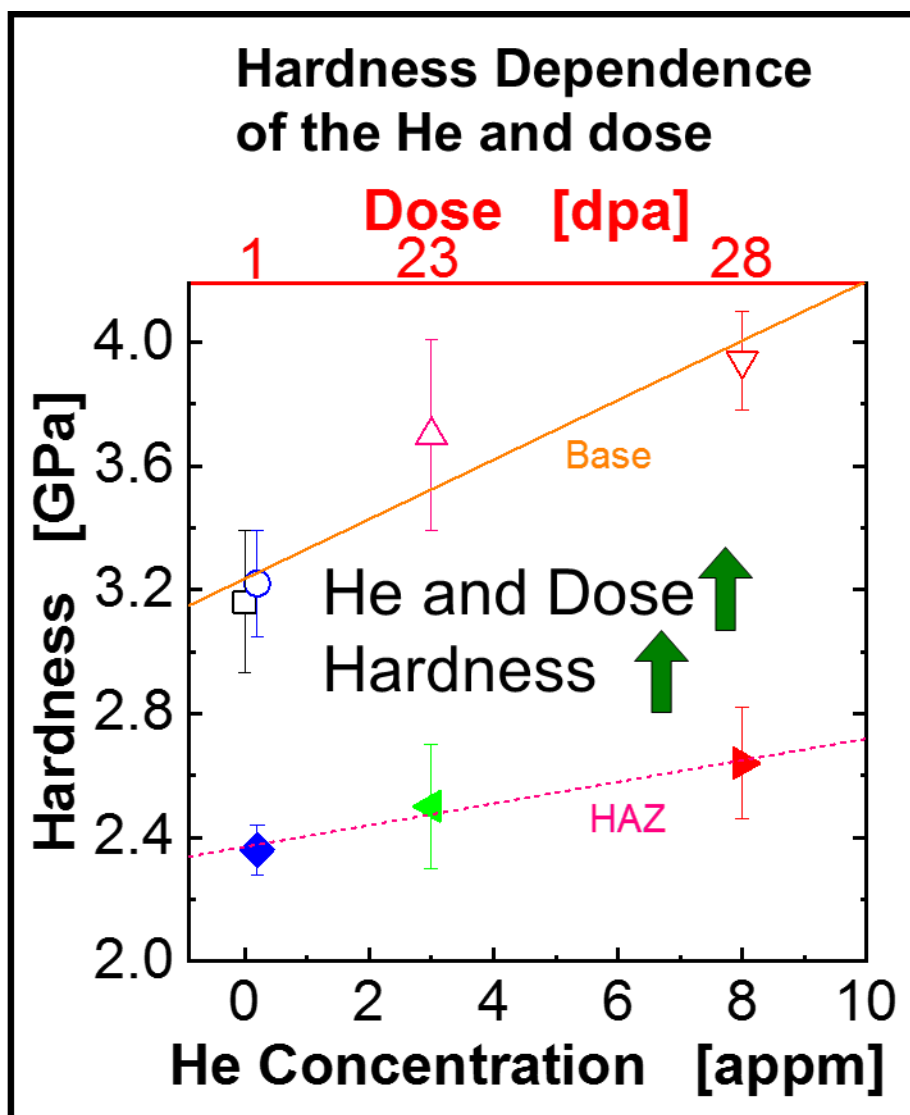


Figure 7.2 Nanoindentation measurements of hardness in the base metal and HAZ with regard to the He concentration and dose levels.

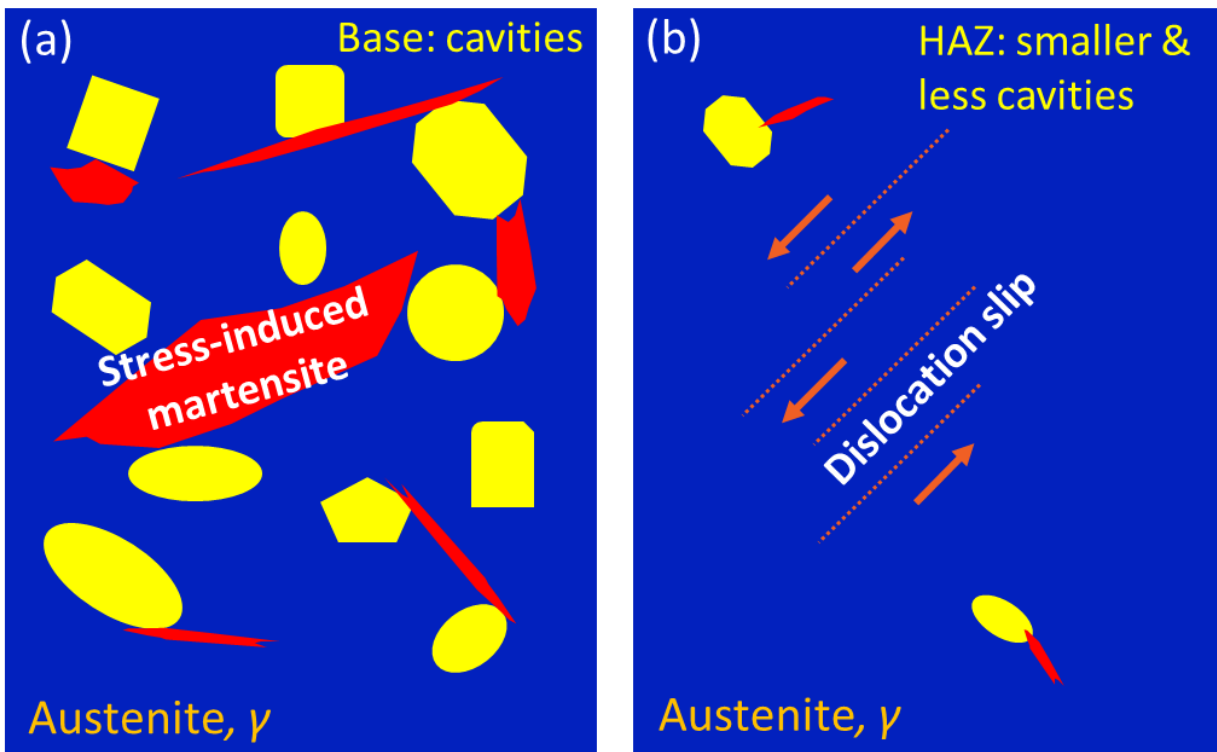


Figure 7.3 (a) Schematic diagram of stress-induced martensite nucleating through the cavities of direct $\gamma \rightarrow \alpha'$ transformation. (d) Smaller and less cavities retard the nucleation of α' martensite, enabling the dislocation slip for hcp- ϵ plates and further $\gamma \rightarrow \epsilon \rightarrow \alpha'$ transformation.

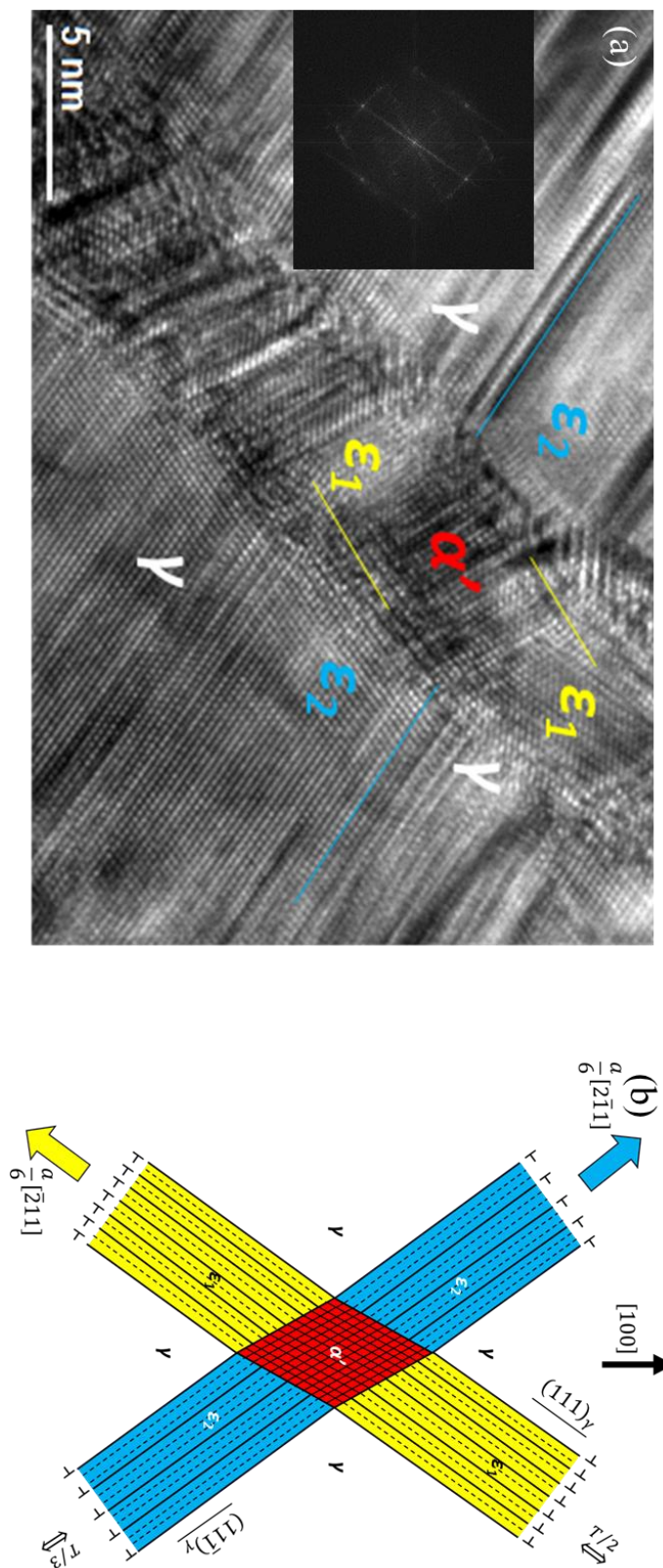


Figure 7.4 (a) Two hcp plates shear and form bcc structure at the intersection. (b) Schematic diagram of the Bogers-Burgers-Olson-Cohen (BBOC) model [194,195].

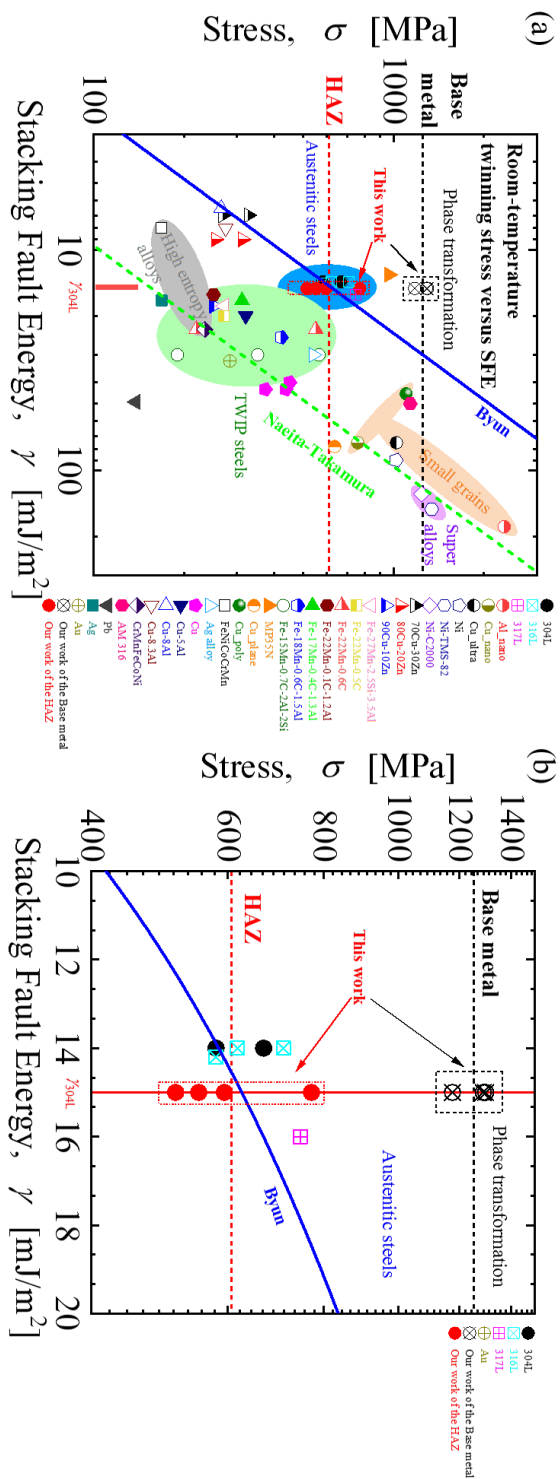


Figure 7.5 (a) Critical twinning stress for fcc metals and alloys, with (b) higher magnification of critical twinning stress map, focusing on austenitic steels. The current work is enveloped by dashed black (base metal) and red (HAZ) rectangular boxes. Irradiation-induced cavities change the critical twinning stress and cause phase transformation.

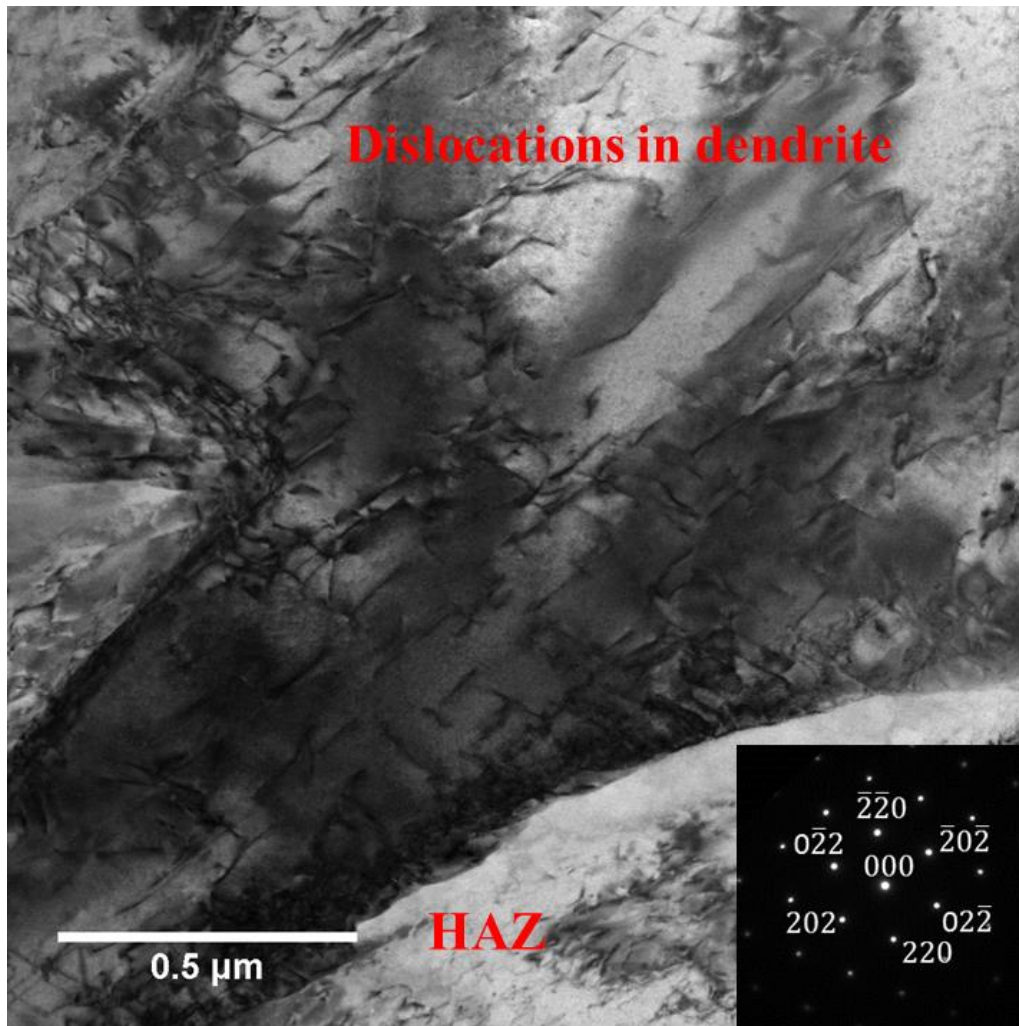


Figure 7.6 Dislocations and dendrites in the HAZ imaged using the bright-field STEM method.

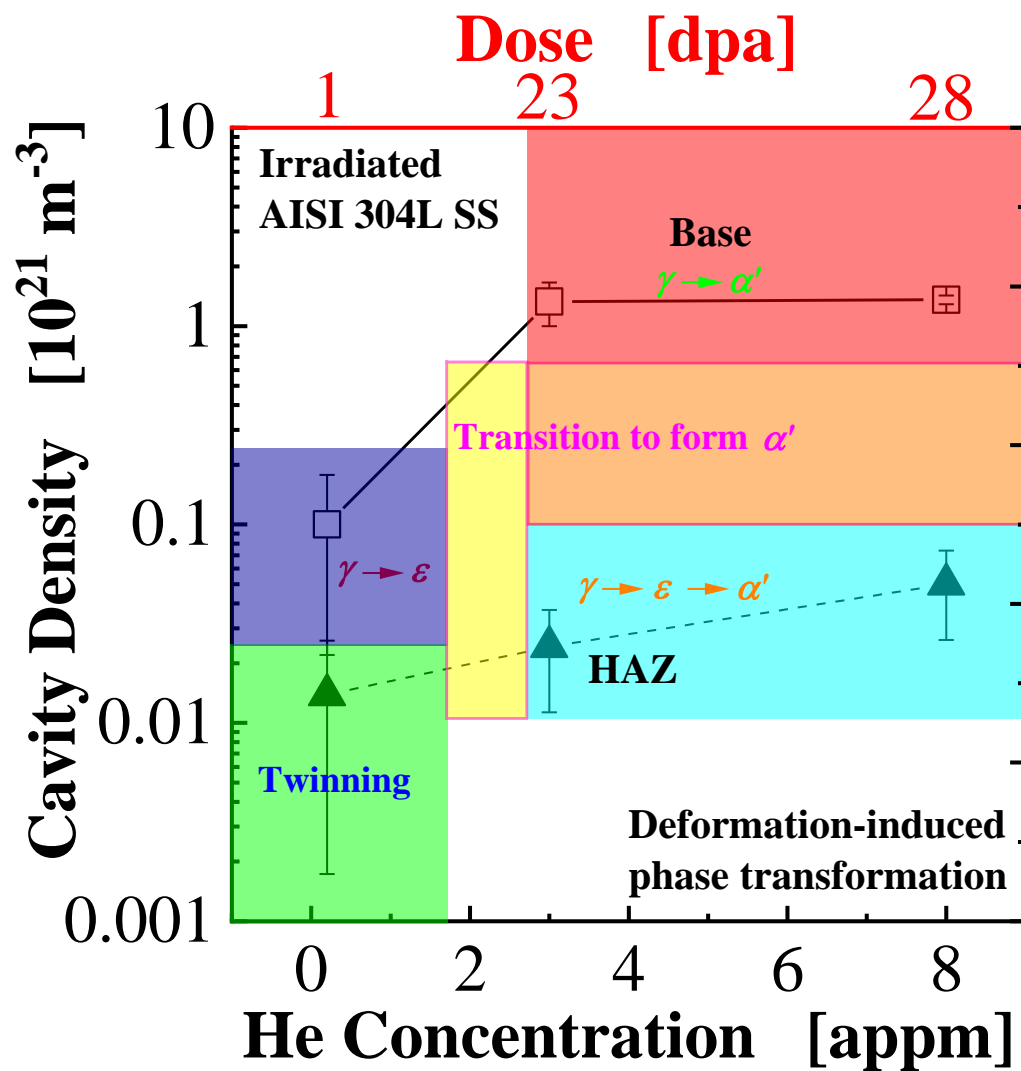


Figure 7.7 Deformation map of irradiated AISI 304L SS in the domain of cavity density and dose level and He concentration.

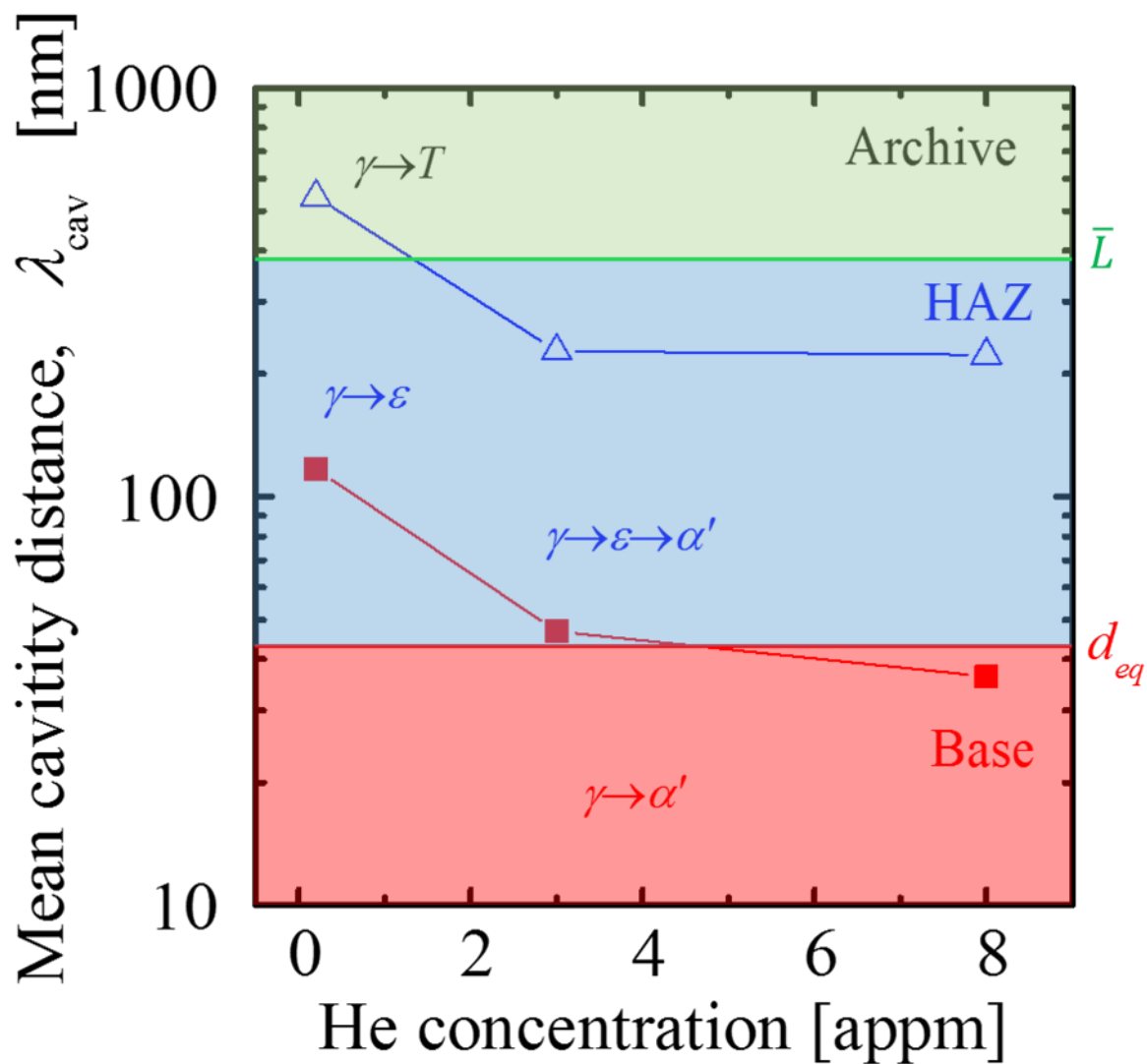


Figure 7.8 Proposed deformation regime map compared with experimental data for irradiated AISI 304L SS. Horizontal green line is the average mean-free path of dislocations. Horizontal red line is the separation distance of partials at equilibrium state.

8. CONCLUSIONS AND FUTURE WORKS

Despite the “low heat input” of laser welding, the HAZ in irradiated AISI 304L SS is affected by the welding process:

1. Comprehensive microstructural characterization of the laser welds shows the evolution of grain structure, dislocation lines, loops, cavities, and precipitates. The HAZ has a lower density of cavities and loops compared to the base metal at each dose and He condition due to the laser weld-induced annealing.
2. The softening and reduction of anisotropy have been observed during both the nanoindentation and microcompression experiments. The dispersed barrier hardening model can explain the irradiation hardening and laser weld softening by accounting for each type of defect in both the metal and the HAZ. As the dose level and He concentration increase, the hardness of both the base metal and the HAZ increase.
3. Grain orientation-dependent nanoindentation experiments are performed on archive and neutron irradiated AISI 304L SSs of 23 dpa at room temperature. Compared to {100} and {111} planes, the {110} planes exhibit the largest irradiation-induced increase in hardness and modulus. Deformation twinning occurs in the unirradiated specimen, while austenite-to-martensite phase transformation arises in the irradiated specimen.
4. Room-temperature nanoindentation experiments have been performed on the base metal and the HAZ of the laser welds of a neutron irradiated AISI 304L SS. Anisotropy has been reduced in the HAZ. During the nanoindentation of {101} grains, deformation-induced $\gamma \rightarrow \alpha'$ martensitic transformation has been observed in the base metal, while deformation-induced $\gamma \rightarrow \varepsilon \rightarrow \alpha'$ martensitic transformation twinning occurs in the HAZ. The irradiation-induced cavities create a high number of nucleation sites for direct $\gamma \rightarrow \alpha'$ martensitic transformation. The dislocation slip becomes easier for an intermediate step of forming hcp- ε plates for $\gamma \rightarrow \varepsilon \rightarrow \alpha'$ martensitic transformation. The competition between the dislocation slip and the direction nucleation of α' phase indicates the potential of irradiation-controlled martensitic transformation by modulation of the irradiation-induced cavities.

5. *In-situ* micropillar compression experiments were performed on the base metal and the HAZ of a laser weld on a neutron irradiated AISI 304L SS at room temperature. On {101} grains, deformation-induced γ to hcp- ϵ martensitic transformation occurs in the base metal, while deformation twinning arises in the HAZ.
6. Compared to the HAZ, a higher density of irradiation-induced cavities in the base metal could create a higher number density of nucleation sites for martensitic transformation and increase the CRSS on the deformation plane for twinning. The surface area created by irradiation-induced cavities could sufficiently compensate the martensite surface energy. As a result, the sum of the Gibbs free energy and the mechanical strain energy of the irradiated microstructure will exceed the critical martensitic transformation energy.
7. A phenomenological model for the deformation transition criteria has been proposed based on the mean inter-cavity distance. Depending on the magnitude of the mean cavity distance compared with the two characteristic lengths, namely, separation distance of partials and mean free paths of dislocations, the deformation mode alters between austenite-to-martensite phase transformation and deformation twinning.

Based on our results from this thesis, the following recommendations are suggested for future works:

1. Large-scale dislocation dynamics simulations will be performed to determine the mechanical state of the dislocations near the cavities. This will enable us to compare the localized stress concentration with the twinning criteria, as well as validate the proposed deformation transition criteria.
2. An *in-situ* SEM microcompression test will be performed on a laser weldment of higher dose and He concentration condition. This will enable us to directly compare the results with our data on the lower dose and He sample, which validates the role of the irradiation-induced cavities on deformation-induced martensitic phase transformation.
3. An *in-situ* TEM nanomechanical test on laser welds on different He and dose combinations will be performed during the loading condition to observe the nucleation sites of martensitic transformation, either around cavities or partials.
4. Further ion-irradiation on these laser weldments will be performed to examine the integrity of these welds under an extended irradiation service period.

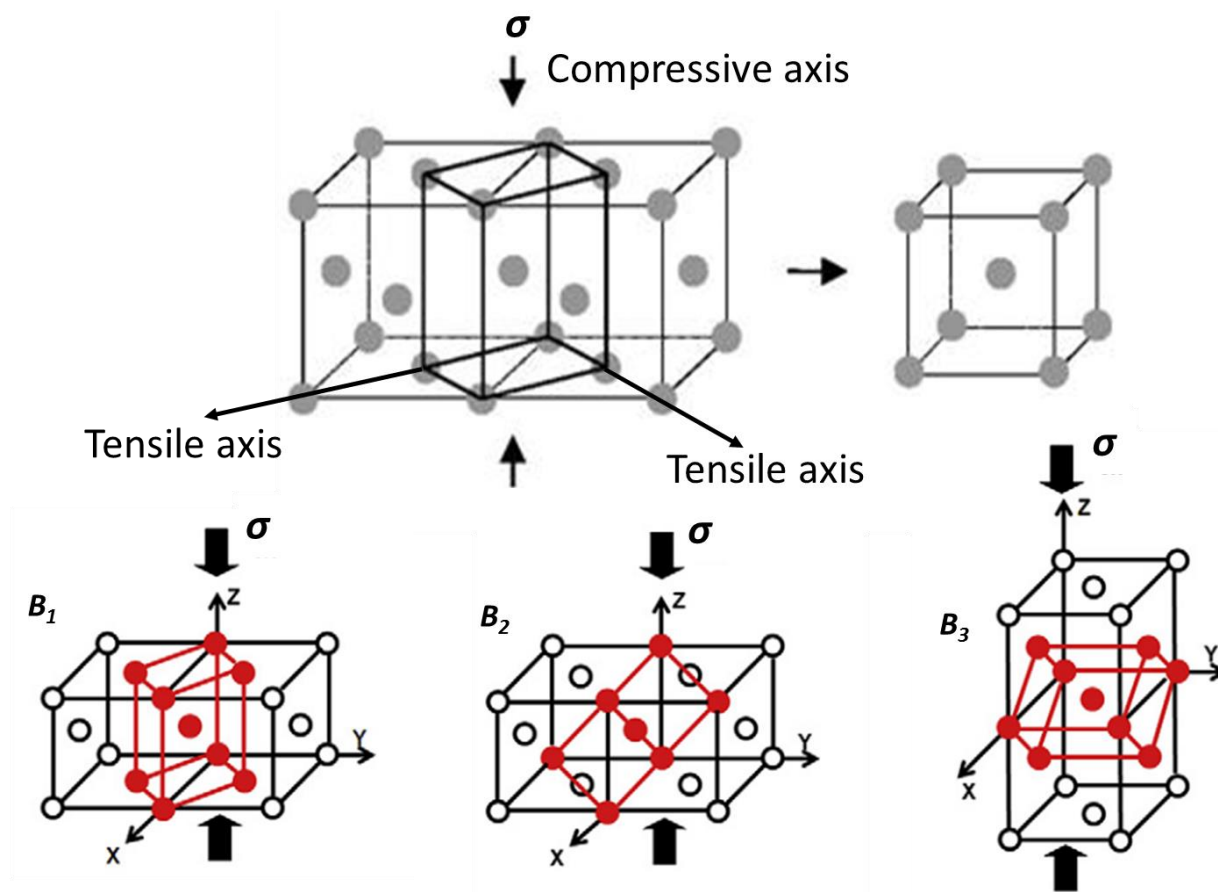


Figure A 2 Schematic representation of the austenite-to-martensite transformation through lattice deformation.

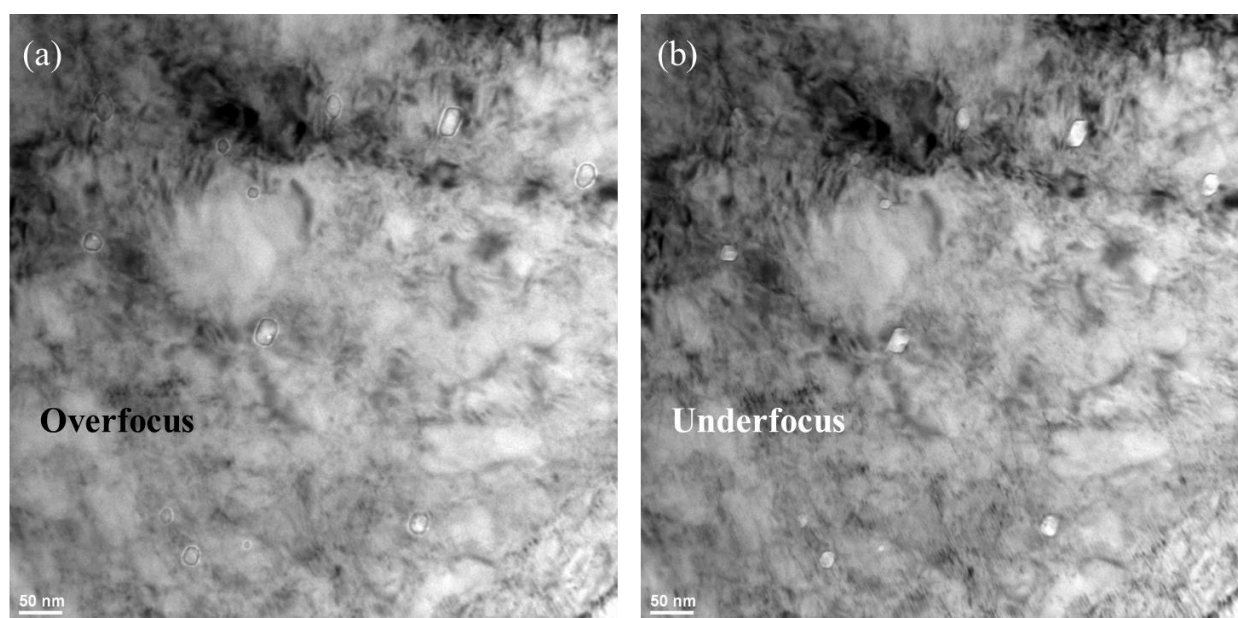


Figure A 3 Irradiation-induced voids in the base metal of laser welds of AISI 304L SS of 1 dpa and 0.2 appm He: in the (a) overfocused, and (b) underfocused conditions.

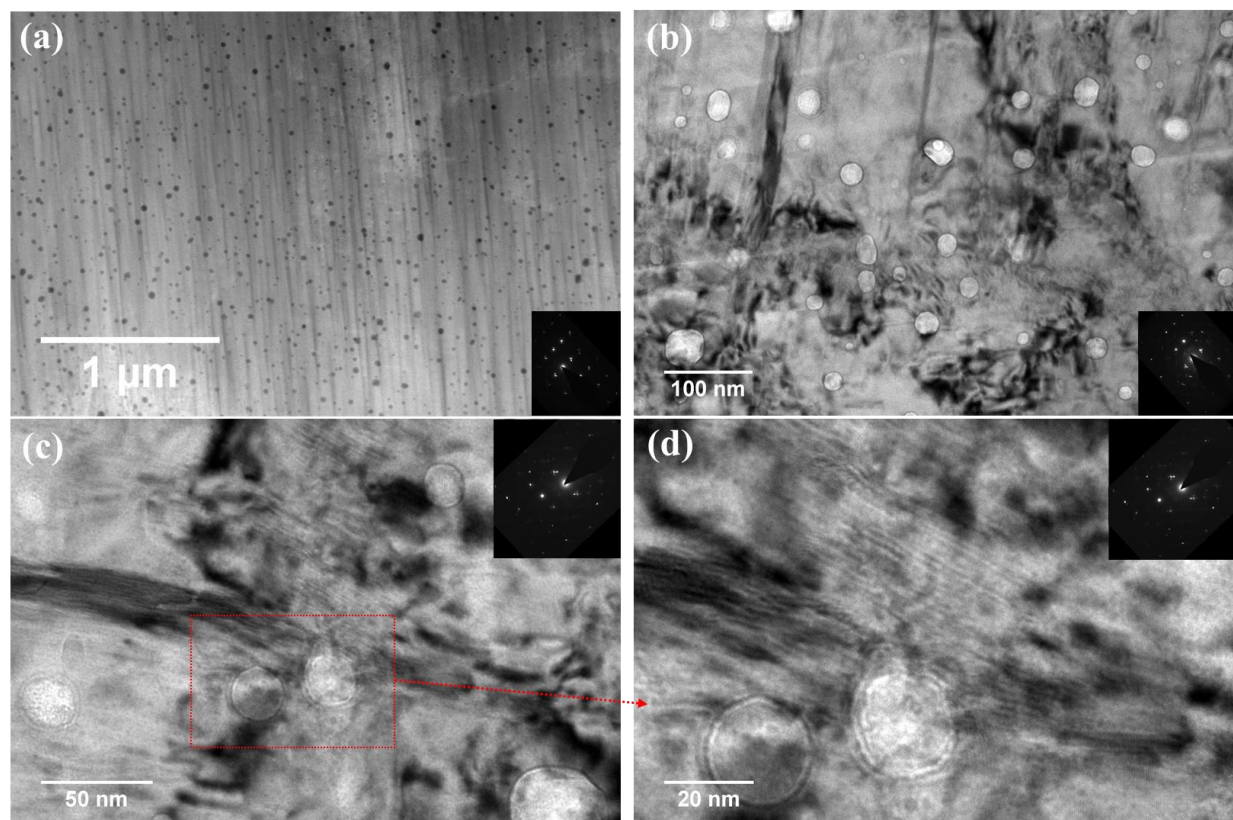


Figure A 4 Martensite-void interface in the irradiated AISI 304L SS of 23 dpa and 3 appm He, shown at different magnifications: (a) STEM image, and (b)-(d) BFTEM images of the voids with martensite laths penetrating through.

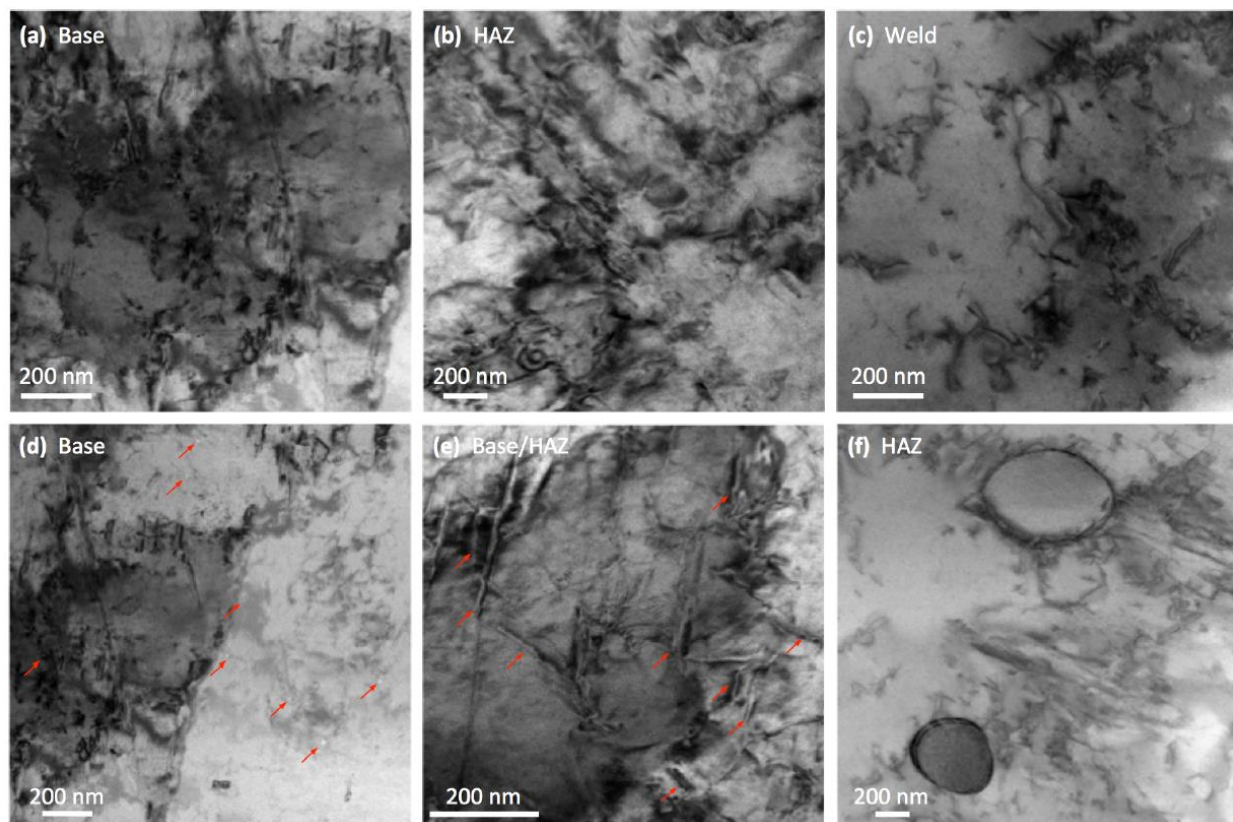


Figure A 5 TEM micrographs of as-welded 304SS, neutron irradiated to 0.4 dpa, 1 appm He, 0.2-0.5% swelling, showing dislocation morphologies in (a) weld metal, (b) heat affected zone, and (c) base metal; (d) voids and (e) dislocation loops in weld metal indicated by arrows; and (f) Cr precipitates in HAZ.

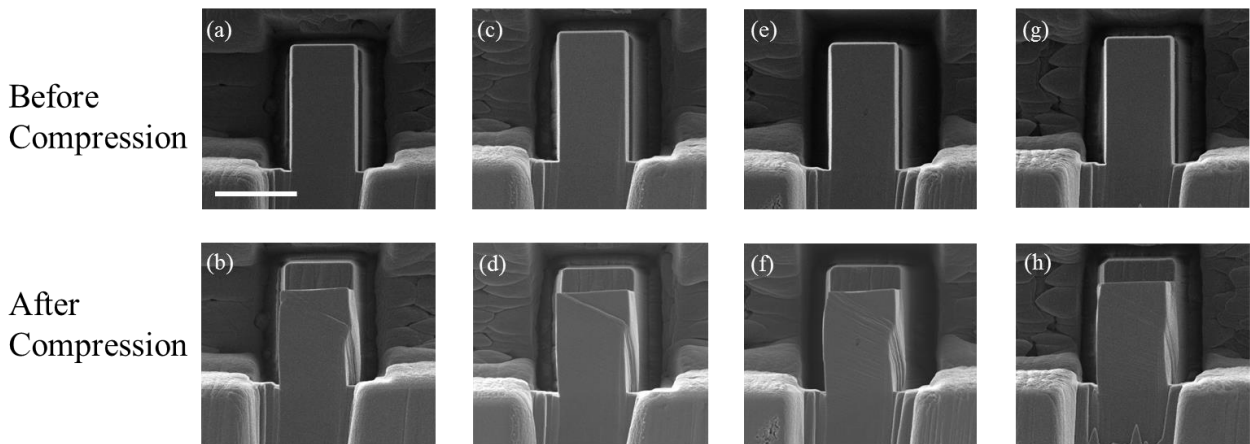


Figure A 6 SEM images of additional pillars (i.e., other than those shown in [Fig. 6.13](#)) of the $\{101\}$ grains from the HAZ before and after compression (a-b), (c-d), (e-f), and (g-h).

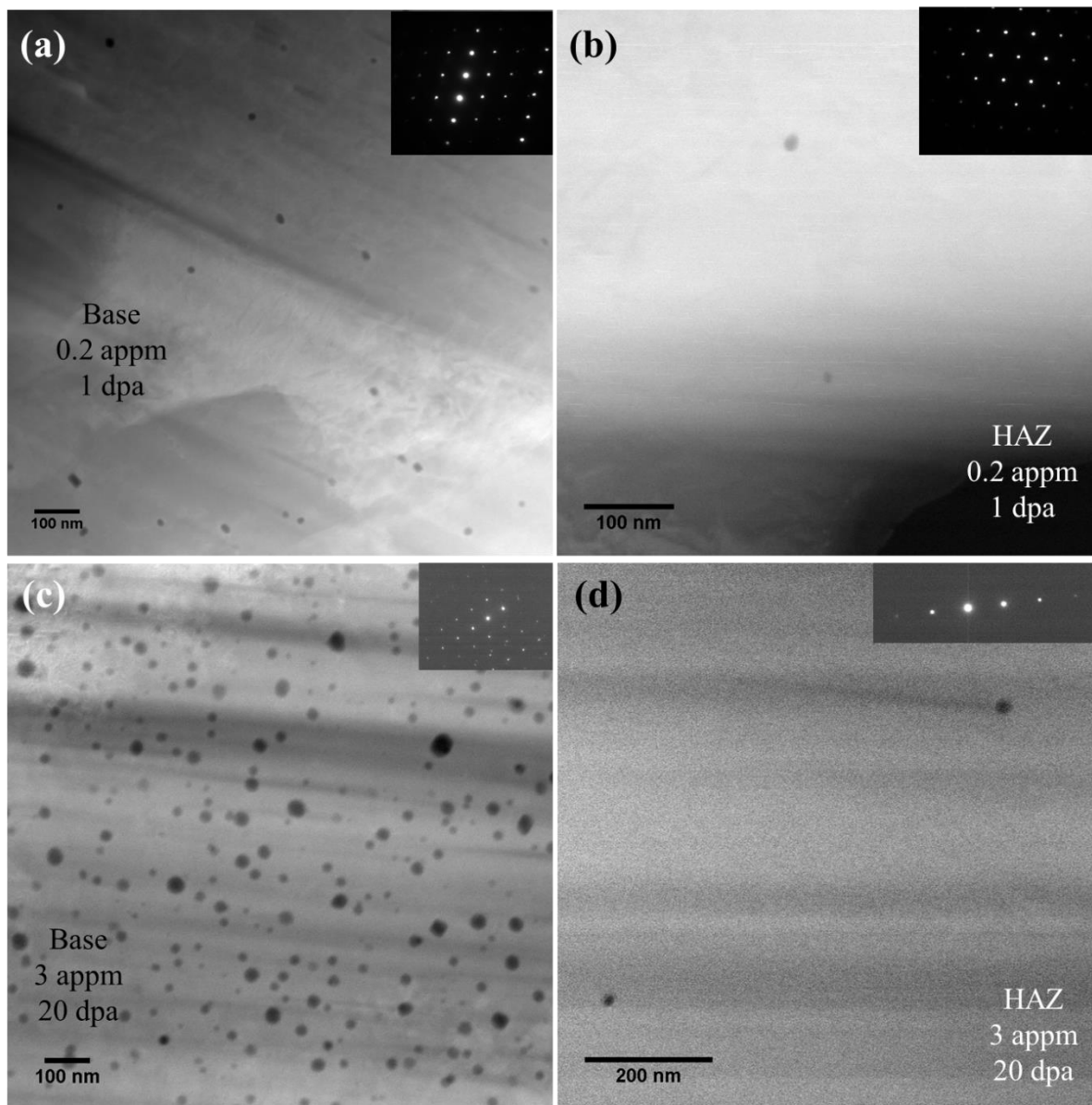


Figure A 7 Cavities of the 0.2 appm, 1dpa (a) base, (b) HAZ and 3appm, 20dpa (c) base and (d) HAZ neutron irradiated 304L SS.

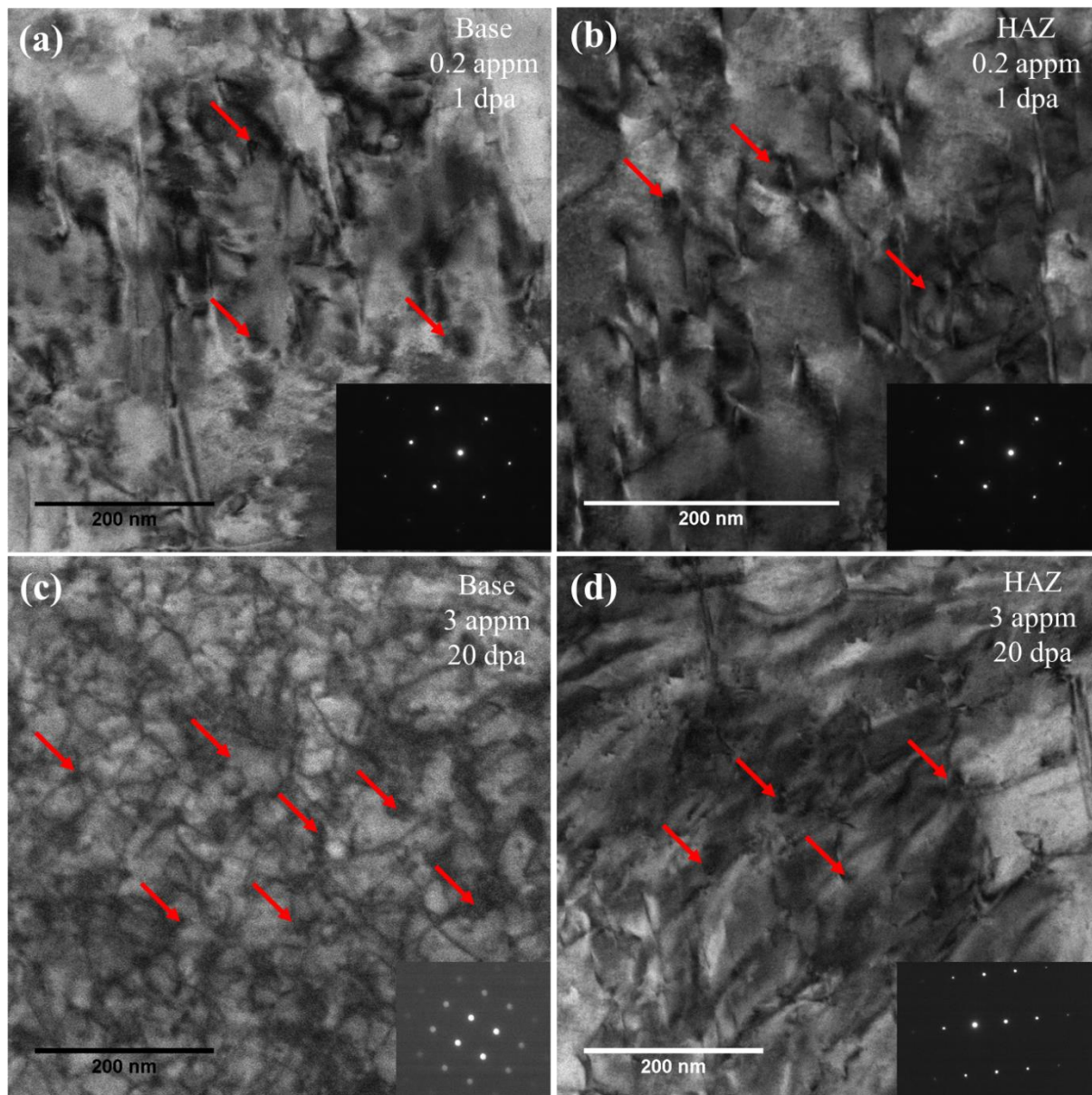


Figure A 8 Bright-field STEM micrographs of loops of the 0.2 appm, 1dpa (a) base, (b) HAZ and 3appm, 20dpa (c) base and (d) HAZ neutron irradiated 304L SS.

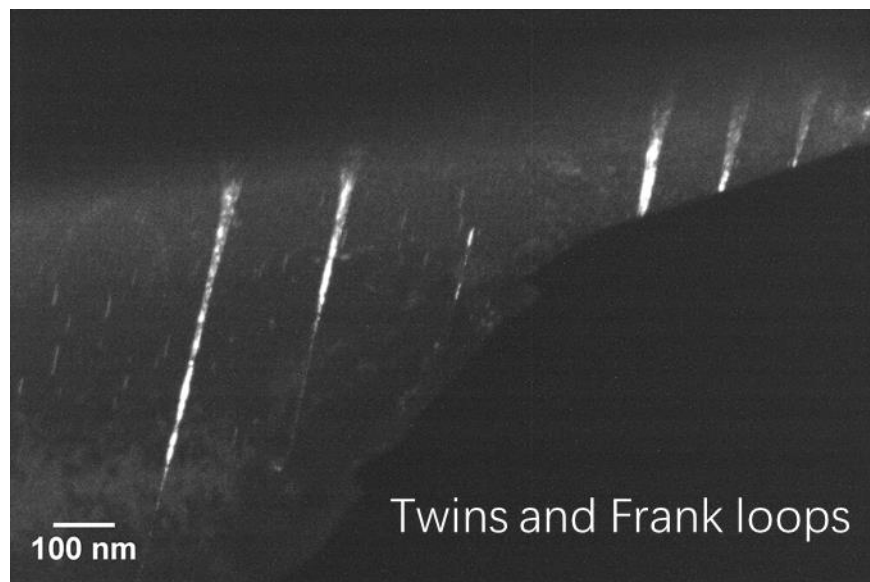


Figure A 9 Twins and Frank loops in the HAZ of laser welds of irradiated AISI 304L SS of 28 dpa and 8 appm He.

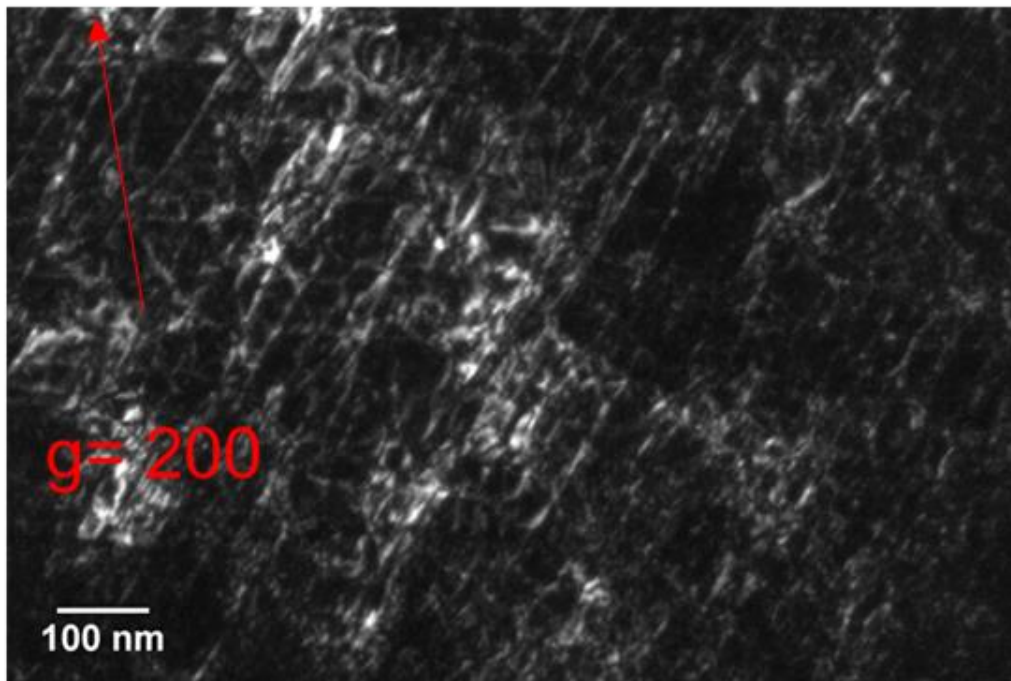


Figure A 10 Dislocations in the HAZ of laser welds of irradiated AISI 304L SS of 28 dpa and 8 appm He.

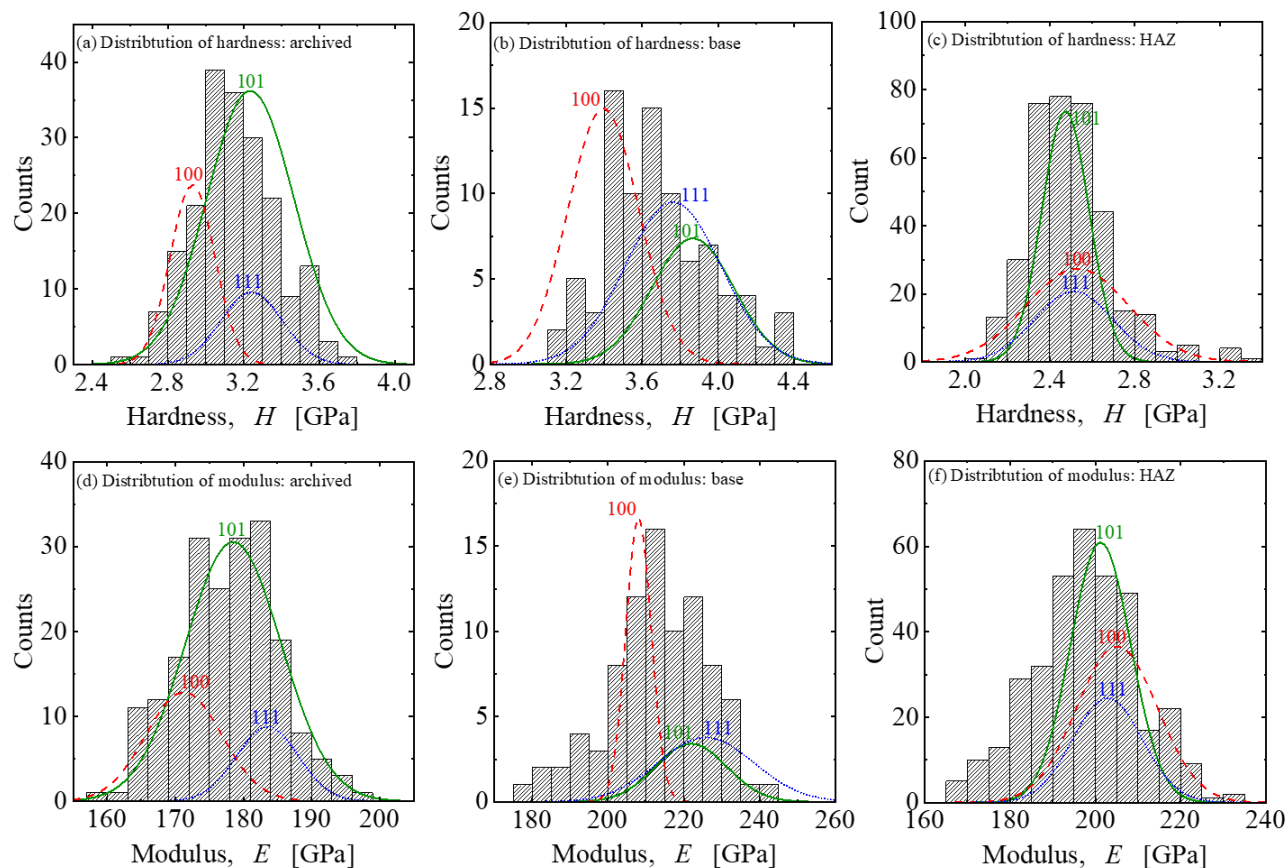


Figure A 11 Histogram for hardness and modulus with predicted Gaussian distribution fitting of hardness and modulus of indents at {100}, {101}, {111} grains (a)-(c) distribution of hardness and (d)- (f) distribution of modulus for archived 304L SS, base metal of the laser weld and HAZ.

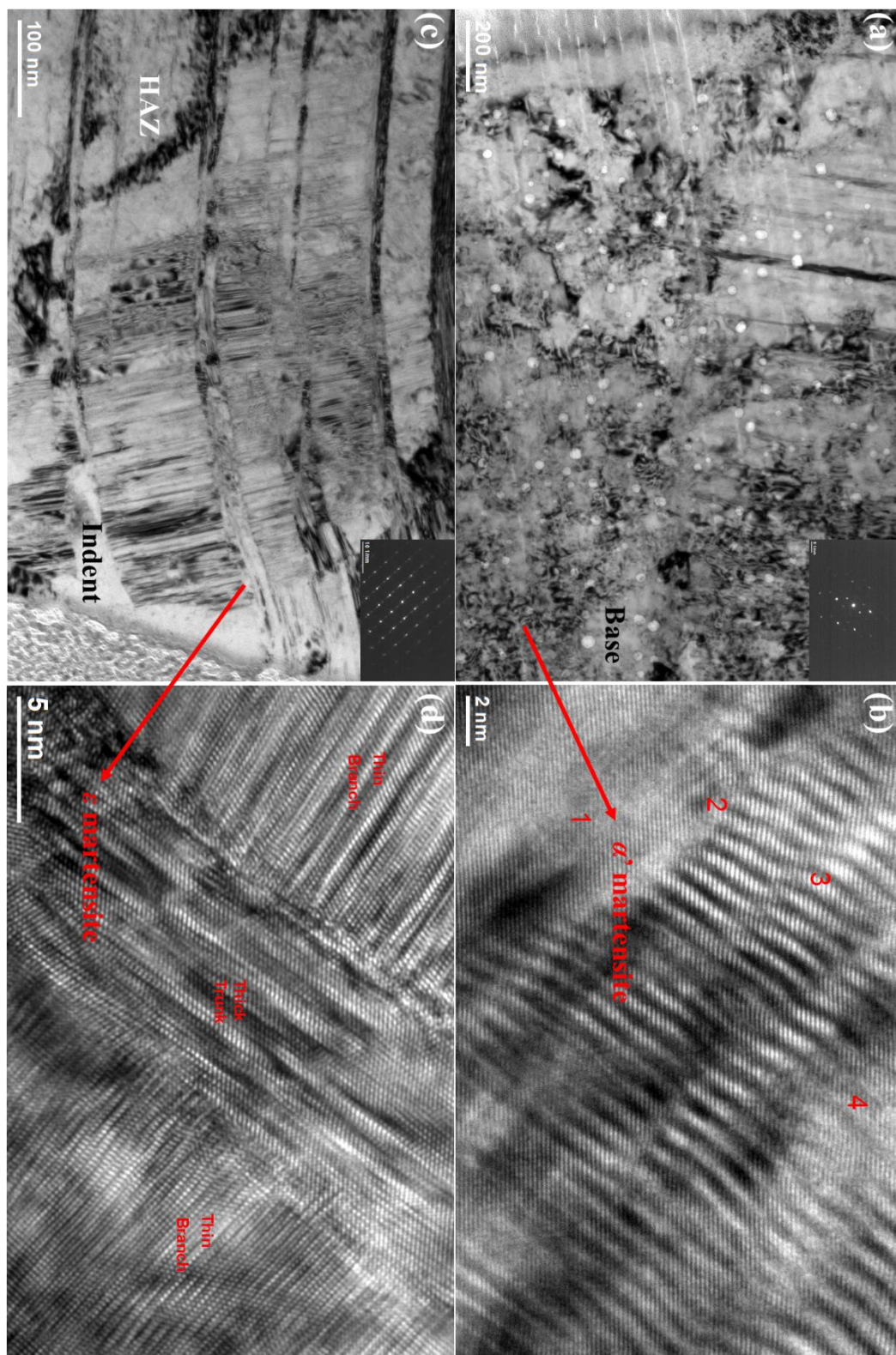


Figure A 12 Nanoindentation-induced martensitic transformation (a) base and (b) alpha prime bct martensite, (c) HAZ and (d) alpha prime bct and epsilon hcp martensite.

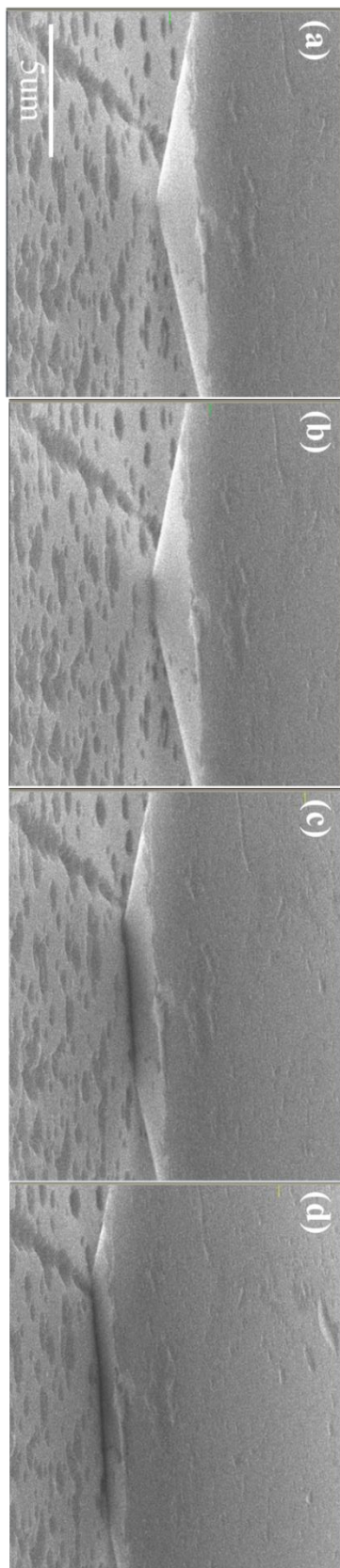


Figure A 13 *In-situ* nanoindentation on 0.2 appm, 1 dpa neutron irradiated AISI 304L SS.

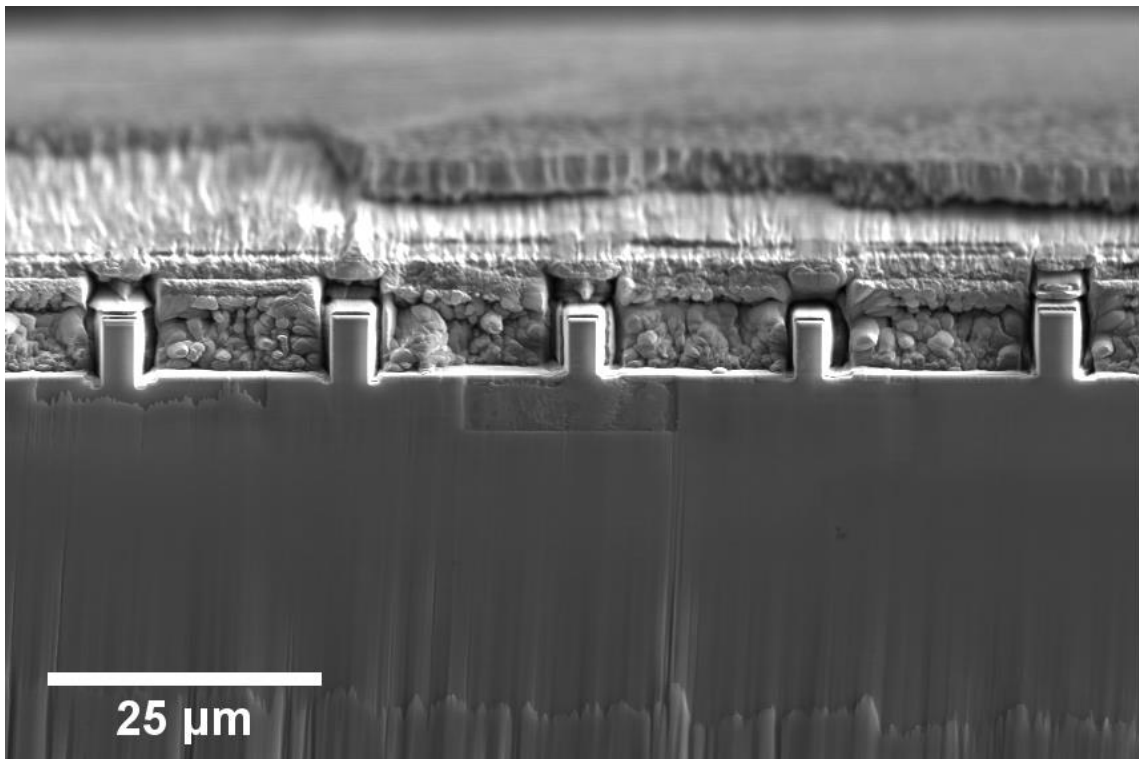


Figure A 14 Finished micropillars at $\{112\}$ grains using FIB milling technique.

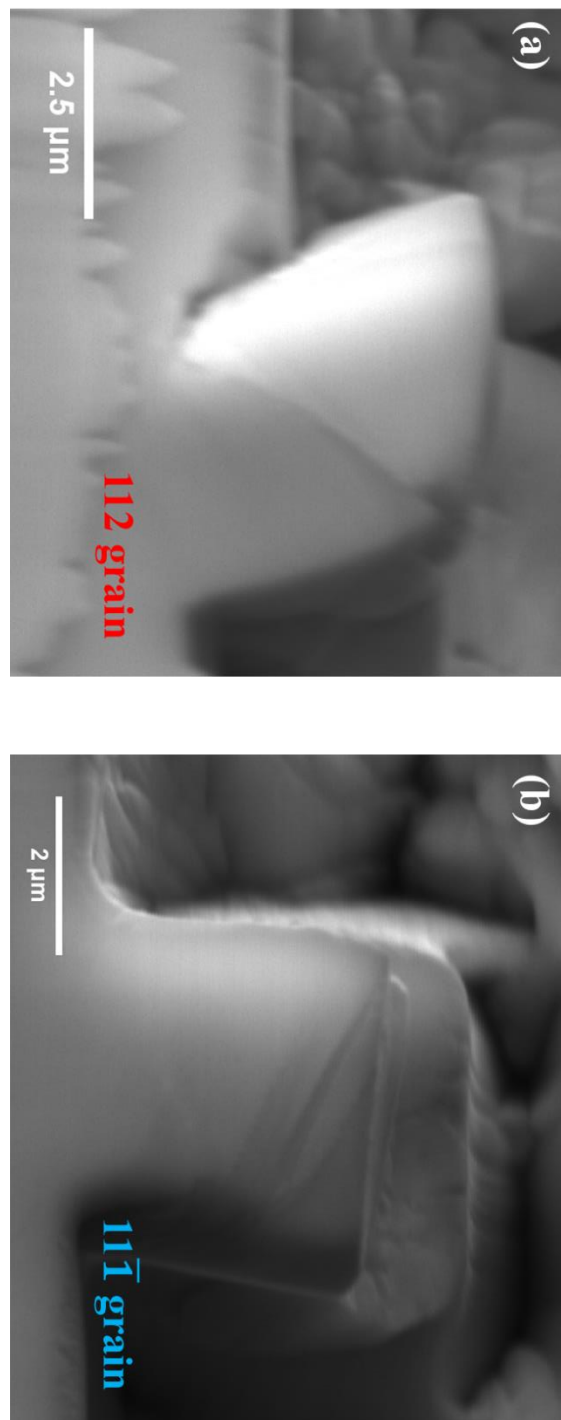


Figure A 15 0.2 appm, 1 dpa neutron irradiated 304L SS sample: slip bands and twinning after microcompression pillar test (a) single slip band at $\{112\}$ grain and (b) multiple slip bands in $\{11\bar{1}\}$ grain.

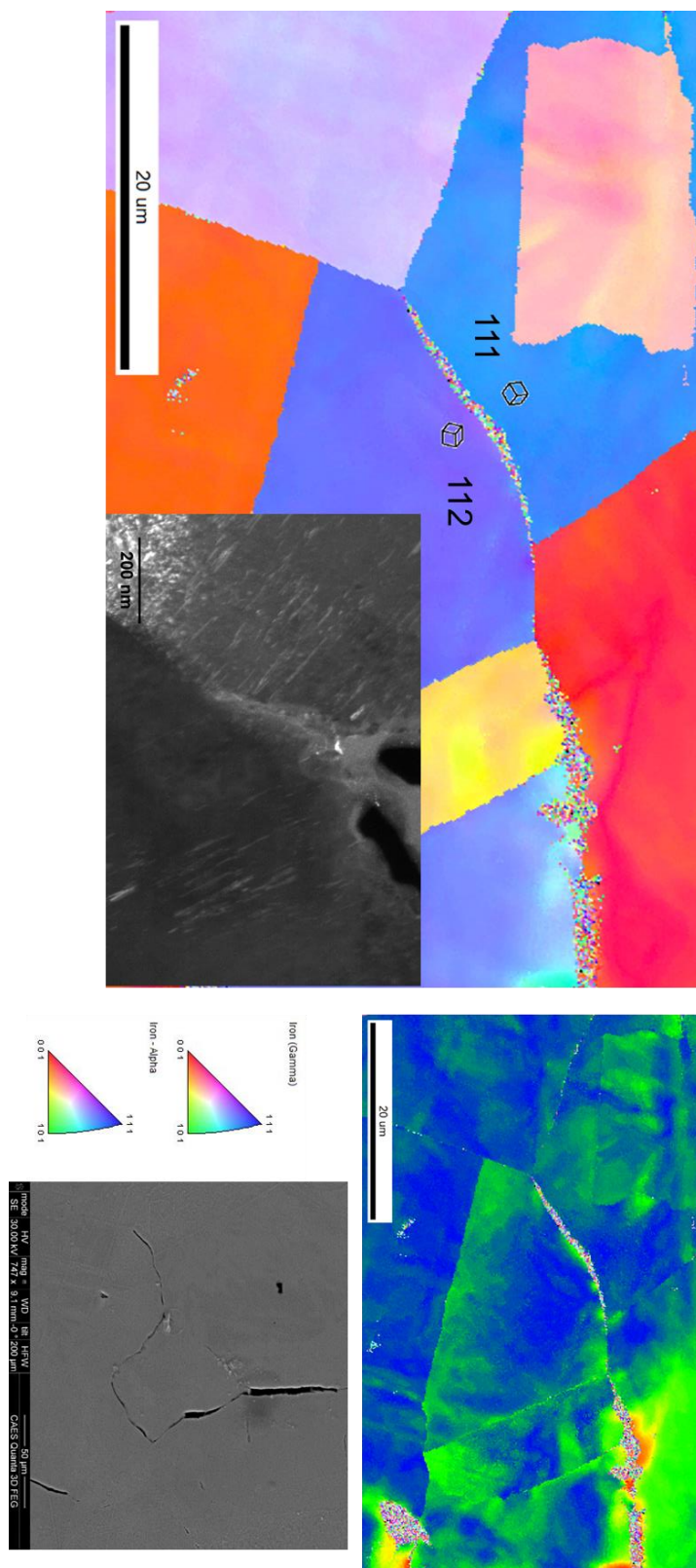


Figure A 16 Crack analysis of the HAZ ([111] and [112] of $\Sigma 5$ boundary) in laser welds of AISI 304 L SS of 23 dpa and 3 appm He.

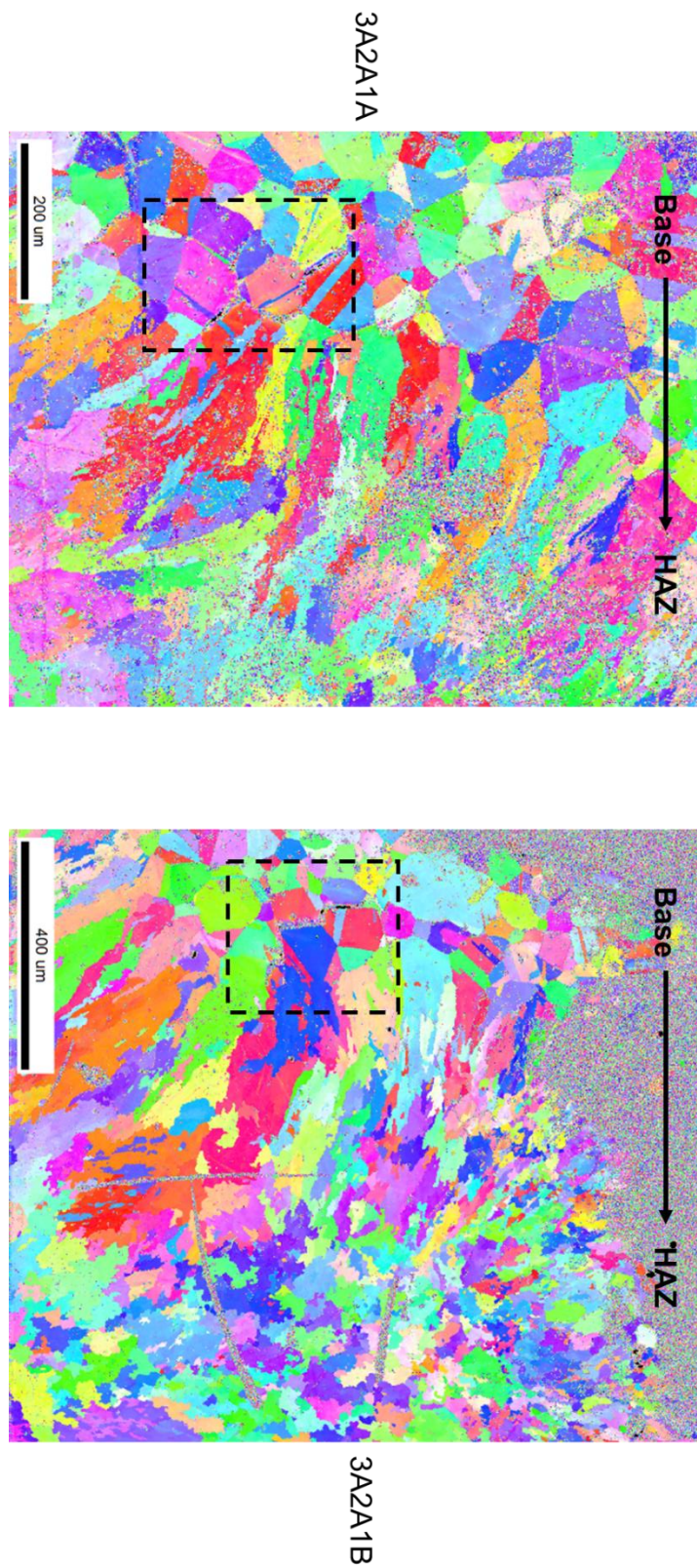


Figure A 17 OIM mapping of the grains from base to HAZ in the laser welds of irradiated AISI 304L SS of 23 dpa and 3 appm He.

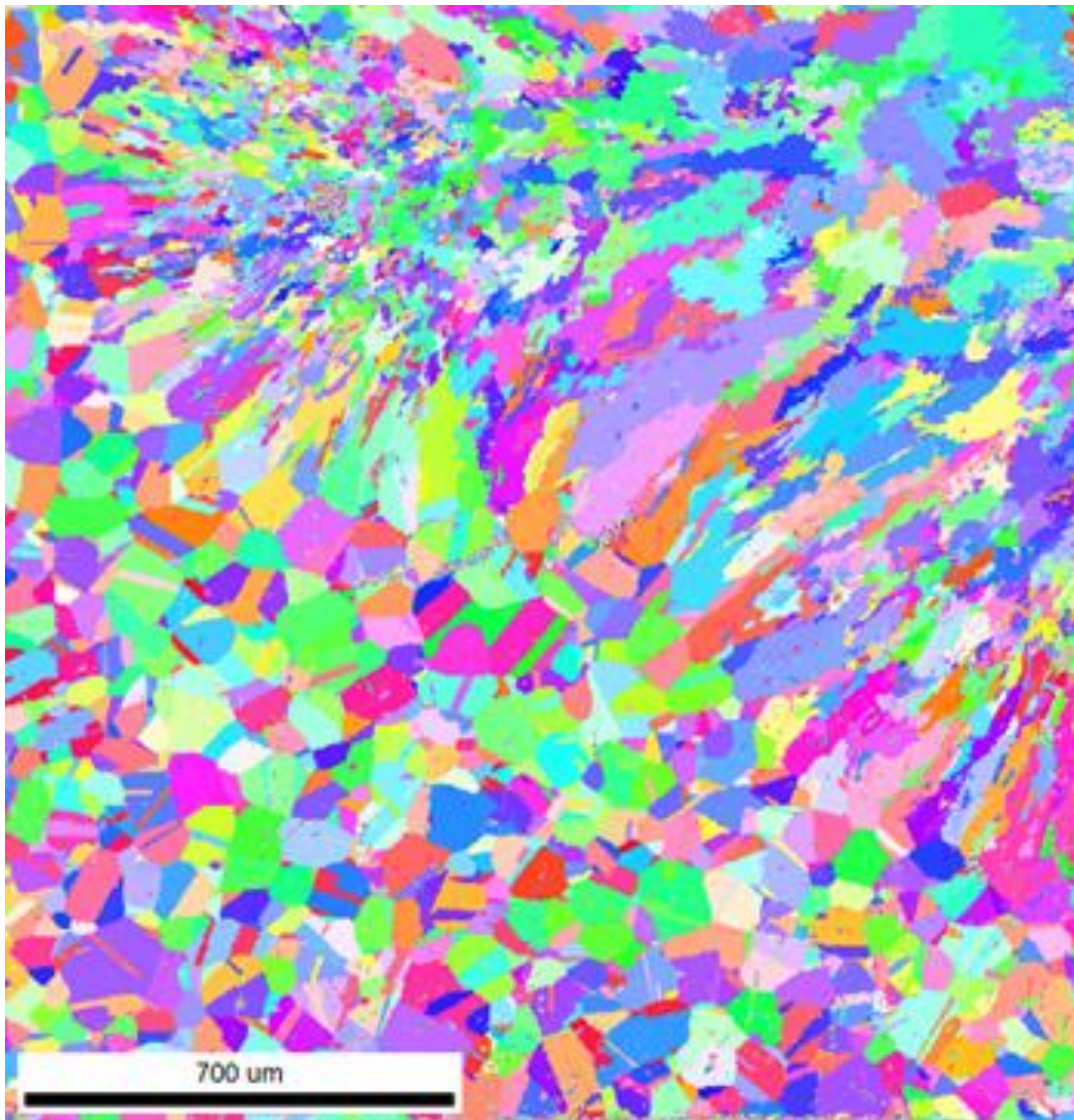


Figure A 18 OIM mapping of the grains from base to HAZ in the laser welds of irradiated AISI 304L SS of 28 dpa and 8 appm He.

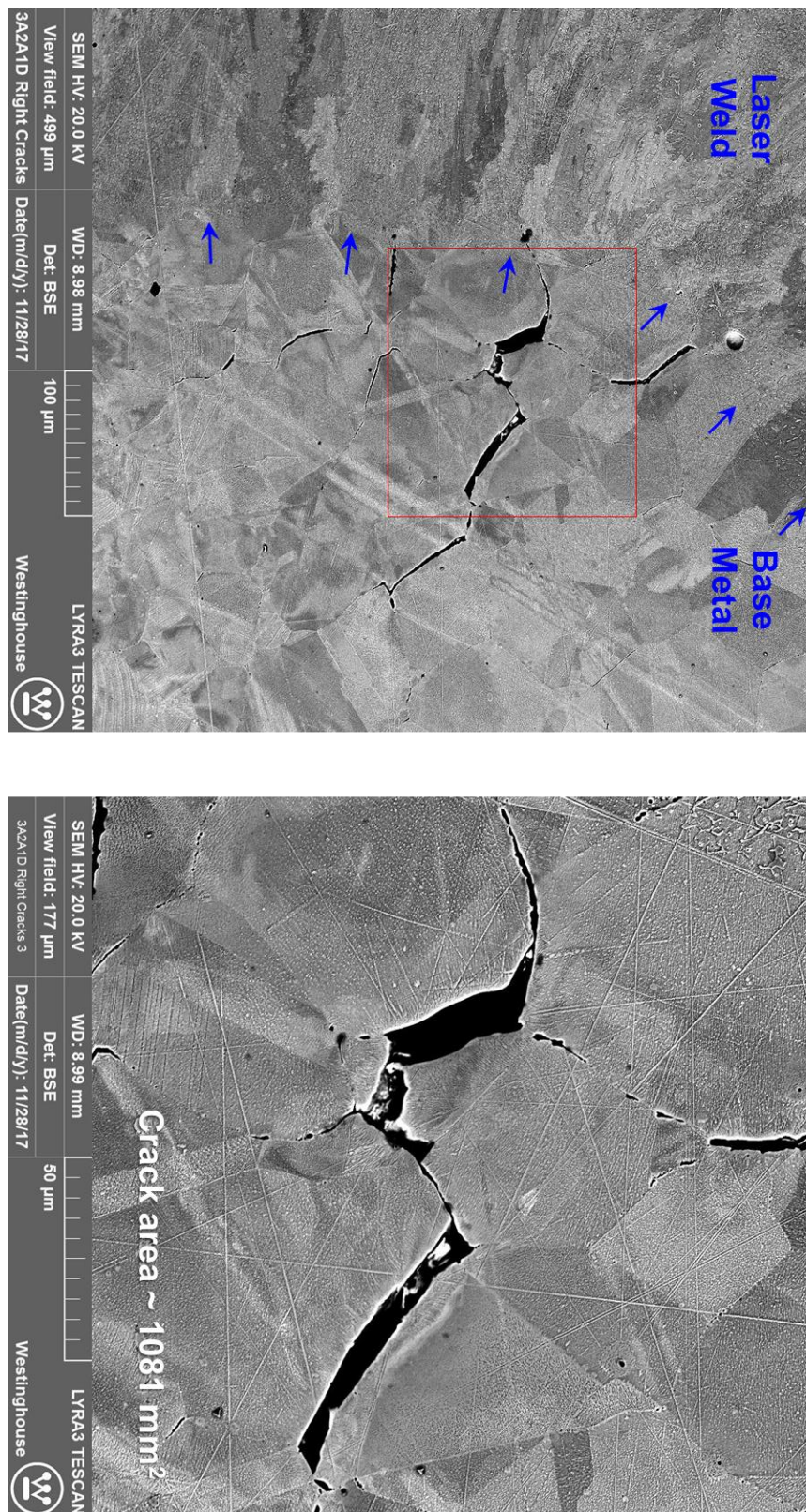


Figure A 19 Crack analysis of the HAZ in the laser weldment on block 3 of 23 dpa and 3 appm He.

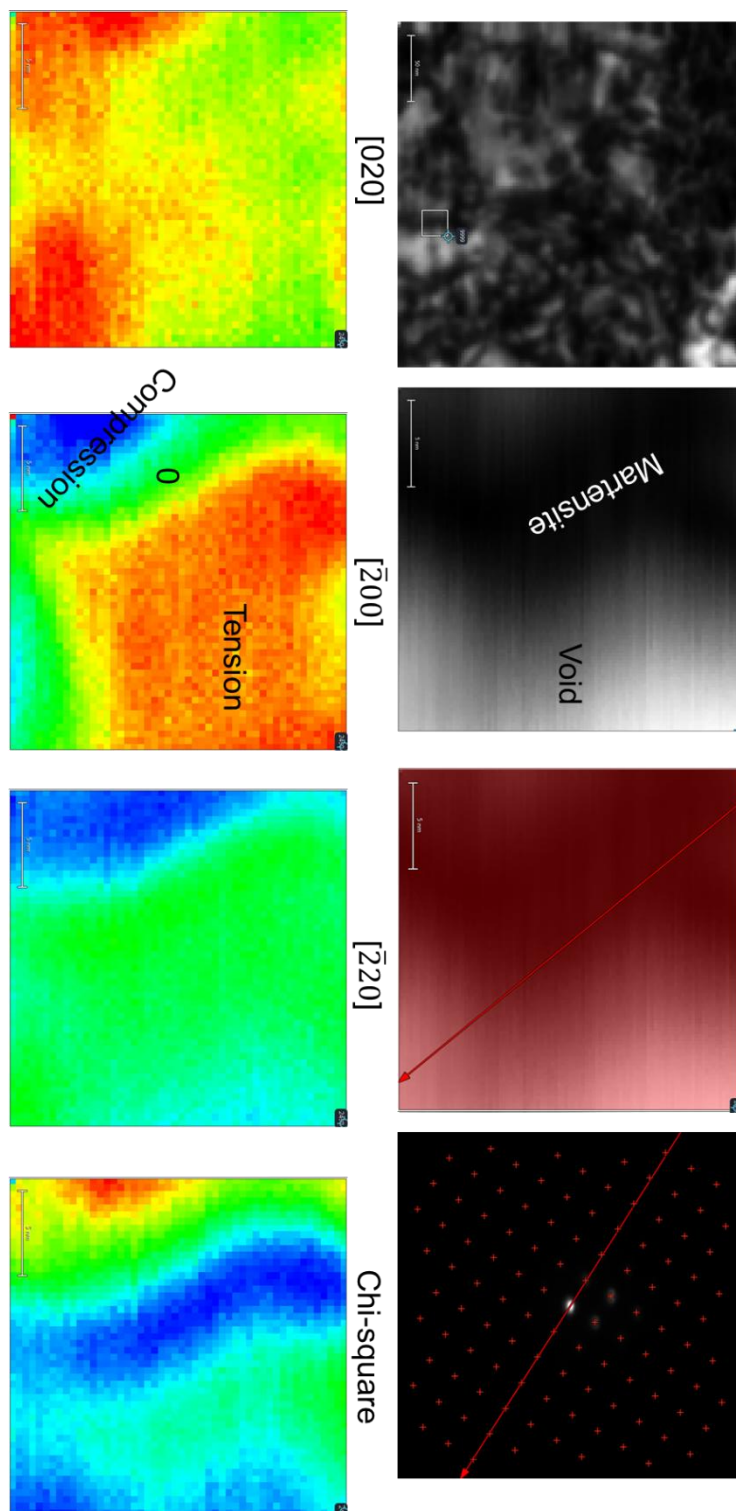


Figure A 20 Strain mapping of a void-martensite interface of the base metal of irradiated AISI 304L SS of 23 dpa and 3 appm He.

REFERENCES

- [1] W.R. Kanne, G.T. Chandler, D.Z. Nelson, E.A. Franco-Ferreira, Welding irradiated stainless steel, *J. Nucl. Mater.* 225 (1995) 69–75. doi:10.1016/0022-3115(94)00439-0.
- [2] C.A. Wang, M.L. Grossbeck, B.A. Chin, Threshold helium concentration required to initiate cracking during welding of irradiated stainless steel, *J. Nucl. Mater.* 225 (1995) 59–68. doi:10.1016/0022-3115(95)00014-3.
- [3] S.E. Donnelly, The density and pressure of helium in bubbles in implanted metals: A critical review, *Radiat. Eff.* 90 (1985) 1–47. doi:10.1080/00337578508222514.
- [4] S. Sharafat, A. Takahashi, K. Nagasawa, N. Ghoniem, A description of stress driven bubble growth of helium implanted tungsten, *J. Nucl. Mater.* 389 (2009) 203–212. doi:10.1016/j.jnucmat.2009.02.027.
- [5] S. Kawano, S. Nakahigashi, K. Uesugi, H. Nakamura, W. Kono, K. Fukuya, F. Kano, A. Hasegawa, K. Abe, Weldability of helium-containing stainless steels using a YAG laser, *J. Nucl. Mater.* 258-263 (1998) 2018–2022. doi:10.1016/S0022-3115(98)00342-0.
- [6] Y. Morishima, M. Koshiishi, K. Kashiwakura, T. Hashimoto, S. Kawano, Re-weldability of neutron irradiated Type 304 and 316L stainless steels, *J. Nucl. Mater.* 329-333 (2004) 663–667. doi:10.1016/j.jnucmat.2004.04.094.
- [7] H. Yamada, H. Kawamura, K. Tsuchiya, G. Kalinin, W. Kohno, Y. Morishima, Re-weldability tests of irradiated 316L(N) stainless steel using laser welding technique, *J. Nucl. Mater.* 307-311 (2002) 1584–1589. doi:10.1016/S0022-3115(02)00967-4.
- [8] S. Nishimura, R. Katsura, Y. Saito, W. Kono, H. Takahashi, M. Koshiishi, T. Kato, K. Asano, Yag laser welding of neutron irradiated stainless steels, *J. Nucl. Mater.* 258-263 (1998) 2002–2007. doi:10.1016/S0022-3115(98)00127-5.
- [9] F. Malekghaini, M. Hamed, M. Torkamany, J. Sabbaghzadeh, Weld metal microstructural characteristics in pulsed Nd: YAG laser welding, *Scr. Mater.* 56 (2007) 955–958. doi:10.1016/j.scriptamat.2007.02.019.

- [10] Z. Li, G. Fontana, Autogenous laser welding of stainless steel to free-cutting steel for the manufacture of hydraulic valves, *J. Mater. Process. Technol.* 74 (1998) 174–182. doi:10.1016/S0924-0136(97)00265-3.
- [11] S. Katayama, Laser welding of aluminium alloys and dissimilar metals, *Weld. Int.* 18 (2004) 618–625. doi:10.1533/wint.2004.3315.
- [12] S.A.A. Akbari Mousavi, A.R. Sufizadeh, Metallurgical investigations of pulsed Nd:YAG laser welding of AISI 321 and AISI 630 stainless steels, *Mater. Des.* 30 (2009) 3150–3157. doi:10.1016/j.matdes.2008.11.026.
- [13] N. Arivazhagan, S. Singh, S. Prakash, G.M. Reddy, Investigation on AISI 304 austenitic stainless steel to AISI 4140 low alloy steel dissimilar joints by gas tungsten arc, electron beam and friction welding, *Mater. Des.* 32 (2011) 3036–3050. doi:10.1016/j.matdes.2011.01.037.
- [14] M. Vedani, Microstructural evolution of tool steels after Nd-YAG laser repair welding, *J. Mater. Sci.* 39 (2004) 241–249. doi:10.1023/B:JMISC.0000007750.16970.4e.
- [15] G.N. Haidemenopoulos, Coupled thermodynamic/kinetic analysis of diffusional transformations during laser hardening and laser welding, *J. Alloys Compd.* 320 (2001) 302–307. doi:10.1016/S0925-8388(00)01493-6.
- [16] A.R. Sufizadeh, S.A.A. Akbari Mousavi, Microstructures and mechanical properties of dissimilar Nd:YAG laser weldments of AISI4340 and AISI316L steels, *Int. J. Miner. Metall. Mater.* 24 (2017) 538–549. doi:10.1007/s12613-017-1435-0.
- [17] N. Kumar, M. Mukherjee, A. Bandyopadhyay, Comparative study of pulsed Nd:YAG laser welding of AISI 304 and AISI 316 stainless steels, *Opt. Laser Technol.* 88 (2017) 24–39. doi:10.1016/j.optlastec.2016.08.018.
- [18] J.R. Berretta, W. de Rossi, M. David Martins das Neves, I. Alves de Almeida, N. Dias Vieira Junior, Pulsed Nd:YAG laser welding of AISI 304 to AISI 420 stainless steels, *Opt. Lasers Eng.* 45 (2007) 960–966. doi:10.1016/j.optlaseng.2007.02.001.

- [19] M. Rossini, P.R. Spena, L. Cortese, P. Matteis, D. Firrao, Investigation on dissimilar laser welding of advanced high strength steel sheets for the automotive industry, *Mater. Sci. Eng. A.* 628 (2015) 288–296. doi:10.1016/j.msea.2015.01.037.
- [20] A. De, C.A. Walsh, S.K. Maiti, H.K. D H Bhadeshia, Prediction of cooling rate and microstructure in laser spot welds, (n.d.). doi:10.1179/136217103225005633.
- [21] A.P. Mackwood, R.C. Crafer, Thermal modelling of laser welding and related processes: a literature review, *Opt. Laser Technol.* 37 (2005) 99–115. doi:10.1016/j.optlastec.2004.02.017.
- [22] K. Mao, H. Wang, Y. Wu, V. Tomar, J.P. Wharry, Microstructure-property relationship for AISI 304/308L stainless steel laser weldment, *Mater. Sci. Eng. A.* 721 (2018) 234–243. doi:10.1016/j.msea.2018.02.092.
- [23] M.M.A. Khan, L. Romoli, M. Fiaschi, G. Dini, F. Sarri, Laser beam welding of dissimilar stainless steels in a fillet joint configuration, *J. Mater. Process. Technol.* 212 (2012) 856–867. doi:10.1016/j.jmatprotec.2011.11.011.
- [24] H. Zuhailawati, M.A. Jamaluddin, A.A. Seman, S. Ismail, Welding Investigation and Prediction of Tensile Strength of 304 Stainless Steel Sheet Metal Joint by Response Surface Methodology, *Procedia Chem.* 19 (2016) 217–221. doi:10.1016/j.proche.2016.03.096.
- [25] K. Mao, Y. Wu, J.P. Wharry, EBSD and TEM Analysis of the Heat Affected Zone of Laser Welded AISI 304/308 Stainless Steel, *Microsc. Microanal.* 23 (2017) 2212–2213. doi:10.1017/S1431927617011722.
- [26] A.P. Mackwood, R.C. Crafer, Thermal modelling of laser welding and related processes: a literature review, *Opt. Laser Technol.* 37 (2005) 99–115. doi:10.1016/j.optlastec.2004.02.017.
- [27] K.H. Yano, K.S. Mao, J.P. Wharry, D.M. Porterfield, Investing in a permanent and sustainable nuclear waste disposal solution, *Prog. Nucl. Energy.* 108 (2018) 474–479. doi:10.1016/j.pnucene.2018.07.003.
- [28] K.S. Mao, Y. Wu, C. Sun, E. Perez, J.P. Wharry, Laser weld-induced formation of amorphous Mn–Si precipitate in 304 stainless steel, *Materialia.* 3 (2018) 174–177. doi:10.1016/j.mtla.2018.08.012.

- [29] W.M. Garrison, M.O.H. Amuda, *Stainless Steels: Martensitic*, Ref. Modul. Mater. Sci. Mater. Eng. (2017). doi:10.1016/B978-0-12-803581-8.02527-3.
- [30] A.L. Lund, *Feasibility of Underwater Welding of Highly Irradiated In-Vessel Components of Boiling-Water Reactors A Literature Review*, 1997. <http://www.osti.gov/scitech/biblio/560861>.
- [31] W.R. Kanne, *REMOTE REACTOR REPAIR: GTA WELD CRACKING CAUSED BY ENTRAPPED HELIUM*, Weld. J. (1988).
- [32] W.R. Kanne, M.R. Louthan, D.T. Rankin, M.H. Tosten, *Weld repair of irradiated materials*, Mater. Charact. (1999). doi:10.1016/S1044-5803(99)00032-7.
- [33] K. Asano, S. Nishimura, Y. Saito, H. Sakamoto, Y. Yamada, T. Kato, T. Hashimoto, *Weldability of neutron irradiated austenitic stainless steels*, J. Nucl. Mater. 264 (1999) 1–9.
- [34] W.R. Kanne, E.A. Franco-Ferreira, M.R. Louthan, M.H. Tosten, *WSRC-MS-90-222X WELD REPAIR OF AUSTENITIC STAINLESS STEELS CONTAINING HELIUM (U)*, in: 72nd Am. Weld. Soc. Conv., Detroit, 1991.
- [35] P. 'l, W.R. Kanne, G.J. Bruck, A. Madeyski, D.A. Lohmeier, M.R. Louthan, D.T. Rankin, R.P. Shogan, G.G. Lcssmann, E.A. Franco-Femiral, W.R. Kanne, A. Lohmeier, M.R. Huthan, T. Rankin, E.A. Franco-Femira, *REACTOR VESSEL MATERIAL (U)*, in: Fifth Int. Symp. Environ. Degrad. Mater. Nucl. Power Syst. - Water React., Monterey, 1991.
- [36] E.A. Franco-Ferreira, and W. R. Kanne., *Remote reactor repair: Avoidance of helium-induced cracking using GMA welding*, Weld. J. 71 (1992) 43–51.
- [37] F. Legendre, S. Poissonnet, P. Bonnaille, L. Boulanger, L. Forest, *Some microstructural characterisations in a friction stir welded oxide dispersion strengthened ferritic steel alloy*, J. Nucl. Mater. (2009). doi:10.1016/j.jnucmat.2008.12.170.
- [38] D.T. Hoelzer, K.A. Unocic, M.A. Sokolov, Z. Feng, *Joining of 14YWT and F82H by friction stir welding*, J. Nucl. Mater. (2013). doi:10.1016/j.jnucmat.2013.04.027.
- [39] C.L. Chen, A. Richter, R. Kögler, L.T. Wu, *Dual-beam irradiation of friction stir spot welding of nanostructured ferritic oxide dispersion strengthened alloy*, in: J. Alloys Compd., 2012. doi:10.1016/j.jallcom.2011.11.055.

- [40] S. Nishimura, R. Katsura, Y. Saito, W. Kono, H. Takahashi, M. Koshiishi, T. Kato, K. Asano, Yag laser welding of neutron irradiated stainless steels, *J. Nucl. Mater.* 258 (1998) 2002–2007.
- [41] H. Yamada, H. Kawamura, K. Tsuchiya, G. Kalinin, W. Kohno, Y. Morishima, Re-weldability tests of irradiated 316L(N) stainless steel using laser welding technique, *J. Nucl. Mater.* 307 (2002) 1584–1589.
- [42] J. Tatman, *Welding on Irradiated Material*, (2014).
- [43] C.A.A. Wang, M.L.L. Grossbeck, H. Aglan, B.A.A. Chin, The effect of an applied stress on the welding of irradiated steels, *J. Nucl. Mater.* 239 (1996) 85–89. doi:10.1016/S0022-3115(96)00490-4.
- [44] W.R. Kanne, G.T. Chandler, D.Z. Nelson, E.A. Franco-Ferreira, Welding irradiated stainless steel, *J. Nucl. Mater.* 225 (1995) 69–75. doi:10.1016/0022-3115(94)00439-0.
- [45] M.M.A. Khan, L. Romoli, G. Dini, Laser beam welding of dissimilar ferritic/martensitic stainless steels in a butt joint configuration, *Opt. Laser Technol.* (2013). doi:10.1016/j.optlastec.2012.12.025.
- [46] H.J.K. Lemmen, K.J. Sudmeijer, I.M. Richardson, S. Van Der Zwaag, Laser beam welding of an oxide dispersion strengthened super alloy, *J. Mater. Sci.* (2007). doi:10.1007/s10853-006-0168-7.
- [47] J. Tatman, Development of Advanced Laser Welding and Models for Repair of Irradiated Reactor Components AWS Lasers Conference, in: *Am. Weld. Soc. Laser Conf.*, San Francisco, 2016.
- [48] et al. Li, S., The Effect of Helium on Welding Irradiated Materials, *Weld. J.* 90 (2011) 19S–26S. https://app.aws.org/wj/supplement/wj201101_s19.pdf.
- [49] F.A. Garner, B.M. Oliver, L.R. Greenwood, D.L. Porter, T. Allen, Measurement of Helium Generation in AISI 304 Reflector and Blanket Assemblies after Long-term Irradiation in EBR-II, in: *React. Dosim. 12th Int. Symp.*, ASTM International, 100 Barr Harbor Drive, PO Box C700, West Conshohocken, PA 19428-2959, 2007: pp. 109–109–8. doi:10.1520/STP45432S.

- [50] F.A. Garner, et. al., Measurement of void swelling in thick non-uniformly irradiated 304 stainless steel blocks using nondestructive ultrasonic techniques, in: Fontevraud 8 - Contrib. Mater. Investig. Oper. Exp. to LWRs' Safety, Perform. Reliab., Avignon, 2015. <https://indigitallibrary.inl.gov/sti/6303751.pdf>.
- [51] E.M. Rabenberg, B.J. Jaques, B.H. Sencer, F.A. Garner, P.D. Freyer, T. Okita, D.P. Butt, Mechanical behavior of AISI 304SS determined by miniature test methods after neutron irradiation to 28 dpa, *J. Nucl. Mater.* (2014). doi:10.1016/j.jnucmat.2014.02.018.
- [52] M.N. Gussev, K.G. Field, J.T. Busby, Strain-induced phase transformation at the surface of an AISI-304 stainless steel irradiated to 4.4 dpa and deformed to 0.8% strain, *J. Nucl. Mater.* 446 (2014) 187–192. doi:10.1016/J.JNUCMAT.2013.11.041.
- [53] K.G. Field, M.N. Gussev, J.T. Busby, Microstructural characterization of deformation localization at small strains in a neutron-irradiated 304 stainless steel, *J. Nucl. Mater.* 452 (2014) 500–508. doi:10.1016/j.jnucmat.2014.05.053.
- [54] Y. Huang, J.M.K. Wiezorek, F.A. Garner, P.D. Freyer, T. Okita, M. Sagisaka, Y. Isobe, T.R. Allen, Microstructural characterization and density change of 304 stainless steel reflector blocks after long-term irradiation in EBR-II, *J. Nucl. Mater.* 465 (2015) 516–530. doi:10.1016/j.jnucmat.2015.06.031.
- [55] J.M.K. Wiezorek, Y. Huang, F.A. Garner, P.D. Freyer, M. Sagisaka, Y. Isobe, T. Okita, Transmission Electron Microscopy of 304-type Stainless Steel after Exposure to Neutron Flux and Irradiation Temperature Gradients, *Microsc. Microanal.* 20 (2014) 1822–1823. doi:10.1017/S1431927614010848.
- [56] D. Edwards, E. Simonen, S. Bruemmer, Evolution of fine-scale defects in stainless steels neutron-irradiated at 275 °C, *J. Nucl. Mater.* 317 (2003) 13–31. doi:10.1016/S0022-3115(03)00002-3.
- [57] M. Jenkins, M. Kirk, Characterisation of Radiation Damage by Transmission Electron Microscopy, Taylor & Francis, 2000. doi:10.1201/9781420034646.
- [58] C.M. Parish, K.G. Field, A.G. Certain, J.P. Wharry, Application of STEM characterization for investigating radiation effects in BCC Fe-based alloys, *J. Mater. Res.* 30 (2015) 1275–1289. doi:10.1557/jmr.2015.32.
- [59] M.L. Jenkins, M.A. Kirk, Characterization of radiation-damage by transmission electron microscopy, Institute of Physics Pub, 2001.

- [60] M.L. Jenkins, Characterisation of radiation-damage microstructures by TEM, *J. Nucl. Mater.* 216 (1994) 124–156. doi:10.1016/0022-3115(94)90010-8.
- [61] Y. Dong, B.H. Sencer, F.A. Garner, E.A. Marquis, Microchemical and microstructural evolution of AISI 304 stainless steel irradiated in EBR-II at PWR-relevant dpa rates, *J. Nucl. Mater.* 467 (2015) 692–702. doi:10.1016/j.jnucmat.2015.10.041.
- [62] M.J. Swenson, J.P. Wharry, The comparison of microstructure and nanocluster evolution in proton and neutron irradiated Fe–9%Cr ODS steel to 3 dpa at 500 °C, *J. Nucl. Mater.* 467 (2015) 97–112. doi:10.1016/j.jnucmat.2015.09.022.
- [63] C. Sun, S. Zheng, C.C. Wei, Y. Wu, L. Shao, Y. Yang, K.T. Hartwig, S.A. Maloy, S.J. Zinkle, T.R. Allen, H. Wang, X. Zhang, Superior radiation-resistant nanoengineered austenitic 304L stainless steel for applications in extreme radiation environments, *Sci. Rep.* 5 (2015) 7801. doi:10.1038/srep07801.
- [64] V.I. Pastukhov, S.A. Averin, V.L. Panchenko, I.A. Portnykh, P.D. Freyer, L.A. Giannuzzi, F.A. Garner, Application of backscatter electrons for large area imaging of cavities produced by neutron irradiation, *J. Nucl. Mater.* 480 (2016) 289–300. doi:10.1016/j.jnucmat.2016.07.059.
- [65] Q. Yan, J. Gigax, D. Chen, F.A. Garner, L. Shao, Monte Carlo modeling of cavity imaging in pure iron using back-scatter electron scanning microscopy, *J. Nucl. Mater.* 480 (2016) 420–428. doi:10.1016/J.JNUCMAT.2016.08.016.
- [66] C. Sun, F.A. Garner, L. Shao, X. Zhang, S.A. Maloy, Influence of injected interstitials on the void swelling in two structural variants of 304L stainless steel induced by self-ion irradiation at 500 °C, *Nucl. Instruments Methods Phys. Res. Sect. B Beam Interact. with Mater. Atoms.* 409 (2017) 323–327. doi:10.1016/j.nimb.2017.03.070.
- [67] J.F. Ziegler, J.M. Manoyan, The stopping of ions in compounds, *Nucl. Instruments Methods Phys. Res. Sect. B Beam Interact. with Mater. Atoms.* 35 (1988) 215–228. doi:10.1016/0168-583X(88)90273-X.
- [68] L.K. Mansur, Correlation of neutron and heavy-ion damage: II. The predicted temperature shift if swelling with changes in radiation dose rate, *J. Nucl. Mater.* 78 (1978) 156–160. doi:10.1016/0022-3115(78)90514-7.
- [69] N.H. Packan, K. Farrell, J.O. Stiegler, Correlation of neutron and heavy-ion damage, *J. Nucl. Mater.* 78 (1978) 143–155. doi:10.1016/0022-3115(78)90513-5.

- [70] T. Toyama, Y. Nozawa, W. Van Renterghem, Y. Matsukawa, M. Hatakeyama, Y. Nagai, A. Al Mazouzi, S. Van Dyck, Irradiation-induced precipitates in a neutron irradiated 304 stainless steel studied by three-dimensional atom probe, *J. Nucl. Mater.* 418 (2011) 62–68. doi:10.1016/j.jnucmat.2011.07.027.
- [71] J.M.K. Wiezorek, Y. Huang, F.A. Garner, P.D. Freyer, M. Sagisaka, Y. Isobe, T. Okita, Transmission Electron Microscopy of 304-type Stainless Steel after Exposure to Neutron Flux and Irradiation Temperature Gradients, *Microsc. Microanal.* 20 (2014) 1822–1823. doi:10.1017/S1431927614010848.
- [72] M.J. Swenson, J.P. Wharry, Nanocluster irradiation evolution in Fe-9%Cr ODS and ferritic-martensitic alloys, *J. Nucl. Mater.* 496 (2017) 24–40. doi:10.1016/J.JNUCMAT.2017.08.045.
- [73] G.S. Was, *Fundamentals of Radiation Materials Science*, Springer New York, New York, NY, NY, 2017. doi:10.1007/978-1-4939-3438-6.
- [74] A.J. Ardell, P. Bellon, Radiation-induced solute segregation in metallic alloys, *Curr. Opin. Solid State Mater. Sci.* 20 (2016) 115–139. doi:10.1016/J.COSSMS.2015.11.001.
- [75] J.P. Wharry, G.S. Was, The mechanism of radiation-induced segregation in ferritic-martensitic alloys, *Acta Mater.* 65 (2014) 42–55. doi:10.1016/J.ACTAMAT.2013.09.049.
- [76] O. Senninger, F. Soisson, E. Martínez, M. Nastar, C.-C. Fu, Y. Bréchet, Modeling radiation induced segregation in iron-chromium alloys, *Acta Mater.* 103 (2016) 1–11. doi:10.1016/J.ACTAMAT.2015.09.058.
- [77] G.S. Was, J.P. Wharry, B. Frisbie, B.D. Wirth, D. Morgan, J.D. Tucker, T.R. Allen, Assessment of radiation-induced segregation mechanisms in austenitic and ferritic-martensitic alloys, *J. Nucl. Mater.* 411 (2011) 41–50. doi:10.1016/J.JNUCMAT.2011.01.031.
- [78] G.S. (Gary S. Was, *Fundamentals of radiation materials science : metals and alloys*, n.d.
- [79] D.. Edwards, E.. Simonen, F.. Garner, L.. Greenwood, B.. Oliver, S.. Bruemmer, Influence of irradiation temperature and dose gradients on the microstructural evolution in neutron-irradiated 316SS, *J. Nucl. Mater.* 317 (2003) 32–45. doi:10.1016/S0022-3115(03)00003-5.

- [80] W.J. Choyke, J.N. Mcgruer, J.R. Townsend, J.A. Spitznagel, N.J. Doyle, F.J. Venskytis, Helium effects in ion-bombarded 304 stainless steel, *J. Nucl. Mater.* 85-86 (1979) 647–651. doi:10.1016/0022-3115(79)90333-7.
- [81] R.E. Stoller, The influence of helium on microstructural evolution: Implications for DT fusion reactors, *J. Nucl. Mater.* 174 (1990) 289–310. doi:10.1016/0022-3115(90)90242-F.
- [82] P. Hosemann, D. Kiener, Y. Wang, S.A. Maloy, Issues to consider using nano indentation on shallow ion beam irradiated materials, *J. Nucl. Mater.* 425 (2012) 136–139. <https://www.sciencedirect.com/science/article/pii/S0022311511010269> (accessed March 27, 2018).
- [83] P. Hosemann, C. Shin, D. Kiener, Small scale mechanical testing of irradiated materials, *J. Mater. Res.* 30 (2015) 1231–1245. doi:10.1557/jmr.2015.26.
- [84] C. Shin, S. Lim, H. Jin, P. Hosemann, J. Kwon, Development and testing of microcompression for post irradiation characterization of ODS steels, *J. Nucl. Mater.* 444 (2014) 43–48. doi:10.1016/J.JNUCMAT.2013.09.025.
- [85] D. Kiener, A.M. Minor, O. Anderoglu, Y. Wang, S.A. Maloy, P. Hosemann, Application of small-scale testing for investigation of ion-beam-irradiated materials, *J. Mater. Res.* 27 (2012) 2724–2736. doi:10.1557/jmr.2012.303.
- [86] D.E.J. Armstrong, C.D. Hardie, J.S.K.L. Gibson, A.J. Bushby, P.D. Edmondson, S.G. Roberts, Small-scale characterisation of irradiated nuclear materials: Part II nanoindentation and micro-cantilever testing of ion irradiated nuclear materials, *J. Nucl. Mater.* 462 (2015) 374–381. doi:10.1016/j.jnucmat.2015.01.053.
- [87] R. Young, C. Rue, S. Randolph, C. Chandler, G. Franz, R. Schampers, A. Klumpp, L. Kwakman, A Comparison of Xenon Plasma FIB Technology with Conventional Gallium LMIS FIB: Imaging, Milling, and Gas-Assisted Applications, *Microsc. Microanal.* 17 (2011) 652–653. doi:10.1017/S1431927611004132.
- [88] H. Vo, A. Reichardt, C. Howard, M.D. Abad, D. Kaoumi, P. Chou, P. Hosemann, Small-Scale Mechanical Testing on Proton Beam-Irradiated 304 SS from Room Temperature to Reactor Operation Temperature, *JOM.* 67 (2015) 2959–2964. doi:10.1007/s11837-015-1596-0.

- [89] P. Hosemann, Small-scale mechanical testing on nuclear materials: bridging the experimental length-scale gap, *Scr. Mater.* 143 (2018) 161–168. doi:10.1016/j.scriptamat.2017.04.026.
- [90] C.A. Schuh, Nanoindentation studies of materials, *Mater. Today.* 9 (2006) 32–40. doi:10.1016/S1369-7021(06)71495-X.
- [91] X. Li, B. Bhushan, A review of nanoindentation continuous stiffness measurement technique and its applications, *Mater. Charact.* 48 (2002) 11–36. doi:10.1016/S1044-5803(02)00192-4.
- [92] D.A. Lucca, K. Herrmann, M.J. Klopstein, Nanoindentation: Measuring methods and applications, *CIRP Ann. - Manuf. Technol.* 59 (2010) 803–819. doi:10.1016/j.cirp.2010.05.009.
- [93] W. Oliver, G. Pharr, An improved technique for determining hardness and elastic modulus using load and displacement sensing indentation experiments, *J. Mater. Res.* (1992). http://journals.cambridge.org/abstract_S0884291400017039 (accessed October 26, 2016).
- [94] N.A. Sakharova, J.V. Fernandes, J.M. Antunes, M.C. Oliveira, Comparison between Berkovich, Vickers and conical indentation tests: A three-dimensional numerical simulation study, *Int. J. Solids Struct.* 46 (2009) 1095–1104. doi:10.1016/j.ijsolstr.2008.10.032.
- [95] L. Qian, M. Li, Z. Zhou, H. Yang, X. Shi, Comparison of nano-indentation hardness to microhardness, *Surf. Coatings Technol.* 195 (2005) 264–271. doi:10.1016/j.surfcoat.2004.07.108.
- [96] M. Saleh, Z. Zaidi, M. Ionescu, C. Hurt, K. Short, J. Daniels, P. Munroe, L. Edwards, D. Bhattacharyya, Relationship between damage and hardness profiles in ion irradiated SS316 using nanoindentation – Experiments and modelling, *Int. J. Plast.* 86 (2016) 151–169. doi:10.1016/J.IJPLAS.2016.08.006.
- [97] M. Gan, V. Tomar, Role of length scale and temperature in indentation induced creep behavior of polymer derived Si-C-O ceramics, *Mater. Sci. Eng. A.* 527 (2010) 7615–7623. doi:10.1016/j.msea.2010.08.016.
- [98] C. Pokor, Y. Brechet, P. Dubuisson, J.-P. Massoud, X. Averty, Irradiation damage in 304 and 316 stainless steels: experimental investigation and modeling. Part II: Irradiation induced hardening, *J. Nucl. Mater.* 326 (2004) 30–37. doi:10.1016/J.JNUCMAT.2003.12.008.

- [99] A. Prasitthipayong, S.J. Vachhani, S.J. Tumey, A.M. Minor, P. Hosemann, Indentation size effect in unirradiated and ion-irradiated 800H steel at high temperatures, *Acta Mater.* 144 (2018) 896–904. doi:10.1016/j.actamat.2017.11.001.
- [100] H. Somekawa, T. Tsuru, A. Singh, S. Miura, C.A. Schuh, Effect of crystal orientation on incipient plasticity during nanoindentation of magnesium, *Acta Mater.* 139 (2017) 21–29. doi:10.1016/j.actamat.2017.07.052.
- [101] H. Somekawa, C.A. Schuh, Effect of Crystal Orientation on Nanoindentation Behavior in Magnesium, *Metall. Mater. Trans. A.* 47 (2016) 3227–3234. doi:10.1007/s11661-016-3479-6.
- [102] T. Chen, L. Tan, Z. Lu, H. Xu, The effect of grain orientation on nanoindentation behavior of model austenitic alloy Fe-20Cr-25Ni, *Acta Mater.* 138 (2017) 83–91. doi:10.1016/j.actamat.2017.07.028.
- [103] P. Maier, A. Richter, R.G. Faulkner, R. Ries, Application of nanoindentation technique for structural characterisation of weld materials, *Mater. Charact.* 48 (2002) 329–339. doi:10.1016/S1044-5803(02)00274-7.
- [104] Z. Zong, J. Lou, O.O. Adewoye, A.A. Elmustafa, F. Hammad, W.O. Soboyejo, Indentation size effects in the nano- and micro-hardness of fcc single crystal metals, *Mater. Sci. Eng. A.* 434 (2006) 178–187. doi:10.1016/j.msea.2006.06.137.
- [105] W.D. Nix, H. Gao, Indentation size effects in crystalline materials: A law for strain gradient plasticity, *J. Mech. Phys. Solids.* 46 (1998) 411–425. doi:10.1016/S0022-5096(97)00086-0.
- [106] M.D. Uchic, Sample Dimensions Influence Strength and Crystal Plasticity, *Science* (80-.). 305 (2004) 986–989. doi:10.1126/science.1098993.
- [107] B. Winiarski, G.S. Schajer, P.J. Withers, Surface Decoration for Improving the Accuracy of Displacement Measurements by Digital Image Correlation in SEM, *Exp. Mech.* 52 (2012) 793–804. doi:10.1007/s11340-011-9568-y.
- [108] P.G. Sanders, J.A. Eastman, J.R. Weertman, Elastic and tensile behavior of nanocrystalline copper and palladium, *Acta Mater.* 45 (1997) 4019–4025. doi:10.1016/S1359-6454(97)00092-X.

- [109] B. Kondori, A. Needleman, A. Amine Benzerga, Discrete dislocation simulations of compression of tapered micropillars, *J. Mech. Phys. Solids*. 101 (2017) 223–234. doi:10.1016/j.jmps.2017.01.015.
- [110] G. Dehm, B.N. Jaya, R. Raghavan, C. Kirchlechner, Overview on micro- and nanomechanical testing: New insights in interface plasticity and fracture at small length scales, *Acta Mater.* 142 (2018) 248–282. doi:10.1016/j.actamat.2017.06.019.
- [111] H.T. Vo, A. Reichardt, D. Frazer, N. Bailey, P. Chou, P. Hosemann, In situ micro-tensile testing on proton beam-irradiated stainless steel, *J. Nucl. Mater.* 493 (2017) 336–342. doi:10.1016/J.JNUCMAT.2017.06.026.
- [112] D. Kiener, W. Grosinger, G. Dehm, R. Pippan, A further step towards an understanding of size-dependent crystal plasticity: In situ tension experiments of miniaturized single-crystal copper samples, *Acta Mater.* 56 (2008) 580–592. doi:10.1016/J.ACTAMAT.2007.10.015.
- [113] D.S. Gianola, C. Eberl, Micro- and nanoscale tensile testing of materials, *JOM*. 61 (2009) 24–35. doi:10.1007/s11837-009-0037-3.
- [114] H. Gleiter, E. Hornbogen, G. ro, Der mechanismus des korngrenzengleitens, *Acta Metall.* 16 (1968) 1053–1067. doi:10.1016/0001-6160(68)90094-1.
- [115] Z. Shen, R.H. Wagoner, W.A.T. Clark, Dislocation and grain boundary interactions in metals, *Acta Metall.* 36 (1988) 3231–3242. doi:10.1016/0001-6160(88)90058-2.
- [116] P.H. Pumphrey, H. Gleiter, The annealing of dislocations in high-angle grain boundaries, *Philos. Mag.* 30 (1974) 593–602. doi:10.1080/14786439808206584.
- [117] R. Maaß, P.M. Derlet, Micro-plasticity and recent insights from intermittent and small-scale plasticity, *Acta Mater.* 143 (2018) 338–363. doi:10.1016/J.ACTAMAT.2017.06.023.
- [118] N. Mara, D. Bhattacharyya, P. Dickerson, R. Hoagland, A. Misra, TEM Characterization of Deformation and Failure Mechanisms in 40 nm and 5nm Cu/Nb Nanolayered Micro Compression Pillars, *Microsc. Microanal.* 15 (2009) 352–353. doi:10.1017/S1431927609098596.
- [119] G. Dehm, B.J. Inkson, T. Wagner, Growth and microstructural stability of epitaxial Al films on (0001) α -Al₂O₃ substrates, *Acta Mater.* 50 (2002) 5021–5032. doi:10.1016/S1359-6454(02)00347-6.

- [120] J. Ding, Q. Li, J. Li, S. Xue, Z. Fan, H. Wang, X. Zhang, Mechanical behavior of structurally gradient nickel alloy, *Acta Mater.* 149 (2018) 57–67. doi:10.1016/j.actamat.2018.02.021.
- [121] U. Helmersson, S. Todorova, S.A. Barnett, J. -E. Sundgren, L.C. Markert, J.E. Greene, Growth of single-crystal TiN/VN strained-layer superlattices with extremely high mechanical hardness, *J. Appl. Phys.* 62 (1987) 481–484. doi:10.1063/1.339770.
- [122] N.A. Mara, D. Bhattacharyya, P. Dickerson, R.G. Hoagland, A. Misra, Deformability of ultrahigh strength 5nm Cu/Nb nanolayered composites, *Appl. Phys. Lett.* 92 (2008) 231901. doi:10.1063/1.2938921.
- [123] T. Nizolek, N.A. Mara, I.J. Beyerlein, J.T. Avallone, J.E. Scott, T.M. Pollock, Processing and Deformation Behavior of Bulk Cu–Nb Nanolaminates, *Metallogr. Microstruct. Anal.* 3 (2014) 470–476. doi:10.1007/s13632-014-0172-2.
- [124] J.Y. Zhang, S. Lei, Y. Liu, J.J. Niu, Y. Chen, G. Liu, X. Zhang, J. Sun, Length scale-dependent deformation behavior of nanolayered Cu/Zr micropillars, *Acta Mater.* 60 (2012) 1610–1622. doi:10.1016/J.ACTAMAT.2011.12.001.
- [125] A. Misra, X. Zhang, D. Hammon, R.G. Hoagland, Work hardening in rolled nanolayered metallic composites, *Acta Mater.* 53 (2005) 221–226. doi:10.1016/J.ACTAMAT.2004.09.018.
- [126] M. Yang, Y. Pan, F. Yuan, Y. Zhu, X. Wu, Back stress strengthening and strain hardening in gradient structure, *Mater. Res. Lett.* 4 (2016) 145–151. doi:10.1080/21663831.2016.1153004.
- [127] A. Reichardt, A. Lupinacci, D. Frazer, N. Bailey, H. Vo, C. Howard, Z. Jiao, A.M. Minor, P. Chou, P. Hosemann, Nanoindentation and in situ microcompression in different dose regimes of proton beam irradiated 304 SS, *J. Nucl. Mater.* 486 (2017) 323–331. doi:10.1016/j.jnucmat.2017.01.036.
- [128] P.J. Imrich, C. Kirchlechner, D. Kiener, G. Dehm, In Situ TEM Microcompression of Single and Bicrystalline Samples: Insights and Limitations, *JOM.* 67 (2015) 1704–1712. doi:10.1007/s11837-015-1440-6.
- [129] P.J. Imrich, C. Kirchlechner, C. Motz, G. Dehm, Differences in deformation behavior of bicrystalline Cu micropillars containing a twin boundary or a large-angle grain boundary, *Acta Mater.* 73 (2014) 240–250. doi:10.1016/J.ACTAMAT.2014.04.022.

- [130] Y. Liu, N. Li, M. Arul Kumar, S. Pathak, J. Wang, R.J. McCabe, N.A. Mara, C.N. Tomé, Experimentally quantifying critical stresses associated with basal slip and twinning in magnesium using micropillars, *Acta Mater.* 135 (2017) 411–421. doi:10.1016/J.ACTAMAT.2017.06.008.
- [131] Z. Zhang, T.-S. Jun, T.B. Britton, F.P.E. Dunne, Determination of Ti-6242 α and β slip properties using micro-pillar test and computational crystal plasticity, *J. Mech. Phys. Solids.* 95 (2016) 393–410. doi:10.1016/J.JMPS.2016.06.007.
- [132] G. Meric de Bellefon, J.C. van Duysen, Tailoring plasticity of austenitic stainless steels for nuclear applications: Review of mechanisms controlling plasticity of austenitic steels below 400 °C, *J. Nucl. Mater.* 475 (2016) 168–191. doi:10.1016/j.jnucmat.2016.04.015.
- [133] M.D. McMurtrey, G.S. Was, B. Cui, I. Robertson, L. Smith, D. Farkas, Strain localization at dislocation channel–grain boundary intersections in irradiated stainless steel, *Int. J. Plast.* 56 (2014) 219–231. doi:10.1016/J.IJPLAS.2014.01.001.
- [134] T.S. Byun, N. Hashimoto, K. Farrell, E.H. Lee, Characteristics of microscopic strain localization in irradiated 316 stainless steels and pure vanadium, *J. Nucl. Mater.* 349 (2006) 251–264. doi:10.1016/J.JNUCMAT.2005.10.011.
- [135] Z. Jiao, G.S. Was, The role of irradiated microstructure in the localized deformation of austenitic stainless steels, *J. Nucl. Mater.* 407 (2010) 34–43. doi:10.1016/j.jnucmat.2010.07.006.
- [136] M.D. McMurtrey, B. Cui, I. Robertson, D. Farkas, G.S. Was, Mechanism of dislocation channel-induced irradiation assisted stress corrosion crack initiation in austenitic stainless steel, *Curr. Opin. Solid State Mater. Sci.* 19 (2015) 305–314. doi:10.1016/J.COSSMS.2015.04.001.
- [137] E.H. Lee, T.S. Byun, J.D. Hunn, M.H. Yoo, K. Farrell, L.K. Mansur, On the origin of deformation microstructures in austenitic stainless steel: part I—microstructures, *Acta Mater.* 49 (2001) 3269–3276. doi:10.1016/S1359-6454(01)00193-8.
- [138] M.N. Gussev, K.G. Field, J.T. Busby, Strain-induced phase transformation at the surface of an AISI-304 stainless steel irradiated to 4.4 dpa and deformed to 0.8% strain, *J. Nucl. Mater.* 446 (2014) 187–192. doi:10.1016/J.JNUCMAT.2013.11.041.

- [139] K.S. Mao, C. Sun, Y. Huang, C.-H. Shiau, F.A. Garner, P.D. Freyer, J.P. Wharry, Grain orientation dependence of nanoindentation and deformation-induced martensitic phase transformation in neutron irradiated AISI 304L stainless steel, *Materialia*. 5 (2019) 100208. doi:10.1016/J.MTLA.2019.100208.
- [140] N. Hashimoto, T.S. Byun, Deformation-induced martensite formation and dislocation channeling in neutron-irradiated 316 stainless steel, *J. Nucl. Mater.* 367-370 (2007) 960–965. doi:10.1016/j.jnucmat.2007.03.204.
- [141] T. Byun, N. Hashimoto, K. Farrell, Temperature dependence of strain hardening and plastic instability behaviors in austenitic stainless steels, *Acta Mater.* 52 (2004) 3889–3899. doi:10.1016/j.actamat.2004.05.003.
- [142] D. Hull, D.J. Bacon, *Introduction to dislocations*, Butterworth-Heinemann, 2011.
- [143] M. Peach, J.S. Koehler, The Forces Exerted on Dislocations and the Stress Fields Produced by Them, *Phys. Rev.* 80 (1950) 436–439. doi:10.1103/PhysRev.80.436.
- [144] T.S. Byun, On the stress dependence of partial dislocation separation and deformation microstructure in austenitic stainless steels, *Acta Mater.* 51 (2003) 3063–3071. doi:10.1016/S1359-6454(03)00117-4.
- [145] W. Vorbrugg, H.C. Goetting, C. Schwink, Work-Hardening and Surface Investigations on Copper Single Crystals Oriented for Multiple Glide, *Phys. Status Solidi*. 46 (1971) 257–264. doi:10.1002/pssb.2220460123.
- [146] U. Kocks, Polyslip in single crystals, *Acta Metall.* 8 (1960) 345–352. doi:10.1016/0001-6160(60)90001-8.
- [147] P. Franciosi, A. Zaoui, Multislip in f.c.c. crystals a theoretical approach compared with experimental data, *Acta Metall.* 30 (1982) 1627–1637. doi:10.1016/0001-6160(82)90184-5.
- [148] T. Takeuchi, Work Hardening of Copper Single Crystals with Multiple Glide Orientations, *Trans. Japan Inst. Met.* 16 (1975) 629–640. doi:10.2320/matertrans1960.16.629.
- [149] R. Honeycombe, *The plastic deformation of metals*, (1968). <http://www.bcin.ca/bcin/detail.app?id=20924> (accessed May 5, 2019).

- [150] L. Kubin, *Dislocations, Mesoscale Simulations and Plastic Flow*, Oxford University Press, 2013. doi:10.1093/acprof:oso/9780198525011.001.0001.
- [151] B. Devincre, T. Hoc, L.P. Kubin, Collinear interactions of dislocations and slip systems, *Mater. Sci. Eng. A*. 400-401 (2005) 182–185. doi:10.1016/J.MSEA.2005.02.071.
- [152] I. Salehinia, D.F. Bahr, Crystal orientation effect on dislocation nucleation and multiplication in FCC single crystal under uniaxial loading, *Int. J. Plast.* 52 (2014) 133–146. doi:10.1016/J.IJPLAS.2013.04.010.
- [153] A.M. Hussein, S.I. Rao, M.D. Uchic, D.M. Dimiduk, J.A. El-Awady, Microstructurally based cross-slip mechanisms and their effects on dislocation microstructure evolution in fcc crystals, *Acta Mater.* 85 (2015) 180–190. doi:10.1016/J.ACTAMAT.2014.10.067.
- [154] C. Déprés, C.F. Robertson *, M.C. Fivel, Low-strain fatigue in AISI 316L steel surface grains: a three-dimensional discrete dislocation dynamics modelling of the early cycles I. Dislocation microstructures and mechanical behaviour, *Philos. Mag.* 84 (2004) 2257–2275. doi:10.1080/14786430410001690051.
- [155] Z.Q. Wang, I.J. Beyerlein, R. LeSar, Slip band formation and mobile dislocation density generation in high rate deformation of single fcc crystals, *Philos. Mag.* 88 (2008) 1321–1343. doi:10.1080/14786430802129833.
- [156] N. Hansen, X. Huang, G. Winther, Effect of Grain Boundaries and Grain Orientation on Structure and Properties, *Metall. Mater. Trans. A*. 42 (2011) 613–625. doi:10.1007/s11661-010-0292-5.
- [157] N. Hansen, X. Huang, W. Pantleon, G. Winther, Grain orientation and dislocation patterns, *Philos. Mag.* 86 (2006) 3981–3994. doi:10.1080/14786430600654446.
- [158] N. Hansen, X. Huang, Microstructure and flow stress of polycrystals and single crystals, *Acta Mater.* 46 (1998) 1827–1836. doi:10.1016/S1359-6454(97)00365-0.
- [159] R.P. Reed, R.E. Schramm, Relationship between stacking-fault energy and x-ray measurements of stacking-fault probability and microstrain, *J. Appl. Phys.* 45 (1974) 4705–4711. doi:10.1063/1.1663122.
- [160] R.E. Smallman, K.H. Westmacott, Stacking faults in face-centred cubic metals and alloys, *Philos. Mag.* 2 (1957) 669–683. doi:10.1080/14786435708242709.

- [161] M. Kang, W. Woo, Y.-K. Lee, B.-S. Seong, Neutron diffraction analysis of stacking fault energy in Fe–18Mn–2Al–0.6C twinning-induced plasticity steels, *Mater. Lett.* 76 (2012) 93–95. doi:10.1016/J.MATLET.2012.02.075.
- [162] L. Rémy, A. Pineau, B. Thomas, Temperature dependence of stacking fault energy in close-packed metals and alloys, *Mater. Sci. Eng.* 36 (1978) 47–63. doi:10.1016/0025-5416(78)90194-5.
- [163] J. Lu, L. Hultman, E. Holmström, K.H. Antonsson, M. Grehk, W. Li, L. Vitos, A. Golpayegani, Stacking fault energies in austenitic stainless steels, *Acta Mater.* 111 (2016) 39–46. doi:10.1016/j.actamat.2016.03.042.
- [164] S. Kibey, J.B. Liu, D.D. Johnson, H. Sehitoglu, Predicting twinning stress in fcc metals: Linking twin-energy pathways to twin nucleation, *Acta Mater.* 55 (2007) 6843–6851. doi:10.1016/J.ACTAMAT.2007.08.042.
- [165] S. Kibey, J.B. Liu, M.J. Curtis, D.D. Johnson, H. Sehitoglu, Effect of nitrogen on generalized stacking fault energy and stacking fault widths in high nitrogen steels, *Acta Mater.* 54 (2006) 2991–3001. doi:10.1016/J.ACTAMAT.2006.02.048.
- [166] V. Vitek, Intrinsic stacking faults in body-centred cubic crystals, *Philos. Mag.* 18 (1968) 773–786. doi:10.1080/14786436808227500.
- [167] B. De Cooman, K. Chin, J.K.-N. trends and developments in, undefined 2011, High Mn TWIP steels for automotive applications, Intechopen.com. (n.d.). <https://www.intechopen.com/download/pdf/13349> (accessed May 7, 2019).
- [168] B. Qin, H.K.D.H. Bhadeshia, Plastic strain due to twinning in austenitic TWIP steels, *Mater. Sci. Technol.* 24 (2008) 969–973. doi:10.1179/174328408X263688.
- [169] G.B. Olson, M. Cohen, A general mechanism of martensitic nucleation: Part III. Kinetics of martensitic nucleation, *Metall. Trans. A.* 7 (1976) 1915–1923. doi:10.1007/BF02659824.
- [170] T. Mori, H. Fujita, Dislocation reactions during deformation twinning in Cu-11at.% Al single crystals, *Acta Metall.* 28 (1980) 771–776. doi:10.1016/0001-6160(80)90154-6.

- [171] S. Miura, J. Takamura, ... N.N. the J., undefined 1968, Orientation dependence of flow stress for twinning in silver crystals, JAPAN INST Met. AOBA (n.d.). <https://scholar.google.com/scholar?hl=en&q=Orientation+dependence+of+the+flow+stress+for+twinning+in+silver+crystals> (accessed May 7, 2019).
- [172] M.A. Meyers, O. Vöhringer, V.A. Lubarda, The onset of twinning in metals: a constitutive description, *Acta Mater.* 49 (2001) 4025–4039. doi:10.1016/S1359-6454(01)00300-7.
- [173] I. Karaman, H. Sehitoglu, K. Gall, Y.. Chumlyakov, H.. Maier, Deformation of single crystal Hadfield steel by twinning and slip, *Acta Mater.* 48 (2000) 1345–1359. doi:10.1016/S1359-6454(99)00383-3.
- [174] H. Idrissi, K. Renard, L. Ryelandt, D. Schryvers, P.J. Jacques, On the mechanism of twin formation in Fe–Mn–C TWIP steels, *Acta Mater.* 58 (2010) 2464–2476. doi:10.1016/J.ACTAMAT.2009.12.032.
- [175] I. Gutierrez-Urrutia, S. Zaefferer, D. Raabe, The effect of grain size and grain orientation on deformation twinning in a Fe–22 wt.% Mn–0.6 wt.% C TWIP steel, *Mater. Sci. Eng. A.* 527 (2010) 3552–3560. doi:10.1016/J.MSEA.2010.02.041.
- [176] J.W. Christian, S. Mahajan, Deformation twinning, *Prog. Mater. Sci.* 39 (1995) 1–157. doi:10.1016/0079-6425(94)00007-7.
- [177] J. Talonen, H. Hänninen, Formation of shear bands and strain-induced martensite during plastic deformation of metastable austenitic stainless steels, *Acta Mater.* 55 (2007) 6108–6118. doi:10.1016/J.ACTAMAT.2007.07.015.
- [178] P. Yang, Q. Xie, L. Meng, H. Ding, Z. Tang, Dependence of deformation twinning on grain orientation in a high manganese steel, *Scr. Mater.* 55 (2006) 629–631. doi:10.1016/J.SCRIPTAMAT.2006.06.004.
- [179] X. FANG, P. YANG, F. LU, L. MENG, Dependence of Deformation Twinning on Grain Orientation and Texture Evolution of High Manganese TWIP Steels at Different Deformation Temperatures, *J. Iron Steel Res. Int.* 18 (2011) 46–52. doi:10.1016/S1006-706X(11)60116-7.
- [180] L. Bracke, L. Kestens, J. Penning, Direct observation of the twinning mechanism in an austenitic Fe–Mn–C steel, *Scr. Mater.* 61 (2009) 220–222. doi:10.1016/J.SCRIPTAMAT.2009.03.045.

- [181] L. Rémy, The interaction between slip and twinning systems and the influence of twinning on the mechanical behavior of fcc metals and alloys, *Metall. Trans. A.* 12 (1981) 387–408. doi:10.1007/BF02648536.
- [182] B.C. De Cooman, Y. Estrin, S.K. Kim, Twinning-induced plasticity (TWIP) steels, *Acta Mater.* 142 (2018) 283–362. doi:10.1016/J.ACTAMAT.2017.06.046.
- [183] J. Mohd Jani, M. Leary, A. Subic, M.A. Gibson, A review of shape memory alloy research, applications and opportunities, *Mater. Des.* 56 (2014) 1078–1113. doi:10.1016/J.MATDES.2013.11.084.
- [184] Z. Konôpková, R.S. McWilliams, N. Gómez-Pérez, A.F. Goncharov, Direct measurement of thermal conductivity in solid iron at planetary core conditions, *Nature.* 534 (2016) 99–101. doi:10.1038/nature18009.
- [185] P.-C. Wei, S. Bhattacharya, J. He, S. Neeleshwar, R. Podila, Y.Y. Chen, A.M. Rao, The intrinsic thermal conductivity of SnSe, *Nature.* 539 (2016) E1–E2. doi:10.1038/nature19832.
- [186] C. Niu, C.R. LaRosa, J. Miao, M.J. Mills, M. Ghazisaeidi, Magnetically-driven phase transformation strengthening in high entropy alloys, *Nat. Commun.* 9 (2018) 1363. doi:10.1038/s41467-018-03846-0.
- [187] Z. Li, K.G. Pradeep, Y. Deng, D. Raabe, C.C. Tasan, Metastable high-entropy dual-phase alloys overcome the strength–ductility trade-off, *Nature.* 534 (2016) 227–230. doi:10.1038/nature17981.
- [188] X. Moya, S. Kar-Narayan, N.D. Mathur, Caloric materials near ferroic phase transitions, *Nat. Mater.* 13 (2014) 439–450. doi:10.1038/nmat3951.
- [189] A. Jain, R.D. Vale, RNA phase transitions in repeat expansion disorders, *Nature.* 546 (2017) 243–247. doi:10.1038/nature22386.
- [190] F. Nestola, N. Korolev, M. Kopylova, N. Rotiroti, D.G. Pearson, M.G. Pamato, M. Alvaro, L. Peruzzo, J.J. Gurney, A.E. Moore, J. Davidson, CaSiO₃ perovskite in diamond indicates the recycling of oceanic crust into the lower mantle, *Nature.* 555 (2018) 237–241. doi:10.1038/nature25972.

- [191] Y.F. Shen, X.X. Li, X. Sun, Y.D. Wang, L. Zuo, Twinning and martensite in a 304 austenitic stainless steel, *Mater. Sci. Eng. A.* 552 (2012) 514–522. doi:10.1016/J.MSEA.2012.05.080.
- [192] C.X. Huang, G. Yang, Y.L. Gao, S.D. Wu, S.X. Li, Investigation on the nucleation mechanism of deformation-induced martensite in an austenitic stainless steel under severe plastic deformation, *J. Mater. Res.* 22 (2007) 724–729. doi:10.1557/jmr.2007.0094.
- [193] A.. Bogers, W.. Burgers, Partial dislocations on the {110} planes in the B.C.C. lattice and the transition of the F.C.C. into the B.C.C. lattice, *Acta Metall.* 12 (1964) 255–261. doi:10.1016/0001-6160(64)90194-4.
- [194] G.B. Olson, M. Cohen, A mechanism for the strain-induced nucleation of martensitic transformations, *J. Less Common Met.* 28 (1972) 107–118. doi:10.1016/0022-5088(72)90173-7.
- [195] X.-S. Yang, S. Sun, X.-L. Wu, E. Ma, T.-Y. Zhang, Dissecting the Mechanism of Martensitic Transformation via Atomic-Scale Observations, *Sci. Rep.* 4 (2015) 6141. doi:10.1038/srep06141.
- [196] X.-S. Yang, S. Sun, T.-Y. Zhang, The mechanism of bcc α' nucleation in single hcp ϵ laths in the fcc $\gamma \rightarrow$ hcp $\epsilon \rightarrow$ bcc α' martensitic phase transformation, *Acta Mater.* 95 (2015) 264–273. doi:10.1016/J.ACTAMAT.2015.05.034.
- [197] X.-S. Yang, S. Sun, H.-H. Ruan, S.-Q. Shi, T.-Y. Zhang, Shear and shuffling accomplishing polymorphic fcc $\gamma \rightarrow$ hcp $\epsilon \rightarrow$ bct α martensitic phase transformation, *Acta Mater.* 136 (2017) 347–354. doi:10.1016/J.ACTAMAT.2017.07.016.
- [198] V. Seetharaman, R. Krishnan, Influence of the martensitic transformation on the deformation behaviour of an AISI 316 stainless steel at low temperatures, *J. Mater. Sci.* 16 (1981) 523–530. doi:10.1007/BF00738646.
- [199] P.L. Mangonon, G. Thomas, The martensite phases in 304 stainless steel, *Metall. Trans.* 1 (1970) 1577–1586. doi:10.1007/BF02642003.
- [200] B. Petit, N. Gey, M. Cherkaoui, B. Bolle, M. Humbert, Deformation behavior and microstructure/texture evolution of an annealed 304 AISI stainless steel sheet. Experimental and micromechanical modeling, *Int. J. Plast.* 23 (2007) 323–341. doi:10.1016/J.IJPLAS.2006.07.002.

- [201] D.T. Pierce, J.A. Jiménez, J. Bentley, D. Raabe, J.E. Wittig, The influence of stacking fault energy on the microstructural and strain-hardening evolution of Fe–Mn–Al–Si steels during tensile deformation, *Acta Mater.* 100 (2015) 178–190. doi:10.1016/J.ACTAMAT.2015.08.030.
- [202] G.B. Olson, M. Cohen, A general mechanism of martensitic nucleation: Part I. General concepts and the FCC \rightarrow HCP transformation, *Metall. Trans. A.* 7 (1976) 1897–1904. doi:10.1007/BF02659822.
- [203] Y. Tian, O.I. Gorbatov, A. Borgenstam, A. V. Ruban, P. Hedström, Deformation Microstructure and Deformation-Induced Martensite in Austenitic Fe-Cr-Ni Alloys Depending on Stacking Fault Energy, *Metall. Mater. Trans. A.* 48 (2017) 1–7. doi:10.1007/s11661-016-3839-2.
- [204] H. Fujita, S. Ueda, Stacking faults and f.c.c. (γ) \rightarrow h.c.p. (ϵ) transformation in 188-type stainless steel, *Acta Metall.* 20 (1972) 759–767. doi:10.1016/0001-6160(72)90104-6.
- [205] L.E. Murr, K.P. Staudhammer, S.S. Hecker, Effects of Strain State and Strain Rate on Deformation-Induced Transformation in 304 Stainless Steel: Part II. Microstructural Study, *Metall. Trans. A.* 13 (1982) 627–635. doi:10.1007/BF02644428.
- [206] M.G. Stout, P.S. Follansbee, Strain Rate Sensitivity, Strain Hardening, and Yield Behavior of 304L Stainless Steel, *J. Eng. Mater. Technol.* 108 (1986) 344. doi:10.1115/1.3225893.
- [207] J.A. Lichtenfeld, C.J. Van Tyne, M.C. Mataya, Effect of strain rate on stress-strain behavior of alloy 309 and 304L austenitic stainless steel, *Metall. Mater. Trans. A.* 37 (2006) 147–161. doi:10.1007/s11661-006-0160-5.
- [208] S.S. Hecker, M.G. Stout, K.P. Staudhammer, J.L. Smith, Effects of Strain State and Strain Rate on Deformation-Induced Transformation in 304 Stainless Steel: Part I. Magnetic Measurements and Mechanical Behavior, *Metall. Trans. A.* 13 (1982) 619–626. doi:10.1007/BF02644427.
- [209] P.J. Ferreira, J.B. Vander Sande, M.A. Fortes, A. Kyrolainen, Microstructure development during high-velocity deformation, *Metall. Mater. Trans. A.* 35 (2004) 3091–3101. doi:10.1007/s11661-004-0054-3.
- [210] H. Chen, S. Zhu, B. Zeng, Design of non-separable transforms for directional 2-D sources, in: 2011 18th IEEE Int. Conf. Image Process., IEEE, 2011: pp. 3697–3700. doi:10.1109/ICIP.2011.6116522.

- [211] L. Tan, R.E. Stoller, K.G. Field, Y. Yang, H. Nam, D. Morgan, B.D. Wirth, M.N. Gussev, J.T. Busby, Microstructural Evolution of Type 304 and 316 Stainless Steels Under Neutron Irradiation at LWR Relevant Conditions, *JOM*. 68 (2016) 517–529. doi:10.1007/s11837-015-1753-5.
- [212] L. Tan, J.T. Busby, Formulating the strength factor α for improved predictability of radiation hardening, *J. Nucl. Mater.* 465 (2015) 724–730. doi:10.1016/J.JNUCMAT.2015.07.009.
- [213] E.. Lee, M.. Yoo, T.. Byun, J.. Hunn, K. Farrell, L.. Mansur, On the origin of deformation microstructures in austenitic stainless steel: Part II—Mechanisms, *Acta Mater.* 49 (2001) 3277–3287. doi:10.1016/S1359-6454(01)00194-X.
- [214] D. Rodney, Atomic-scale modeling of clear band formation in FCC metals, *Nucl. Instruments Methods Phys. Res. Sect. B Beam Interact. with Mater. Atoms.* 228 (2005) 100–110. doi:10.1016/J.NIMB.2004.10.029.
- [215] Y.. Osetsky, R.. Stoller, Y. Matsukawa, Dislocation–stacking fault tetrahedron interaction: what can we learn from atomic-scale modelling, *J. Nucl. Mater.* 329–333 (2004) 1228–1232. doi:10.1016/J.JNUCMAT.2004.04.257.
- [216] Y.N. Osetsky, D. Rodney, D.J. Bacon, Atomic-scale study of dislocation–stacking fault tetrahedron interactions. Part I: mechanisms, *Philos. Mag.* 86 (2006) 2295–2313. doi:10.1080/14786430500513783.
- [217] T. Okita, K. Asari, S. Fujita, & M. Itakura, Effect of the Stacking Fault Energy on Interactions between an Edge Dislocation and a Spherical Void in FCC Metals at Various Spatial Geometries, *Fusion Sci. Technol.* 66 (2014) 289–294. doi:10.13182/FST13-756.
- [218] K. Asari, O.S. Hetland, S. Fujita, M. Itakura, T. Okita, The effect of stacking fault energy on interactions between an edge dislocation and a spherical void by molecular dynamics simulations, *J. Nucl. Mater.* 442 (2013) 360–364. doi:10.1016/J.JNUCMAT.2013.05.076.
- [219] X. Li, A. Almazouzi, Deformation and microstructure of neutron irradiated stainless steels with different stacking fault energy, *J. Nucl. Mater.* 385 (2009) 329–333. doi:10.1016/J.JNUCMAT.2008.12.008.
- [220] W.J. Weber, D.M. Duffy, L. Thomé, Y. Zhang, The role of electronic energy loss in ion beam modification of materials, *Curr. Opin. Solid State Mater. Sci.* 19 (2015) 1–11. doi:10.1016/j.cossms.2014.09.003.

- [221] T.S. Byun, N. Hashimoto, K. Farrell, Deformation mode map of irradiated 316 stainless steel in true stress–dose space, *J. Nucl. Mater.* 351 (2006) 303–315. doi:10.1016/J.JNUCMAT.2006.02.033.
- [222] P.J. Brofman, G.S. Ansell, On the Effect of Carbon on the Stacking Fault Energy of Austenitic Stainless Steels, *Metall. Trans. A.* 9 (1978) 879–880. doi:10.1007/BF02649799.
- [223] G. Meric de Bellefon, J.C. van Duysen, K. Sridharan, Composition-dependence of stacking fault energy in austenitic stainless steels through linear regression with random intercepts, *J. Nucl. Mater.* 492 (2017) 227–230. doi:10.1016/j.jnucmat.2017.05.037.
- [224] M. Ojima, Y. Adachi, Y. Tomota, Y. Katada, Y. Kaneko, K. Kuroda, H. Saka, Weak Beam TEM Study on Stacking Fault Energy of High Nitrogen Steels, *Steel Res. Int.* 80 (2009) 477–481. doi:10.2374/SRI09SP038.
- [225] F.B. Pickering, *Physical metallurgy and the design of steels*, Applied Science Publishers, 1978. <https://catalogue.nla.gov.au/Record/1029479> (accessed May 6, 2019).
- [226] D. Qi-Xun, W.A.-D.C. Xiao-Nong, L. Xin-Min, Stacking fault energy of cryogenic austenitic steels, *Chinese Phys.* 11 (2002) 315. doi:10.1088/1009-1963/11/6/315.
- [227] C.G. Rhodes, A.W. Thompson, The composition dependence of stacking fault energy in austenitic stainless steels, *Metall. Trans. A.* 8 (1977) 1901–1906. doi:10.1007/BF02646563.
- [228] A. Saeed-Akbari, J. Imlau, U. Prah, W. Bleck, Derivation and Variation in Composition-Dependent Stacking Fault Energy Maps Based on Subregular Solution Model in High-Manganese Steels, *Metall. Mater. Trans. A.* 40 (2009) 3076–3090. doi:10.1007/s11661-009-0050-8.
- [229] R.E. Schramm, R.P. Reed, Stacking fault energies of seven commercial austenitic stainless steels, *Metall. Trans. A.* 6 (1975) 1345–1351. doi:10.1007/BF02641927.
- [230] T. Yonezawa, K. Suzuki, S. Ooki, A. Hashimoto, The Effect of Chemical Composition and Heat Treatment Conditions on Stacking Fault Energy for Fe-Cr-Ni Austenitic Stainless Steel, *Metall. Mater. Trans. A.* 44 (2013) 5884–5896. doi:10.1007/s11661-013-1943-0.

- [231] T. Toyama, Y. Nozawa, W. Van Renterghem, Y. Matsukawa, M. Hatakeyama, Y. Nagai, A. Al Mazouzi, S. Van Dyck, Grain boundary segregation in neutron-irradiated 304 stainless steel studied by atom probe tomography, *J. Nucl. Mater.* 425 (2012) 71–75. doi:10.1016/j.jnucmat.2011.11.072.
- [232] T.. Byun, E.. Lee, J.. Hunn, Plastic deformation in 316LN stainless steel – characterization of deformation microstructures, *J. Nucl. Mater.* 321 (2003) 29–39. doi:10.1016/S0022-3115(03)00195-8.
- [233] H. Föll, Twinning, Shear Deformation and Martensite Formation, *Iron, Steel and Swords*. (n.d.). https://www.tf.uni-kiel.de/matwis/amat/iss/kap_5/illustr/s5_4_3.html (accessed April 3, 2019).
- [234] V.I. Pastukhov, S. Verin, V.L. Panchenko, I. Portnykh, P.D. Freyer, L.A. Giannuzzi, F. Garner, Application of backscatter electrons for large area imaging of cavities produced by neutron irradiation, *J. Nucl. Mater.* (2016). doi:10.1016/j.jnucmat.2016.07.059.
- [235] J.M.K. Wiezorek, Y. Huang, F.A. Garner, P.D. Freyer, M. Sagisaka, Y. Isobe, T. Okita, Transmission Electron Microscopy of 304-type Stainless Steel after Exposure to Neutron Flux and Irradiation Temperature Gradients, *Microsc. Microanal.* 20 (n.d.). doi:10.1017/S1431927614010848.
- [236] J. Etoh, M. Sagisaka, T. Matsunaga, Y. Isobe, T. Okita, A simulation model of ultrasonic wave changes due to irradiation-induced microstructural evolution of thick 304 stainless steel blocks, in: *J. Nucl. Mater.*, 2013. doi:10.1016/j.jnucmat.2013.07.007.
- [237] T. Okita, J. Etoh, M. Sagisaka, T. Matsunaga, Y. Isobe, P.D. Freyer, Y. Huang, J.M.K. Wiezorek, F.A. Garner, Validation of ultrasonic velocity measurements for detecting void swelling in first-wall structural materials, *Fusion Sci. Technol.* (2014). doi:10.13182/FST13-755.
- [238] F.A. Garner, T. Okita, Y. Isobe, J. Etoh, M. Sagisaka, T. Matsunaga, P.D. Freyer, Y. Huang, J.M.K. Wiezorek, D.L. Porter, Measurement of void swelling in thick non-uniformly irradiated 304 stainless steel blocks using nondestructive ultrasonic techniques, (n.d.).
- [239] F.A. Garner, Assessment of the swelling equation used for predict swelling of AISI 304 stainless steel in LWR and LMR environments, (n.d.).

- [240] F. Garner, P.D. Freyer, D.L. Porter, J. Wiest, C. Knight, B.H. Sencer, T. Okita, Y. Huang, J. Wiezorek, Void swelling and resultant strains in thick 304 stainless steel components in response to spatial gradients in neutron flux-spectra and irradiation temperature, (n.d.).
- [241] Y. Isobe, J. Etoh, M. Sagisaka, T. Matsunaga, P. Freyer, F. Garner, T. Okita, NDE | Inspection techniques Using UT to assess neutron-induced damage, (2014).
- [242] J. Etoh, M. Sagisaka, T. Matsunaga, Y. Isobe, F.A. Garner, P.D. Freyer, Y. Huang, J.M.K. Wiezorek, T. Okita, Development of a nondestructive inspection method for irradiation-induced microstructural evolution of thick 304 stainless steel blocks, in: *J. Nucl. Mater.*, 2013. doi:10.1016/j.jnucmat.2013.02.036.
- [243] F.A. Garner, T. Okita, Y. Isobe, J. Etoh, M. Sagisaka, T. Matsunaga, P.D. Freyer, Y. Huang, J.M. K. Wiezorek, D.L. Porter, Measurement of void swelling in thick non-uniformly irradiated 304 stainless steel blocks using nondestructive ultrasonic techniques Fontevraud 8 -Contribution of Materials Investigations and Operating Experience to LWRs' Safety, Performance and Reliability, (2015). <https://inldigitallibrary.inl.gov/sites/sti/sti/6303751.pdf> (accessed March 27, 2018).
- [244] E.M. Rabenberg, B.J. Jaques, B.H. Sencer, F.A. Garner, P.D. Freyer, T. Okita, D.P. Butt, Mechanical behavior of AISI 304SS determined by miniature test methods after neutron irradiation to 28 dpa, *J. Nucl. Mater.* 448 (2014) 315–324. doi:10.1016/J.JNUCMAT.2014.02.018.
- [245] J. Etoh, M. Sagisaka, T. Matsunaga, Y. Isobe, T. Okita, A simulation model of ultrasonic wave changes due to irradiation-induced microstructural evolution of thick 304 stainless steel blocks, *J. Nucl. Mater.* 441 (2013) 503–509. doi:10.1016/j.jnucmat.2013.07.007.
- [246] T. Okita, J. Etoh, M. Sagisaka, T. Matsunaga, Y. Isobe, P.D. Freyer, Y. Huang, J.M.K. Wiezorek, F.A. Garner, Validation of Ultrasonic Velocity Measurements for Detecting Void Swelling in First-Wall Structural Materials, *Fusion Sci. Technol.* 66 (2014) 77–82. doi:10.13182/FST13-755.
- [247] J. Etoh, M. Sagisaka, T. Matsunaga, Y. Isobe, F.A. Garner, P.D. Freyer, Y. Huang, J.M.K. Wiezorek, T. Okita, Development of a nondestructive inspection method for irradiation-induced microstructural evolution of thick 304 stainless steel blocks, *J. Nucl. Mater.* 440 (2013) 500–507. doi:10.1016/j.jnucmat.2013.02.036.

- [248] F.A. Stevie, C.B. Vartuli, L.A. Giannuzzi, T.L. Shofner, S.R. Brown, B. Rossie, F. Hillion, R.H. Mills, M. Antonell, R.B. Irwin, B.M. Purcell, Application of focused ion beam lift-out specimen preparation to TEM, SEM, STEM, AES and SIMS analysis, *Surf. Interface Anal.* 31 (2001) 345–351. doi:10.1002/sia.1063.
- [249] T. Chen, L. Tan, Z. Lu, H. Xu, The effect of grain orientation on nanoindentation behavior of model austenitic alloy Fe-20Cr-25Ni, *Acta Mater.* 138 (2017) 83–91. doi:10.1016/J.ACTAMAT.2017.07.028.
- [250] T.-H. Ahn, C.-S. Oh, D.H. Kim, K.H. Oh, H. Bei, E.P. George, H.N. Han, Investigation of strain-induced martensitic transformation in metastable austenite using nanoindentation, *Scr. Mater.* 63 (2010) 540–543. doi:10.1016/J.SCRIPTAMAT.2010.05.024.
- [251] B.B. He, M.X. Huang, Z.Y. Liang, A.H.W. Ngan, H.W. Luo, J. Shi, W.Q. Cao, H. Dong, Nanoindentation investigation on the mechanical stability of individual austenite grains in a medium-Mn transformation-induced plasticity steel, *Scr. Mater.* 69 (2013) 215–218. doi:10.1016/J.SCRIPTAMAT.2013.03.030.
- [252] T. Tsuru, Y. Shibutani, Anisotropic effects in elastic and incipient plastic deformation under (001), (110), and (111) nanoindentation of Al and Cu, *Phys. Rev. B.* 75 (2007) 035415. doi:10.1103/PhysRevB.75.035415.
- [253] R. Seymour, A. Hemeryck, K. Nomura, W. Wang, R.K. Kalia, A. Nakano, P. Vashishta, Nanoindentation of NiAl and Ni 3 Al crystals on (100), (110), and (111) surfaces: A molecular dynamics study, *Appl. Phys. Lett.* 104 (2014) 141904. doi:10.1063/1.4867168.
- [254] A. Gouldstone, H.-J. Koh, K.-Y. Zeng, A.E. Giannakopoulos, S. Suresh, Discrete and continuous deformation during nanoindentation of thin films, *Acta Mater.* 48 (2000) 2277–2295. doi:10.1016/S1359-6454(00)00009-4.
- [255] J.J. Vlassak, W.D. Nix, Indentation modulus of elastically anisotropic half spaces, *Philos. Mag. A.* 67 (1993) 1045–1056. doi:10.1080/01418619308224756.
- [256] G. Nolze, Characterization of the fcc/bcc orientation relationship by EBSD using pole figures and variants, *Zeitschrift Für Met.* 95 (2004) 744–755. doi:10.3139/146.018017.
- [257] A. Oila, S.J. Bull, Atomistic simulation of Fe–C austenite, *Comput. Mater. Sci.* 45 (2009) 235–239. doi:10.1016/j.commatsci.2008.09.013.

- [258] R. Hill, *The mathematical theory of plasticity*, Clarendon Press, 1998.
- [259] C.K. Dolph, D.J. da Silva, M.J. Swenson, J.P. Wharry, Plastic zone size for nanoindentation of irradiated Fe-9%Cr ODS, *J. Nucl. Mater.* 481 (2016) 33–45. doi:10.1016/J.JNUCMAT.2016.08.033.
- [260] D. Kiener, C. Motz, T. Schöberl, M. Jenko, G. Dehm, Determination of Mechanical Properties of Copper at the Micron Scale, *Adv. Eng. Mater.* 8 (2006) 1119–1125. doi:10.1002/adem.200600129.
- [261] X.-S. Yang, S. Sun, X.-L. Wu, E. Ma, T.-Y. Zhang, Dissecting the Mechanism of Martensitic Transformation via Atomic-Scale Observations, *Sci. Rep.* 4 (2015) 6141. doi:10.1038/srep06141.
- [262] R.G. Stringfellow, D.M. Parks, G.B. Olson, A constitutive model for transformation plasticity accompanying strain-induced martensitic transformations in metastable austenitic steels, *Acta Metall. Mater.* 40 (1992) 1703–1716. doi:10.1016/0956-7151(92)90114-T.
- [263] H.N. Han, C.G. Lee, C.-S. Oh, T.-H. Lee, S.-J. Kim, A model for deformation behavior and mechanically induced martensitic transformation of metastable austenitic steel, *Acta Mater.* 52 (2004) 5203–5214. doi:10.1016/j.actamat.2004.07.031.
- [264] E.C. Bain, The nature of martensite, *Trans. Metall. Soc. AIME.* 70 (1924) 25–47.
- [265] K. Koumatos, A. Muehleemann, Optimality of general lattice transformations with applications to the Bain strain in steel, *Proc. R. Soc. A Math. Phys. Eng. Sci.* 472 (2016) 20150865. doi:10.1098/rspa.2015.0865.
- [266] A. Muehleemann, K. Koumatos, A Theoretical Investigation of Orientation Relationships and Transformation Strains in Steels, (2016). doi:10.1107/S2053273316020350.
- [267] W. Pitsch, The martensite transformation in thin foils of iron-nitrogen alloys, *Philos. Mag.* 4 (1959) 577–584. doi:10.1080/14786435908238253.
- [268] G. Kurdjumow, G. Sachs, Über den Mechanismus der Stahlhärtung, *Zeitschrift Für Phys.* 64 (1930) 325–343. doi:10.1007/BF01397346.

- [269] S. Alkan, A. Ojha, H. Sehitoglu, Determination of latent hardening response for FeNiCoCrMn for twin-twin interactions, *Acta Mater.* 147 (2018) 149–164. doi:10.1016/J.ACTAMAT.2017.12.058.
- [270] T.-H. Lee, H.-Y. Ha, J.-Y. Kang, J. Moon, C.-H. Lee, S.-J. Park, An intersecting-shear model for strain-induced martensitic transformation, *Acta Mater.* 61 (2013) 7399–7410. doi:10.1016/j.actamat.2013.08.046.
- [271] K. Mao, In-situ compression videos on laser welds of irradiated 304L SS, (2019). doi:10.4231/G2WP-M551.
- [272] G. Wassermann, Ueber den Mechanismus der $[\alpha]$ - $[\gamma]$ -Umwandlung des Eisens, Verlag Stahleisen. 17 (1935).
- [273] Z. Nishiyama, *Sci. Rep., Tohoku Imp. Univ. Tokyo.* 23 (1934).
- [274] A.B. Greninger and A.R. Troiano., The mechanism of martensite formation, *Trans. Metall. Soc. AIME.* 185 (1949) 590–598.
- [275] T.L. Li, Y.F. Gao, H. Bei, E.P. George, Indentation Schmid factor and orientation dependence of nanoindentation pop-in behavior of NiAl single crystals, *J. Mech. Phys. Solids.* 59 (2011) 1147–1162. doi:10.1016/J.JMPS.2011.04.003.
- [276] J. Lu, L. Hultman, E. Holmström, K.H. Antonsson, M. Grehk, W. Li, L. Vitos, A. Golpayegani, Stacking fault energies in austenitic stainless steels, *Acta Mater.* 111 (2016) 39–46. doi:10.1016/j.actamat.2016.03.042.
- [277] G.S. WAS, *Fundamentals of Radiation Materials Science*, Springer New York, NY, 2017. doi:10.1007/978-1-4939-3438-6.
- [278] A. Seeger, J. Diehl, S. Mader, H. Rebstock, Work-hardening and work-softening of face-centred cubic metal crystals, *Philos. Mag.* 2 (1957) 323–350. doi:10.1080/14786435708243823.
- [279] C. Sun, K.Y. Yu, J.H. Lee, Y. Liu, H. Wang, L. Shao, S.A. Maloy, K.T. Hartwig, X. Zhang, Enhanced radiation tolerance of ultrafine grained Fe–Cr–Ni alloy, *J. Nucl. Mater.* 420 (2012) 235–240. doi:10.1016/J.JNUCMAT.2011.10.001.

- [280] C. Pokor, Y. Brechet, P. Dubuisson, J.-P. Massoud, X. Averty, Irradiation damage in 304 and 316 stainless steels: experimental investigation and modeling. Part II: Irradiation induced hardening, *J. Nucl. Mater.* 326 (2004) 30–37. doi:10.1016/j.jnucmat.2003.12.008.
- [281] G. Monnet, Multiscale modeling of irradiation hardening: Application to important nuclear materials, *J. Nucl. Mater.* (2018). doi:10.1016/j.jnucmat.2018.06.020.
- [282] M.J. Swenson, C.K. Dolph, J.P. Wharry, The effects of oxide evolution on mechanical properties in proton- and neutron-irradiated Fe-9%Cr ODS steel, *J. Nucl. Mater.* 479 (2016) 426–435. doi:10.1016/J.JNUCMAT.2016.07.022.
- [283] G.E. Lucas, The evolution of mechanical property change in irradiated austenitic stainless steels, *J. Nucl. Mater.* 206 (1993) 287–305. doi:10.1016/0022-3115(93)90129-M.
- [284] E.J. Pavlina, C.J. Van Tyne, Correlation of Yield Strength and Tensile Strength with Hardness for Steels, *J. Mater. Eng. Perform.* 17 (2008) 888–893. doi:10.1007/s11665-008-9225-5.
- [285] J.T. Busby, M.C. Hash, G.S. Was, The relationship between hardness and yield stress in irradiated austenitic and ferritic steels, *J. Nucl. Mater.* 336 (2005) 267–278. doi:10.1016/J.JNUCMAT.2004.09.024.
- [286] J. Gao, H. Huang, X. Liu, C. Wang, J.F. Stubbins, Y. Li, A special coarsening mechanism for intergranular helium bubbles upon heating: A combined experimental and numerical study, *Scr. Mater.* 147 (2018) 93–97. doi:10.1016/J.SCRIPTAMAT.2018.01.006.
- [287] T.E. Volin, R.W. Balluffi, Annealing kinetics of voids and the Self-diffusion coefficient in aluminum, *Phys. Status Solidi.* 25 (1968) 163–173. doi:10.1002/pssb.19680250116.
- [288] Z. Jiao, J. Hesterberg, G.S. Was, Effect of post-irradiation annealing on the irradiated microstructure of neutron-irradiated 304L stainless steel, *J. Nucl. Mater.* 500 (2018) 220–234. doi:10.1016/J.JNUCMAT.2017.12.030.
- [289] X. Cao, W. Wallace, J.-P. Immarigeon, C. Poon, Research and Progress in Laser Welding of Wrought Aluminum Alloys. II. Metallurgical Microstructures, Defects, and Mechanical Properties, *Mater. Manuf. Process.* 18 (2003) 23–49. doi:10.1081/AMP-120017587.
- [290] G.B. Olson, M. Cohen, Kinetics of strain-induced martensitic nucleation, *Metall. Trans. A.* 6 (1975) 791–795. doi:10.1007/BF02672301.

- [291] W.-Z. Han, J. Zhang, M.-S. Ding, L. Lv, W.-H. Wang, G.-H. Wu, Z.-W. Shan, J. Li, Helium Nanobubbles Enhance Superelasticity and Retard Shear Localization in Small-Volume Shape Memory Alloy, *Nano Lett.* 17 (2017) 3725–3730. doi:10.1021/acs.nanolett.7b01015.
- [292] K. Doihara, T. Okita, M. Itakura, M. Aichi, K. Suzuki, Atomic simulations to evaluate effects of stacking fault energy on interactions between edge dislocation and spherical void in face-centred cubic metals, *Philos. Mag.* 98 (2018) 2061–2076. doi:10.1080/14786435.2018.1472401.
- [293] V.A. Levin, V.I. Levitas, K.M. Zingerman, E.I. Freiman, Phase-field simulation of stress-induced martensitic phase transformations at large strains, *Int. J. Solids Struct.* 50 (2013) 2914–2928. doi:10.1016/J.IJSOLSTR.2013.05.003.
- [294] J. Christian, J.W. Christian, TWINNING AND MARTENSITIC TRANSFORMATION, *J. Phys. Collo-Ques.* 35 (1974). doi:10.1051/jphyscol:1974705.
- [295] N. Naeita, J. Takamura, Deformation twinning in silver-and copper-alloy crystals, *Philos. Mag.* 29 (1974) 1001–1028. doi:10.1080/14786437408226586.
- [296] A.A.S. Mohammed, E.A. El-Danaf, A.-K.A. Radwan, Equivalent twinning criteria for FCC alloys under uniaxial tension at high temperatures, *Mater. Sci. Eng. A.* 457 (2007) 373–379. doi:10.1016/J.MSEA.2006.12.113.
- [297] E. El-Danaf, S.R. Kalidindi, R.D. Doherty, Influence of grain size and stacking-fault energy on deformation twinning in fcc metals, *Metall. Mater. Trans. A.* 30 (1999) 1223–1233. doi:10.1007/s11661-999-0272-9.
- [298] S. Kibey, J.B. Liu, D.D. Johnson, H. Sehitoglu, Predicting twinning stress in fcc metals: Linking twin-energy pathways to twin nucleation, *Acta Mater.* 55 (2007) 6843–6851. doi:10.1016/j.actamat.2007.08.042.
- [299] M.S. Szczerba, T. Bajor, T. Tokarski, Is there a critical resolved shear stress for twinning in face-centred cubic crystals?, *Philos. Mag.* 84 (2004) 481–502. doi:10.1080/14786430310001612175.
- [300] S.A. Kibey, L.L. Wang, J.B. Liu, H.T. Johnson, H. Sehitoglu, D.D. Johnson, Quantitative prediction of twinning stress in fcc alloys: Application to Cu-Al, *Phys. Rev. B.* 79 (2009) 214202. doi:10.1103/PhysRevB.79.214202.

- [301] P. Haasen, Plastic deformation of nickel single crystals at low temperatures, *Philos. Mag.* 3 (1958) 384–418. doi:10.1080/14786435808236826.
- [302] F. Sun, J. Zhang, H. Harada, The Critical Resolved Shear Stress for Twinning in a Modern Single Crystal Ni-Based Superalloy TMS-82, *Adv. Eng. Mater.* 15 (2013) 1034–1039. doi:10.1002/adem.201300136.
- [303] L.L. Shaw, J. Villegas, J.-Y. Huang, S. Chen, Strengthening via deformation twinning in a nickel alloy, *Mater. Sci. Eng. A.* 480 (2008) 75–83. doi:10.1016/J.MSEA.2007.06.072.
- [304] G. Laplanche, A. Kostka, O.M. Horst, G. Eggeler, E.P. George, Microstructure evolution and critical stress for twinning in the CrMnFeCoNi high-entropy alloy, *Acta Mater.* 118 (2016) 152–163. doi:10.1016/J.ACTAMAT.2016.07.038.
- [305] V. Yamakov, D. Wolf, S.R. Phillpot, A.K. Mukherjee, H. Gleiter, Dislocation processes in the deformation of nanocrystalline aluminium by molecular-dynamics simulation, *Nat. Mater.* 1 (2002) 45–49. doi:10.1038/nmat700.
- [306] V. Sriram, J.-M. Yang, J. Ye, A.M. Minor, Determining the stress required for deformation twinning in nanocrystalline and ultrafine-grained copper, *JOM.* 60 (2008) 66–70. doi:10.1007/s11837-008-0121-0.
- [307] S.S. Cai, X.W. Li, N.R. Tao, Orientation dependence of deformation twinning in Cu single crystals, *J. Mater. Sci. Technol.* 34 (2018) 1364–1370. doi:10.1016/J.JMST.2017.10.004.
- [308] C.X. Huang, K. Wang, S.D. Wu, Z.F. Zhang, G.Y. Li, S.X. Li, Deformation twinning in polycrystalline copper at room temperature and low strain rate, *Acta Mater.* 54 (2006) 655–665. doi:10.1016/J.ACTAMAT.2005.10.002.
- [309] F. Teng, Investigation of Thermal Degradation in Structural Alloys for Nuclear Power Systems, (2018). https://ir.library.oregonstate.edu/concern/graduate_thesis_or_dissertations/qz20sz66q (accessed February 27, 2019).
- [310] P. Hertz, \blacklozenge ber den gegenseitigen durchschnittlichen Abstand von Punkten, die mit bekannter mittlerer Dichte im Raume angeordnet sind, *Math. Ann.* 67 (1909) 387–398. doi:10.1007/BF01450410.

- [311] S. Chandrasekhar, Stochastic Problems in Physics and Astronomy, *Rev. Mod. Phys.* 15 (1943) 1–89. doi:10.1103/RevModPhys.15.1.
- [312] B. Devincre, T. Hoc, L.K.- Science, undefined 2008, Dislocation mean free paths and strain hardening of crystals, [Science.sciencemag.org](http://science.sciencemag.org). (n.d.). <http://science.sciencemag.org/content/320/5884/1745.short> (accessed May 28, 2019).
- [313] P. Franciosi, M. Berveiller, A. Zaoui, Latent hardening in copper and aluminium single crystals, *Acta Metall.* 28 (1980) 273–283. doi:10.1016/0001-6160(80)90162-5.
- [314] M. Klinger, More features, more tools, more *CrysTBox*, *J. Appl. Crystallogr.* 50 (2017) 1226–1234. doi:10.1107/S1600576717006793.

VITA

Mr. Keyou Mao is a Ph.D. candidate in the Materials Engineering department at Purdue University. He was born in Wuxi, China on August 5th, 1992. His dissertation title is *Influence of irradiation and laser welding on deformation mechanisms in austenitic stainless steels*. His research focus is on the manufacturing-microstructure-mechanical property relationships of materials under neutron/ion irradiation, which includes advanced stainless steels, nickel-based super alloys, metallic fuels, etc. His primary area of experimental expertise includes advanced electron microscopy characterization and small-scale mechanical testing. He was a graduate research intern in the Characterization and Advanced PIE division at Idaho National Laboratory since October 2017 to September 2018. He has worked on multiple DOE projects, including the Nuclear Energy University Program (NEUP), Nuclear Energy Enabling Technology (NEET), and Laboratory Directed Research and Development (LDRD) and NSUF Rapid Turnaround Experiments (RTE) projects. He holds a M.S. in nuclear engineering from Purdue University in 2016. His master thesis is *Development of drift-flux correlation and flow pattern transition criteria for two-phase crossflow in horizontal tube bundles*. He also holds bachelor's degree in Engineering Science in Xi'an Jiaotong University with collaborative program with Mechanical Engineering in University of California, San Diego from 2013 to 2014. In 2014, He performed the senior thesis design on *AP1000 severe accident early-phase fuel rod cladding oxidation model theory and code development* with Dr. Michael L. Corradini at the Engineering physics department in University of Wisconsin, Madison. Before undergraduate study, he attended Wuxi No.1 High School. His research interests includes development of advanced fuels and materials for nuclear energy systems; microstructural and mechanical characterization of nuclear fuels and materials, with focus on small-scale mechanical testing; neutron/ion irradiation damage of nuclear materials; process-microstructure-mechanical property relationships of nuclear materials in extreme environments; spent fuel analysis and radioactive waste management; severe accident analysis; energy policy. He has mentored 12 graduate and undergraduate researchers. He has memberships of professional societies such as The Minerals, Metals & Materials Society, Tau Beta Pi, Microscopy Society of America, American Nuclear Society and Alpha Nu Sigma. Upon graduation, he will join Oak Ridge National Laboratory as a postdoctoral research associate.

PUBLICATIONS

- [1] E. Getto, B. Tobie, E. Bautista, A.L. Bullens, Z.T. Kroll, M.J. Pavel, K.S. Mao, D.W. Gandy, J.P. Wharry, Thermal Aging and the Hall–Petch Relationship of PM-HIP and Wrought Alloy 625, *JOM*. (2019) 1–9. doi:10.1007/s11837-019-03532-6.
- [2] K.S. Mao, C. Sun, Y. Huang, C.-H. Shiau, F.A. Garner, P.D. Freyer, J.P. Wharry, Grain orientation dependence of nanoindentation and deformation-induced martensitic phase transformation in neutron irradiated AISI 304L stainless steel, *Materialia*. 5 (2019) 100208. doi:10.1016/J.MTLA.2019.100208.
- [3] K.S. Mao, Y. Wu, C. Sun, E. Perez, J.P. Wharry, Laser weld-induced formation of amorphous Mn–Si precipitate in 304 stainless steel, *Materialia*. 3 (2018) 174–177. doi:10.1016/j.mtla.2018.08.012.
- [4] Y. Bazarbayev, M. Kattoura, K.S. Mao, J. Song, V.K. Vasudevan, J.P. Wharry, Effects of corrosion-inhibiting surface treatments on irradiated microstructure development in Ni-base alloy 718, *J. Nucl. Mater.* 512 (2018) 276–287. doi:10.1016/j.jnucmat.2018.10.006.
- [5] K.H. Yano, K.S. Mao, J.P. Wharry, D.M. Porterfield, Investing in a permanent and sustainable nuclear waste disposal solution, *Prog. Nucl. Energy*. 108 (2018) 474–479. doi:10.1016/j.pnucene.2018.07.003.
- [6] A.L. Bullens, E. Bautista, E.H. Jaye, N.L. Vas, N.B. Cain, K. Mao, D.W. Gandy, J.P. Wharry, Comparative Thermal Aging Effects on PM-HIP and Forged Inconel 690, *JOM*. 70 (2018) 2218–2223. doi:10.1007/s11837-018-2818-z.
- [7] K. Mao, H. Wang, Y. Wu, V. Tomar, J.P. Wharry, Microstructure-property relationship for AISI 304/308L stainless steel laser weldment, *Mater. Sci. Eng. A*. 721 (2018) 234–243. doi:10.1016/j.msea.2018.02.092.
- [8] K. Mao, Y. Wu, J.P. Wharry, EBSD and TEM Analysis of the Heat Affected Zone of Laser Welded AISI 304/308 Stainless Steel, *Microsc. Microanal.* 23 (2017) 2212–2213. doi:10.1017/S1431927617011722.